Development of a high-power, ultrashort pulse duration optical parametric amplification system

by

Hugo Giordano

June 1998

This thesis is entirely my own work,
except where explicitly indicated.

Hugo Giordano

Laser Physics Centre
Research School of Physical Sciences and Engineering
Australian National University
Canberra.

Acknowledgments

There are many people who have helped me along this very long, windy path towards completing my PhD. Without them I would never have found the way to the end.

I would like to thank my supervisors Prof. Barry Luther-Davies, Dr Andrei Rode and Prof. Eugene Gamaly. Barry was always there asking poignant questions which would send me scurrying away back to the lab or computer in search for an answer. More often than not finding that the answer was helpful to continuing my work. Thanks to Andrei who was always there to lend a hand with experiments and to complain too when things weren't working. I would also like to thank Dr Yanjie Wang, who worked as a Post-Doctoral Fellow in the same lab when I first started, for his kind assistance and instruction.

Many people in the Centre deserve thanks because without their practical skills I would still be staring at an empty optical bench. Thanks to Ian McRae, Wally Hopkinson, Craig MacLeod and John Bottega for constructing and dealing with all things mechanical. It was great to go to the workshop with an idea of what I thought was needed and to leave with something that would actually work much better than my original idea. Thanks to Mike Pennington, Warren Baker and Paul Morrison who were always willing to make electronic devices, despite often having only vague ideas from me on what I wanted. Thanks to Anita Smith for her help. She had to put up with me and my PhD more than anyone else in the Centre for a quite a while.

To the Samocs, Neil Manson, Maryla and Wieslaw, Alex Boiko, John Martin, Robbie Charters, Changjiang Wei, Matt Sellars and everyone else, you were ever helpful in providing advice and information. Diane Hodges and Karen Montefiore were always there to be Oracles on whatever I needed to know or to do regarding the School or University or whatever.

To the crazy dudes who live in Greenacres and the surrounding PhD student environs, many thanks. Always a source of fun, information, friendship and stupid postcards; without you I would have gone completely insane many years ago. Thanks to Sleepy Max, Chief Administrator Esa, Bruce the Snake, Sex Rocket Subho, Smelly Phil, Double Dougster, Jason, David, Jen, Andrew, Kylie, Tim, Weijian, Andy G, Geoff, Wenqian, Scott and Max L.

I have meet many people who became friends throughout my stay in Canberra, they deserve thanks for the many good times I have enjoyed and providing an escape from the PhD. Special thanks go to my family and to my girlfriend Leanne Murdoch who were always there to support me, especially during the last two difficult years.

For my Parents

Abstract

This thesis presents work carried out into the design and construction of an optical parametric amplification system to produce ~ GW power, sub-500 fs pulses that are wavelength tunable from 1.3 μm to 1.6 μm. Instead of using femtosecond lasers and amplifiers, such as those based on Ti:Sapphire, the system was based on the longer pulse duration Nd:YLF lasers and amplifiers. A cw, mode-locked Nd:YLF laser acted as the master oscillator to provide initial 60 ps pulses for use by a synchronously pumped optical parametric oscillator (OPO) and two optical parametric amplifiers (OPAs).

The OPO, based on Lithium Triborate (LBO), was pumped by the frequency doubled, compressed pulse from the Nd:YLF laser. Utilising a optical fibre-diffraction grating pulse compressor the pulses were compressed from 60 ps to ~ 2.5 ps in duration and the available peak power enhanced from 4.5 kW to 16 kW. After SHG the 527 nm pulses were 2.3 ps in duration and had peak powers of 6.5 kW. This was more than enough to drive the OPO up to six times above threshold with minimal cavity losses. With the addition of an intracavity dispersion compensating prism pair the OPO produced ~ 200 W, ~ 1.5 ps Gaussian pulses from 780 nm to 900 nm that displayed no discernible phase modulation. These pulses were planned to be used as seed pulses for OPAs.

The OPO displayed the novel behaviour of the resonated signal pulse oscillating on several widely spaced, multiple wavelengths and there were radical changes in the idler beam profile from a Gaussian-like beam into a ring shaped beam with small shifts in the cavity length. Both effects were linked to the ability to drive the OPO many times above threshold where the parametric gain was saturated and the internal conversion efficiency was maximised.

It was envisaged that a group velocity mismatched second harmonic generation (GVMSHG) system would produce high power, sub-500 fs, 527 nm pulses to amplify the seed signal pulses from the OPO in the OPAs. Nd:YLF regenerative and single pass amplifiers boosted the energy of frequency chirped pulses from the Nd:YLF laser to ~ 18 mJ while reducing the pulse duration to ~ 6 ps, through the narrow gain bandwidth of Nd:YLF, to provide the high power fundamental pulse. Using type II SHG in Potassium Dihydrogen Phosphate (KDP) a second harmonic (SH) pulse can be efficiently generated and compressed in time through careful use of the intrinsic group velocity mismatch (GVM) in KDP and by delaying the e-ray fundamental with respect to the o-ray fundamental before entering the KDP SHG crystal(s). Even under the non-optimal conditions in the experiment it was expected that a 2 mJ, sub-500 fs SH pulse would result from the GVMSHG system.

Significant problems became apparent during the experiments with the GVMSHG system that inhibited the GVM compression mechanism from performing efficiently. Considerable effort was out into fixing these problems; which were finally solved shortly before this thesis was due for submission. It is expected that future experiments will produce the expected SH pulses.

While experiments were not performed, numerical simulations were undertaken to optimise the design of the OPAs. Using a two crystal optical parametric amplification system it is expected that ~ 600 MW, ~ 300 fs signal pulses, tunable from 780 nm to 900 nm, and ~300 MW, ~ 300 fs idler pulses, tunable from 1270 nm to 1625 nm, will be produced by the seed signal pulses from the OPO when pumped by the compressed SH pulse from the GVMSHG system.

This thesis has been reviewed and corrected.

Contents

1. Introduction

This thesis presents work carried out into the construction of a high power (~ 1 GW), ultra-short pulse duration (~ 300 fs) optical parametric amplification system that could produce wavelength tunable pulses from 780 nm to 900 nm and from 1270 nm to 1625 nm. High power, short pulses, tunable across the important telecommunication windows centred at 1.3 μm and 1.55 μm were needed by researchers at the Laser Physics Centre for material testing of organic polymers that are potentially useful photonic devices [1, 2]. The main novelty of the work was the attempt to base this system solely on Nd:YLF laser technology in combination with various optical parametric oscillators and amplifiers and incorporating the novel group velocity mismatched frequency doubling process to obtain the ultra-short optical parametric amplifier (OPA) pump pulses. This approach was intended as an alternative to the more conventional route of using broad bandwidth lasers such as Ti:Sapphire to drive the optical parametric oscillator (OPO) and OPA.

This chapter serves as a guide for the rest of the thesis. It introduces and explains the major components of the system, as well as, placing each one in context with previous work.

1.1 Optical parametric processes

Optical parametric amplification and second harmonic generation (SHG) rely upon a nonlinear response from a suitable material when illuminated by an intense optical beam. When a low powered optical beam propagates through a material the electrical charges in the material will normally respond in linear fashion to the applied electric field, absorbing or remitting the radiation at the same frequency. The electric field of the optical beam can be thought of as perturbing the orbits of the valence electrons of atoms in the material. Thereby creating electric dipoles and generating a polarisation wave.

When the strength of the applied electric field is increased, by illuminating the material with a much more intense optical beam, the highly perturbed dipoles no longer respond in just a linear fashion but in a nonlinear fashion as well. This leads to the creation of new frequencies and other effects.

The induced polarisation wave, $\mathbf{P}$, in a material exposed to an intense optical beam can be described as a function of the applied electric field, $\mathbf{E}$, of the optical beam.

$$\mathbf{P}_j(\omega_a) = \varepsilon_0 \sum_k \chi_{jk}^{(1)}(\omega_a) : \mathbf{E}_k(\omega_a) + \varepsilon_0 g_1 \sum_{kl} \chi_{jkl}^{(2)}(-\omega_a;\omega_1,\omega_2) : \mathbf{E}_k(\omega_1)\mathbf{E}_l(\omega_2) +$$

$$\varepsilon_0 g_2 \sum_{klm} \chi_{jklm}^{(3)}(-\omega_a;\omega_1,\omega_2,\omega_3) : \mathbf{E}_k(\omega_1)\mathbf{E}_l(\omega_2)\mathbf{E}_m(\omega_3) + \ ...$$

where χ is the susceptibility tensor; g_i are degeneracy factors; a, 1, 2, 3, ... are the different frequency components and j, k, l, m, ... are Cartesian subscripts denoting the indices x, y, z.

The first term, that is directly proportional to $\mathbf{E}$, describes linear effects such as absorption, reflection and refraction. The second term in the expansion is responsible for effects such as SHG, optical parametric generation (OPG) and amplification and only occurs in noncentrosymmetric crystals (no center of symmetry). The last term is responsible for effects such as third harmonic generation and the optical Kerr effect.

For SHG the induced polarisation wave is at twice the frequency of the incident radiation. SHG is a special case of the parametric process where $\omega_1 = \omega_2 = \omega$ which add together to generate a wave at twice the frequency (degenerate sum frequency generation).

$$\mathbf{P}_j(2\omega) = \frac{\varepsilon_0}{2} \sum_{kl} \chi_{jkl}^{(2)} \mathbf{E}_k(\omega)\mathbf{E}_l(\omega)$$

For optical parametric generation and amplification there are two incident fields with different frequencies, ω_3 and ω_1, which generate or amplify another frequency at $\omega_2 = \omega_3 - \omega_1$ (difference frequency generation).

$$\mathbf{P}_j(\omega_3 - \omega_1) = \varepsilon_0 \sum_{kl} \chi_{jkl}^{(2)} \mathbf{E}_k(\omega_3)\mathbf{E}_l(\omega_1)$$

In the case of optical parametric generation the incident field at ω_3 is much more intense than the fields at ω_1 or ω_2, the fields at these frequencies are amplified from quantum noise. This is the process that occurs in the OPO. Of these frequencies one is called the signal (1) and the other is called the idler (2); with the lower frequency of the two being the idler, ie. $\omega_3 > \omega_1 > \omega_2$.

While energy is conserved in these parametric processes, ie.

$$\omega_3 = \omega_1 + \omega_2 \ \text{(OPA)} \quad \text{or} \quad 2\omega = \omega + \omega \ \text{(SHG)} \ (\omega_1 = \omega_2)$$

for the processes to be efficient momentum needs to be conserved as well.

$$\mathbf{k_3} = \mathbf{k_1} + \mathbf{k_2} \quad \text{or} \quad \frac{n_3(\theta, T)}{\lambda_3} = \frac{n_1(\theta, T)}{\lambda_1} + \frac{n_2(\theta, T)}{\lambda_2}$$

where n is the refractive index of the material at that frequency. This is known as phase matching. By choosing the polarisation of the interacting waves momentum is conserved in birefringent crystals through careful adjustment of the angle, θ, or temperature, T, of the crystal.

With SHG or OPA of pulses shorter than a few picoseconds the material dispersion plays an important role. Most crystals will have enough dispersion to create differences in the group velocities, group velocity mismatch (GVM), on the order of ~ 1 ps / cm between the interacting waves. If the pulse is short enough and the crystal length long enough the GVM will cause the pulses to "walk away" from each other while interacting in the crystal; limiting the efficiency of the process and changing the dynamics of the interaction.

1.2 Overview

The optical parametric amplification system consisted of a number of different components and is shown in Figure 1-1. A mode-locked, cw Nd:YLF laser (Coherent Antares 76-YLF), labelled *Antares Laser* in the figure, acted as a master oscillator providing seed pules to drive not only the OPO but also the amplifiers. Since the Antares system produced pulses more than two orders of magnitude longer than required from the system, the output pulses were chirped in optical fibres as part of the pulse compression schemes. The output from one of the fibres was compressed using a diffraction grating (*Pulse Compressor* in the figure) and then frequency doubled, (labelled *SHG*) to create short pump pulses for a synchronously pumped, cw, Lithium Triborate (LBO) optical parametric oscillator (OPO) (*LBO OPO* in the figure). The power from the
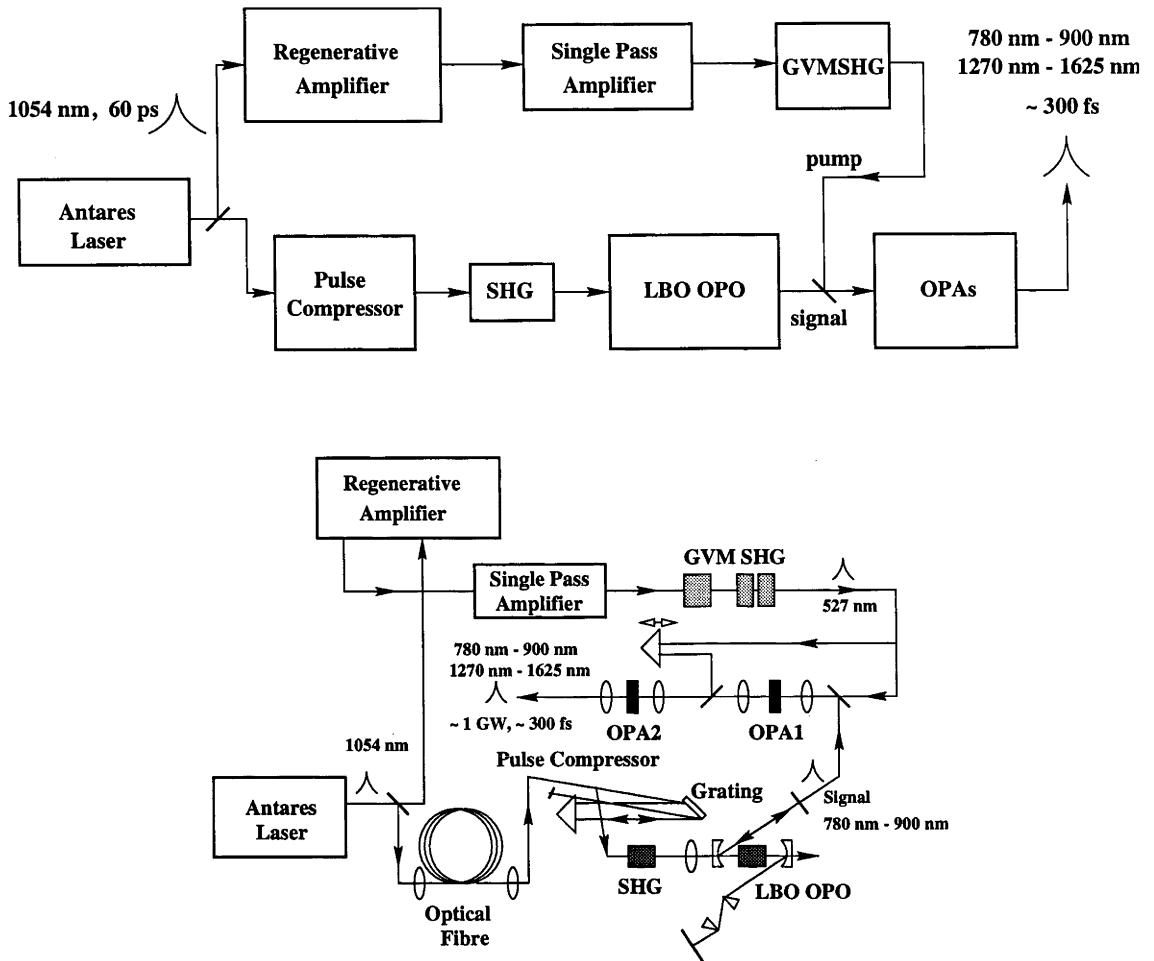
Figure 1-1 : The basic schematic (top) and a more detailed experimental layout (bottom) of the optical parametric amplification system.

second fibre was used as a source of seed pulses for a Nd:YLF based amplifier system (*Regenerative Amplifier* and *Single Pass Amplifier*). The high power pulses from this amplifier system were to be frequency doubled (*GVM SHG*) to generate 300 - 500 fs pulses at 527 nm to pump two optical parametric amplifiers (*OPAs*). The OPAs were intended to amplify the signal pulses from the LBO OPO to generate high power, ultrashort, wavelength tunable pulses in the infra-red.

A pulse compressor, apart from reducing the duration of the output pulses from the Antares also served to boost the peak pulse power to a level where the OPO could be driven well above threshold and therefore operated stably. The pulse compressor was a conventional fibre-grating system chosen for its ease of implementation; its ability to enhance the peak power of the pulses more than other methods; and its ability to reduce the pulse duration to the desired ps range. When the pulse from the Antares laser was coupled into the optical fibre, self phase modulation (SPM) resulted in the development of a linear frequency chirp across a portion of the pulse (the frequencies are lower in the leading edge of the pulse and higher in the trailing edge) and the spectrum of the pulse was broadened. This frequency chirp allowed the pulse to be compressed in time in a linearly dispersive delay line. The delay line consisted of a single diffraction grating and a right angle prism that folded the beam so that the pulse from the optical fibre made four reflections from the diffraction grating. The angular dispersion of the diffraction grating was used to correct the SPM induced dispersion in the pulse. The lower frequency components of the pulse travelled further than the higher frequency components. With the propagation distance carefully set

3

so that all the frequency components emerged in synchronisation when the pulse exited the pulse compressor; thereby compressing the pulse in time from 60 ps from the Antares laser down to ~ 2.5 ps.

These pulses were then frequency doubled using a single pass LBO SHG crystal. The 527 nm pulses produced were used to pump an LBO OPO. In the OPO, the 527 nm pump pulse was converted into two, different, lower frequency signal and idler pulses [3].

For the case of the LBO OPO, the generated signal pulses were resonated in an optical cavity (singly resonant oscillator). The length of the cavity was carefully adjusted so that the circulating signal pulse arrived in synchronisation with the pump pulses at the LBO crystal, ie. the OPO was synchronously pumped. In this way the signal and idler pulses could be efficiently amplified from noise to reach power levels that were on the order of the pump pulse. The LBO OPO used type I, temperature tuned, non-critical phase matching and hence the operating wavelength range theoretically lay between 650 nm and 1053 nm (degeneracy) for the signal and 1053 nm to 2600 nm for the idler. In practice the range was limited by the reflectivity range of the mirrors used in the OPO cavity (from 780 nm to 900 nm typically). Some of the signal pulse energy was coupled from the cavity through the output mirror and these signal pulses were to be used as seed pulses for the OPAs.

It was decided to use an OPO to produce seed pulses for the OPAs instead of, for example, a Ti:Sapphire laser, or a optical parametric generator (OPG) for a number of reasons. Firstly, the LBO OPO has an intrinsically greater wavelength tuning range than a Ti:Sapphire laser. To cover the wavelength range from 780 nm to 900 nm and to maintain the peak power of the output pulses normally requires 2 to 3 mirrors set for a ps Ti:Sapphire laser whereas it can easily be covered by an OPO with a single mirror set without the problems in the loss of the peak power of output pulses. A singly resonant OPO has the added advantage of producing broadly tunable idler pulses which can be coupled from the cavity with small loss. An OPG (where the signal and idler pulses are amplified from noise by a high gain OPA) was not favoured either on the grounds it is difficult to obtain transform limited pulses from an OPG whereas OPO pulses can be constrained by intracavity elements. Finally, the OPO pulses are naturally synchronised with the pump pulses which makes it relatively easy to synchronise the short OPO pulses with the pump pulses of the OPAs if the same laser oscillator is used in both systems.

A small fraction of the power from the Antares laser was used to provide input pulses for a Nd:YLF amplifier system. The amplifier system consisted of a ring regenerative amplifier and a single pass power amplifier. The system as a whole amplified the pulses from the Antares to the several mJ (~ GW) level, while simultaneously reducing the duration of the pulses from 60 to around 6 ps.

These high power pulses were to intended to be frequency doubled and used as pump pulses for the OPAs. The frequency doubling scheme used group velocity mismatched second harmonic generation (GVMSHG) in the so-called alternating-Z crystal geometry. GVMSHG has been demonstrated to be capable of producing sub-ps second harmonic pulses from much longer (several picosecond) fundamental pulses. GVMSHG works efficiently for type II SHG in KDP and requires a delay crystal, that "splits" the 1054 nm pulses into two, temporally separated e-ray and o-ray pulses (known as predelay). In the doubler crystals the intrinsic GVM between the e- ray and o-ray fundamental pulses and the predelay interact to efficiently generate a compressed second harmonic pulse. The process uses a fortuitous relationship between the group velocities of the e- and o-ray fundamentals and the e-ray second harmonic which leads to the fast e-ray fundamental pulse overtaking the slow o-ray fundamental pulse in a transit of the crystal. The short second harmonic pulse, which travels with a group velocity approximately equal to the arithmetic mean of the fundamentals, interacts with all time points in both fundamentals and can therefore accumulate energy in a much shorter second harmonic pulse. Simulations showed that the

GVMSHG system could efficiently generate a pulse at 527 nm that was at least an order of magnitude shorter in duration. The alternating-Z scheme employed two SHG, type II Potassium DiHydrogen Phosphate (KDP) crystals with their optic axes aligned as mirror images alleviated problems associated with the small angular acceptance angle of type II SHG in KDP. Significant problems became apparent while working with the GVMSHG system that were not successfully resolved until just before this thesis was due for submission. It is expected that the GVMSHG system will perform efficiently in future experiments and allow testing of the whole optical parametric amplification system.

This GVMSHG system was employed to extend previous work carried out in the Laboratory and because it provided an elegant solution to efficiently generating a short, second harmonic pulse from a longer fundamental pulse. If this method was not used it would have been necessary to compress the fundamental pulse and then carry out SHG. The GVMSHG does both of these functions at once in a much simpler experimental apparatus.

While experiments with the two OPAs (referred to as OPA1 and OPA2) could not be carried out because of problems with the GVMSHG system, simulations were performed to optimise the design of the OPAs. These indicated that the low power signal pulses from the OPO should be amplified using two separate OPAs, when pumped by the compressed second harmonic pulse from the GVMSHG system, to produce high power, ultrashort signal and idler pulses tunable across the desired wavelength range. The simulations looked in detail at many factors that could have influenced the performance of the OPAs. In particular the use of two OPAs rather than a single higher gain amplifier crystal provided a more controllable parametric gain process.

1.3 Brief review of previous work

1.3.1 Pulse compressors

Fibre-diffraction grating pulse compressors have been in use since the start of the 1980s for compressing pulses in time to the picosecond [4] or femtosecond ranges [5]. Long lengths of optical fibre, typically much greater than 50 metres, employ GVD to extend the SPM induced frequency chirp from the central portion to the entire pulse [6], improving the quality and reducing the duration of the compressed pulse. A draw back of the use of long fibres is, however, associated with their limited peak power handling due to the onset of Stimulated Raman Scattering [7]. Two stage pulse compressors can be used to circumvent this problem and can result in high power, high quality, femtosecond pulses [8]. Since high power, picosecond pulses were needed to pump the OPO, a single stage pulse compressor was chosen, employing a relatively short length of fibre (less than 50 metres). This was capable of handling close to the full power of the Antares laser without problems from Raman scattering, whilst also permitting efficient compression of the 60 ps, 1054 nm pulses (a system that was similar to that used to pump a KTP OPO reported in [9]). Spectral windowing [10] and the nonlinear polarisation rotation in the fibre [11] can be used to improve the quality of the compressed pulses. However, the extra complexity of spectral windowing was not required in our pulse compressor because, as will be shown, the SHG improved the quality of the pulses dramatically; though the polarisation state of the pulses was adjusted to provide the "best" compressed pulse (effectively making use of nonlinear polarisation rotation). A complete review of previous work and background theory can be found in Chapter 6 of "Nonlinear Fibre Optics" by Agrawal [12].

1.3.2 Optical parametric oscillators

Numerous OPOs have been constructed and their development began shortly after the laser was invented. They have covered a wide range of optical and infrared wavelengths and have been pumped both by ultra-short femtosecond pulses and recently using pure cw beams. In relation to LBO OPOs, LBO was introduced by Chen, *et. al.*, [13] in 1989 and was soon used as the nonlinear crystal in OPOs synchronously pumped by a diode-pumped, frequency doubled, Q-switched, mode-locked Nd:YLF laser [14, 15] and a flashlamp-pumped, frequency doubled, Q-switched, mode-locked Nd:YAG laser [16]. With their LBO based OPO the University of Strathclyde group (Nd:YLF laser) built on their previous synchronously pumped OPO work with MgO:LiNbO$_3$ [17] and KTP [18]. Also in 1992 the first cw synchronously pumped LBO OPO was reported [19]; pumped by a frequency doubled, diode-pumped, mode-locked Nd:YLF laser. It generated ps pulses from 650 nm to 2.7 µm. However, this OPO operated very close to threshold when working as a singly-resonant oscillator. This was due to lack of the high peak power pulses from the Nd:YLF laser. This work was soon followed by another OPO with a Brewster-Brewster angled LBO crystal, synchronously pumped by a frequency doubled, diode-pumped, cw, mode-locked Nd:YLF laser, that operated further above threshold and provided ~ 200 to 300 W , 1.6 ps pulses from 720 nm to 1.91 µm [20]. Reviews of the work are presented in [21, 22].

At the same time work was presented by Chung and Siegman [9] on a KTP OPO synchronously pumped by a pulse compressed, flashlamp-pumped, cw, mode-locked Nd:YAG laser. To achieve higher peak power pump pulses for their KTP OPO they compressed the 1.5 kW, ~ 90 ps pulses from a conventional mode-locked Nd:YAG laser to 25 kW, ~ 2.2 ps pulses using a optical fibre-diffraction grating pulse compressor. They obtained ~ 1 kW, 2 to 3 ps signal and idler pulses tunable across the narrow wavelength ranges of 1.57 to 1.59 µm and 3.21 µm to 3.3 µm. A similar frequency doubled, laser system used with LBO rather than KTP would provide similar high peak powers and ps pulses, but would be tunable between 0.65 µm to 2.6 µm. Furthermore such an OPO could be operated much higher above threshold, where efficient, stable operation could be obtained, compared to previous LBO OPOs. This provided the motivation for developing an LBO OPO pumped by a frequency doubled, pulse compressed Antares laser to provide stable, broadly tunable seed pulses for the OPAs.

Other reports of synchronously pumped LBO OPOs included the use of a ring cavity [23]; synchronous pumping using a ps Ti:Sapphire laser [24-27]; frequency doubling of the output from this last type of LBO OPO [28]; and [29] with synchronously pumping using an amplified version of the diode-pumped Nd:YLF laser used in earlier experiments [30]. In all cases the OPOs could be driven further above threshold than in earlier devices allowing the insertion of intracavity, dispersion compensating prism pairs to control the GVD and SPM in the cavity and to make the output pulses close to transform limited.

1.3.3 Group velocity mismatched second harmonic generation

The use of a predelay between the e-ray and o-ray fundamental pulses to efficiently compress the SH pulse was first investigated by Wang, *et. al.*, [31-33] and Stabinis, *et. al.* [34]. Using a predelay of 1.4 ps a 240 % power conversion and ~ 240 fs SH pulses resulted from type II SHG of 1.2 ps, 1054 nm pulses in a 25 mm thick KDP crystal.

GVMSHG [35] has also produced ~ 360 fs SH pulses from a 4 cm long KDP crystal pumped by a 12 ps, 20 mJ, 1064 nm amplified pulse from a Nd:YAG amplifier laser system using predelays roughly equal to the fundamental pulse duration. While the compressed SH pulses from this system had short central peaks they suffered from large sidelobe peaks that were due to SPM in the fundamental pulses. Strong spatial filtering and apodized apertures, centred on the beam, were required to ensure a uniform beam profile and useable quality

pulse. Their GVMSHG system was therefore limited by the available fundamental peak power.

The GVMSHG system in this thesis was designed to compress ~ 6 ps, 18 mJ pulses to ~ 500 fs or less, > 1 mJ SH pulses using two 1.75 cm KDP crystals in an alternating-Z configuration [36] that alleviated problems with the small angular acceptance angle and beam walk-off off KDP.

1.3.4 Optical parametric amplifiers

Numerous OPA systems have been constructed using a number of different nonlinear crystals and pump lasers in the last decade. Of the systems constructed for amplification of sub-ps visible to near infra-red pulses the most popular pump lasers are the Ti:Sapphire regenerative amplifier and the Nd based amplifier laser systems.

The Ti:Sapphire pump laser or its harmonic has been used in the optical parametric amplification of white light continuum seed radiation [37-43] using type I and II phasematching in β-barium borate (BBO) to generate femtosecond, near transform-limited pulses tunable through the visible and the near IR. The Ti:Sapphire laser has also been used with KTP and $KNbO_3$ [44] and BBO [45, 46] to generate and amplify wavelength tunable, femtosecond pulses.

Mode-locked, mJ energy, ~ 30 ps, frequency doubled Nd based lasers have been used with LBO [47, 48], BBO [49-51] and a LBO/BBO combination [52, 53] to generate and amplify broadly tunable, picosecond pulses. Highly tunable, ps, OPA systems have been developed based on KTP [54], tunable between 0.6 μm to 4 μm, and on a LBO / $AgGaS_2$ (Silver Thiogallate) [55], tunable between 0.41 μm to 12.9 μm. An OPA with a very broad spectral gain bandwidth has been developed using type I, noncollinear phase matching in BBO [56]. The same phase matching scheme that has been used to make spectrally broad pulses in an OPO [57].

Perhaps the closest OPA system to the one modelled in this thesis was a triple-pass, 4 mm long, type II, BBO OPA that was pumped by a 1.1 mJ, 200 fs, compressed 527 nm pulse from a GVMSHG system and that produced wavelength tunable, 200 fs signal and idler pulses between 635 nm to 3000 nm [58].

The OPA system modelled in this thesis can efficiently produce ~ 300 fs, ~ 1 GW pulses between 1.27 μm to 1.625 μm. It examines the effect of variation in input parameters on the performance of the OPAs.

1.4 Thesis outline

Chapter 2 presents the relevant theory behind optical fibre-grating pulse compressors; explains the construction of the pulse compressor and the limitations and performance of the pulse compressor. It also describes the LBO SHG and provides detailed measurements and analysis of the compressed 1054 nm and the second harmonic pulses.

Chapter 3 presents the background theory that is relevant to the ps, synchronously pumped LBO OPO, as well as, details on the design, construction and alignment of the OPO. Initially, the cw beam from the Antares laser was chopped, reducing the average power to protect the optical fibre in the pulse compressor. In later experiments, the fibre mount was modified so that the full cw power of the Antares could be used. Measurements and analysis of the LBO OPO operating with the chopped cw pump beam and the full cw pump beam are

presented. Details are also presented on the performance of the OPO operating with a dispersion compensating prism pair that improved the quality of the resonated signal pulses.

Chapter 4 introduces further information on novel behaviour that occurred in the LBO OPO. The resonated signal pulse in the LBO OPO (without a prism pair) sometimes oscillated on multiple, widely spaced frequencies. Also, while the signal beam profile always remained close to a TEM_{00} Gaussian the idler beam profiles displayed radical changes in shape with small shifts in the cavity length. An explanation of the behaviour of the idler beam profiles and a discussion of factors that cause the multiple frequency oscillation are presented.

Chapter 5 describes the theory of GVMSHG and the benefits of using two crystals in an alternating-Z configuration. Numerical simulations are presented based on measured experimental parameters. Initial experiments did fit theoretical expectations and details related to tracking down and solving the causes of these problems are presented and discussed. As mentioned previously, all the problems were not rectified until shortly before this thesis was due for submission. It is expected that the GVMSHG will produce compressed SH pulses that closely match theoretical expectations in future experiments.

Chapter 6 reports on numerical simulations carried out into a high gain OPA system that consisted of two nonlinear crystals. The simulations look at how variations in parameters such as the pump peak power, the seed peak power, and different nonlinear crystals affected the performance of the system.

Chapter 7 describes the various diagnostic tools used throughout experiments in this thesis. Most of the tools were involved with measuring the temporal amplitude and / or phase of pulses.

Chapter 8 summarises all the chapters, discusses the results and suggests further work that can be carried out.

1.5 References

[1]   F. Kajzar and J. D. Swalen, *Organic thin films for waveguiding nonlinear optics*, vol. 3: Gordon and Breach, 1996.
[2]   C. P. Wong, *Polymers for electronic and photonic applications*. San Diego: Academic Press, Inc., 1993.
[3]   R. L. Byer, *Optical Parametric Oscillators*, in Quantum Electronics: A Treatise, Ed. H. Rabin and C. L. Tang, vol. 1, pt B, p. 587: Acedemic Press, New York, 1975.
[4]   W. Hodel, "Investigation of nonlinear effects in optical single mode fibers," : University of Bern, 1986.
[5]   W. H. Knox, R. L. Fork, M. C. Downer, R. H. Stolen, C. V. Shank, and J. A. Valdmanis, "Optical pulse compression to 8 fs at a 5-kHz repetition rate," *Appl. Phys. Lett.*, vol. 46, p. 1120, 1985.
[6]   Y. Wang, "Development of a high contrast Nd:Glass laser using chirped pulse amplification," PhD, *Laser Physics Centre, RSPhySE*: Australian National University, 1993.
[7]   R. Stolen, "Nonlinearity in fiber transmission," *Procs. IEEE*, vol. 68, p. 1232, 1980.
[8]   B. Zysset, W. Hodel, P. Beaud, and H. P. Weber, "200 femtosecond pulses at 1.06 μm generated with a double stage compressor," *Optics Letters*, vol. 11, p. 156, 1986.
[9]   J. Chung and A. E. Siegman, "Singly resonant continuous-wave mode-locked KTP optical parametric oscillator pumped by a Nd:YAG laser," *JOSA B*, vol. 10, p. 2201, 1993.

[10]   J. P. Heritage, R. N. Thurston, W. J. Tomlinson, A. M. Weiner, and R. H. Stolen, "Spectral windowing of frequency-modulated optical pulses in a grating compensator," *Appl. Phys. Lett.*, vol. 47, p. 87, 1985.

[11]   R. H. Stolen, J. Botineau, and A. Ashkin, "Intensity discrimination of optical pulses with birefringent fibers," *Optics Letters*, vol. 7, p. 512, 1982.

[12]   G. P. Agrawal, *Nonlinear fiber optics*: Academic press, Inc., 1989.

[13]   C. Chen, Y. Wu, A. Jiang, B. Wu, G. You, R. Li, and S. Lin, "New nonlinear-optical crystal : LiB_3O_5," *JOSA B*, vol. 6, p. 616, 1989.

[14]   M. Ebrahimzadeh, G. J. Hall, and A. I. Ferguson, "Temperature-tuned noncritically phase-matched picosecond LiB3O5 optical parametric oscillator," *Appl. Phys. Lett.*, vol. 60, p. 1421, 1992.

[15]   M. Ebrahimzadeh, G. J. Hall, and A. I. Ferguson, "Single resonant, all-solid-state, mode-locked LiB_3O_5 optical parametric oscillator tunable from 652 nm to 2.65 μm," *Optics Letters*, vol. 17, p. 652, 1992.

[16]   H. Zhou, J. Zhang, T.Chen, C. Chen, and Y. R. Shen, "Picosecond, narrow-band, wdiely-tunable optical parametric oscillator using a temperature-tuned lithium borate crystal," *Appl. Phys. Lett.*, vol. 62, p. 1457, 1993.

[17]   G. T. Maker and A. I. Ferguson, "Doubly resonant optical parametric oscillator synchronously pumped by a frequency-doubled, mode-locked, and Q-switched diode laser pumped neodymium yttrium fluoride laser," *Appl. Phys. Lett.*, vol. 56, p. 1614, 1990.

[18]   M. Ebrahimzadeh, G. J. Hall, and A. I. Ferguson, "Picosecond infrared optical parametric generation in KTP using a diode-laser-pumped solid-state laser.," *Optics Letters*, vol. 16, p. 1744, 1991.

[19]   A. Robertson, G. P. A. Malcolm, M. Ebrahimzadeh, and A. I. Ferguson, "Continuous generation of tunable picosecond pulses from 650 nm to 2.7 μm using a CW, synchronously-pumped, all-solid-state, four-colour LiB_3O_5 optical parametric oscillator," presented at Conference on Lasers and Electro-Optics, Anaheim CA., 1992.

[20]   M. J. McCarthy, S. D. Butterworth, and D. C. Hanna, "High-power widely-tunable picosecond pulses from an all-solid-state synchronously-pumped optical parametric oscillator," *Optics Communs.*, vol. 102, p. 297, 1993.

[21]   G. J. Hall, M. Ebrahimzadeh, A. Robertson, G. P. A. Malcolm, and A. I. Ferguson, "Synchronously pumped optical parametric oscillators using all-solid-state pump lasers.," *JOSA B*, vol. 10, p. 2168, 1993.

[22]   M. J. McCarthy and D. C. Hanna, "All-solid-state synchronously pumped optical parametric oscillator," *JOSA B*, vol. 10, p. 2180, 1993.

[23]   A. Robertson and A. I. Ferguson, "Synchronously pumped all-solid-state lithium triborate optical parametric oscillator in a ring configuration," *Optics Letters*, vol. 19, p. 117, 1994.

[24]   M. Ebrahimzadeh, S. French, W. Sibbett, and A. Miller, "Picosecond Ti:Sapphire-pumped optical parametric oscillator based on LiB_3O_5," *Optics Letters*, vol. 20, p. 166, 1995.

[25]   J. D. Kafka, M. L. Watts, and J. W. Pieterse, "Synchronously pumped optical parametric oscillators with LBO," *JOSA B*, vol. 12, p. 2147, 1995.

[26]   M. Ebrahimzadeh, S. French, and A. Miller, "Design and performance of a singly resonant picosecond LBO optical parametric oscillator synchronously pumped by a self-mode-locked Ti:sapphire laser," *JOSA B*, vol. 12, p. 2180, 1995.

[27]   S. French, M. Ebrahimzadeh, and A. Miller, "High-power, high-repetition-rate picosecond optical parametric oscillator for the near- to mid-infrared.," *J. Modern Optics*, vol. 43, p. 929, 1996.

[28]   S. French, M. Ebrahimzadeh, and A. Miller, "Visble picosecond pulse generation in a frequency doubled optical parametric oscillator based on LiB_3O_5," *Opt. Commun.*, vol. 128, p. 166, 1996.

[29]   S. D. Butterworth, S. Girad, and D. C. Hanna, "High-power, broadly tunable all-solid-state synchronously pumped lithium triborate optical parametric oscillator," *JOSA B*, vol. 12, p. 2158, 1995.

[30]   S. D. Butterworth, W. A. Clarkson, N. Moore, G. J. Friel, and D. C. Hanna, "High-power quasi-cw laser pulses via hgih-gain diode-pumped bulk amplifiers," *Opt. Commun.*, vol. 131, p. 84, 1996.

[31]   Y. Wang and R. Dragila, "Efficient conversion of picosecond laser pulses into second-harmonic frequency using group-velocity dispersion," *Phys. Rev. A*, vol. 41, p. 5645, 1990.

[32]   Y. Wang, B. Luther-Davies, Y. H. Chuang, R. S. Craxton, and D. D. Meyerhofer, "Highly efficient conversion of picosecond Nd laser pulses with the use group-velocity-mismatched frequency doubling in KDP," *Optics Letters*, vol. 16, p. 1862, 1991.

[33]   Y. Wang and B. Luther-Davies, "Frequency-doubling pulse compressor for picosecond high-power neodymium laser pulses," *Optics Letters*, vol. 17, p. 1459, 1992.

[34]   A. Stabinis, G. Valiulis, and E. A. Ibragimov, "Effective sum frequency pulse compression in nonlinear crystals," *Opt. Commun.*, vol. 86, p. 301, 1991.

[35]   A. Umbrasas, J.-C. Diels, J. Jacob, G. Valiulis, and A. Piskarskas, "Generation of femtosecond pulses through second-harmonic compression of the output of a Nd:YAG laser," *Optics Letters*, vol. 20, p. 2228, 1995.

[36]   M. A. Norton, D. Eimerl, C. A. Ebbers, S. P. Velsko, and C. S. Petty, "KD*P frequency doubler for high average power applications," *SPIE, Solid State Lasers*, vol. 1223, p. 75, 1990.

[37]   V. V. Yakovlev, B. Kohler, and K. R. Wilson, "Broadly tunable 30 fs pulses produced by optical parametric amplification," *Optics Letters*, vol. 19, p. 2000, 1994.

[38]   M. K. Reed, M. K. Steiner-Shepard, M. S. Armas, and D. K. Negus, "Microjoule-energy ultrafast optical parametric amplifiers," *JOSA B*, vol. 12, p. 2229, 1995.

[39]   R. Danielius, A. Piskarkas, A. Stabinis, G. P. Banfi, P. d. Trapani, and R. Righini, "Traveling-wave parametric generation of widely tunable, highly coherent femtosecond light pulses," *JOSA B*, vol. 10, p. 2222, 1993.

[40]   G. Cerullo, M. Nisoli, and S. d. Silvestri, "Generation of 11 fs pulses tunable across the visible by optical parametric amplification," *Appl. Phys. Lett.*, vol. 71, p. 3616, 1997.

[41]   T. S. Sosnowski, P. B. Stephens, and T. B. Norris, "Production of 30 fs pulses tunable throughout the visible spectral region by a new technique in optical parametric amplification," *Optics Letters*, vol. 21, p. 140, 1996.

[42]   S. R. Greenfield and M. R. Wasielewski, "Near-transform-limited visible and near-IR femtosecond pulses from optical parametric amplification using Type II β-barium borate," *Optics Letters*, vol. 20, p. 1394, 1995.

[43]   H. Wong, K. S. Wong, D. Deng, Z. Xu, G. K. L. Wong, and J. Zhang, "Kilohertz femtosecond UV-pumped visible B-barium borate and lithium triborate optical parametric generator and amplifier," *Appl. Optics*, vol. 36, p. 1889, 1997.

[44]   B. Vezin, M. Douard, P. Rambaldi, and J. P. Wolf, "Tunable no-tracking OPO-OPA tandem in the near-infrared pumped by a Ti:Sapphire laser," *Appl. Phys. B*, vol. 63, p. 199, 1996.

[45]   M. Sueptitz, R. A. Kaindl, S. Lutgen, M. Woerner, and E. Riedle, "1 kHz solid state laser system for the generation of 50 fs pulses tunable in the visible," *Optics Commun.*, vol. 131, p. 195, 1996.

[46]   F. Seifert, V. Petrov, and F. Noack, "Sub-100-fs optical parametric generator pumped by a high-reptition-rate Ti:Sapphire regenerative amplifier system," *Optics Letters*, vol. 19, p. 837, 1994.

[47]   S. Lin, J. Y. Huang, J. Ling, C. Chen, and Y. R. Shen, "Optical parametric amplification in a lithium triborate tunable from 0.65 μm to 2.5 μm," *Appl. Phys. Lett.*, vol. 59, p. 2805, 1991.

[48]   Z. Xu, X. Liu, D. Deng, Q. Wong, L. Wu, B. Wu, S. Lin, B. Lin, C. Chen, and P. Wang, "Multiwavelength optical parametric amplification with angle-tuned lithium triborate," *JOSA B*, vol. 12, p. 2222, 1995.

[49]   F. Huang and L. Huang, "Picosecond optical parametric amplification in β-BaB$_2$O$_4$," *IEEE J. Quant. Electron.*, vol. QE-30, p. 2601, 1994.

[50]   X. D. Zhu and L. Deng, "Broadly tunable picoseond pulses generated in a β-BaB$_2$O$_4$ optical parametric amplifier pumped by 0.532 μm pulses," *Appl. Phys. Lett.*, vol. 61, p. 1490, 1992.

[51]   J. Y. Huang, J. Y. Zhang, Y. R. Shen, C. Chen, and B. Wu, "High-power, widely tunable, picosecond coherent source from optical parametric amplification in barium borate," *Appl. Phys. Lett.*, vol. 57, p. 1961, 1990.

[52]   F. Huang and L. Huang, "Picosecond optical parametric generation and amplification in LBO and BBO," *Appl. Phys. Lett*, vol. 61, p. 1769, 1992.

[53]   J. Y. Zhang, J. Y. Huang, Y. R. Shen, and C. Chen, "Optical parametric generation and amplification in barium borate and lithium triborate crystals," *JOSA B*, vol. 10, p. 1758, 1993.

[54]   H. Vanherzeele, "Picosecond laser system continuously tunable in the 0.6 - 4 μm range," *Appl. Optics*, vol. 29, p. 2246, 1990.

[55]   H. J. Krause and W. Daum, "High-power source of coherent picosecond light pulses tunable from 0.41 μm to 12.9 μm," *Appl. Phys. B*, vol. 56, p. 8, 1993.

[56]   A. Shirakawa and T. Kobayashi, "Noncollinearly phase-matched femtosecond optical parametric amplification with a 2000cm^{-1} bandwidth," *Appl. Phys. Lett.*, vol. 72, p. 147, 1997.

[57]   J. Wang, M. H. Dunn, and C. F. Rae, "Polychromatic optical parametric generation by simultaneous phase matching over a large spectral bandwidth," *Optics Letters*, vol. 22, p. 763, 1997.

[58]   R. Danielius, A. Dubietis, G. Valiulis, and A. Piskarskas, "Femtosecond high-contrast pulses from a parametric generator pumped by the self-compressed second harmonic of a Nd:Glass laser.," *Optics Letters*, vol. 20, p. 2225, 1995.

2. The OPO pump laser system

2.1 Introduction

An Optical Parametric Oscillator (OPO) down-converts a pulse from a pump laser into two other pulses at longer wavelengths. By tradition the shorter of these generated wavelengths is called the signal and the longer the idler. To a very large extent the properties of the laser system used to "pump" the OPO have a great influence on the performance that can be obtained from the OPO itself. Most applications of pulsed OPOs require that the signal and idler pulses be transform-limited; have a well-defined (TEM_{oo} mode) beam profile; and have low amplitude noise and timing jitter. Unless the pump pulse itself has such properties it will be difficult to achieve signal and idler pulses with the desired properties.

Another important property required of the pump laser is that it has sufficient peak power to drive the OPO well above threshold where stable operation can be expected. An OPO reaches threshold when the single-pass gain through the OPO crystal is equal to the round trip cavity losses of the resonator. However, close to threshold the system will be very unstable since small gain or loss fluctuations will lead to large power fluctuations in the signal and idler pulses. Such fluctuations can have several causes: they may originate from power fluctuations in the pump itself; or, for synchronous pumping of the OPO by a laser pulse train, due to timing jitter in the arrival of the pump pulses relative to the circulating pulse in the OPO resonator. The OPO's sensitivity to fluctuations reduces as it is driven further above threshold since the gain becomes saturated.

As a result the pump laser should be chosen to produce transform limited pulses with peak powers at least four times higher than needed to achieve threshold in the OPO; the pump laser should also preferably emit a TEM_{oo} mode beam with high pointing stability. Since the LBO OPO is required to emit wavelengths between 750 nm and 1600 nm, the pump wavelength will generally have to lie between 375 nm and about 700 nm for either the signal or idler to fall in the desired range.

As will be shown later, the threshold pump power for the synchronously pumped LBO OPO developed during this work was calculated to be ~ 1 kW, and hence a pump laser capable of around 5 kW peak power was planned. This is a rather high value: for example, a typical arc-lamp pumped Nd based laser (Coherent Antares: $P_{average}$ ~ 20 W at 1053 nm; τ_p ~ 50 ps; at 76 MHz) emits only about 5 kW peak power pulses at its fundamental wavelength and typically only 1 kW[1] (corresponding to 3 - 4 W average power) at the second harmonic around 530 nm. Additive pulse mode-locked Nd lasers oscillators (see [2] for an example) emitting 1 W of average power in 3 ps duration pulses at 76 MHz produce, similarly, 4 kW at 1064 nm and around 1.5 kW at 532 nm. These second harmonic pump powers are generally too low to obtain stable operation. As a result a different higher power pump system was required.

The system which was developed is shown in Figure 2-1. The OPO was pumped by a frequency doubled, externally pulse compressed, arc lamp-pumped, mode-locked Nd:YLF laser. The fibre–grating pulse compressor was used to temporally compress the pulses from the Nd:YLF laser as a means of increasing the peak power at the output. The main advantage of using a fibre–grating pulse compressor is that it is experimentally easy to

---

[1] Though this is less than can be achieved through direct SHG of a Coherent Antares Nd:YAG laser (see [1]) with ~11 W cw being the best recorded performance or 6 W cw typical performance.

implement and a relatively efficient method for increasing the peak power of a mode-locked laser which can be applied with a high average power source (such as the Antares laser). As will be shown below, it proved possible to create second harmonic pulses more than six times more powerful (6.5 kW in 2.3 ps) than those obtained by direct second harmonic generation from the Nd:YLF laser. It also has the other advantage of producing pulses twenty six times shorter, making it easier to produce the wavelength tunable, sub-picosecond pulses required for our applications. The main disadvantage is that the laser output pulses are not transform limited. This will be explained in greater detail below.

Other methods that were considered for increasing the peak power of the second harmonic pump pulses were external, resonant enhancement second harmonic generation [3]; and double-pass second harmonic generation [4, 5].

Resonantly enhanced SHG uses a doubling crystal located in an optical cavity. The cavity resonates the fundamental and/or the second harmonic beams increasing the intracavity circulating power and therefore the generated second harmonic. The main advantage is that if the internal cavity losses can be made low enough, large power enhancement factors and conversion efficiencies can be achieved resulting in high power, transform-limited, spatially uniform, second harmonic pulses (approaching the power of the pump laser). The main disadvantage is that the resonant enhancement cavity requires its length to be actively stabilised to better than $\lambda/2$. This is more complex than constructing a fibre–grating pulse compressor. Furthermore it is difficult to achieve sufficient enhancement to obtain second harmonic powers [2, 6] comparable with those obtained using the fibre-grating pulse compressor (or even through optimised direct SHG [1]). Yang, et. al., [6] reported only 6.5 W cw SHG power using a resonant cavity for a laser system with similar properties to the system used in this work. The large internal power enhancements needed to achieve even this level of performance raised concerns about thermal loading in the SHG crystal. Thermal loading causes dephasing across the circulating spatial beam profile, reducing the efficiency of the process. For LBO, the power limit before thermal loading becomes a problem is estimated to be ~ 100 W cw [6, 7]. In our work, therefore, the method was not adopted because of the experimental complications it introduces; the apparently limited peak power enhancement that could be expected; and the fact that preferable, shorter pulses could be achieved using the fibre-diffraction pulse compressor.
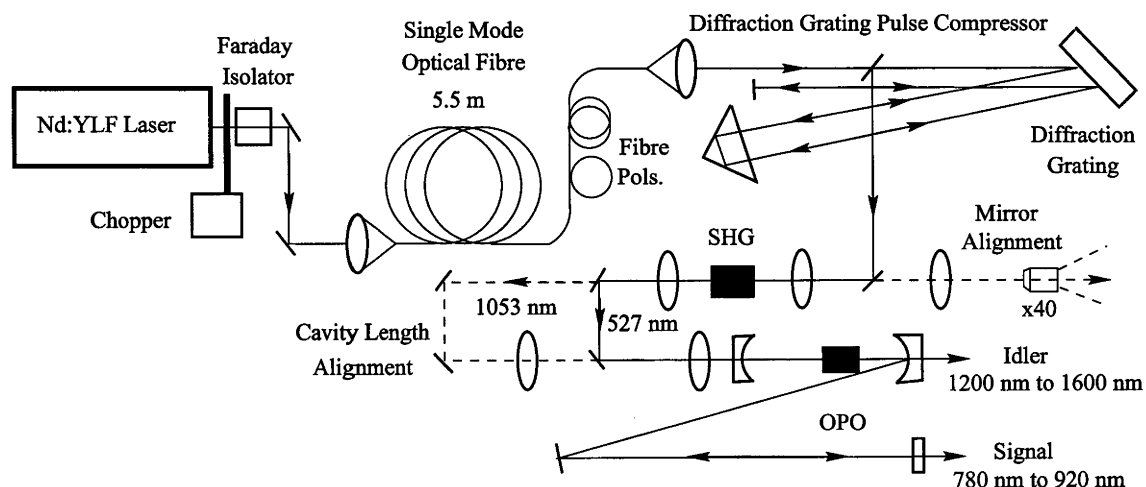

Figure 2-1 The experimental layout of the pump laser and optical parametric oscillator.

The second alternative method examined would have involved double passing the LBO crystal used for SHG [4] or using two LBO crystals in series to generate higher second harmonic peak powers [5]. By double passing or doubling the interaction length of the second harmonic crystal one can increase the second harmonic power by up to a factor of four. The main difficulty in this method is extracting the SHG power efficiently and adjusting the phase between the fundamental and SHG beams before the second pass. Again, the fibre-diffraction grating pulse compressor was favoured because it could potentially produce shorter, higher peak power pulses.

2.2 The Nd:YLF laser.

A Coherent Antares 76-YLF, arc lamp-pumped, mode-locked Nd:YLF laser was used in these experiments. It produces 60 ps pulses at a repetition rate of 75.4 MHz with a maximum peak power of 4 kW (equivalent to 18 W average power). Nd:YLF was preferred as the gain medium because of it provides superior pointing stability and polarisation (>100:1) compared with equivalent lasers using Nd:YAG. The Antares 76-YLF produces transform-limited pulses and a slightly elliptical (1:1.15), Gaussian beam profile.

Power fluctuations are always present on the output from lamp pumped mode-locked Nd lasers induced by processes such as rapid variations in thermal distortion in the laser rod from turbulence in the water cooling jackets. Such fluctuations could prove to a potential problem because any amplitude noise is amplified through frequency conversion processes (SHG, OPA), roughly doubling each time [8]. The laser should, therefore, have as low an amplitude noise as possible. The Antares laser does have a facility for active noise suppression, and this reduces the amplitude fluctuations from ~ 4 % down to less than 1 % during normal operation. As will be shown later the noise level was low enough to that it did not significantly affect the operating stability of the OPO. Long term power drift also occurs in the laser output due to thermalization of the whole laser system over a period of several hours. It was not considered to be a significant problem, and only minor adjustments to the cavity length were occasionally required to regain optimum mode-locking and OPO performance.

Another possible problem is phase noise in the laser which manifests itself as timing jitter of the output pulses. Timing jitter could create substantial noise problems at the output of the OPO because of variations in the parametric gain caused by the pump pulses moving out of synchronisation with the signal pulses circulating in the OPO resonator. Timing jitter on the pump laser was diagnosed using a fast (rise time of 2 ns) Si PIN detector and a spectrum analyser (0 to 3 GHz). Noise sidebands were detected at the laser repetition frequency of 75.4 MHz (and its harmonics) at 100 Hz, ~ 2.3 kHz and weak sidebands at 200 kHz. The 100 Hz sidebands were attributed to noise from the laser's environment (cooling water, etc); the 2 kHz to 2.5 kHz sidebands are associated with resonances due to the spontaneous emission lifetime of Nd:YLF[2]; whilst the origin of the 200 kHz sidebands is unknown. Figure 2-2 shows sample data from the spectrum analyser displaying the different sidebands close to the carrier frequency and its harmonics. Figure 2-3 shows the variation in relative power of the 100 Hz and 2 kHz sidebands increases quadratically with harmonic number. For an imperfectly mode-locked, cw laser the timing jitter in the output pulses will cause the noise sidebands to increase roughly quadratically with increasing harmonic number. This is because the contribution to the temporal intensity profile of a noisy laser pulse from timing jitter is proportional to the time derivative of the intensity of the transform-limited laser pulse. This results in an intensity autocorrelation of the laser pulse with a noise term that increases with repetition time squared [8]. Since the measured power spectrum is the Fourier transform of the intensity autocorrelation function of the noisy

---

[2] The spontaneous emission lifetime of Nd:YLF is $t \cong 0.44$ ms. $1/t \cong 2.3$ kHz.
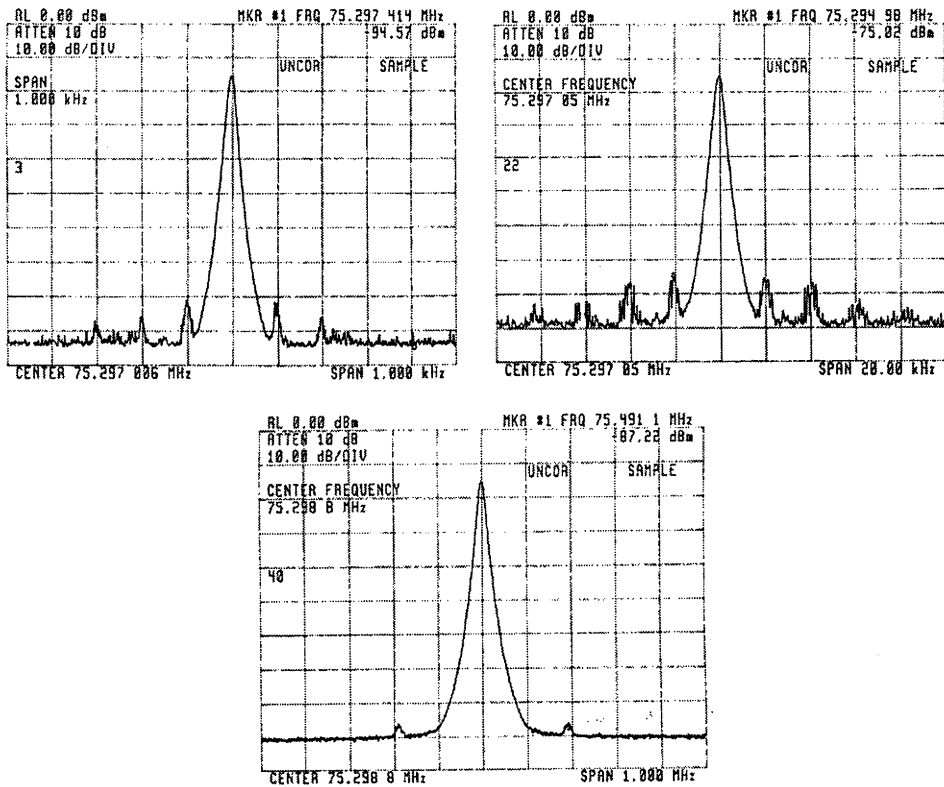
Figure 2-2 : The phase noise sidebands on the Antares Nd:YLF laser repetition frequency of 75.4 MHz. There were three different sideband frequencies detected; The top left shows sidebands at 100 Hz from the central frequency, the top right shows sidebands at 2 kHz and the bottom shows sidebands at ~ 200 kHz. The vertical scale is 10 dbm per division.

laser pulse, the noise in the power spectrum will increases quadratically with harmonic number if timing jitter is significant. Using calculations from [8] it was found that the timing jitter was to 1.3 ps due to the 100 Hz sidebands; 2.8 ps for the 2.3 kHz sidebands; and 0.76 ps for the 200 kHz sidebands.

However, in all cases the period of the fluctuations (equal to 1/sideband frequency) was much greater than the build-up time needed for the OPO to reach steady-state operation. For the highest observed frequency sidebands of 200 kHz the fluctuation period is 5μs. In this time the signal in the OPO makes 377 passes through the crystal. Since the OPO requires roughly 30 to 35 passes to reach threshold it can compensate for any changes in repetition rate of the pump pulses for fluctuation rates less than 2 MHz, much higher than any fluctuation frequency observed.

2.3 The pulse compressor

The design of the fibre–grating pulse compressor follows the work of Chung and Siegman [9] who constructed a synchronously pumped, KTP (Potassium Titanyl Phosphate) OPO driven by a pulse compressed, lamp-pumped, Nd:YAG laser at 1064 nm. Their success in developing such a pump laser for a KTP OPO was a strong incentive for using a similar method for our LBO OPO.
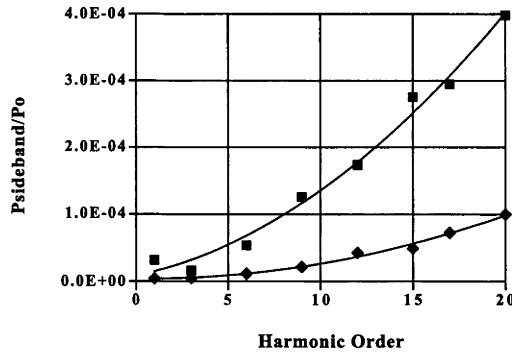
15

Figure 2-3 : The variation of the relative power of the 2.3 kHz and 100 Hz frequency sidebands with increasing harmonic order. The squares are for the 2.3 kHz sidebands and the triangles are for the 100 Hz. P_0 is the peak power of the harmonic of the fundamental frequency.

2.3.1 Theory

2.3.1.1 Self-phase modulation

Any fibre–grating pulse compressor relies upon Self -Phase Modulation (SPM) inside the optical fibre to both increase the spectral bandwidth of the pulse and to produce a roughly linear frequency chirp across the pulse. A frequency-dependent optical delay line is then used to compensate the chirp thereby compressing the pulse. SPM arises from the optical Kerr effect which describes a nonlinear, intensity dependent change in the refractive index of a material. (See [10] for more details). That is:

$$n = n_o + n_2 I$$

For SiO_2 , n_2 = 3.2 x 10^{-16} cm^2/W. This means that the optical Kerr effect only produces significant changes in the properties of a pulse either at very high intensities and/or for propagation over long distances. Both conditions can be achieved during propagation through a single mode optical fibre. The phase change for a pulse propagating through an optical fibre of length L is:

$$\Delta\phi = n_2 k_0 I(t) L$$

where $k_0 = \dfrac{2\pi}{\lambda}$ is the vacuum wavenumber.

As is evident, the phase change for a pulse will be time dependent, reflecting the temporal shape of the pulse propagating in the fibre. This time dependent phase modulation leads to the creation of new frequencies and broadens the pulse spectrum.

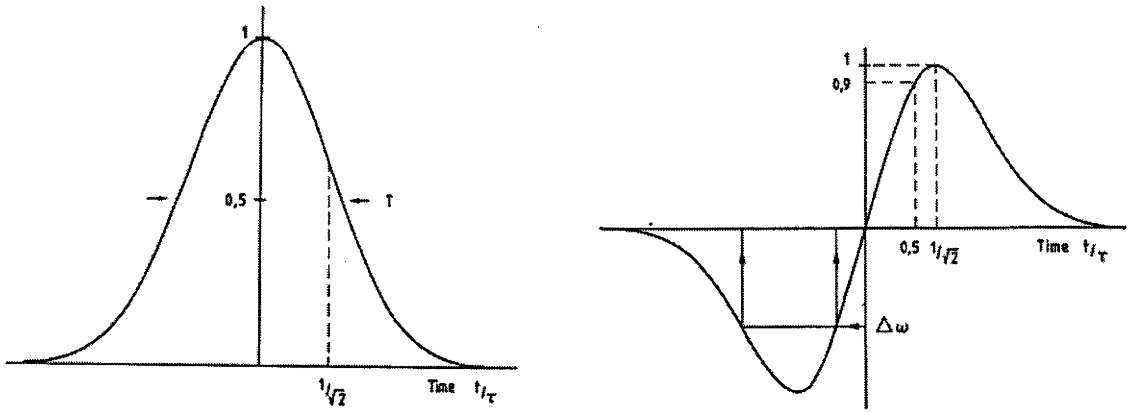$$\Delta v(t) = -\frac{\partial\phi}{\partial t} \propto -\frac{\partial I}{\partial t}$$

16

Figure 2-4 : The intensity temporal profile (left) and instantaneous frequency (right) of a Gaussian pulse that has only undergone SPM. τ is defined in Eqn 2-2. As can be seen in the figure of the instantaneous frequency the linear frequency chirp extends from -0.5 t/τ to 0.5 t/τ. (Figure taken from [11])

The frequency broadening is directly proportional to the slope of the pulse profile with time. This means that the central frequency remains unshifted but the frequencies in the leading part of the pulse decrease ($v \leq v_o$), whilst those in the trailing edge of the pulse increase ($v \geq v_o$).

For a Gaussian pulse profile with a FWHM pulse duration of Δt and peak intensity I_0.

$$I(t) = I_o \exp\left(-4\ln 2\left(\frac{t}{\Delta t}\right)^2\right)$$

The resulting frequency broadening is

$$\Delta v(t) = 8\ln 2\left(\frac{t}{\Delta t}\right)I(t)n_2 k_o L = 8\ln 2\left(\frac{t}{\Delta t}\right)\Delta\phi(t)$$

Figure 2-4 shows the case for the Gaussian pulse profile and the frequency as a function of time resulting from SPM. As can been seen a linear frequency chirp develops across the central section of the spectrum. The maximum frequency shift that results can be estimated as:

$$\Delta v_{max} = \frac{\sqrt{2}\exp(-0.5)}{\tau_0}\Delta\phi_{max} \approx 0.858\Delta v_0 \Delta\phi_{max}$$

Eqn 2-1

$$\text{where } \tau_0 = \frac{\Delta t}{2\sqrt{\ln 2}} = \frac{1}{\Delta v_0}$$

Eqn 2-2

$$\text{and } \Delta\phi_{max} = n_2 I_0 k_0 L.$$

or it can be determined from a measured bandwidth of the power spectrum of the pulse. The maximum frequency shift depends on the peak intensity of the pulse; the length of the fibre; and the width of the initial spectral bandwidth, Δv_0. The extent of the linear portion

17

of the frequency chirp is $\sim 0.9 \, \Delta\nu_{max}$. SPM only affects the spectrum of the pulse, the temporal profile does not change if SPM is the only effect.

The temporal profile can, however, be affected by Group Velocity Dispersion (GVD) if the fibre is sufficiently long. Since a frequency chirp exists across the central portion of the pulse, different parts of the pulse travel with different group velocities. The leading part of the pulse, whose frequencies are lower than the central frequency, travel fastest whilst the trailing edge of the pulse, with frequencies higher than the central frequency, travel slower than the rest of the pulse. The effect of this is that the temporal profile of pulse develops steep trailing and leading edges as the leading part of the pulse "overtakes" the rest of the pulse and the trailing edge is left behind. This eventually leads to the development of a rectangular pulse shape. The steep edges undergo further, strong SPM because of the rapid change in intensity at these points. This leads to creation of new frequencies and the linear frequency chirp spreading from just the central portion to fill the entire pulse. Figure 2-5 illustrates the development of the temporal pulse profile and instantaneous frequency as a Gaussian pulse propagates through an optical fibre with increasing length.

The dispersion length z_o [10] is the length over which GVD becomes significant.

$$z_o = \frac{\pi^2 c \Delta t^2}{\lambda_o^2 |D|}$$

where D is the GVD. Typically $D \approx 30$ ps/nm/km for silica and a wavelength λ_o near 1 μm. For a pulse of 60 ps , $z_o \approx 300$ km. In our case the fibre length is $2 \times 10^{-5} \, z_o$ so, GVD plays no effect in these experiments since the length of the optical fibre used is much less than z_o . SPM is the dominant effect in this experiment.

2.3.1.2 Stimulated Raman scattering

There are limits to how much power can be launched into a fibre. The limits are due to thermal loading from the high average power of the laser or due to the onset of undesirable nonlinear processes occurring due to the high peak powers.

It was found that the fibre could suffer failure due to the high average power affecting its plastic cladding. Specifically, it was found that the soft plastic jacket melted and eventually broke the fibre through local heating. As will be described later, this problem was eventually solved by encapsulating the fibre in a index matched jacket to ensure any radiation in the cladding did not couple to the plastic encapsulation.

A particularly important nonlinear process that occurs due to the high peak power in the pulses and the long propagation length is Stimulated Raman scattering (SRS) and this can limit the maximum phase modulation $\Delta\phi_{max}$ that can be achieved or, equivalently, the maximum peak power of the incident pulse. SRS shifts energy from the pump pulse into a spectrally broad, lower frequency pulse called a Stokes wave, which for a 1054 nm pump is centred at a wavelength around 1120 nm. This process involves the scattering of the incident pump photons from molecular vibrational energy states in the medium. The frequency shift is determined by the molecular vibrational energy states in the medium. SRS can affect the compression of the pulse by depleting one side of the frequency chirp of energy and shifting it to a lower frequency [12, 13] (see Figure 2-6). The Stokes wave can grow very rapidly, effectively limiting the peak power of the pulse that can be launched into the fibre and the length of fibre that can be used. A usual criterion for SRS is the critical power level above which the Stokes wave will be greater than the pump wave [12].
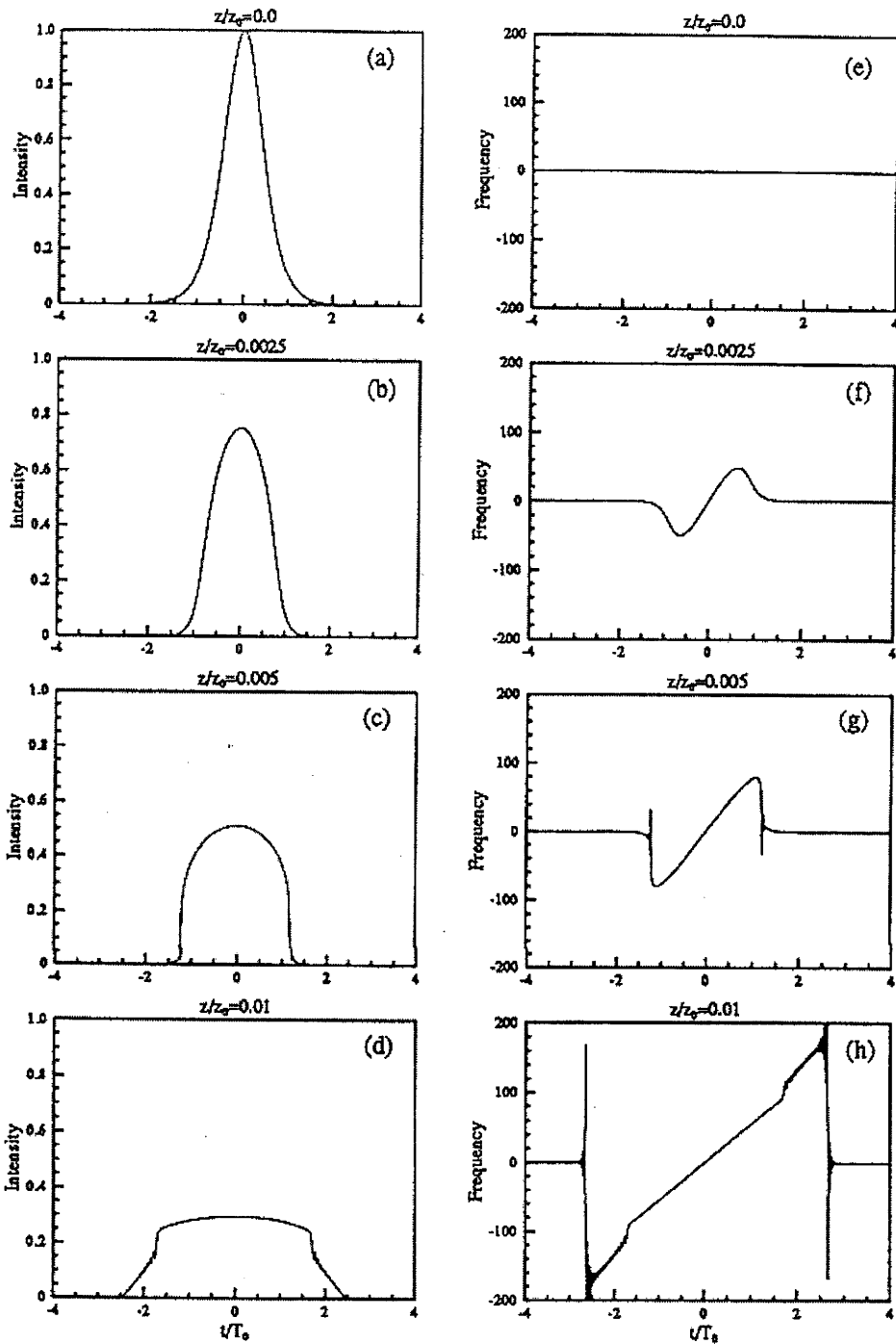
Figure 2-5 : The variation in the intensity temporal profile (left) and instantaneous frequency (right) as a function of time/pulse duration (t/T_0) of a Gaussian pulse as it propagates in a single mode optical fibre undergoing the effects of SPM and GVD. (a) and (e) are respectively, the initial temporal intensity distribution and frequency distribution with time of a Gaussian pulse. (b) and (f) display the temporal profile and instantaneous frequency after propagating 0.0025 z_0 . (c) and (g) display the temporal profile and instantaneous frequency after propagating 0.005 z_0 . (d) and (h) display the temporal profile and instantaneous frequency after propagating 0.01 z_0 . GVD extends the frequency chirp developed through SPM across the entire pulse. (Taken from [14])
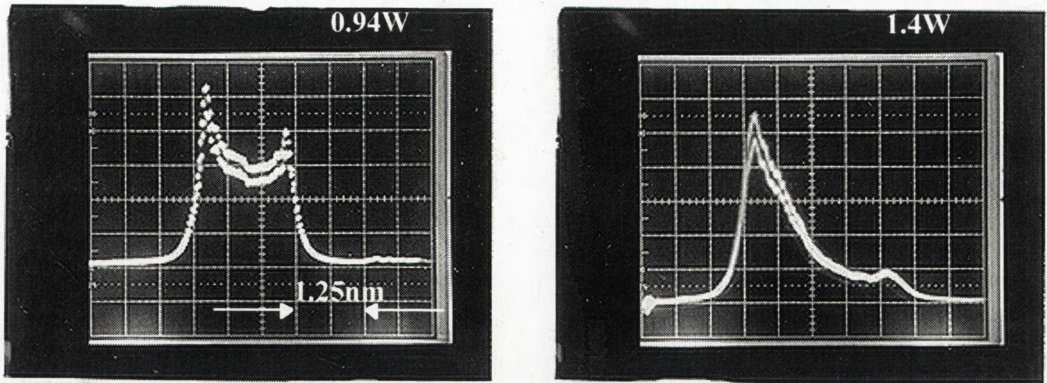
19

Figure 2-6 : The photo on the left displays the SPM power spectrum of the pulse from the Antares Nd:YLF laser at a cw power of 0.94 W focussed into a 45 m length of single-mode fibre. The photo on the right is the SPM power spectrum of the pulse at 1.4 W cw. SRS has depleted the higher wavelength side of the spectrum, shifting energy into a Stokes wave at ~ 1120 nm. The scale is 6.25 Angstroms per division.

$$P_{cr} = \frac{16A}{gL}$$

In this equation A is the fibre core area, g is the Raman gain coefficient $\approx 4.5 \times 10^{-14}$ m/W and L is the length of the fibre. This simply formula gives a indicator of the maximum peak power that can propagate through a fibre of length L before SRS becomes an important consideration. Figure 2-7 shows how the fibre length was chosen experimentally to provide maximum spectral bandwidth (which is dependent on the peak power of the 1054 nm pulse coupled into the fibre) while minimising SRS. As shown in the figure the SRS power is inversely proportional to the fibre length while the SPM induced spectral bandwidth is directly proportional to the fibre length, as expected. As will be later shown the chosen fibre length is long enough to be able to compress the 1054 nm pulses down to the desired ~ 2.5 ps in duration while coupling the maximum possible peak power into the fibre and being short enough to minimise SRS.

2.3.1.3 Grating compressors

After the fibre, a grating compressor provided anomalous (negative) GVD to counteract the normal dispersion (positive) frequency chirp to compress the pulse. The compressor has the property that the leading part of the pulse, which has lower frequencies, travels further than the trailing part of the pulse, which has higher frequencies. This difference in path length allows the trailing part of the pulse to catch up to the leading part of the pulse thereby compressing the pulse in time. To first approximation the delay is a linear function of frequency. However, since the pulse contains an approximately linear frequency chirp only near its centre, some of the pulse energy cannot be compressed and creates a low power pedestal and sidelobes (See [10] for more details).

For a Gaussian shaped pulse that only experiences SPM, the resulting compressed pulse will have a central peak with two sidelobes superimposed on a broad pedestal. The central peak, formed by compression of the linearly chirped component of the pulse, contains 50 to 60 % of the pulse energy. The sidelobes contain ~ 20 % of the energy, and arise due to the fact that the pulse has a significant nonlinear frequency chirp component. The broad background, which contains ~ 20 % of the energy, arises from the unchirped parts of the pulse.
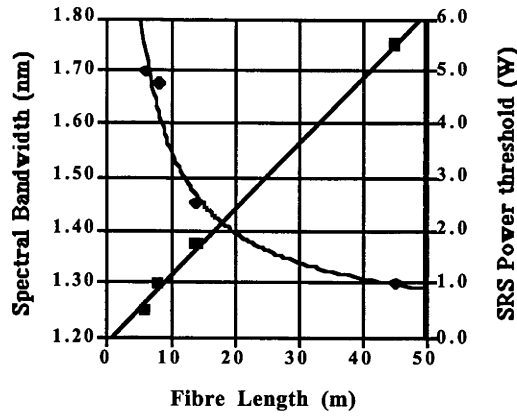
20

Figure 2-7 : This graph shows the spectral bandwidth (squares) of the pulse, after propagating through a length of fibre, at the point were the Stoke's wave becomes detectable (diamonds). The left vertical axis shows the bandwidth and the left vertical axis shows the full cw power coupled out of the fibre when the Stoke's wave becomes detectable. As can be seen the bandwidth increases linearly with fibre length, whereas, the power threshold for the onset of SRS is proportional with 1/ fibre length.

Since the grating compressor uses anomalous dispersion to delay the frequency components of the pulse so that they all emerge from the compressor at the same time, the separation of the grating pair is critical to successfully compressing the pulse. The grating separation can be estimated by setting the anomalous dispersion due to the grating equal to the dispersion due to the frequency chirp in the pulse. The quadratic dispersion of a grating pair is (see [14])

$$a_c = \frac{b\lambda}{2\pi c^2}\left(\frac{\lambda}{d}\right)^2\left[1 - \left(\frac{\lambda}{d} - Sin\theta_i\right)^2\right]^{-3/2}$$

Eqn 2-3

where b is the grating separation, d is the grating period and θ_i is the angle of incidence. The dispersion of the frequency chirped pulse can be estimated to be

$$a_p = \frac{\tau}{0.9\Delta\omega_{max}}$$

Eqn 2-4

where $\Delta\omega_{max} = 2\pi\Delta v_{max}$. Δv_{max} and τ have been defined in Eqn 2-1 and Eqn 2-2.

A 1200 line/mm grating was chosen for the pulse compressor because it gave a conveniently small grating separation, but also because a grating with a smaller period would have introduced a larger distortion in the compressed pulse due to a larger cubic term in the grating response. Cubic phase shifts are due to the next higher order in the dispersion of the grating pair. A condition for minimum distortion from the cubic orders is (see [14])

$$\Omega = \frac{\Delta t\Delta\omega_{max}\alpha}{\omega_o} \leq 1$$

$$where \qquad \alpha = \frac{1 + Sin\theta_i \left(\lambda/_d - Sin\theta_i\right)}{1 - \left(\lambda/_d - Sin\theta_i\right)^2} \qquad see \ Figure \ 2-8$$

Since α increases rapidly for smaller grating periods at any particular angle of incidence care must be taken to chose the appropriate grating. For our particular case of $\theta_i \sim 30° - 40°$, $\Delta t = 60$ ps and $\Delta\lambda_{max} \sim 20$ Angstroms (corresponding to $\Delta\omega_{max}$) this condition is only fulfilled for gratings of 1200 lines/mm or less.

2.3.2 Predicted Compressor Performance

The extent of the frequency broadening of the power spectrum through SPM can be estimated from Eqn 2-1 and Eqn 2-2. For a 1.3 kW peak power pulse of 60 ps in duration coupled into a single mode fibre with a mode field diameter of 7.7 μm, the peak intensity is $I_o = P/(\pi w_o^2 /2) = 5.6$ GW/cm^2. The nonlinear refractive index, n_2 , of silica is $\sim 3.2 \times 10^{-16}$ cm^2/W and taking the fibre length as 6 m gives a maximum phase shift, $\Delta\phi_{max}$, of $\sim 20\pi$. For $\Delta t \sim 60$ ps (τ_o of 36 ps) we expect the maximum frequency shift, $\Delta\nu_{max}$, to be 2.4×10^{11} Hz and the spectral width, $\Delta\lambda$, of the pulse to be (see [10])

$$\Delta\lambda_{rms} \cong \Delta\lambda_o \left(\frac{4}{3\sqrt{3}}\Delta\phi_{max}^2\right)^{1/2}$$

where $\Delta\lambda_o$ is the initial rms spectral width of 0.27 Angstroms (the pulse from the Antares laser is transform-limited). Hence, the predicted spectral bandwidth is ~ 15 Angstroms.

A theoretical estimate of the duration of the compressed pulse can be obtained by considering the width of the linear frequency chirp [11]. Assuming that all the frequencies within the linear frequency chirp, extending over a range $\sim 0.9 \ \Delta\nu_{max}$, are compressed into a Gaussian pulse and that time-bandwidth products for the uncompressed and compressed pulse are equal, the compressed pulse duration is predicted to be:

$$\Delta t_{compressed} = \frac{\Delta\nu_{uncompressed}}{0.9 \Delta\nu_{max}} \Delta t_{uncompressed}$$

For a $\Delta\nu_{max}$ of 2.4×10^{11} Hz, a $\Delta\nu_{uncompressed}$ of 7.3×10^9 Hz and a initial pulse duration $\Delta t_{uncompressed}$ of 60 ps gives a compressed pulse duration of 2 ps.

Using Eqn 2-3 and Eqn 2-4 with a $\Delta\omega_{max}$ of 1.5×10^{12} Hz and $\tau_o = 36$ ps gives an $a_p \approx 2.7 \times 10^{-23}$. The grating has 1200 lines/mm and with the incident angle being 35° and the reflected angle being 43°, gives $a_c \approx 7.7 \times 10^{-26}$ b(cm). Hence the predicted grating separation is b ~ 350 cm..

2.3.2.1 Polarisation control

Another factor that determines the quality of the compressed pulse is its polarisation state. Gratings typically have higher reflectance for certain polarisations. Since it is desirable to have as high a reflectance as possible to minimise energy loss in the compressor it is necessary to control the polarisation state of the pulses emerging from the fibre. Any normal (non polarisation preserving) single-mode fibre will change the polarisation of pulses propagating through it through stress induced birefringence due to bending or twisting of the fibre. Additionally, nonlinear polarisation rotation [10] can occur. Care was taken to
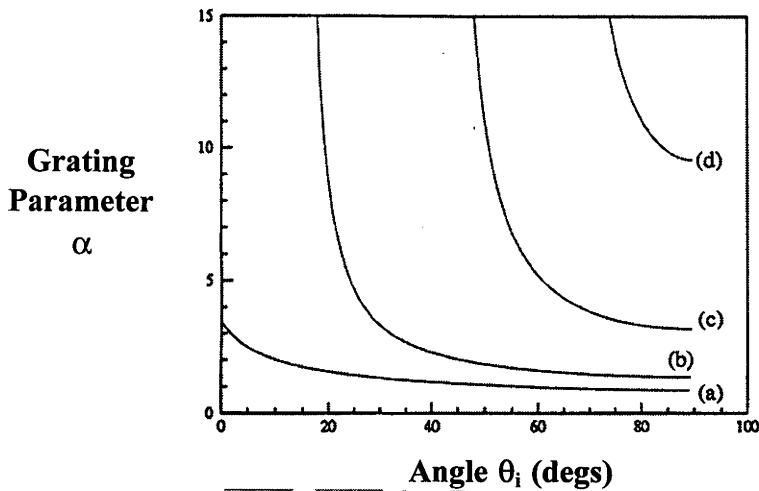
Figure 2-8 : The grating parameter α (vertical axis) as a function of the incident angle θ_i (horizontal axis) at 1054 nm for different grating periods; (a) d^{-1} = 800 lines/mm, (b) d^{-1} = 1200 lines/mm, (c) d^{-1} = 1600 lines/mm and (d) d^{-1} = 1800 lines/mm. (Figure taken from [14])

ensure the SPM broadened spectrum of the pulse remained the same shape throughout these experiments through the correct setting of the waveplates after the fibre. This polarisation state gave the "best" compressed pulse shape that could be achieved.

For most of the work, $\lambda/4$ and $\lambda/2$ zero-order waveplates were used at the output of the fibres to compensate any polarisation rotation. However, in some early work, fibre loops configured as $\lambda/4$ and $\lambda/2$ waveplates were used instead [15, 16] although they were less efficient than the bulk-optic waveplates.

2.3.3 Experimental performance

As can be seen in Figure 2-1 the beam from the Nd:YLF Antares laser passed through a chopper to reduce its average power before being coupled into the fibre. The chopper was a Stanford Research Systems, Inc. Model SRS540. Using a chopping frequency of 160 Hz (period of 6.2 ms) reduced the cw power by a factor of 8.8 times, and provided bursts of pulses 800 μs long.

After passing through a Faraday isolator (which introduced a loss of ~ 10 %) to prevent any back reflections from disturbing the mode-locking of the Antares laser, the beam was coupled into a length of single-mode optical fibre using a Melles Griot 10x microscopic objective lens within a New Focus model 9091 fibre manipulator which were chosen for its long term mechanical stability. An AR coated, aspheric lens was used to couple the beam from the fibre into the pulse compressor. The optical fibre (Newport F-SY fibre) was between 5 to 6 meters long and had a core diameter of 6.4 μm and a mode field diameter of 7.7 μm.

The fibre position was optimised by monitoring the transmitted power with a cw power meter. A coupling efficiency approaching 70 % was typical. Unfortunately, the microscope objective has a power loss of 11 % at 1054 nm and combined with the 4 % Fresnel losses from each of the cleaved fibre ends meant that the fibre has an overall power transmission efficiency of ~ 57 % (this was later increased to ~ 63 % by replacing the microscope objective by an AR coated aspheric lens).

23

In later experiments it became desirable to eliminate the chopper and use the full cw power of the laser. While this posed no problems for the grating or the rest of the optics, the higher cw power was more than enough to burn and break the fibre when mounted in an ordinary fibre chuck. The problem was due to the presence of a plastic jacket protecting the fibre and the use of a plastic material to clamp the fibre in the chuck. When the beam was coupled into the fibre, some light invariably became trapped in the cladding and would propagate as far as the plastic jacket or fibre clamp where it was absorbed. This caused the plastic to heat up and eventually melt, often moving the fibre in the process and increasing the power coupled into the cladding. This localised over-heating generally resulted in the fibre breaking.

It proved quite difficult to prevent this happening but the problem was finally solved by replacing the normal fibre chuck with a 5 cm long glass capillary tube. The fibre, having been stripped of its plastic jacket for the first 10 cm, was glued into the glass chuck using an index matching, UV curing, optical epoxy. Radiation propagating in the cladding could then refract into the glass capillary tube and was dissipated harmlessly at its outer surface. While quite delicate to use, the design was successful and up to 63 % of the cw launched power was obtained at the fibre output. However, the in this cw mode it proved more difficult to obtain a linear polarisation state at the output of the fibre, apparently due to depolarisation because of thermal blooming in the Faraday rotator.

The pulse compressor consisted of a gold-coated, 1200 lines/mm Milton Roy (1122 master) grating with a reflectivity for p-polarised light > 90 % and a AR coated right-angle prism which was used to fold the beam 180° so that only a single grating was needed within the compressor. The beam made 4 reflections from the grating and hence the distance between the grating and the prism was equal to a quarter of the required separation for a single pass compressor using two parallel gratings. To extract the beam from the pulse compressor it was angled slightly downwards by the folding mirror. The gratings were used within 8° of Littrow configuration to maximise the grating reflectivity. The grating compressor itself had a power transmission efficiency between 50 % and 55 %. After four reflections from the grating the transmission was $(0.9)^4 = 0.65$. The rest of the losses are due to limitations in the correction of the polarisation using the $\lambda/4$ and $\lambda/2$ zero-order waveplates.

To align the compressor, the grating separation was first estimated from the values of a_c (see Eqn 2-3) and a_p (see Eqn 2-4). The dispersion of the frequency chirp a_p was estimated from the power spectrum of the pulse after it has emerged from the fibre. This was measured using a GCA/McPherson 2021 1m scanning monochromator with a 2048 pixel Reticon array Si detector with a resolution better than 1 Angstrom (0.6 to 0.8 Angstroms). The grating separation was fine tuned about the predicted value, by optimising the SHG intensity autocorrelation of the output pulses (see Chapter 7). The "best" compressed pulse was taken to be the one which had the narrowest central peak and smallest side-lobes [11]. The waveplates were adjusted to maximise the output power from the pulse compressor. The optimised grating-prism spacing was typically 77 cm, ie. b $\approx$ 308 cm. Quite close to the theoretical prediction.

After the initial set up of the compressor, further length adjustments were avoided and fine tuning of the system was achieved by varying the power injected into the fibre to obtain the "best" compressed pulse. This was more convenient than changing the grating separation and permitted small drifts in the Antares laser (which typically manifest themselves as slow variations in the pulse duration due to mechanical drifts in the Antares system) to be compensated.

Typical powers available from the laser when the chopper was in use were as follows: the cw power before the microscope lens was typically 1.1 W (2.1 kW peak in 60 ps); ~ 630 mW of this emerged from the fibre and about 350 mW from the compressor. Without the

chopper the average launched power was 10.5 W, yielding ~ 6.3 W after the fibre and 3.5 W after the compressor.

2.3.3.1 Measurements

Sample data obtained with the pulse compressor are shown in Figure 2-9 and Figure 2-10 . As can be seen the pulse was compressed from a transform-limited pulse of 61 ps in duration down to 2.3 ps duration. For fibres in the range 5 to 6 m long, the durations of the narrow central peak lay in the 2.3 ps to 2.7 ps range and were accompanied, as expected, by two side lobes, with the whole structure being superimposed on a broad background extending over 15 to 20 ps. Measurements demonstrated that the spectral bandwidth had expanded from 0.27 Angstroms to ~ 12.5 Angstroms due to SPM in the fibre. Both the measured pulse durations and the spectral bandwidth are in good agreement with the predictions given in the previous section. From these measurements and using the chopped beam whose average output power after the compressor was 340 to 350 mW, the peak pulse power increases from 2.1 kW in 61 ps to 16 kW in 2.5 ps after the compressor. The pulse is compressed in duration by a factor of 24 times and the peak power is enhanced by 8 times.

As was mentioned previously, SRS limits the peak power of the compressed pulses and their duration. SRS was kept sufficiently low (Raman average power < 10 mW) to avoid strong distortion of the spectrum and hence the compressed pulse, although generally to obtain the maximum SPM, the system was operated very close to the SRS threshold.

The effect of varying the grating separation on the quality of the compressed pulse was characterised using a 6 m long fibre. Figure 2-11 shows autocorrelation traces for increasing grating separation at a fixed power. As the separation was increased the sidelobes grew indicating that there was too much anomalous dispersion. As the separation was reduced there was insufficient anomalous dispersion to compress the pulse fully leading to broadening of the central peak. It is worth noting that the autocorrelation traces varied relatively slowly with grating separation indicating that this was not a very critical parameter.

Figure 2-12 shows the effect of varying the pulse power launched into the fibre at a fixed grating separation. As can be seen, the effect of varying the power mirrors that of varying the grating separation. Obviously changing the pulse power affects the chirp parameter a_p, until it balances the grating dispersion parameter, a_c, whereas for fixed pulse power tuning the grating separation changes a_c until it matches a_p. The results justify the use of changes in power to fine tune the system.

As mentioned previously, through the autocorrelations the polarisation state of the pulse from the fibre was chosen to produce the best possible compressed pulse (see Figure 2-13).

Figure 2-14 shows the power spectra and SHG intensity autocorrelations (see Chapter 7) of the chopped cw beam using the fibre mounted in the glass fibre chuck. Also shown in the intensity autocorrelations is the transform-limited pulse derived from the measured power spectrum (See Chapter 7). As can be seen the pulse is not transform-limited.

Figure 2-15 shows the power spectra, SHG intensity and SHG interferometric autocorrelations (see Chapter 7) of the compressed pulse using full cw power launched into the fibre. The intensity and interferometric autocorrelations plots also include the transform-limited pulse profile derived from the measured power spectrum. The interferometric autocorrelation traces show the pulse envelopes only. It should be noted that the sidelobes in the interferometric autocorrelations are not necessarily due to chirp in
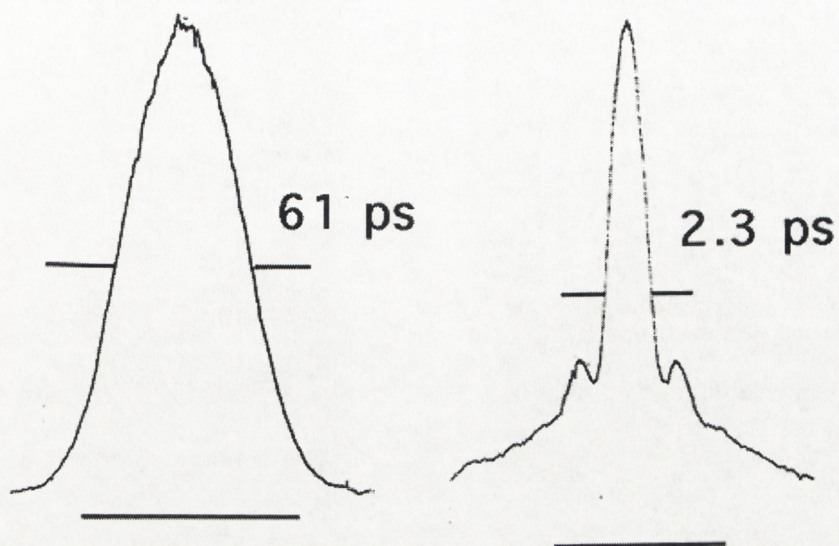
Figure 2-9: The SHG intensity autocorrelations of the pulse before and after compression. The pulse durations (FWHM) are indicated in the traces. The lines at the bottom of each trace mark zero intensity.
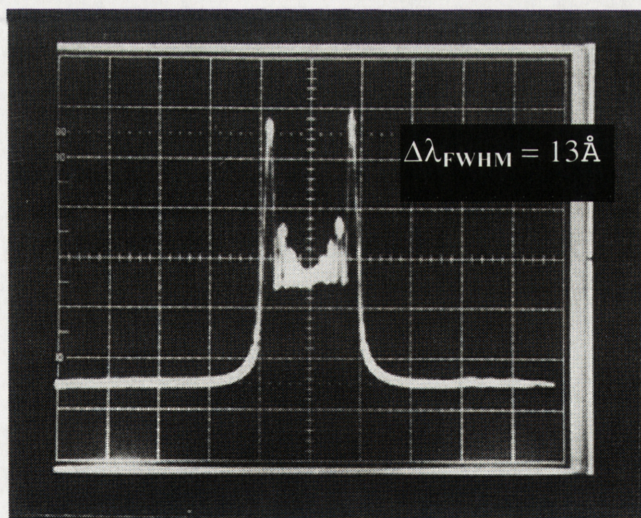

Figure 2-10: The SPM power spectrum of the compressed after the grating pulse compressor. The scale is 6.25 Angstroms per division. The spectral width is typically 12.5 to 13 Angstroms.
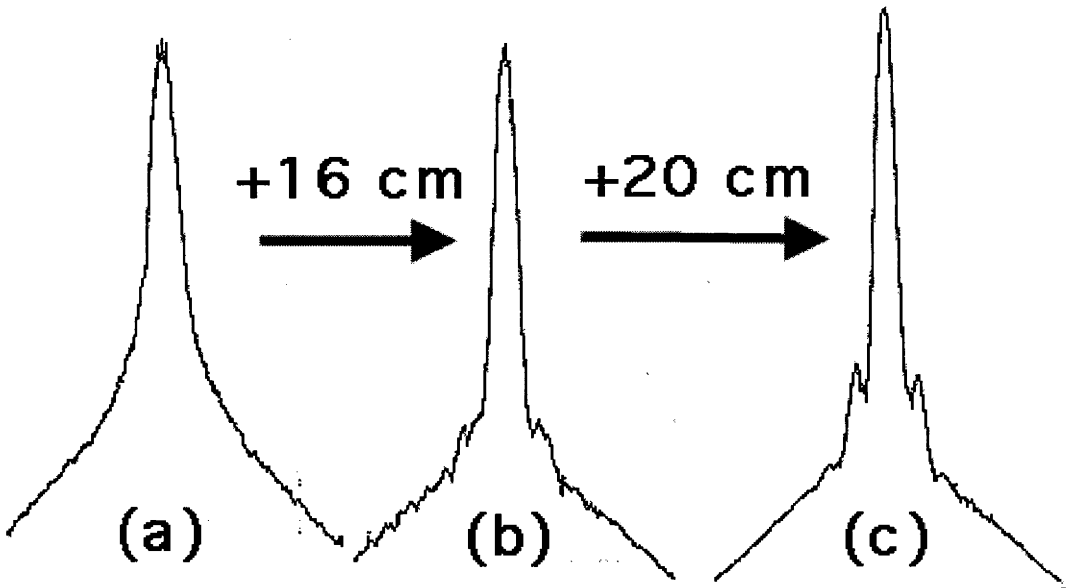
Figure 2-11: The effect of varying the grating separation on the temporal profile of the compressed pulse. The chopped cw power after the compressor is 340 mW or ~ 16 kW peak power in ~ 2.5 ps. (a) is the intensity autocorrelation at a grating separation of 292 cm, (b) is at 308 cm and (c) is at 328 cm.
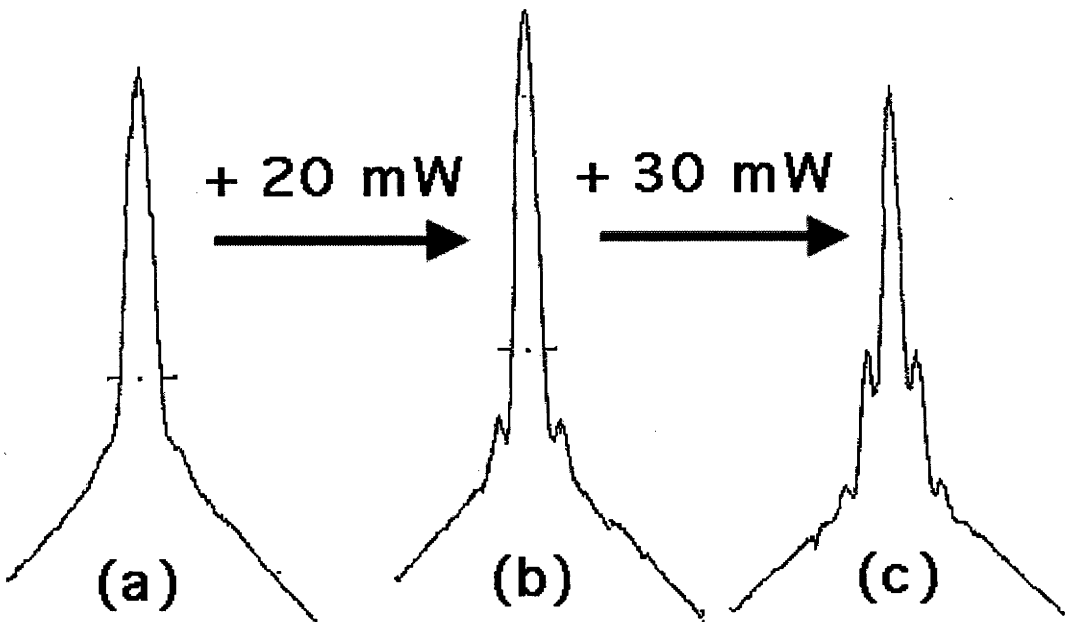
Figure 2-12: The effect of varying the power focussed into the fibre on the temporal profile of the compressed pulse. The grating separation is 308 cm. (a) The chopped cw power before the fibre is 1.05 W (2.1 kW peak in 60 ps) and 600 mW after the fibre, in (b) the power before the fibre is 1.1 W and 620 mW after the fibre and in (c) the power before the fibre is 1.17 W and 650 mW after the fibre.

27
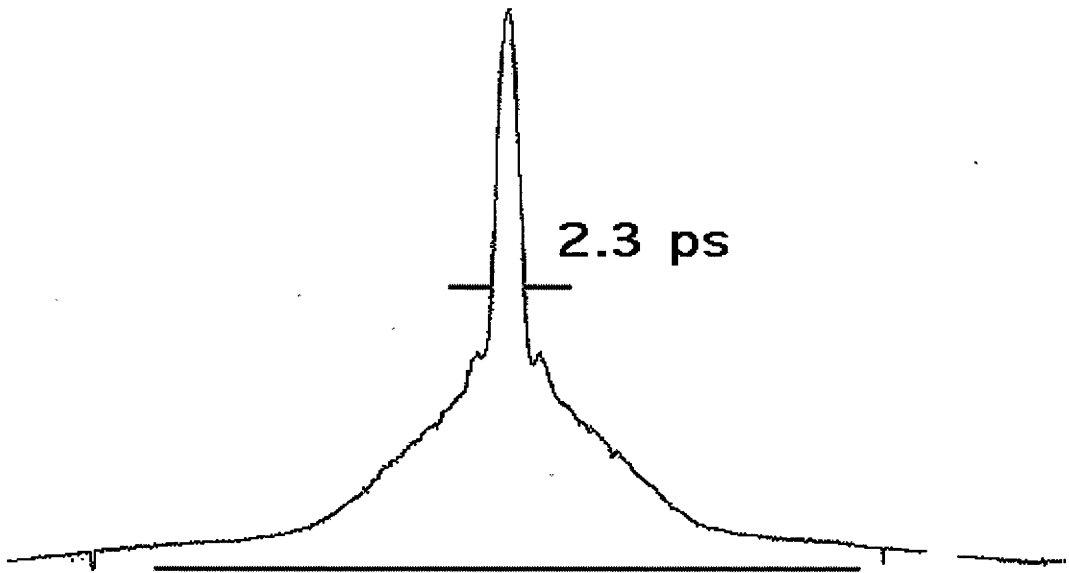
Figure 2-13: An intensity autocorrelation trace of the compressed pulse showing all features of the pulse; the narrow central peak, the two sidelobes and the broad pedestal. The peak power is 16 kW and the pulse duration is 2.3 ± 0.2 ps. The grating separation 308 cm. This is considered the "best" compressed pulse shape. The line at the bottom of the trace marks zero intensity.

the pulse but naturally result from pulses with multiple peaks (such as a Sinc^2 pulse shape) [17]. From the figure showing the interferometric autocorrelation one would conclude that the pulse is close to being a transform-limited Gaussian pulse. However, we know from the intensity autocorrelation that this is incorrect. To check that the measurement was correct, the intensity autocorrelation of the pulse was extracted from the interferometric autocorrelation data following the analysis of [18] and compared with the measured intensity autocorrelation. The extracted intensity autocorrelation is not background free, as is the measured intensity autocorrelation. Since the contrast ratio is 3:1 for an intensity autocorrelation with a background, as opposed to infinite without a background, the retrieved intensity autocorrelation shows a Gaussian like pulse with low sidelobes on an essentially constant background (see Figure 2-16). The pedestal structure apparent in the measured intensity autocorrelation is not seen by the interferometric autocorrelation. The measured interferometric autocorrelation is essentially one of the central peak of the compressed pulse with low sidelobes on a constant background.
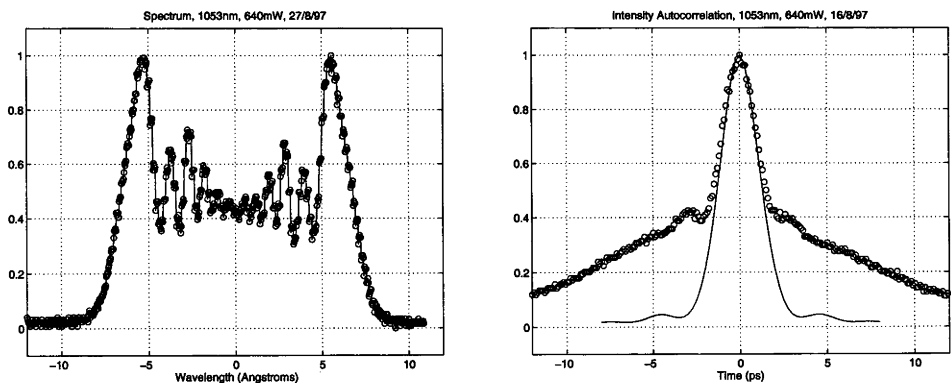

Figure 2-14 : The power spectrum (left) and the intensity autocorrelation (right) of the compressed pulse. The chopped cw power is 640 mW after the fibre using the glass chuck. The expected transform-limited pulse is also shown with the measured intensity autocorrelation.
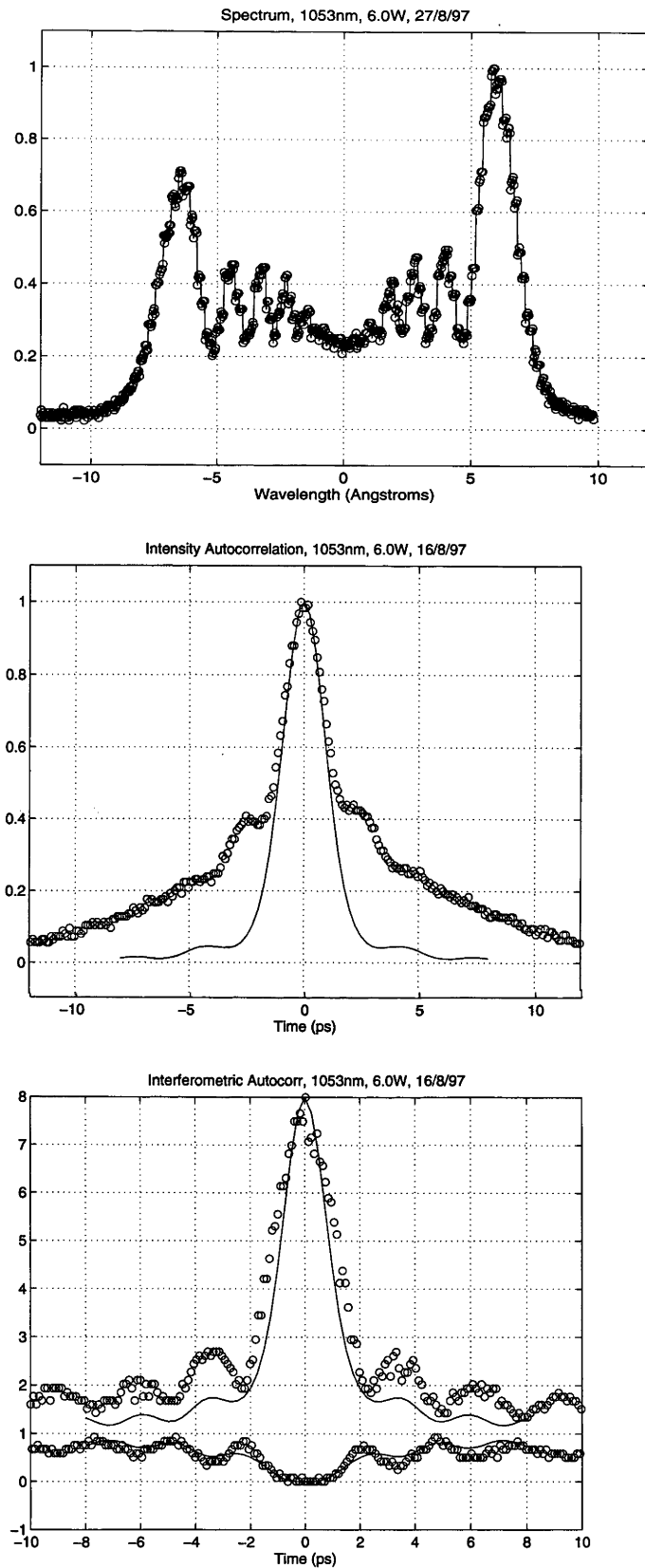
Figure 2-15 : The power spectrum (top), the intensity autocorrelation (middle) and the envelope of the interferometric autocorrelation of the compressed pulse at 6.0 full cw. The solid line in the intensity and interferometric autocorrelations are the transform-limited autocorrelations derived from the power spectrum. The distortion of one side of the spectrum is due to the spectrometer and not due to SRS.
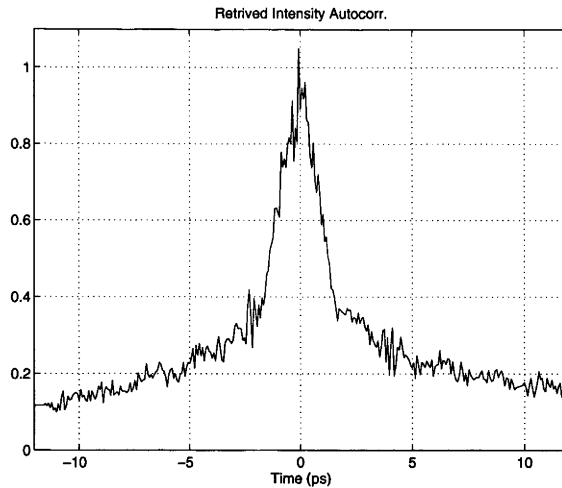
Retrived Intensity Autocorr.

Figure 2-16 : The retrieved intensity autocorrelation from the interferometric autocorrelation measurement shown in Figure 2-15. Refer to the text for more details.

In summary, the fibre-grating pulse compressor provided an 8 times power enhancement from 2.1 kW to 16 kW after the pulse compressor when an average power of ~ 10 W from the Antares laser was coupled into the fibre. This represented more than a factor of 4 increase over the maximum power available from the Antares laser operating at a maximum of 18 W average power. The maximum power that could be coupled into the ~ 5.5m long single-mode optical fibre, used to generate a linear frequency chirped pulse via SPM, was determined by the onset of stimulated Raman scattering. The compressor used a 1200 lines/mm gold coated diffraction grating to eliminate the linear frequency chirp on the pulse and reduced the laser pulse duration from 60 ps to ~ 2.5 ps making it more suitable for generating ps OPO pulses. The measured pulse duration, the spectral width of the SPM pulse and the grating separation were all close to what was theoretically expected. Losses of 30% due to fibre coupling and 30-35% due to the limited grating reflectivity also restricted the available output power.

2.4 The second harmonic generator

As shown in Figure 2-1 the compressed pulse was frequency doubled to a wavelength of 527 nm to drive the LBO OPO. The frequency doubler used temperature-tuned, Type I (o+o → e), noncritical phasematching (NCPM) in an x-cut, 3 mm by 3 mm by 15 mm long Lithium Triborate (LBO) crystal. The crystal entrance and exit faces were AR coated for 1054 nm and 527 nm respectively, reducing the reflection losses to < 1% per surface. The compressed pulse was focussed into the LBO crystal by a AR coated biconvex lens with a focal length of 130 mm and the generated second harmonic was collimated by an AR coated plano-convex lens with a focal length of 90 mm. The choice of the focal length of the focussing lens was chosen experimentally to maximise the SHG power. The SH and the IR pulses were separated by two 45° turning mirrors with maximum reflectivity at 527 nm.

The LBO was temperature-tuned for phase matching using a high stability (~ 0.1 °C) temperature-controlled oven that could be adjusted between room temperature and 200°C. The calculated operating temperature for 1054 nm radiation was 158°C and NCPM phasematching temperature bandwidth calculated for LBO was ΔT_{FWHM} ≈ 4.2°C-cm [19]. For the 1.5 cm long crystal used here, the temperature bandwidth should therefore be 2.8°C. The temperature bandwidths measured for two LBO crystals used in these experiments were 2.8°C and 2.6°C.
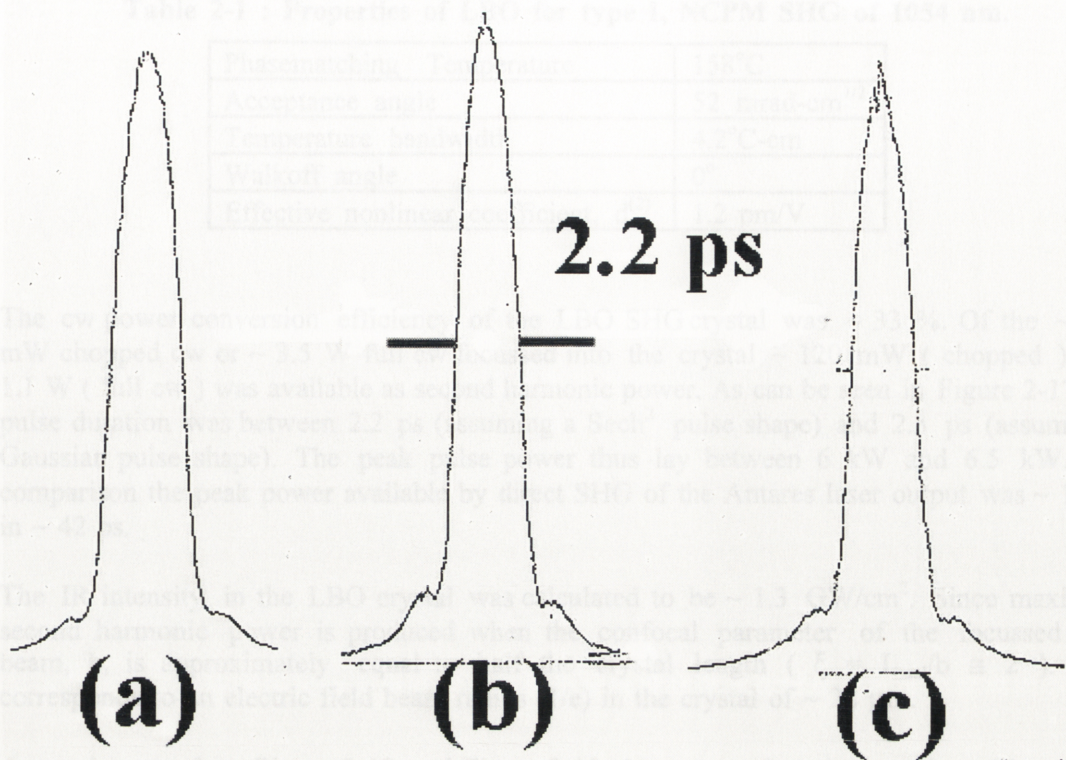
2.2 ps

(a)   (b)   (c)

Figure 2-17 : The intensity autocorrelations of the frequency doubled compressed pulse. The trace (a) is for the case of 600 mW chopped cw power after the fibre and the SH power is 103 mW; trace (b) is for 620 mW after the fibre and the SH power is 111 mW; and trace (c) is for 650 mW after the fibre and the SH power is 100 mW (see Figure 2-12 for compressed pulse intensity autocorrelations). The pulse duration is 2.2 ps (Sech^2 pulse).
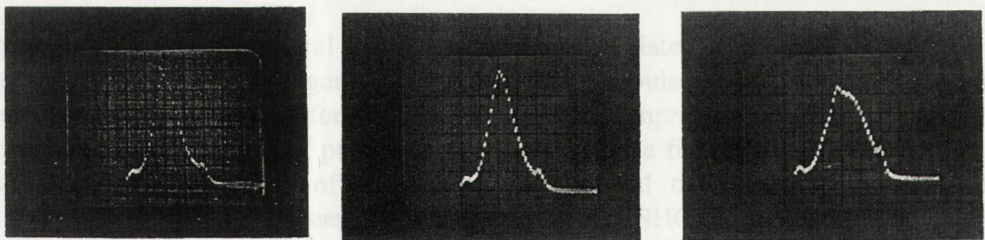

Figure 2-18 : The power spectra corresponding to the intensity autocorrelations shown above. The horizontal scale is 1.25 Angstroms per division.

Type I, temperature-tuned NCPM SHG has advantages over critically phase matched, angle-tuned SHG in LBO crystal, such as, a broader phase matching bandwidth; a higher nonlinear coefficient; greater angular acceptance; and a zero (Poynting vector) walk-off angle between the e-ray SH and the o-ray pump. Practically, this means that temperature-tuning the LBO makes the SHG efficiency less sensitive to variations in phase matching (angle or temperature). NCPM allows tighter focussing of the fundamental beam without problems of beam walkoff or the beam suffering phase mismatch across its profile. As well as being less sensitive to phase mismatch due to a broad spectral bandwidth. The oven was always left at the phase matching temperature since LBO is mildly hydroscopic.

31

Table 2-1 : Properties of LBO for type I, NCPM SHG of 1054 nm.

Phasematching Temperature	158°C
Acceptance angle	52 mrad-cm$^{1/2}$
Temperature bandwidth	4.2°C-cm
Walkoff angle	0°
Effective nonlinear coefficient, $d^{(2)}$	1.2 pm/V

The cw power conversion efficiency of the LBO SHG crystal was ~ 33 %. Of the ~ 340 mW chopped cw or ~ 3.5 W full cw focussed into the crystal ~ 120 mW (chopped) or ~ 1.1 W (full cw) was available as second harmonic power. As can be seen in Figure 2-17 the pulse duration was between 2.2 ps (assuming a Sech^2 pulse shape) and 2.3 ps (assuming a Gaussian pulse shape). The peak pulse power thus lay between 6 kW and 6.5 kW. For comparison the peak power available by direct SHG of the Antares laser output was ~ 1 kW in ~ 42 ps.

The IR intensity in the LBO crystal was calculated to be ~ 1.3 GW/cm^2. Since maximum second harmonic power is produced when the confocal parameter of the focussed laser beam, b, is approximately equal to half the crystal length ($\xi = L_{xtal}/b \cong 2$). This corresponds to an electric field beam radius (1/e) in the crystal of ~ 28 μm.

As can be seen from Figure 2-17 and Figure 2-18 the temporal and spectral profiles of the SHG pulses approximated to either a Sinc^2 or Gaussian pulse shape with low sidelobes. The sidelobes are at a level of ~ 10 % of the peak power. Since the SHG conversion efficiency is proportional to the square of the fundamental intensity the sidelobes and broad pedestal evident on the IR compressed pulse were converted less efficiently to second harmonic than the central peak.

Several other examples of SH intensity autocorrelations and spectra are shown in Figures 2-19 to 2-20. The SHG temporal and spectral pulse profiles were very similar for all conditions; that is using chopped cw power with the normal fibre chuck or using the glass chuck with chopped cw power and full cw power.

The transform-limited temporal pulse shape was calculated from the measured power spectrum. As can be seen in Figures 2-19 to 2-22 the SH pulses were not transform-limited, but were closer to being transform-limited than the compressed IR pulses. There is still some frequency chirp in the SH pulse. As can be seen in the figures the change in the power focussed into the fibre has less of an effect on the temporal or spectral profiles of the SHG pulses than for the IR compressed pulses. However, the SHG power changes strongly with grating separation and input power. The compressed IR pulse with the "best" pulse shape usually produced the maximum SHG power (see Figure 2-23).

It was not possible to record interferometric autocorrelations for the 527 nm pulses because no suitable UV sensitive detector was available at the time of the measurements.

The SHG crystal also acted as a spatial filter and improved the beam quality of the SH relative to the fundamental. The grating used to compressed the IR pulses exhibited "ghosting" effects which appeared as modulations ("stripes") across the intensity distribution of the nominally Gaussian profile beam. Ghosting results from a periodic error in the rulings of the grating. When the compressed pulse was focussed into the SHG crystal the modulation is not focussed as well as the underlying Gaussian beam profile, resulting in efficient conversion of only the energy contained within the Gaussian beam profile. The ghosting was therefore eliminated leaving a good quality Gaussian beam profile.
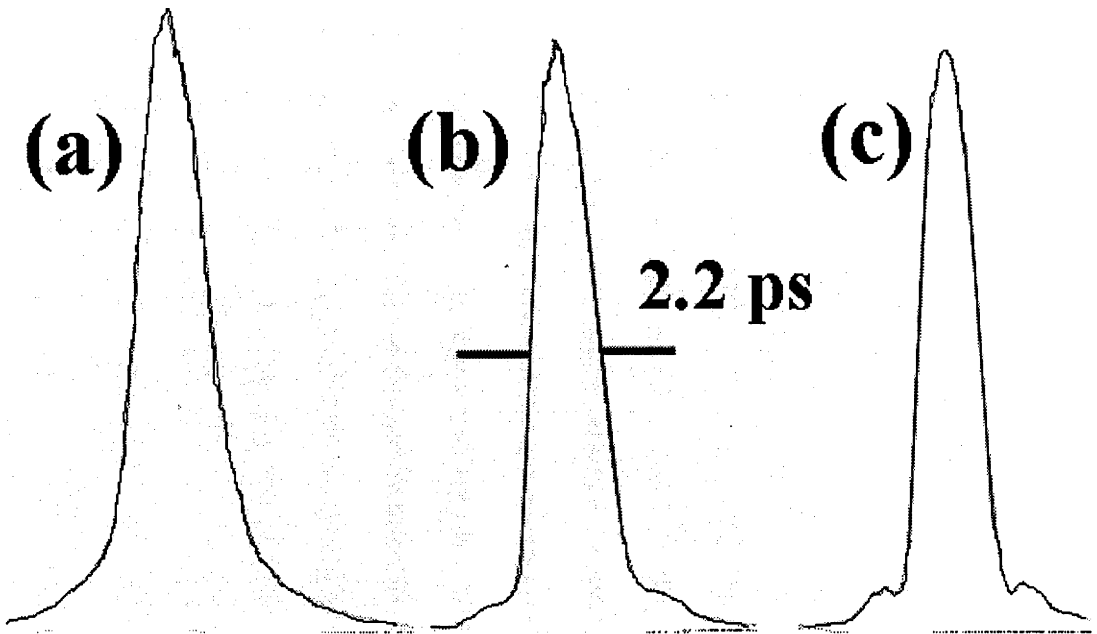
Figure 2-19 : The intensity autocorrelation of the frequency doubled compressed pulse. The trace (a) is for the case of 580 mW chopped cw power after the fibre using the glass chuck and the SH power is 83 mW; trace (b) is for the case of 620 mW after the fibre and the SH power is 112 mW; and trace (c) is for the case of 660 mW after the fibre and the SH power is 120 mW.
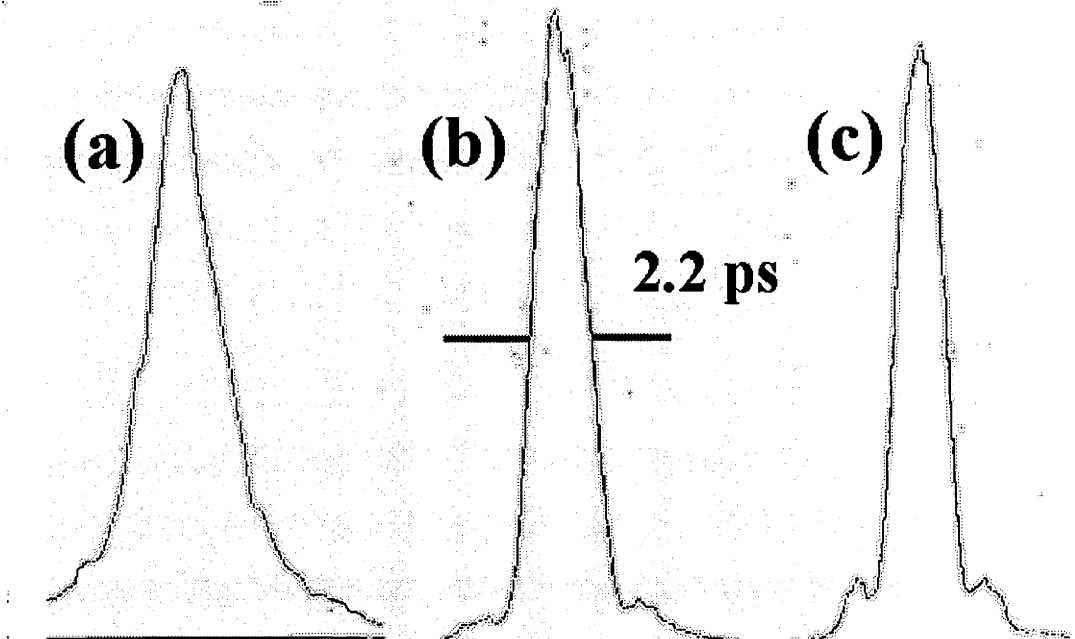

Figure 2-20 : The intensity autocorrelation of the frequency doubled compressed pulse. The trace (a) is for the case of 5.6 W full cw power after the fibre using the glass chuck and the SH power is 740 mW; trace (b) is for the case of 6.2 W after the fibre and the SH power is 1.15 W; and trace (c) is for the case of 6.6 W after the fibre and the SH power is 1.15 W.
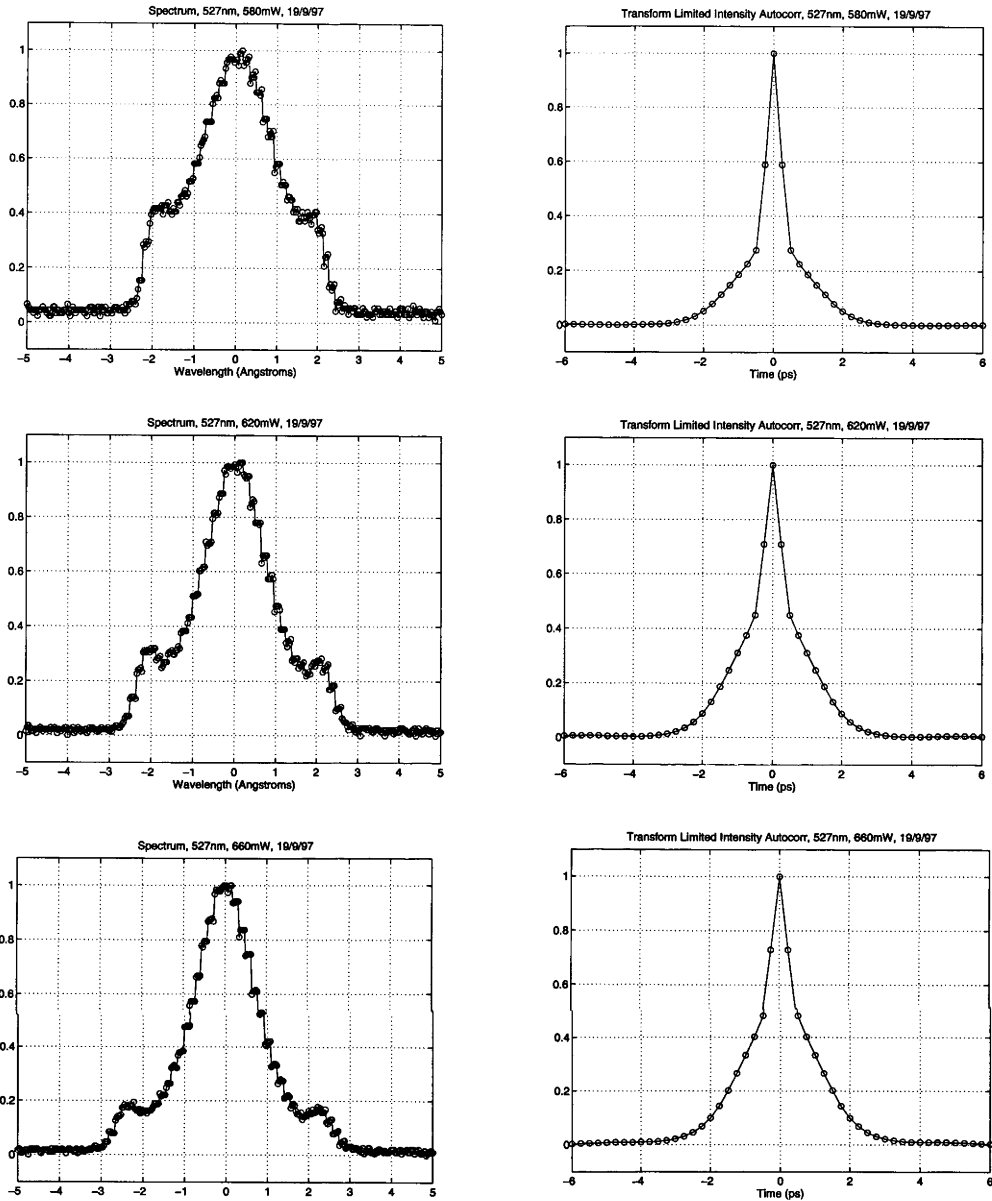
Figure 2-21 : The power spectra and the transform-limited intensity autocorrelations derived from the spectra using the chopped cw beam with the glass fibre chuck. The transform-limited intensity autocorrelations should be compared with those in Figure 2-19.

The SHG system operated stably over long periods of time. If the SHG power fell, a quick adjustment of the waveplates and/or an adjustment to the Antares cavity length to regain optimum mode-locking was sufficient to return to maximum SHG power. Most of the time it is not necessary to monitor the SH power with a cw power meter, the SHG power can be maximised by eye.

In summary, the SHG produced 6 to 6.5 kW pulses that were 2.2 ps ($Sech^2$) to 2.3 ps (Gaussian) in duration. The pulse shape consisted of a central Gaussian-like peak with low sidelobes, with the FWHM time bandwidth product of the pulse estimated to be near ~ 0.47 for the chopped cw beam and ~ 0.5 for the full cw beam. Assuming that the central peak was a Gaussian or $Sech^2$ pulse, then the central peak was approximately 1.1 (chopped cw) to 1.2 (full cw) times the transform limit for a Gaussian pulse and 1.4 (chopped cw) to 1.5 (full cw) times the transform limit for a $Sech^2$ pulse.
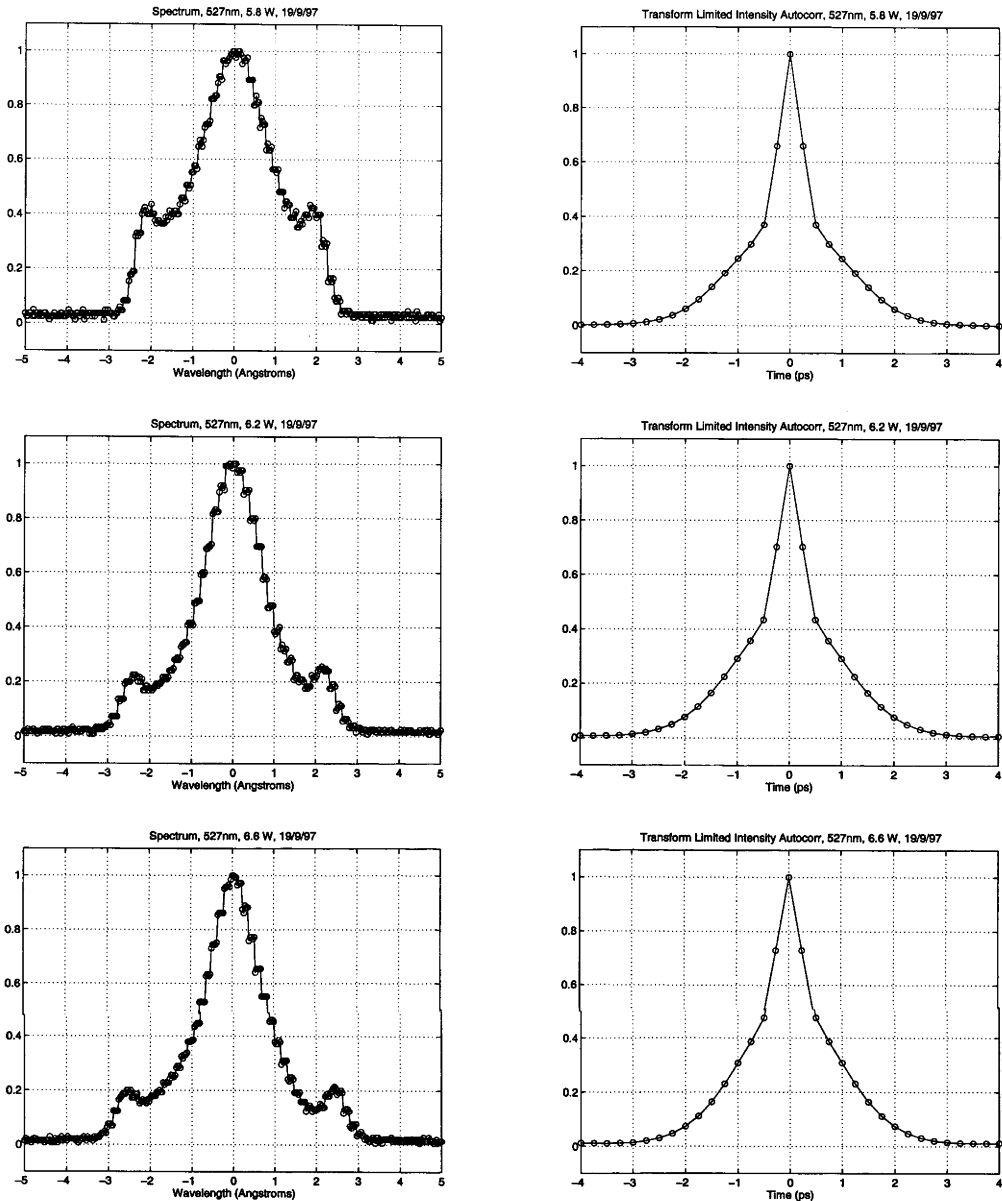
34

Figure 2-22 : The power spectra and the transform-limited intensity autocorrelations derived from the spectra using the full cw beam with the glass fibre chuck. The transform-limited intensity autocorrelations should be compared with those in Figure 2-20.

2.5 Summary

The requirements for the OPO pump laser system are that it produce short, high peak power pulses that are close to being transform-limited. The peak power of the pulses have to be sufficient to drive the OPO well above threshold to achieve stable operation. For these reasons it was decided to use a fibre-diffraction grating pulse compressor to shorten and to increase the peak power of the pulses from the Antares laser; then to frequency double the pulses to a wavelength of 527 nm. Using the Antares laser without this pulse compressor produced pulses with insufficient peak power and with undesirably long pulse durations. Other possible methods were discounted because the fibre-diffraction pulse compressor could provide greater peak power enhancements and shorter the pulses.
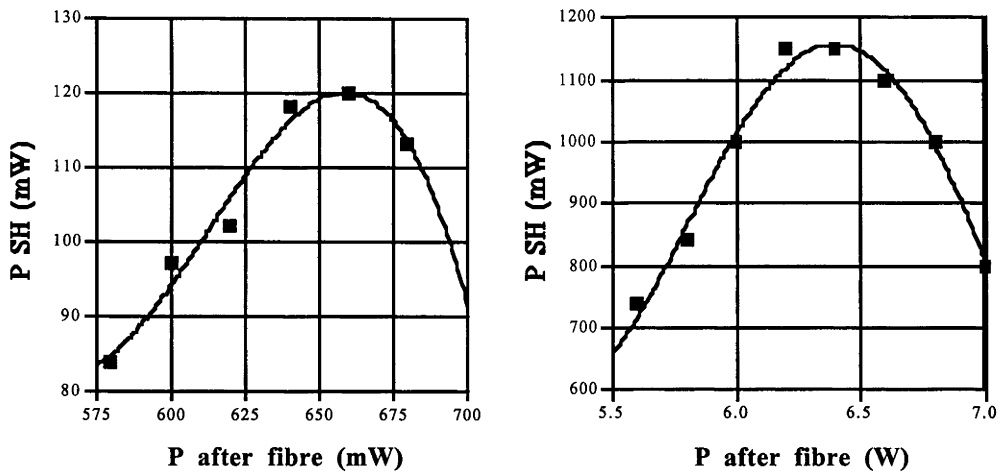
Figure 2-23 : **The variation of cw SHG power with the cw power of the compressed pulse measured after the fibre (using the glass chuck). The left plot is for the chopped cw beam and the right plot is for the full cw beam.**

Specifically the pulse compressor compressed the 60 ps pulse from the Antares Nd:YLF laser down to a pulse ~ 2.5 ps in duration and increased the peak power 8 times, from 2.1 kW to 16 kW. The expected compressed pulse duration and spectral bandwidth of the compressed pulses were 2 ps and 15 Angstroms, close to the measured values of ~2.5 ps and 12.5 Angstroms. The expected grating separation was 350 cm and the actual grating separation was 310 cm. It was found that the compressed pulse shape was not critically sensitive to variations in the grating separation and the power coupled into the fibre. The overall efficiency of the pulse compressor was 32 % with the major losses due to the fibre coupling efficiency and reflection losses of the diffraction grating. The polarisation of the pulses was controlled through fibre polarisation control loops or through waveplates. Any polarisation rotation the pulse experienced by propagating through the fibre was mostly correctable by the fibre loops or the waveplates.

The compressed pulse was frequency doubled using a 15 mm long, x-cut LBO crystal. The LBO crystal used temperature-tuned, type I phasematching. This allowed NCPM to be utilised, with favourably advantages over critical phasematching of LBO. The SHG power conversion efficiency was around 30 % resulting in the 2.5 ps, 16 kW, 1054 nm compressed pulses being converted into 527 nm, 6.5 kW peak power pulses that were 2.2 ps in duration. A peak power that was more than enough to drive the LBO OPO many times above threshold.

The desirable requirement that the pulses be transform-limited was not fulfilled. Though the SHG pulses were not transform-limited they were closer to being transform-limited than the IR compressed pulse; with the central peak at most 1.5 times the transform limit for a Sech^2 pulse. The pulse had a Sinc^2 or a Gaussian with low sidelobes shape.

In conclusion, the OPO pump laser system produced a pulse that was short enough in duration and with a high enough peak power to drive the LBO OPO. The fact that the SHG pulse was not transform-limited was not found to be the principle problem in generating transform-limited pulses from the OPO, as the next chapter will explain.

36

2.6 References

[1]   Coherent, "Technical paper on LBO frequency doubling of Antares," TIB-91-2, 5 Februrary 1991 1991.

[2]   S. D. Butterworth, S. Girad, and D. C. Hanna, "High-power, broadly tunable all-solid-state synchronously pumped lithium triborate optical parametric oscillator," *JOSA B*, vol. 12, p. 2158, 1995.

[3]   A. Ashkin, G. D. Boyd, and J. M. Dziedzic, "Resonant optical second harmonic generation and mixing," *IEEE Journal of Quantum Electronics*, vol. QE-2, p. 109, 1966.

[4]   G. C. Bhar, U. Chatterjee, and P.Datta, "Enhancement of second harmonic generation by double-pass configuration in Barium Borate," *Appl. Phys. B.*, vol. 51, p. 317, 1990.

[5]   S. H. Chakmakjian, M. T. Grunsien, K. Koch, and G. T. Moore, "High-efficiency frequency conversion by phased cascading of nonlinear optical elements," presented at CLEO 94, 1994.

[6]   S. T. Yang, C. C. Pohalski, E. K. Gustafson, R. L. Byer, R. S. Feigelson, R. J. Raymakers, and R. K. Route, "6.5 W, 532 nm radiation by cw resonant external-cavity second-harmonic generation of an 18 W Nd:YAG laser in LBO," *Optics Letters*, vol. 16, p. 1493, 1991.

[7]   H. Komine, "Average-power scaling for ultraviolet-pumped beta-barium borate and lithoum triborate optical parametric oscillators," *JOSA B*, vol. 10, p. 1751, 1993.

[8]   D. v. d. Linde, "Characterization of the noise in continuously operating mode-locked lasers," *Appl. Phys. B*, vol. 39, p. 201, 1986.

[9]   J. Chung and A. E. Siegman, "Singly resonant continuous-wave mode-locked KTP optical parametric oscillator pumped by a Nd:YAG laser," *JOSA B*, vol. 10, p. 2201, 1993.

[10]   G. P. Agrawal, *Nonlinear fiber optics*: Academic press, Inc., 1989.

[11]   W. Hodel, "Investigation of nonlinear effects in optical single mode fibers," PhD : University of Bern, 1986.

[12]   R. Stolen, "Nonlinearity in fiber transmission," *Procs. IEEE*, vol. 68, p. 1232, 1980.

[13]   P. N. Kean, K. Smith, and W. Sibbett, "Spectral and temporal investigation of self-phase modulation and stimulated Raman scattering in a single-mode optical fibre," *IEE Procs.*, vol. 134, Pt J, p. 163, 1987.

[14]   Y. Wang, "Development of a high contrast Nd:Glass laser using chirped pulse amplification," PhD, *Laser Physics Centre, RSPhySE*: Australian National University, 1993.

[15]   H. C. Lefevre, "Single-mode fibre fractional wave devices and polarisation controllers," *Electron. Letts.*, vol. 16, p. 778, 1980.

[16]   R. Ulrich, S. C. Rashleigh, and W. Eickhoff, "Bending-induced birefringence in single mode fibers," *Optics Letters*, vol. 5, p. 273, 1980.

[17]   F. Hache, T. J. Driscoll, M. Cavallari, and G. M. Gale, "Measurements of ultrashort pulse durations by interferometric autocorrelation : influence of various parameters," *Applied Optics*, vol. 35, p. 3230, 1996.

[18]   K. Naganuma, K. Mogi, and H. Yamada, "General method for ultrashort light pulse chirp measurement," *IEEE J. Quant. Electrons.*, vol. QE-25, p. 1225, 1989.

[19]   J. T. Lin, J. L. Montgomery, and K. Kato, "Temperature-tuned noncritically phase-matched frequency conversion in LBO crystal," *Optics Communs.*, vol. 80, p. 159, 1990.

3. The optical parametric oscillator

3.1 Introduction

In order to produce high quality, short, high-power pulses that are tunable in wavelength from 1.27 µm to 1.625 µm, it necessary for the seed pulses for the optical parametric amplifier (OPA) to be as near to transform-limited as possible. Any high-gain frequency conversion process can be sensitive to phase distortion in the seed pulses (see Chapter 5). The seed pulses for the OPA were produced by a synchronously pumped optical parametric oscillator (OPO). The OPO, using a Lithium Triborate (LBO) crystal, was designed to produce wavelength tunable pulses from 650 nm to 2600 nm when pumped at 527 nm. As shown in the previous chapter, the pump pulses for the LBO OPO were not actually transform-limited and as will be shown in this chapter, a simple OPO does not produce transform limited pulses either. As a result a more complex OPO resonator geometry was necessary to make the OPO pulses transform-limited. This chapter outlines the design and construction of the LBO OPO; its operating characteristics using a simple singly resonant OPO cavity (free running OPO); and its characteristics when operating with stabilising elements aimed to produce transform-limited pulses.

The OPO pump system employing a fibre - diffraction grating pulse compressor and an LBO second harmonic generator (SHG) was described in the previous chapter. The result was a 527 nm pump system producing 6.5 kW peak power, 2.2 ps pulses and with a Sinc^2 like spectral and temporal profile. The IR compressed pulses were not transform limited. However, the SH pulses were much closer to being transform-limited than the compressed IR pulses. The FWHM transform-bandwidth products of the SH pulses was 1.4 to 1.5 the transform limit for a Sech^2 shaped central peak and 1.1 to 1.2 the transform limit for a Gaussian shaped central peak.

3.2 Theory

### 3.2.1 Lithium Triborate properties

LBO was chosen as the parametric generation crystal because it has significant advantages over other possible crystals. Other readily available alternative OPO crystals included Potassium Titanyl Phosphate (KTP) and β-Barium Borate (BBO).

KTP [1] is a positive biaxial crystal that has the advantages of being mechanically robust with a high damage threshold; a large effective nonlinear coefficient; a broad transparency range of 350 nm to 4500 nm; and broad angular, spectral and temperature acceptance angles (a measure of how sensitive the process is to a variation in a parameter that affects phase matching). When using KTP as an OPO crystal is it normal to employ phase matching in the x-z (φ = 0°) plane because the effective nonlinear coefficient is greater for this geometry than the other phase matching planes. To generate wavelength tunable pulses between 1.2 µm to 1.6 µm it is necessary to pump the KTP with ~ 530 nm pulses. Though it could be pumped at ~ 1 µm it is not possible to generate signal pulses below 1.4 µm. Using a 527 nm pump, the idler wavelength can be varied between 1.2 µm to 1.6 µm by angle tuning the crystal over a 25° range. Hence, to cover the required tuning range requires a large aperture crystal or rather thin crystal. The inverse group velocity mismatch between the ~ 530 nm pump pulse and the signal pulse is quite large at 1 ps/cm, and 5 ps/cm between the pump and idler pulses, limiting the interaction length for ps duration pump pulses. These characteristics are similar in the other phase matching planes. In addition, the use of angle tuning introduces significant spatial beam walk off between o and e-rays in the crystal. When tight pump focusing is necessary this limits the interaction length since the beams can separate within the crystal.

BBO [2] is a negative uniaxial crystal that has a large nonlinear coefficient and a wide transparency range from 189 nm to 3500 nm. A BBO OPO can easily generate pulses that are wavelength tunable between 1.2 μm to 1.6 μm when pumped by pulses at ~ 530 nm. Using Type I or II phasematching it is possible to cover this wavelength range by angle tuning over ~ 3° for Type I and ~ 10° for Type II phase matching. The main disadvantage is that BBO has a large walk-off angle and a small angular acceptance angle. This means that tight focusing cannot be used with BBO OPOs. This prevents the use of short, medium power pulses, such as those available for these experiments, since tight focusing is required to bring the intensity up to a point where high conversion efficiencies are possible. BBO in used more often with OPOs pumped by ns pump pulses of mJ energies where tight focusing is not necessary.

LBO [3] is a negative biaxial crystal that has a moderate effective nonlinear coefficient of 1.2 pm/V (less than BBO and KTP but about 2.5 times greater than d_{36}(KDP)); a wide transparency range from 160 nm to 2200 nm; an exceptionally high damage threshold; and broad angular, spectral and temperature acceptance angles and no beam walk-off when using non-critical phasematching (NCPM). It has a lower group velocity mismatch (GVM) than both BBO and KTP crystals used as OPOs. Type I NCPM can be achieved by phase matching along the x-axis ($\theta = 90°$, $\varphi = 0°$), see below. The nonlinear coefficient is maximised by NCPM. By temperature tuning the LBO crystal between 100°C and 200°C the it is possible to generate signal and idler pulses with wavelengths between 650 nm to 2600 nm when pumped by pulses at 527 nm. Using temperature tuning relaxes any experimental difficulties with the size and length of the crystal to use, which is not the case for a KTP OPO. Since the wavelength of the generated pulses does not need to change rapidly in our application, NCPM temperature tuning is distinctly better than angle tuning of LBO (where the nonlinear coefficient and the acceptance angles are less) or using BBO or KTP for our application.

LBO NCPM
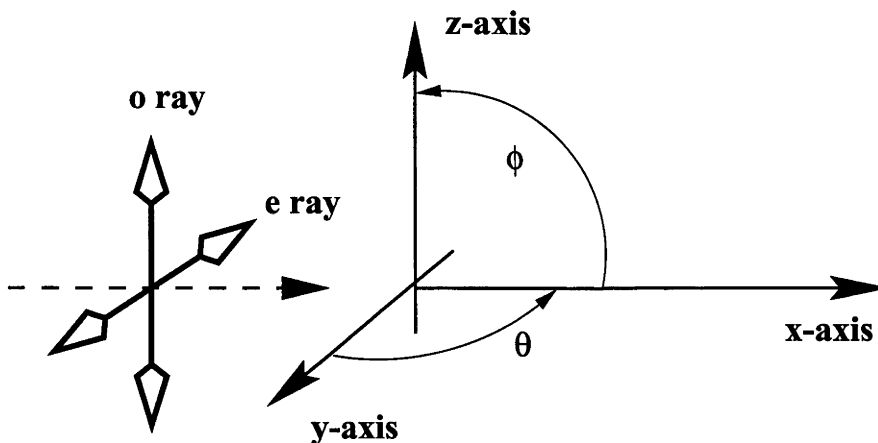
An OPO works by down-converting the pump wave to two lower frequency waves traditionally called the signal wave and the idler wave. This occurs because when any material is exposed to radiation a polarisation wave is induced in the material. If the radiation is intense enough the nonlinear response of the material may be strong enough to produce noticeable nonlinear effects such as SHG, difference frequency mixing (parametric amplification), third harmonic generation and the optical Kerr effect. The second-order nonlinear polarisation wave, P, is

$$P_i = \varepsilon_o \sum_{ijk} \chi_{ijk}^{(2)} : E_j E_k$$

where ε_o is the free space permittivity and χ is the nonlinear susceptibility of the material. For parametric generation involving three frequencies ($\omega_3 = \omega_1 + \omega_2$), the nonlinear polarisation waves are

$$P_1(r,\omega_1) = \varepsilon_o \; 2 \; d_{eff} \; E_2^*(r,\omega_2) \; E_3(r,\omega_3)$$

$$P_2(r,\omega_2) = \varepsilon_o \; 2 \; d_{eff} \; E_1^*(r,\omega_1) \; E_3(r,\omega_3)$$

$$P_3(r,\omega_3) = \varepsilon_o \; 2 \; d_{eff} \; E_1(r,\omega_1) \; E_2(r,\omega_2)$$

The numbers refer to the various waves: 1 corresponds to the signal wave, 2 to the idler wave and 3 to the pump wave. d_{eff} is the effective nonlinear coefficient which depends on the crystallographic properties of the crystal and the direction of propagation of the waves involved.

The description of the interaction of the three waves can be derived from the wave equation

$$\nabla \times (\nabla \times E_i) + \frac{\partial}{\partial t}(\sigma \mu_o E_i) + \mu_o \varepsilon \frac{\partial^2 E_i}{\partial t^2} = -\mu_o \frac{\partial^2 P_i}{\partial t^2}$$

where the subscript i describes each of the three waves. Using the fact the nonlinear interaction occurs over distances much greater than the sinusoidal variations in the electric fields, the slowly varying envelope approximation, and for infinite plane waves the above wave equations lead to three coupled equations

$$\frac{dE_1}{dz} = iK_1 E_2^* E_3 \exp(i\Delta kz)$$

$$\frac{dE_2}{dz} = iK_{21} E_1^* E_3 \exp(i\Delta kz)$$

$$\frac{dE_3}{dz} = iK_3 E_1 E_2 \exp(-i\Delta kz)$$

Eqn 3-1

where $K_i = 2\pi \, d_{eff}/n_i\lambda_i$ is the nonlinear coupling coefficient and z is the propagation distance through the crystal.

These equations describe the variation in the magnitude of the electric field of the pump, signal and idler waves as they propagate through the crystal. Δk describes the momentum or phase mismatch between the waves.

$$\Delta k = k_3 - k_1 - k_2 \qquad \text{where } k_i = \frac{2\pi n_i}{\lambda_i}$$

40

Any phase mismatch reduces the rate at which the signal or idler beams grow. The process is called phase matched when $\Delta k=0$. The variation of the refractive index n with angle or temperature determines the wavelengths of the signal and idler waves since the phase matched process is much more efficient than one that is not. For this analysis the phase of the waves is fixed, with the optimum phase change between the waves being $\Delta \varphi = \varphi_3 - \varphi_1 - \varphi_2 = \pi/2$ (ie. $\varphi_3=0$, $\varphi_2=0$ and $\varphi_1=\pi/2$).

For the case of parametric generation, as the pump wave enters the crystal, the signal and idler waves are amplified from quantum noise, with energy being transferred from the pump wave into the signal and idler waves. As can be seen by the equations if the signal and idler waves grow to have a similar magnitude to the pump, energy can then flow from the signal and idler waves back into the pump wave. This is know as reconversion.

The spectral gain and angular acceptance angles can be determined by considering the phase mismatch Δk. To determine the variation in parametric gain of an OPO crystal with any parameter that causes a phase mismatch Δk, such as the dispersion of the material or tight focusing, it is helpful to consider the gain bandwidth of the parametric amplifier. For a low single-pass gain (gain $\ll \pi^2$) the parametric gain bandwidth is (see [4])

$$\frac{\Delta kl}{2} = \pi$$

When $\Delta k = 2\pi l$ (where l is the crystal length) the parametric gain has fallen to half its maximum value. Since the phase mismatch Δk can be expanded by Taylor expansion, the variation in parametric gain can be found for any parameter that varies the refractive index of the crystal ($n_i = n_i(\theta,\varphi,\omega_i,T)$) and, thereby, the momentum vector k_i .

The spectral gain bandwidth is a measure of how sensitive the parametric process is to variations in wavelengths of the interacting waves, can be determined from the Taylor expansion of Δk with respect to the frequency of the interacting waves.

$$\Delta k = \frac{2\pi}{l} = \Delta k_o + \frac{\partial \Delta k}{\partial \omega}\delta\omega + \frac{1}{2}\frac{\partial^2 \Delta k}{\partial \omega^2}\delta\omega^2$$

Since $\dfrac{\partial k_i}{\partial \omega} = \dfrac{1}{v_g^i} = \dfrac{1}{c}\left(n_i - \lambda\dfrac{\partial n_i}{\partial \lambda}\right)$, where v_g is the group velocity of the wave and

$\dfrac{\partial^2 k_i}{\partial \omega^2} = \dfrac{\partial}{\partial \omega}\left(\dfrac{1}{v_g^i}\right) = \dfrac{\lambda^3}{2\pi c^2}\dfrac{\partial^2 n_i}{\partial \lambda^2} = D_i$ is the group velocity dispersion of the wave. Since

$\Delta k_o = 0$ at phasematching the spectral gain bandwidth becomes

$$\Delta k = \left(\frac{1}{v_{g\,2}} - \frac{1}{v_{g\,1}}\right)\delta\omega_1 + \frac{1}{2}(D_1 + D_2)\delta\omega_1^2 = \beta'\delta\omega_1 + \beta''\delta\omega_1^2$$

For our case it is only necessary to take into account the terms to first order because the second term is negligible compared to the first order term for signal pulses with wavelengths between 780 nm to 920 nm in NCPM LBO. The second order term only becomes comparable in magnitude with the first order term near turning points in the phase matching curve (see Figure 3-3). To estimate the wavelength range over which we can
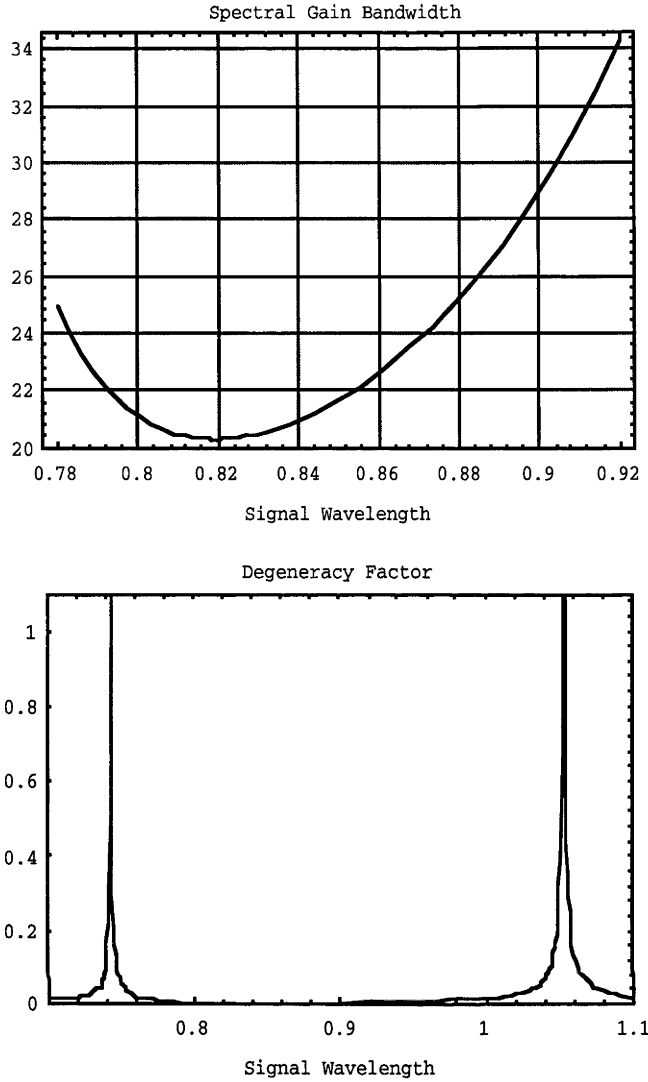
Spectral Gain Bandwidth

34
32
30
28
26
24
22
20

0.78   0.8   0.82   0.84   0.86   0.88   0.9   0.92

Signal Wavelength

Degeneracy Factor

1
0.8
0.6
0.4
0.2
0

0.8   0.9   1   1.1

Signal Wavelength

Figure 3-1 : The spectral gain bandwidth (top figure) in nm of the LBO OPO over the signal wavelength range of interest in μm. The corresponding idler wavelength range is from 1230 nm to 1625 nm. The bottom figure shows the wavelength regions where group velocity dispersion becomes significant in determining the spectral gain bandwidth, where the degeneracy factor > 1.

accurately use the first order expansion to determine the spectral gain bandwidth we can plot the degeneracy factor $\psi = \Delta\omega_o \beta''/\beta'$, where $\Delta\omega_o = 2\pi/\Delta t_3$. If $\psi \ll 1$ then the second order term is insignificant in determining the spectral gain bandwidth. Figure 3-1 shows the spectral gain bandwidth and the degeneracy factor for the LBO OPO using temperature-tuned, type I, NCPM. As can be seen the bandwidth is very broad.

The angular acceptance angle, the angle at which gain falls to half the maximum value, can also be estimated in this manner by expanding Δk with respect to φ and θ. The expansion must be up to second order because for NCPM because $\partial k/\partial\theta$ and $\partial k/\partial\varphi$ are zero. The FWHM angular acceptance angle is given by the following equation.
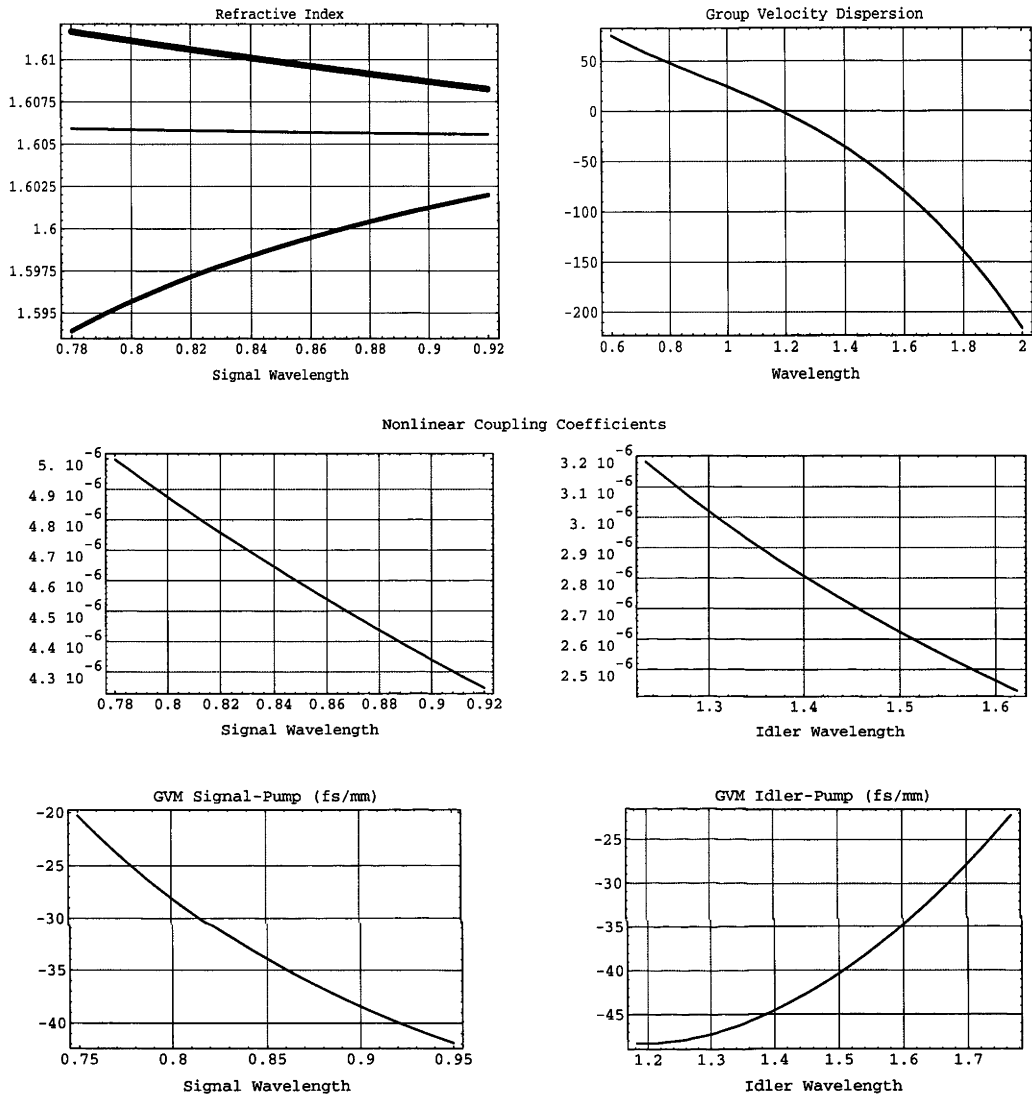
42

Figure 3-2 : The top left figure shows the refractive indices of the pump (thinnest line), the idler and the signal (thickest line) as the signal wavelength varies between 780 nm (1625 nm for the idler) and 920 nm (1230 nm for the idler). The top right figure shows the group velocity dispersion for LBO in fs^2/mm. The middle figures show the nonlinear coupling coefficients in V^{-1} for the signal (left) and the idler (right) over the wavelength range of interest. The nonlinear coupling coefficient for the pump is 7.428×10^{-6} V^{-1} over the entire wavelength region of interest. The bottom figures show the group velocity mismatch between the signal and pump waves, δt_{13} , (left) and between the idler and pump waves, δt_{23} , (right). All these figures are for temperature-tuned, type I, NCPM for LBO. To maintain phase matching the refractive index of the pump wave varies slightly as the signal wavelength is varied.
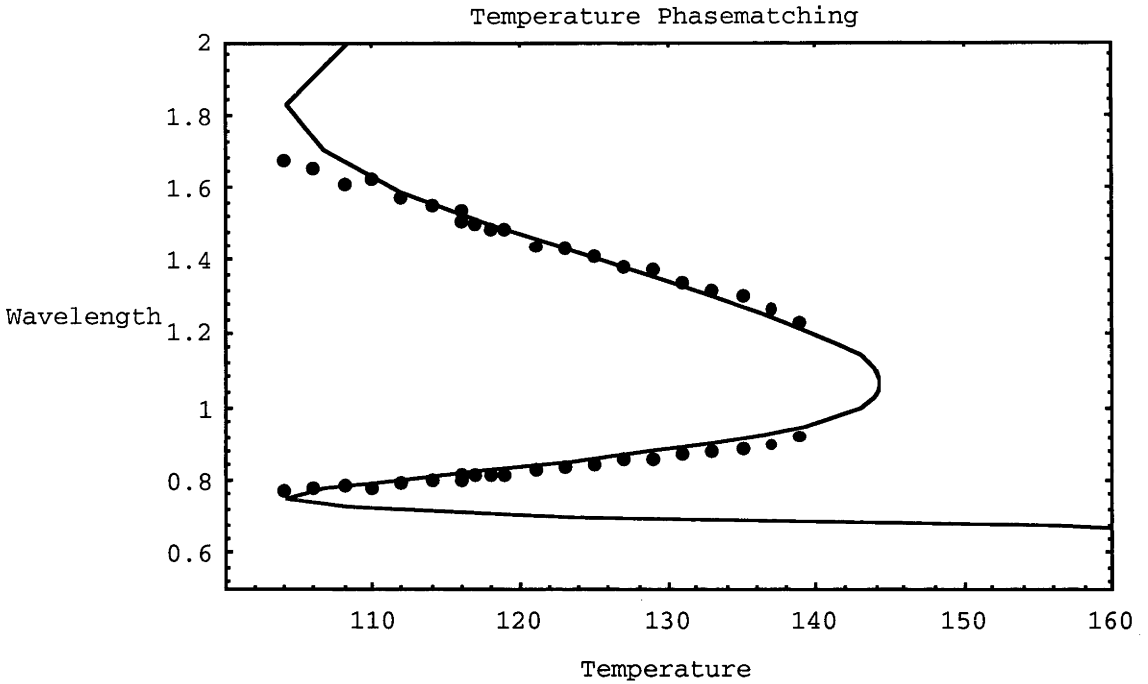
Figure 3-3 : The phase matching curve for temperature-tuned, type I, noncritical phase matching of x-cut LBO pumped at 526.75 nm. The points are experimental values. Note that due to LBO's unique retracing behaviour it is possible to generate four colours at certain temperature. The degeneracy points from Figure 3-1 are at the turning points in the phasematching curve.

$$\Delta\theta = \sqrt{\frac{0.886}{\sqrt{l\left[\left(\frac{n_x(\lambda_1)}{\lambda_1}\right)\left(1-\left(\frac{n_x(\lambda_1)}{n_z(\lambda_1)}\right)^2\right)+\left(\frac{n_x(\lambda_2)}{\lambda_2}\right)\left(1-\left(\frac{n_x(\lambda_2)}{n_z(\lambda_2)}\right)^2\right)\right]}}}$$

l is the crystal length (1 cm) and n_x and n_z are the refractive indices for the principle x and z axes of the LBO crystal. This calculation gives an acceptances angle of roughly 47 mrad-cm$^{1/2}$ across the wavelength range of 780 nm to 920 nm.

Figure 3-2 shows the refractive indices for the pump, signal and idler beams; the group velocity mismatch between the pump and signal waves and the pump and idler waves; the nonlinear coupling coefficients (the nonlinear coupling coefficient for the pump is 7.428x10^{-6} V^{-1}); and the group velocity dispersion for LBO over the wavelength range of interest to us.

Lin, *et. al.*, [5] provided Sellmeier equations for LBO and the temperature relations for the refractive indices. The temperature phase matching curve is shown is Figure 3-3 for LBO pumped at 527 nm. The circles are experimental points taken from the LBO OPO.

In summary, using type I, temperature-tuned, NCPM LBO as the nonlinear crystal for the OPO allows the generation of wavelength tunable radiation from 650 nm to 2600 nm by temperature tuning between 100^{0}C and 200^{0}C; produces no beam walk-off; a wide spectral gain bandwidth and angular acceptance angle thanks to NCPM; a moderate nonlinearity comparable to BBO; and low GVM. These properties make it distinctly better than other crystals such as BBO and KTP as the nonlinear crystal for an OPO pumped by kW, ps pulses at 527 nm.
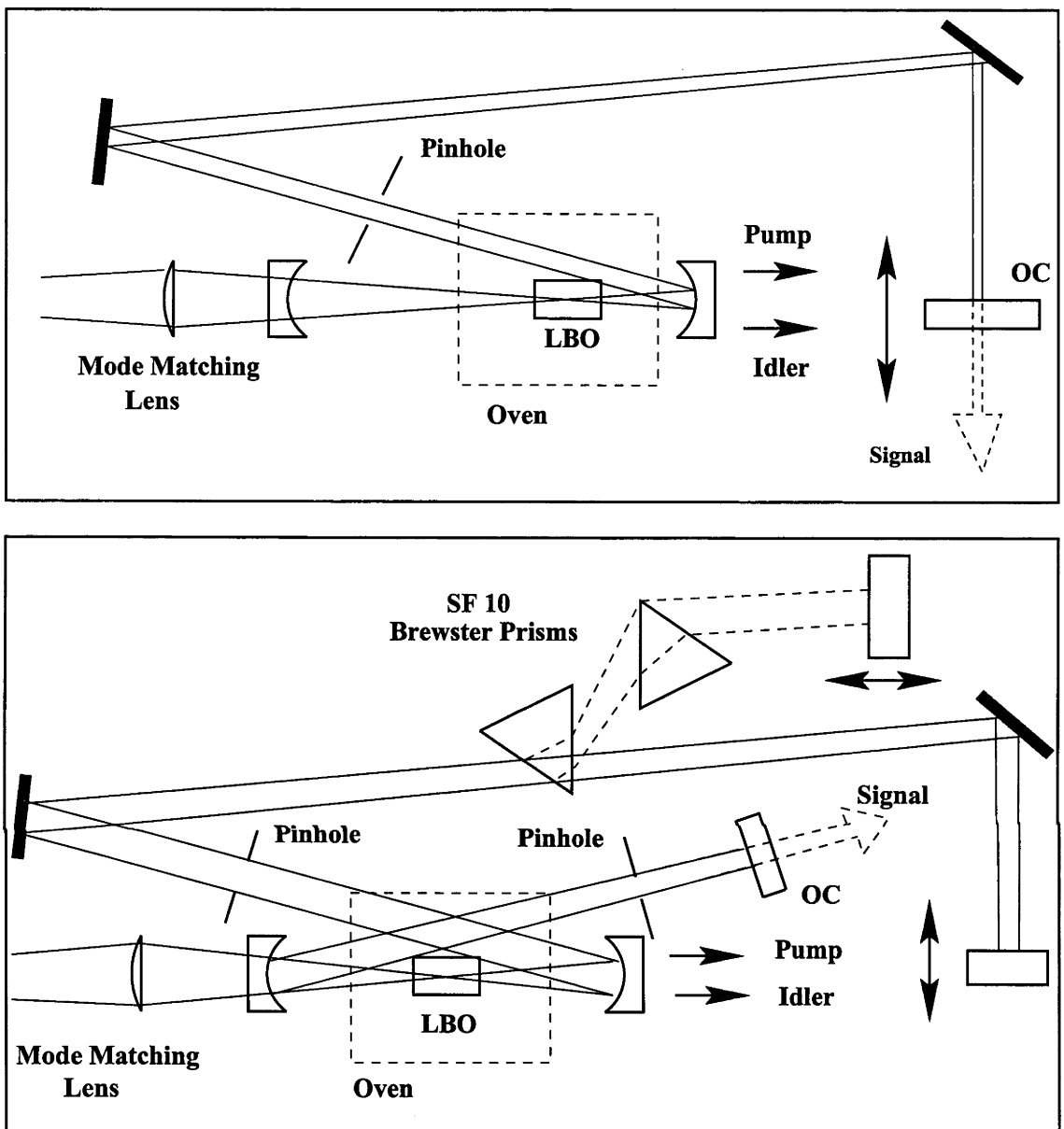
44

Figure 3-4 : The experimental layouts of the LBO OPO. The top figure shows the LBO OPO in the one arm configuration. The bottom figure shows the dual-arm configuration with and without the GVD compensating prism pair.

3.2.2 The optical cavity of the OPO

After choosing a crystal with the best properties for a particular application it is necessary to design a optical cavity to resonate either one or both of the generated waves. When the signal or the idler waves are resonated the OPO is called a singly-resonant oscillator (SRO) and when the cavity resonates both waves it is called a doubly-resonant oscillator (DRO). Both designs have some advantages and disadvantages. The DRO OPO has a much lower threshold than a SRO [4]. Threshold is reached when the parametric gain is equal to the cavity losses. For a DRO operating with low cavity losses (~ few percent) the threshold is reached when the single pass gain $G = \alpha_1 \alpha_2$, where α_1 and α_2 are the round trip power losses in the cavity for the signal (1) and the idler (2) waves respectively. For a SRO, threshold is

45

reached when $G = 2\,\alpha_1$, when the signal wave is resonated. As can be seen for small cavity losses the DRO has a threshold one to two orders of magnitude less than the SRO. However, for cw or quasi-cw OPOs the DRO has a significant disadvantage. It is difficult for the DRO to main cavity frequency resonance conditions for both the signal and idler waves simultaneously. Any fluctuation in cavity length leads to a shift of the resonance reducing the gain of the DRO because oscillation is no longer possible at the signal or idler frequencies for perfect phasematching. Without active cavity stabilisation the DRO suffers from very strong amplitude fluctuations induced by small fluctuations in the resonator length. Hence, whilst the SRO has a higher threshold it is preferable because it leads to more stable operation. As will be shown in the Section 3.3 the LBO OPO can be driven well above threshold as a SRO.

Two resonator designs were used in these experiments (see Figure 3-4). Both are standing wave cavities: the first had one "arm" whilst the second is a "dual arm" configuration. The resonated signal wave was focused into the LBO crystal by two spherical mirrors. The cavity length was adjusted to make the circulating signal pulse arrive in synchronisation with the arrival of the pump pulses at the LBO crystal. The standing wave cavity length, L, was therefore equal to $\frac{c}{2\nu}$, where ν is equal to the repetition rate of the Antares Nd:YLF laser (75.4 MHz). If the cavity length is shifted from synchronisation the signal pulse can arrive earlier or later than the pump pulse. As a result, adjusting the cavity will decrease the gain of the OPO and eventually cause oscillation to cease. The range over which the OPO will operate with changes in cavity length defines the so-called synchroresonance curve. A synchroresonance curve is defined as the output power of the resonated wave as a function of cavity length. The optimum cavity length is usually taken to be the length which maximises the output power of the signal and idler.

Astigmatism appears because both cavities were folded by turning the second focusing mirror, for the one arm case, or both focusing mirrors, for the dual arm case. Commercial software, Paraxia, was used to model the effect of astigmatism and the cavity as a whole using ABCD (EF) ray matrices [6]. The two focusing mirrors had a radius of curvature, R, of 100 mm (f=50mm). In the one arm case, the first mirror was positioned at an effective distance R from the focal point in the LBO crystal, to reimage the focal point. While the second mirror collimated the beam and focused it on the end mirror. In the dual arm case both focusing mirrors are at an effective distance f away from the focal point. For the one arm case the electric field beam radius (1/e) $w_o = 13.8$ µm for the signal at the focus in the 10 mm long LBO crystal. Setting the confocal parameter, $b = \frac{2\pi n w_o^2}{\lambda}$, to be equal for all three waves ($b_1 \approx b_2 \approx b_3$), which, as will be shown, will maximise the parametric gain, gives a beam waist radius for the pump of 10.8 µm and 17.7 µm for the idler.

For the dual arm case the beam waist radius for the signal is not as restricted as for the one arm case, but the cavity was configured to give a beam waist radius of 15.9 µm for the signal. Setting the confocal parameters for the pump and idler equal to the signal confocal parameter gave a beam waist radius of 12.6 µm for the pump and 20.3 µm for the idler. In the experiments using the dual-arm OPO, the pump waist was the same as in the one-arm OPO. Hence the confocal parameters of the signal and the pump are not equal. How this effects the performance of the OPO is described below. To match the confocal parameters of the pump and the resonated signal beam is known as mode-matching. It is desirable to match the confocal parameters of the pump and signal so that the energy of all three wave interacts in the same volume in the crystal. However, as will be shown later, the parametric gain is not very sensitive to variation in confocal parameters. The pump was focused to the required beam waist using a plano-convex lens before the first focusing mirror. Since the first focusing mirror acts a plano-concave lens for the transmitted pump beam, the effect of both the mode-matching lens plus this first mirror must be modelled to determine the pump focus waist size in the LBO crystal.

The Paraxia program proved most useful in determining the effects of astigmatism on the cavity stability. The folded spherical mirror(s) induces astigmatism in the cavity because the
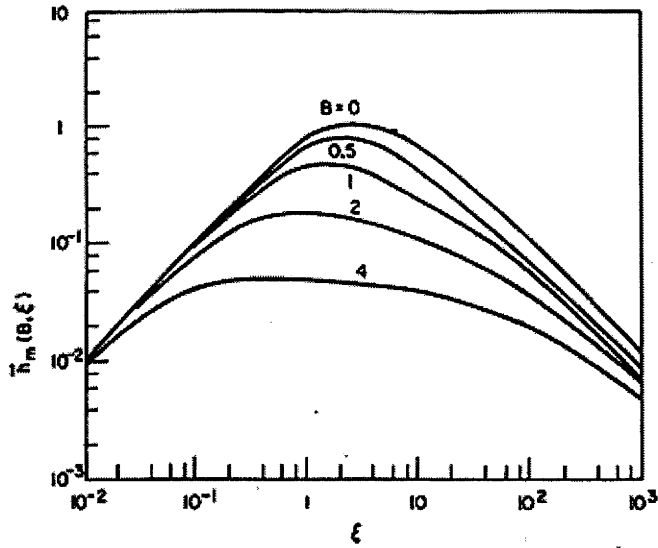
$\tilde{h}_m(B,\xi)$

B = 0
0.5
1
2
4

ξ

Figure 3-5 : The variation in parametric gain due to the focusing of Gaussian beams in a three wave parametric interaction (see Eqn 3-2) for the case where the focusing parameters of all three waves are equal, ie. $\xi_3 = \xi_1 = \xi_2$, and for various cases of walk-off, B. For temperature-tuned, type I, NCPM of LBO the walk-off, B, is zero. The optimum is $\xi = 2.86$. (Taken from [7])

beam experiences different focal lengths in vertical and horizontal planes. The end result is that a spherical beam becomes elliptical. Since the gain will fall if the circulating signal beam is focused to a waist volume which does not optimally overlap with the pump waist it is important to minimise or compensate for astigmatism in the cavity. To minimise astigmatism the folding angle of the mirror(s) was kept as low as possible (2.5° to 3°) . Modelling demonstrated that the astigmatism produced by this folding angle was negligible. For our cavity design the stability range, that is the range over which the focusing mirror separation can be adjusted before the cavity no longer refocusses the circulating signal beam, is ~ 1.5 mm. Therefore the operation of the OPO is not critically dependent on the mirror separation or sensitive to fluctuations in the mirror separation.

3.2.3 Focusing effects on parametric gain

Since we know the pump focus waist size we can estimate the threshold for our OPO. The single pass gain for the signal wave is [4]

$$G_1(l) = \left| \frac{E_1(l)}{E_1(0)} \right|^2 - 1 = Sinh^2 \Gamma l \quad \text{when } \Delta k=0$$

where

$$\Gamma^2 = \frac{2}{\varepsilon_o nc} K_1 K_2 I_3$$

K_1 and K_2 are the nonlinear coupling coefficients for the signal and idler. I_3 is pump intensity at the focus and l is the crystal length. For a pump waist radius of 11 μm the focal area is 1.9×10^{-6} cm^2 ($\pi w_o^2/2$). The peak power of the pump pulses using the frequency doubled pulse compression system is 6 kW in 2.3 ps at the pump focus in the LBO crystal. This gives a maximum pump intensity I_3 of 3.2 GW/cm^2. Using direct SHG of the Antares laser to produce pump pulses, the peak power of the pump pulses would be only 750 W (~ 3 W cw) in ~ 45 ps, giving a maximum pump intensity I_3 of 400 MW/cm^2. Using K_1 =4.5x10^{-6} V^{-1} and K_2 =2.8x10^{-6} V^{-1} the parametric gain coefficient Γ is 19.4 cm^{-1} for the pulse

47

compressed case and 2.4 cm^{-1} for the direct SHG case. This leads to a single pass gain of G_1 = 1.8x10^{16} for the pulse compressed case and G_1 = 30 for the direct SHG case. This simple analysis of course neglects pump depletion and is only valid for infinite plane waves.

To include the effect of focusing on parametric gain requires a more complicated analysis. Boyd and Kleinman [7] first investigated the effects on SHG and parametric gain when using focused Gaussian beams. Their analysis neglected pump depletion, however, at threshold there is negligible pump depletion so their analysis is still valid for estimating the gain required for threshold.

$$G_1 = \frac{2\pi^2 |d_{eff}|^2}{n_o^2 n_3 \varepsilon_o \lambda_3^3 c} P_p l \left(1 - \delta^2\right)^2 h(B, \xi)$$

<div align="right">**Eqn 3-2**</div>

where n_o is the refractive index at degeneracy ($\lambda_o = 2\lambda_3$) and $\left(1 - \delta^2\right)^2 = \frac{\lambda_o^2}{\lambda_1 \lambda_2}$ is the degeneracy factor (the gain decreases the further from degeneracy), P is the peak power of the pump pulses and l is the crystal length. $h(B, \xi)$ is the factor modifying the parametric gain due to focusing. The parameter B is the Poynting vector walkoff, which is zero in our case, and $\xi = l/b$ is the focusing parameter. Eqn 3-2 describes the parametric gain of the signal wave including the effect of the pump beam's Gaussian beam profile. Figure 3-5 shows the variation of $h(B, \xi)$ with ξ and B. For our case with a pump focal beam waist of 11 μm and a 10 mm long LBO crystal, $\xi_p \approx \xi_s \approx \xi_i \approx \xi = 4.3$ and B=0 for the pump, $h(B, \xi) \approx 1.0$.

Therefore, the single pass gain G_1 ($\lambda_1 = 850$nm) = 0.08 or 8 % per pass for direct SHG of the Antares Nd:YLF laser (P = 750 W) and G_1 ($\lambda_1 = 850$nm) = 0.66 or 66 % per pass when using the frequency doubled pulse compressor system (P = 6 kW). This illustrates a very important point. Without pulse compression to provide higher peak power pump pulses, it would be difficult to operate the SRO LBO OPO much above threshold, with the total cavity power losses having to be less than 4 %.

The higher peak power of the pump pulse from the compressor is a major advantage of this LBO OPO compared to other similar LBO OPOs such as the ps, Ti:Sapphire pumped LBO OPO [8, 9] where the maximum pump level was ~ 1.8 times above threshold; an all-solid-state (frequency doubled, diode-pumped Nd:YLF laser) pumped LBO OPO [10-12] where the maximum pump level was ~ 2 times above threshold; and an amplified version of this all-solid-state pumped LBO OPO [13] where the maximum pump level was ~ 4 times above threshold. The LBO OPO used in these experiments can be driven more than 6 times above threshold under similar operating conditions. Higher pump powers also allow the introduction of lossy elements into the cavity, which might be necessary to obtain transform limited pulses, whilst still being able to drive the OPO a few times above threshold to achieve efficient operation.

The analysis of Boyd and Kleinman assumes that the confocal parameters of the pump, signal and idler are equal. The situation when they are not, as in the case for our dual arm OPO, has been discussed by Guha, et. al., [14]. Figure 3-6 shows the variation in the parametric gain with signal focusing parameter ξ_s for a set pump focusing parameter ξ_p. Please note that the factor modifying the parametric gain due to focusing, $h_{sm}(B, \xi)$, is not the same as $h(B, \xi)$ in the analysis of Boyd and Kleinman. The optimum signal focusing parameter is $\xi_s = 2.5$ for ξ_p = 4.3.
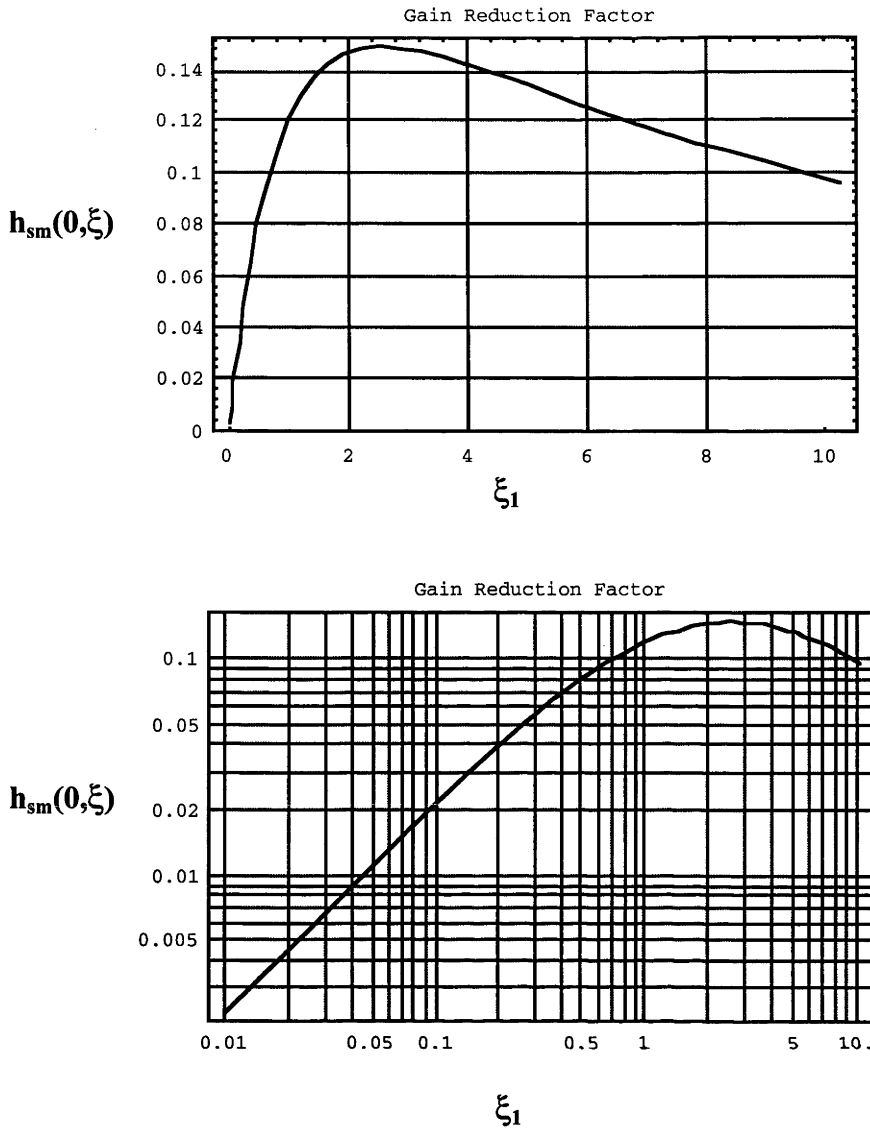
Gain Reduction Factor

$h_{sm}(0,\xi)$

ξ_1

Gain Reduction Factor

$h_{sm}(0,\xi)$

ξ_1

Figure 3-6 : The variation in gain, $h_{sm}(B,\xi)$, versus the signal focusing parameter, ξ_1, where the pump focusing parameter ξ_3 =4.3 and the walk-off B=0. The top figure is a linear plot of $h_{sm}(B,\xi)$ and the bottom plot is a log plot of $h_{sm}(B,\xi)$. As opposed to the case shown in Figure 3-5 there is no restriction on the focusing parameters of all three waves being equal. The optimum for this case is ξ_1 = 2.5. These plots are constructed from the analysis in [14] . Note that the gain reduction factor shown in these figures is not the same as in Figure 3-5. See the text for more details.

In the dual-arm OPO ξ_s = 3.3 and ξ_p = 4.3. From Figure 3-6 it can be seen there is a negligible reduction in gain due to ξ_s =3.3 rather than 2.5. What is important to note is that the parametric gain for either analysis is not very sensitive for ξ_s for a defined ξ_p.

3.4 Factors affecting picosecond OPOs

Group velocity mismatch, group velocity dispersion and self-phase or cross-phase modulation (SPM / XPM) can play important roles in picosecond OPOs. If the group velocity mismatch (GVM) between the pulses is too large it limits the interaction length. If the GVM is comparable with the pulse duration the pulses only overlap over a fraction of the propagation length. This effect can be described analytically by modifying Eqn 3-1 to include GVM where δt_{ij} = ($1/v_{gi}$ - $1/v_{gj}$) is the inverse GVM and τ = t - (z/v_{g3}) is a

coordinate transformation to simplify the equations. τ is the measure of time relative to the pump pulse moving through the crystal.

$$\frac{\partial E_1}{\partial z} = iK_1 E_2^* E_3 \, \exp(i\Delta kz) - \delta t_{13} \frac{\partial E_1}{\partial \tau}$$

$$\frac{\partial E_2}{\partial z} = iK_2 E_1^* E_3 \, \exp(i\Delta kz) - \delta t_{23} \frac{\partial E_2}{\partial \tau}$$

$$\frac{\partial E_3}{\partial z} = iK_3 E_1 E_2 \, \exp(-i\Delta kz)$$

Eqn 3-3

Positive group velocity dispersion (GVD) leads to the development of a linear pulse chirp and temporal broadening in the signal and idler pulses. While the GVD per pass through the LBO crystal is low, the signal pulse (in a singly-resonant oscillator) makes many passes through the crystal since it is trapped within the resonator. So the GVD experienced by the signal pulse is more appreciable than first thought. In a latter section an estimate is made on the level of GVD in the cavity based on measured experimental parameters.

Self-phase modulation (SPM) can also play a role in the dynamics of an OPO when it is driven with sufficient pump power. SPM causes the development of a nonlinear frequency chirp and broadening of the spectra of the signal and idler pulses. The nonlinear refractive index, n_2, for LBO is 3.4 x 10^{-16} cm^2/W [13], close to that of glass. Again the effect of SPM can be low per pass through the LBO crystal but can become significant after many passes through the crystal.

Related to SPM is cross-phase modulation, XPM, and it must be also be taken into account when more than one distinct wave is propagating in the same material. This is because the nonlinear refractive index of a wave, due to the optical Kerr effect, depends not only the intensity of that wave but also the intensity of any other waves propagating in the material as well. For copropagating waves of different frequencies the effect of XPM is 2 times greater than just the effect of SPM. For copropagating waves of the same frequency but orthogonal polarisation, the effect of XPM is 2/3 greater than SPM. XPM is similar to SPM but its effects can be complex [15].

The effects of GVM, GVD, SPM and cavity length detuning on cw, synchronously pumped, ps OPOs has been studied by several authors. One of the first analyses was done by Becker, *et. al.*, [16]. They modelled a degenerate ($\lambda_1 = \lambda_2$), ring OPO that included the effects of pump depletion, GVM and dispersion. The authors were mainly concerned on how these effects influenced the stability and temporal duration of the generated pulses. They concluded that significant pulse shortening (down to 0.1 Δt_3), compared to the duration of the pump pulse, was possible when operating close to threshold but when the OPO is driven well above threshold the pulse duration broadens to become approximately the same duration as the pump pulse. Furthermore, the OPO was only stable when operating well above threshold.

Cheung and Liu [17] improved on the analysis of Becker, *et. al.,* by modelling a cw, synchronously-pumped, picosecond, nondegenerate, SRO OPO and including the effects of GVM, cavity length detuning, pump depletion and phase mismatch between waves ($\Delta k \neq 0$). They found that it is possible to obtain considerable pulse shortening (down to ~ 0.5 Δt_3) when operating close to threshold. The pulse duration of the resonant pulse is shortened close to threshold, where there is negligible pump depletion, because the parametric gain experienced by the generated pulses is proportional to $\exp\left(\sqrt{I_3}\right)$. The peak of the signal pulse is, therefore, amplified more than the wings of the pulse. As the pump level increases the power of the generated waves grows, increasing pump depletion and saturating the gain.

50

The peak of the generated pulse then experiences less gain then the wings of the pulse, leading to pulse broadening. This saturated gain regime also makes the OPO stable to any fluctuations in the gain. The optimum pump level was found to be around four times above threshold and at this level the pulse duration of the resonant wave is roughly equal to pump pulse duration.

However, while operating the OPO well above threshold makes the OPO amplitude stable, cavity fluctuations make the OPO inherently frequency unstable because of a mechanism related to dispersion as was first identified by Edelstein, et. al. [18]. Cavity length fluctuations cause the resonated pulse to arrive early or late with respect to the pump pulse, causing a decrease in gain for the resonated wave. The resonated pulse can, however, experience a higher gain if it shifts frequency to a point where group velocity dispersion is able to compensate for the timing error. The size of the resulting frequency shift is determined by the group velocity mismatch between the pump and resonated pulse. However, it is not generally possible for the resonated wave to shift its frequency to such an extent as to completely compensate for the cavity length detuning because it is constrained by the spectral gain bandwidth of the OPO. The OPO sacrifices frequency stability for amplitude stability. It also follows that inserting frequency stabilising elements, such as an étalon, makes the OPO more susceptible to amplitude instabilities induced by cavity length fluctuations. To obtain low frequency and amplitude noise simultaneously requires the elimination of cavity length fluctuations, or active stabilisation of the cavity length (see [19] for a scheme for active frequency stabilisation of a synchronously pumped, LBO OPO).

Fallnich, et. al., [20] included the effects of GVD and SPM / XPM in numerical simulations and compared the results with an experimental study on the effect of cavity length detuning on a cw, synchronously pumped, ps, KTP OPO. The simulation used the beam propagation method with a split-step Fourier algorithm. Using this method, as opposed to the perturbation method of Cheung and Liu, the phase of the generated waves could also be investigated allowing the inclusion of SPM / XPM and GVD. While being specifically targeted towards describing their KTP OPO, the numerical simulation closely matched most of their experimental measurements and demonstrates the effects of GVD and SPM / XPM on a synchronously pumped, ps OPO. As has been mentioned earlier GVM causes the pulses to walk-away from each while interacting in the crystal. Changing the cavity length causes the resonated pulse to arrive early or late with respect to the pump pulse altering the dynamics of amplification. Depending on the relative group velocities of the three waves, the temporal pulse profiles of the generated waves experience asymmetric gain with cavity length detuning, which can lead to pulse broadening and an asymmetric pulse profile or in some circumstances pulse shortening. It is this effect which causes the synchroresonance curve of an OPO to be asymmetric.

As an example, in the case for the KTP OPO of Fallnich, et. al., where $v_{g1} > v_{g3} > v_{g2}$, as the cavity length was decreased, the resonated signal pulse arrived early and experienced more gain on its trailing edge as it walked away from the slower pump pulse and even slower idler pulse. This led to asymmetry in the signal and idler pulse profiles. When the cavity length was increased the signal pulse arrived later relative to the pump pulse resulting in the generated idler pulse being left behind both the signal and pump pulses significantly reducing the gain by a proportionally greater amount compared to the case when the cavity length was decreased. The OPO can therefore tolerate a larger reduction than an increase in cavity length.

The presence of SPM / XPM in combination with GVD considerably complicates the picture, but in general phase modulation reduces the frequency shifts caused by cavity length detuning by providing a mechanism whereby the phase of the pulses changes so that the parametric gain is optimised. From the analysis of Fallnich, et. al., the individual effects of GVD and SPM / XPM could not be analysed separately. All act together to alter the phase of the waves so that the gain reduction due to cavity length detuning could be compensated.

When both GVD and SPM / XPM were included in their analysis, the predicted behaviour of their KTP OPO was closer to experimental measurements than for the case where only GVM was taken into account. One can conclude that SPM / XPM and GVD play important roles in the dynamics of synchronously pumped, ps, OPOs.

3.3 Free running OPO

In what follows, a "free running" OPO is defined as one which has the OPO crystal as the only intracavity element. Experiments were carried out with the free running LBO OPO in both the one-arm and dual-arm configurations using either the chopped cw pump beam, or for the dual-arm configuration, with the full cw beam. As can be seen in Figure 3-4 the dual-arm configuration allows the use of a dispersion compensating prism pair which cannot be used with the one-arm case. This is because the beam passing through the prism pair becomes spectrally dispersed at one of the end mirrors which is then unsuitable as an output coupler. The dual-arm configuration allows the output coupler to be place at the other end of the resonator. The use of the prism pair will be described in greater detail in Section 3.4.

3.3.1 Alignment

Efficient operation of a synchronously pumped OPO requires not only that the cavity mirrors are aligned properly, but also that the cavity length is correctly adjusted to synchronise the pump and circulating signal pulses.

The alignment procedure differed slightly between the two configurations. To align the one-arm OPO proved to be easier than the dual-arm OPO. The one-arm case will be dealt with first.

Firstly, the mode matching lens and the first focusing mirror of the OPO, which acts as a negative lens, were centred on the pump beam. The location of the focus of the pump beam was then found using the knife-edge technique. The separation between the mode matching lens and the first mirror was adjusted until the separation between the pump focus and the mirror was equal to its radius of curvature, R, (~ 100 mm). The pump focus was then imaged using a lens and a microscope objective (MO) lens (x 40) positioned behind the mirror used to turn the compressed 1054 nm pulse into the SHG crystal (see Figure 2-1). The LBO crystal was placed in the OPO cavity and its position and angle adjusted. The pump focus could be imaged by using the face of the LBO crystal to back reflect a portion of the pump beam. The LBO crystal was translated until a focus appeared at the image plane of the MO lens. The LBO crystal was then translated towards the first focusing mirror by 3.125 mm (which is equal to half the crystal length /refractive index, $(l/2)/n_{LBO}$) to move the focus into the optical centre of the crystal.

The angle and position of the first focusing mirror could be fine tuned using the MO lens imaging system. When the LBO crystal face reflected the pump focus a second focal spot was visible at the output of the imaging system. It was created by a reflection from the curved surface of the first focusing mirror. Since the mirror should be positioned at a distance R away from the pump focus, this reflection is the same size and travels exactly back down the same path as the reflection from the crystal face. The angle of the first mirror was adjusted until the two images overlapped with each other. When this occurs the first mirror will reflect the circulating signal beam exactly back down the beam path.

Once the first mirror and crystal had been aligned, the second focusing mirror was centred on the pump beam transmitted through the LBO crystal at a distance roughly equal to R + f from the first mirror. The mirror was turned slightly (~ 3^0) so that the beam reflected
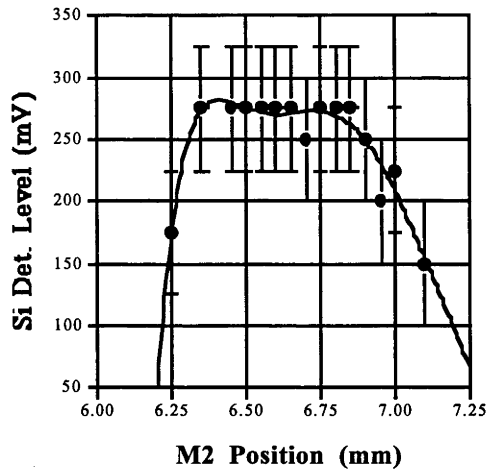
Figure 3-7 : The signal power as detected by a Si:PIN detector versus the change in position in the second focusing mirror of the one-arm LBO OPO pumped by the chopped cw pump beam.

from it passed back through an aperture machined into the crystal oven to one side of the crystal. Using the reflection of the pump beam off the second focusing mirror an alignment aperture was centred on the beam just after it had passed through the oven. The long arm of the OPO was ~ 1830 mm long and had the output coupler (OC) mirror at its end. The OC was aligned so that the reflected pump beam passed back through the centre of the pinhole. The second mirror was translated back and forth, to increase or decrease the separation between the two focusing mirrors, until the pump beam reflection appeared focused on the OC mirror. It was difficult to make the OPO oscillate after only these alignments had been carried out, mainly because it proved difficult to accurately set the position of the second mirror to obtain a beam waist at the output coupler.

To ensure that the basic mirror alignment was correct, a 10 mm long Ti:Sapphire plano-plano rod was inserted into the resonator in place of the LBO crystal to form a cw Ti:Sapphire laser. The rod does not have quite the same path length as the LBO crystal, however, from calculations using the Paraxia program it was found that the second mirror should be only 0.5 mm closer to the rod for optimum stability than for the case using the LBO crystal. Since the stability range for each cavity was ~ 1.5 mm the stability ranges of both cavities overlapped. This allowed the OPO resonator to be aligned using the Ti:Sapphire laser. To align the cavity using the Ti:Sapphire laser the cavity was shortened to ease alignment constraints and after the laser started oscillating the cavity length was increased in steps, while maintaining alignment, until it reached the desired length. At this point the rod was replaced by the LBO crystal after which all that was generally required to get the OPO oscillating was to make a slight adjustment to the cavity length. Once oscillating, the angle of the OC and the separation of the focusing mirrors were fine tuned to optimise the efficiency of the OPO. Oscillation was easy to detect, without the use of CCD cameras or IR beam-finders, by monitoring the pump depletion. When the OPO started oscillating the scattered green SH light intensity dropped dramatically.

Alignment of the dual-arm configuration requires a slightly different procedure. The two focusing mirrors have to be accurately positioned a distance f (~ 50 mm) away from the pump focus. The same knife edge technique was used to set the separation between the first mirror and the pump focus. However, the pump focus imaging system cannot be used. The separation was, therefore, set by measurement. The LBO crystal was inserted into the cavity followed by the second focusing mirror positioned 50 mm after the pump focus. Both focusing mirrors were then angled slightly (~ 3^0) so that the reflections of the pump
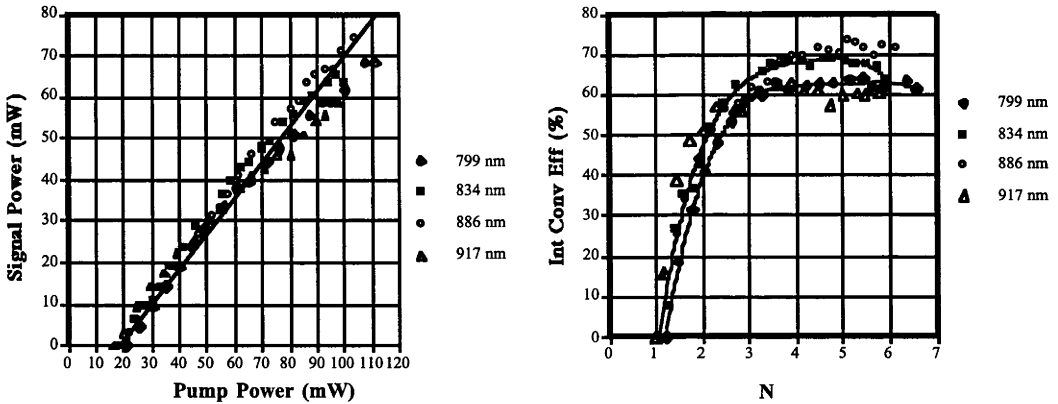
53

Figure 3-8 : The variation (left) of the converted power with the pump power at the focus in the LBO crystal and the internal conversion efficiency versus the number of times above threshold, N, for the LBO OPO in the one-arm configuration with 100 % R output coupler at various wavelengths. The signal wavelengths of 799 nm (1550 nm idler) and 917 nm (1240 nm idler) are at the edge of the mirror reflectivity range where the cavity losses are slightly larger. The slope efficiency for the variation in converted power is ≈ 85 % and the threshold is ≈ 17 mW (900 W peak power for a pump pulse of 2.2 ps).

beam passed through the aperture in the crystal oven. The arm from the first mirror was ~ 500 mm long and contained the output coupler, whilst the second arm was ~ 1300 mm long and could contain the prism pair. The end mirrors of both arms were then adjusted to return the beams back down the axis using two pinholes as alignment aids. As with the one arm OPO, a cw Ti:Sapphire laser was used to ensure the cavity was aligned properly. Once the cavity had been aligned the LBO crystal was reinserted into the cavity. Typically, the OPO started oscillating after only minor adjustments to the cavity length and the angle of the end mirror of the long arm. The internal conversion efficiency was optimised through adjusting the angle of the output coupler.

It is desirable for the OPO to operate in the middle of its stability range. To check this the mirror spacing was gradually first increased and then decreased, optimising the cavity alignment in each case until oscillation could no longer be obtained. Figure 3-7 shows the stability range of the one-arm OPO pumped by the chopped cw pump beam. As can be seen from in the figure the stability range is flat and is roughly 1.5 mm (double the M2 position because it is a standing wave cavity) as was expected from ABCD calculations.

For both configurations the critical length of the resonator was set with the aid of the unconverted IR beam from the SHG (see Figure 2-1). The basic principle was to couple some of this IR light into the OPO resonator and search for interference fringes between pulses transmitted straight though the resonator and those that have travelled one additional round trip of the resonator. The resonator length was adjusted to maximise the fringe contrast, indicating temporal overlap of the pulses had been obtained.

In the LBO OPO synchronisation was typically maintained between the signal and pump pulses for a length variation of 30 µm to 50 µm over the 1985 mm standing wave cavity length. Experimentally, the alignment method was very good at setting the correct cavity length with only minor adjustments being subsequently necessary to make the OPO start oscillating.

3.3.2 Characteristics and performance

Originally it was planned to use the idler pulses from the OPO as the seed pulses for the OPA. Since the idler pulses pass straight out of the OPO cavity through the second focusing mirror (M2) the OPO can be operated without the need for an output coupler. This allows the OPO to be driven many times above threshold giving stable and efficient operation. As a result, when the LBO OPO in the one-arm configuration first started operating, effort was put into experimentally investigating the properties of the OPO and the idler pulses.

Figure 3-8 shows the variation in power converted into signal and idler (converted power) with the pump power at the focus in the LBO crystal and internal conversion efficiency of the LBO OPO with a 100 % reflecting output coupler at signal wavelengths across its range of operation. By measuring the pump depletion at various pump powers the converted power and the threshold can be determined. The threshold lay near 17 mW (using the chopped cw beam) which is equivalent to 900 W peak power for a pump pulse of 2.2 ps in duration. The slope efficiency of the variation in the converted power is $\sim$ 85 %. The OPO can be driven up to six times above threshold (N) where the internal conversion efficiency is well saturated at 60 % (at wavelengths near the edge of the cavity reflectivity range) to 70 %.

The power of the idler beam was measured after M2. The results are shown in Figure 3-9. Typically the idler extraction efficiency was greater than 20 % when the OPO was driven above 3 times above threshold corresponding to a maximum average idler power of 15 to 20 mW (chopped cw power) or 875 W to 1170 W peak power (for a 2 ps pulse).

The pulse durations and spectra of the idler pulses were also measured at various wavelengths; with the OPO driven approximately two times or approximately four times above threshold. Figure 3-10 summarises these results. As is expected from theory the pulse durations became shorter when the OPO was operating closer to threshold. Apart from one point at 1270 nm there was no discernible change of the spectral bandwidth with pumping level. Figure 3-11 shows the temporal pulse profile and spectra of the idler pulse at 1270 nm and Figure 3-12 shows the temporal pulse profile and spectra of the idler pulse at 1435 nm. The spectra and temporal profiles were generally Gaussian-like with no evidence of sidelobes. The closer to threshold the closer the idler pulses were to being transform limited. The spectrum of the 1270 nm pulse displayed a double-peak spectrum and was very broad compared to the other measured spectra. It was not uncommon for the signal or idler spectra to have multiple peaks or even to be oscillating on two or more separate frequencies, especially when the cavity length was detuned from optimum. An explanation of this behaviour is left for later (see Chapter 4 more details).

After measuring the conversion efficiency, power and the pulse characteristics of the idler, the spatial beam profiles of both the signal and the idler beams were measured. Figure 3-13 shows images of the signal beam, in the near and far field, and the beam profile fitted to a Gaussian. To measure the spatial beam profiles it was necessary to replace the 100 % R OC mirror with one that had a transmission of 5 % to 10 % between 920 nm to 780 nm (Coherent 163-654 mirror). A CCD camera was used to capture images of the beam. At all signal wavelengths and all pumping levels with or without cavity length detuning, the spatial profile of the signal beam remained a close approximation to a TEM_{00} Gaussian beam. This was to be expected because the signal beam was constrained by the cavity where the TEM_{00} mode had the lowest losses.

Examples of the idler far-field beam images and profiles are shown in Figure 3-15. The measurements were taken using an IR camera sensitive between 1300 nm to 2100 nm. It was found that a small detuning of the cavity length had a drastic effect on the idler beam profile. From an almost Gaussian shape the beam can diffract into an annular shaped beam.
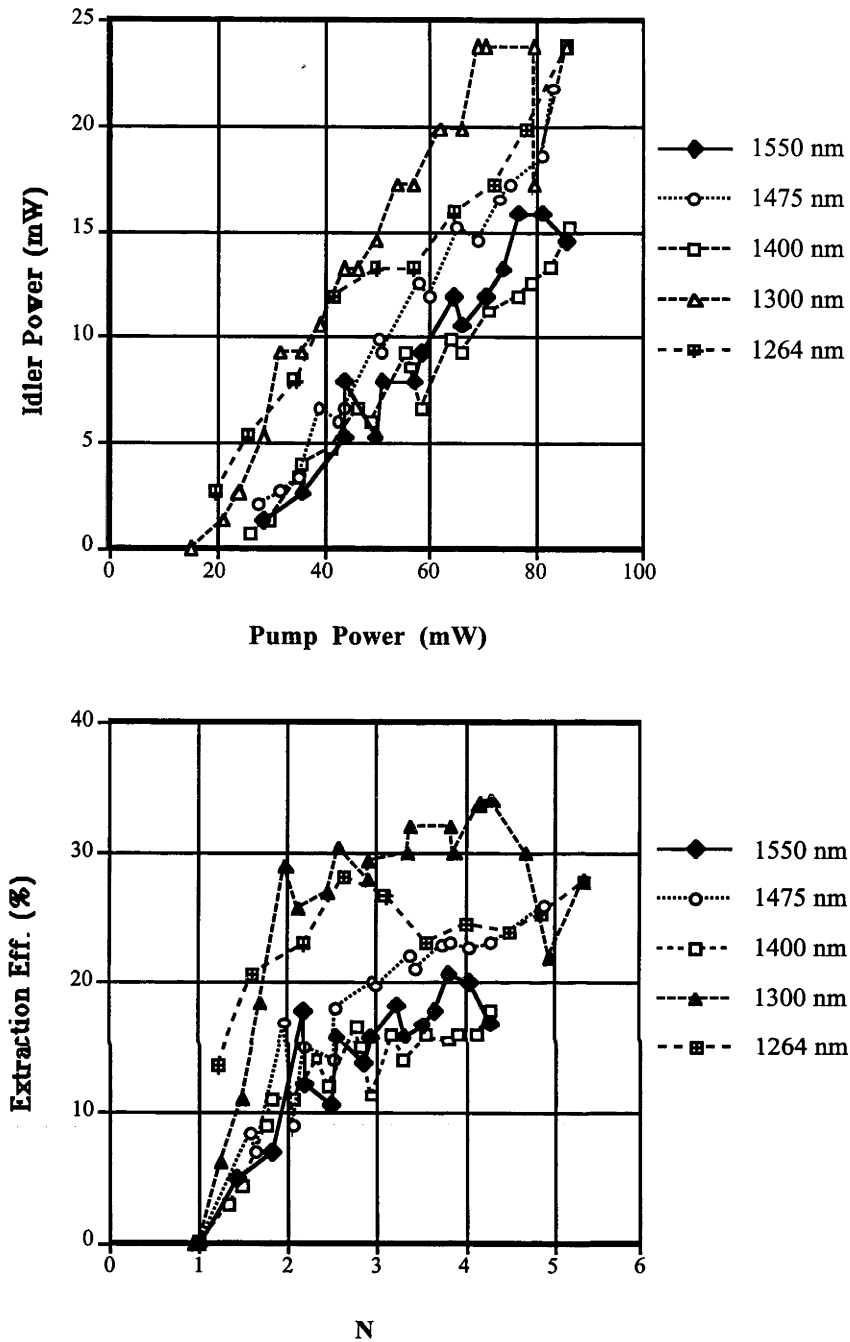
Figure 3-9 : The idler power (top) at various wavelengths extracted through the second focusing mirror of the LBO as a function of the power at the pump focus in the LBO crystal and the idler extraction efficiency (bottom) as a function of the number of times the OPO is driven above threshold (N).

In Figure 3-15 the first beam image (top image) was taken at the optimum cavity length, where the converted power was maximised, whilst the second beam image (bottom) was obtained when the cavity length was detuned -42 μm. The LBO OPO oscillated over a ~ 70 μm range of cavity length for these particular conditions. The main point that was drawn from these measurements was that the idler beam was rather nonuniform and was not well suited for use as a seed pulse for an OPA. Any changes to an OPA seed pulse's beam profile will drastically affect the level of amplification experienced in the OPA since the focal region or area of the seed beam will shift and change inside the OPA crystal. For this reason it was decided to use the signal as the seed pulse for the OPA rather than the idler pulse.
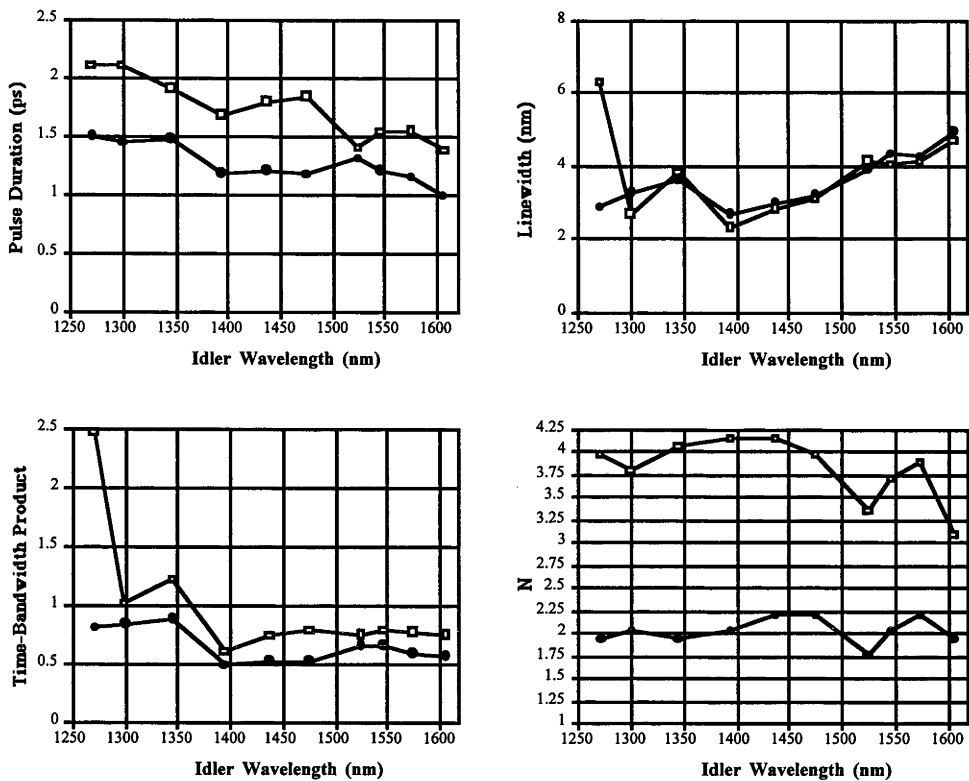
Figure 3-10 : The pulse durations, assuming a Gaussian pulse, (top left); spectral bandwidths (top right) and the time-bandwidth products (bottom left) of the idler pulses at various wavelengths from the one-arm LBO OPO with the 100 % R output coupler. The empty squares correspond to measurements taken at roughly 4 times above threshold and the filled circles correspond to measurements taken at roughly 2 times above threshold (N). The actual pump level for each measurement is shown in the last figure (bottom right).

Measurements were taken of the signal pulses from the one-arm LBO OPO using an output coupler (OC) with a transmission ranging from 4 % to 10 % (see Figure 3-14, Coherent 163-654 mirror) over the operating range of the OPO. The results are summarised in Figure 3-16. Since the transmission of the OC dropped from 10 % at 790 nm to around 4 % at 910 nm, the OPO threshold is lowest at the longer signal wavelengths and hence the OPO could be driven higher above threshold at that end of the tuning range. Some points to be noted from the results are that the maximum extracted power, of 15 mW chopped cw or 875 W peak in 2 ps, is roughly the same for all wavelengths despite the variation in the maximum pump level. This meant the signal power was extracted more efficiently when the cavity losses were lower. The internal conversion efficiency reached ~ 70 % at 3 times above threshold. As is expected from theory the signal pulse duration is much shorter than the pump pulse duration at pump levels close to threshold (near 0.5 Δt_3), rising to become the same as the pump pulse duration when the gain becomes saturated through pump depletion. The temporal and spectral pulse profiles of the signal beam are generally Gaussian like, similar to the idler pulses shown Figure 3-11, when it is oscillating on one frequency rather than one multiple frequencies. The final figure in Figure 3-16 shows that the signal pulses are not transform-limited, with the transform bandwidth product generally being 1.5 to 2 times the transform-limit of a Gaussian pulse or even higher for a $Sech^2$ pulse.

3.3.2.1 Dual-arm OPO

3.3.2.1.1 Chopped cw pump beam

The OPO only produced signal or idler pulses that were close to transform-limited when it was operating close to threshold. However, as has been mentioned before, operating close to threshold is undesirable because the OPO has a large amplitude instability. To make the pulses transform-limited and force operation on a single wavelength, it was decided to change the OPO into the dual-arm configuration and to insert a prism pair in one of the arms to compensate for any frequency chirp in the signal pulse and to provide frequency control of the oscillating signal pulse. The theory and results from this experiment are provided in the next section. Before the experiments with the prism pair, the characteristics and the performance of the free running dual arm OPO were measured so a comparison between the OPO operating with and without the prism pair could be made.

To conclusively determine if a pulse is transform-limited or, in other words, has no phase modulation is difficult using measurements based on measurement of the SHG intensity autocorrelation (IntAC) because this only responds to the amplitude of the electric field and not the phase of the pulse. A number of measurement methods were available that can provide information about both the amplitude and the phase of a pulse, including the SHG interferometric autocorrelation (InfAC) method (see Chapter 7). This method was chosen because it is easy to implement; works well for the available peak powers of the signal pulses; and is very sensitive to phase structure within the pulse. However, the interferometric autocorrelations could only be carried out with the OPO running in a pure cw mode. Using the chopped cw beam the scanning rate of the InfAC is much slower (~ 20 Hz) than the chopper speed (160 Hz) making it impossible to scan through the pulse
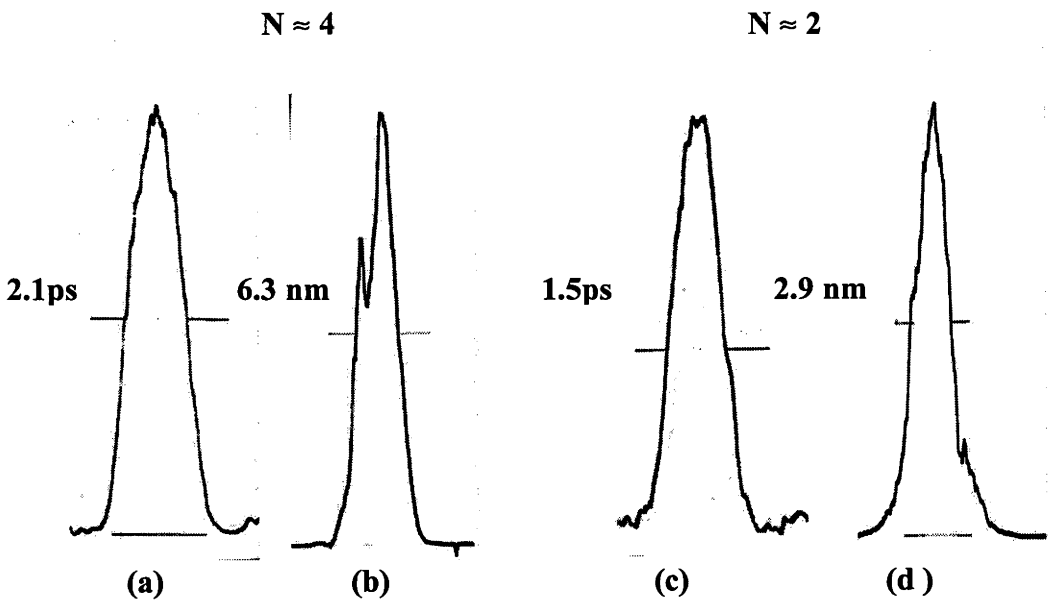
Figure 3-11 : The idler SHG intensity autocorrelation traces and spectra taken from the one-arm LBO OPO with the 100 % R output coupler. These measurements were taken at 1269.2 nm. Assuming a Gaussian pulse shape, (a) is the temporal pulse profile at N = 4 with the FWHM pulse duration = 2.1±0.1 ps; (b) is the corresponding spectrum at N = 4 with the FWHM bandwidth = 6.3±0.3 nm; (c) is the temporal pulse profile at N = 2 with the pulse duration = 1.5±0.1 ps; and (d) is the corresponding spectrum at N = 2 with the bandwidth = 2.9±0.2 nm. The double peak feature in the spectrum in (b) is not due to noise in the measurements but really exists.

N ≈ 4   N ≈ 2

1.8ps   2.8 nm   1.2ps   3.0nm

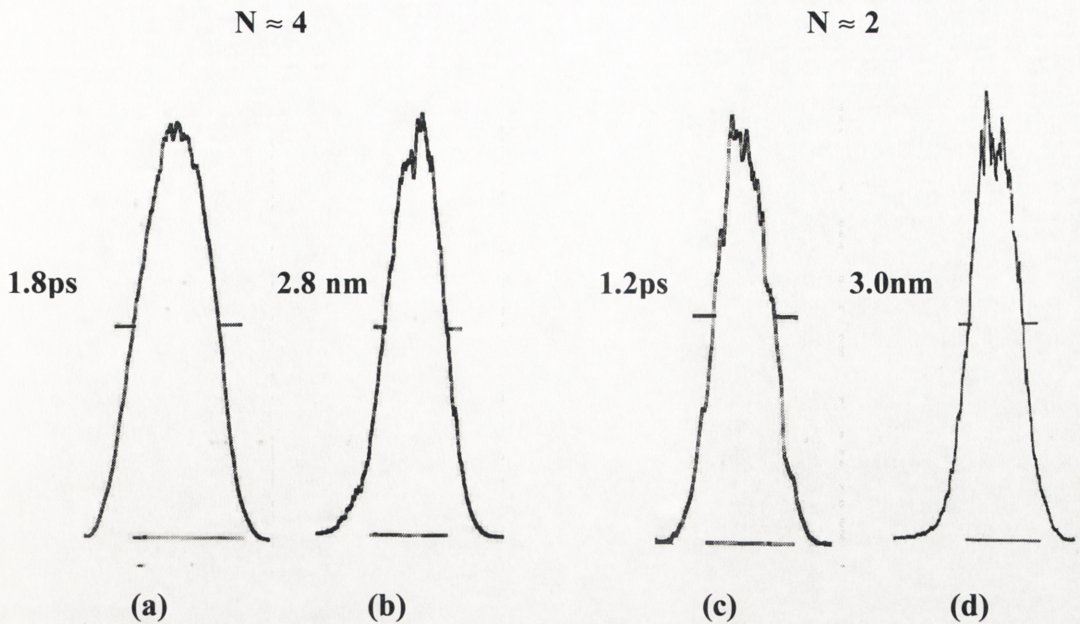(a)   (b)   (c)   (d)

Figure 3-12 : The idler SHG intensity autocorrelations and spectra taken from the one-arm LBO OPO with the 100 % R output coupler. These measurements were taken at 1435.5 nm. Assuming a Gaussian pulse shape, (a) is the temporal pulse profile at N = 4 with the FWHM pulse duration = 1.8±0.05 ps; (b) is the corresponding spectrum at N = 4 with the FWHM bandwidth = 2.8±0.05 nm; (c) is the temporal pulse profile at N = 2 with the pulse duration = 1.2±0.15 ps; and (d) is the corresponding spectrum at N = 2 with the bandwidth = 3.0±0.15 nm.
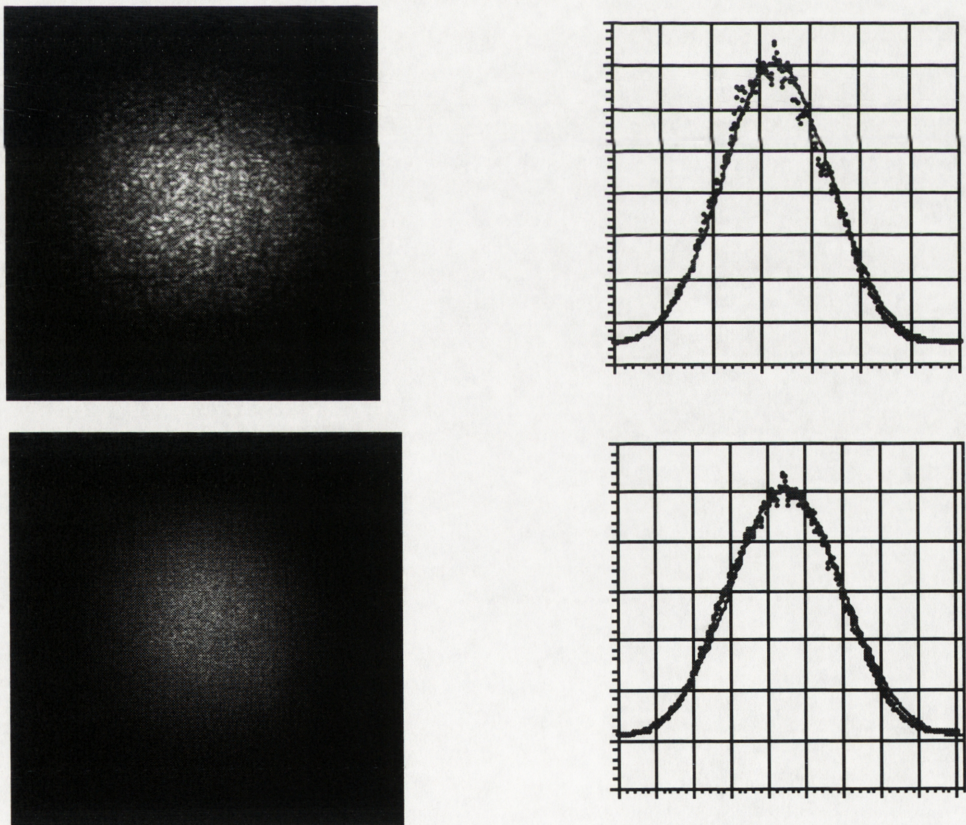
Figure 3-13 : The signal spatial beam images taken from the LBO OPO operating with a ~ 10 % T output coupler (Coherent 163-654 mirror) at a wavelength of 845 nm. The top picture and plot show the far-field beam image and the beam profile fitted to a Gaussian beam profile. The bottom picture and plot show the near-field beam image and the beam profile fitted to a Gaussian beam profile.
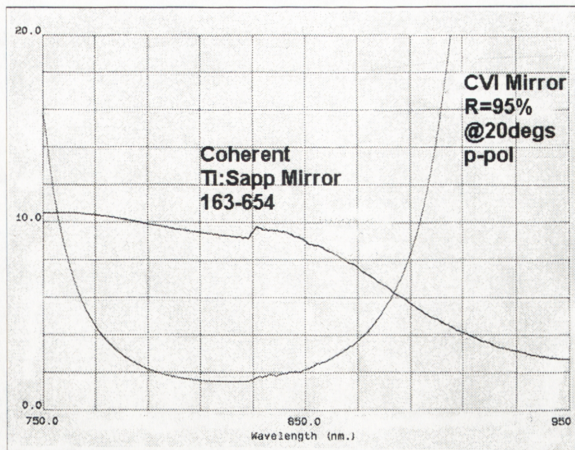
Figure 3-14 : The transmission profiles of two mirrors used as output couplers for the LBO OPO. The measurements were taken using a scanning spectrophotometer with unpolarised light.
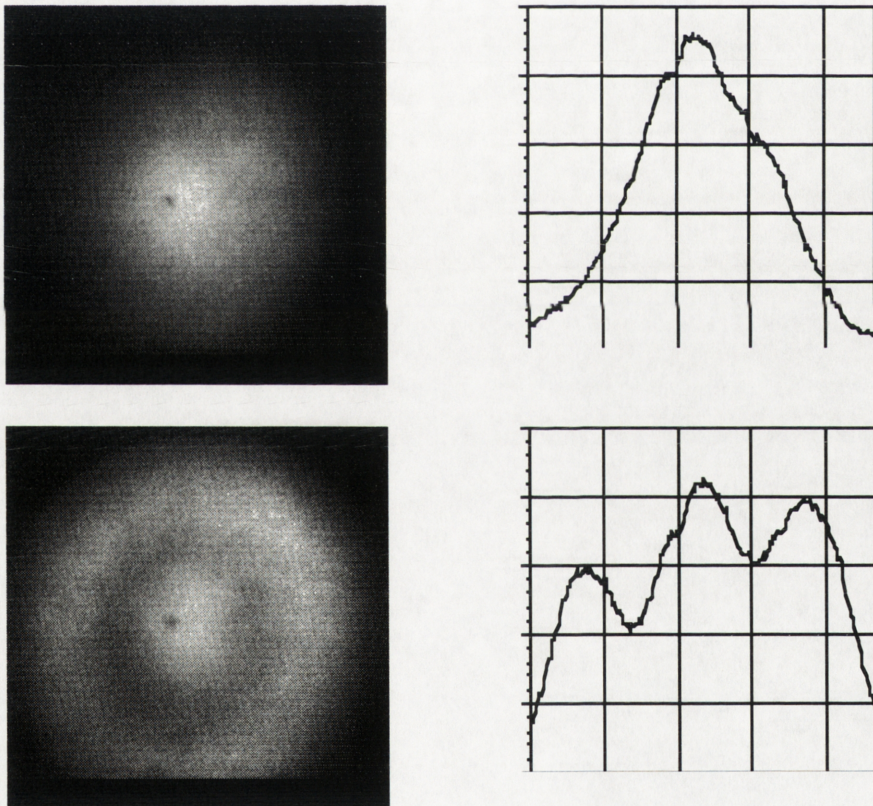
Figure 3-15 : The idler spatial beam images and the beam profiles taken from the one-arm LBO OPO operating with the 100 % R output coupler. The difference between the top plots and the bottom plots is a change of -42 μm in the cavity length.
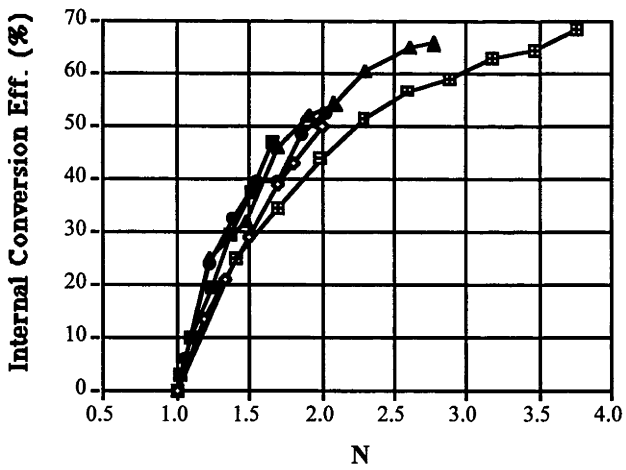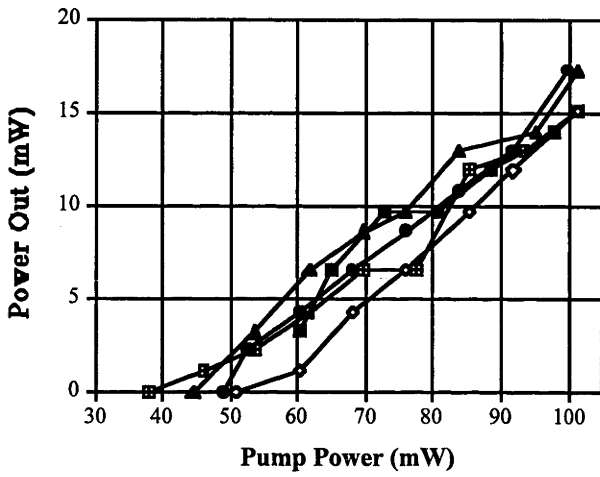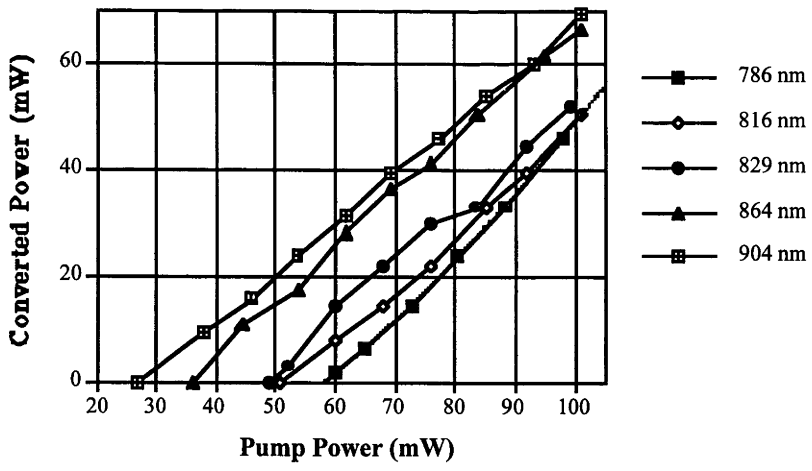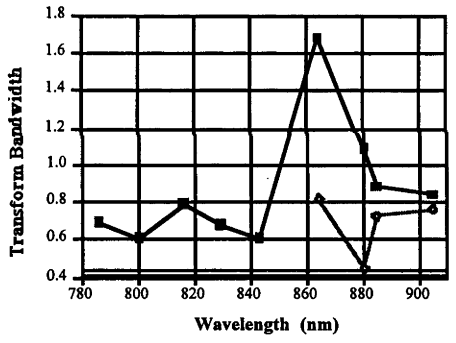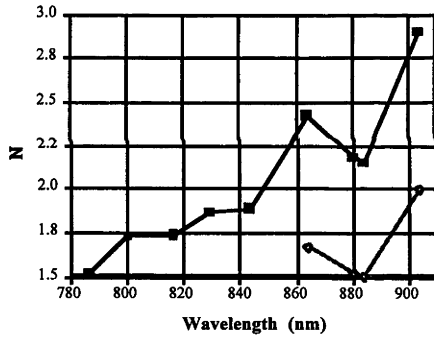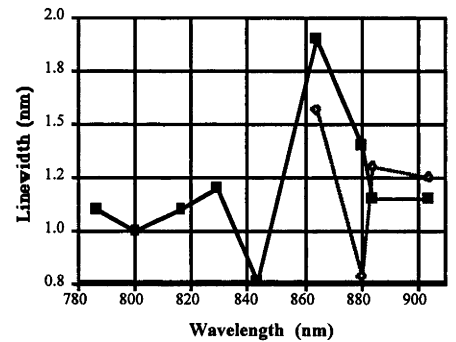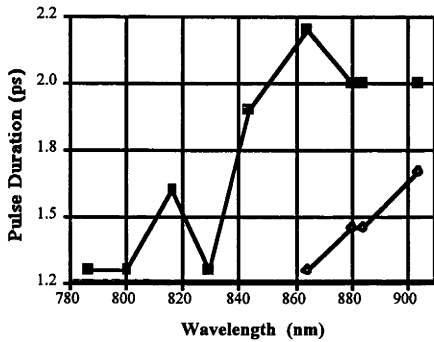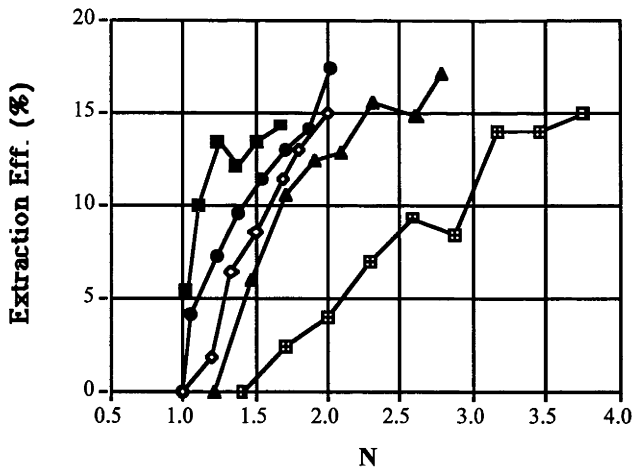
Figure 3-16 : Results from the one-arm LBO OPO with the Coherent 163-654 output coupler mirror. The top pair of figures shows the variation in the converted power and the power of the extracted signal with the pump power at the focus in the LBO crystal for various wavelengths. The next two figures show the internal conversion efficiency and the extraction efficiency at various wavelengths. The bottom four figures show the pulse durations, spectral bandwidths, the number of times above threshold (N) the measurements were taken at and the time-bandwidth products of the signal pulses from the LBO OPO at various wavelengths.
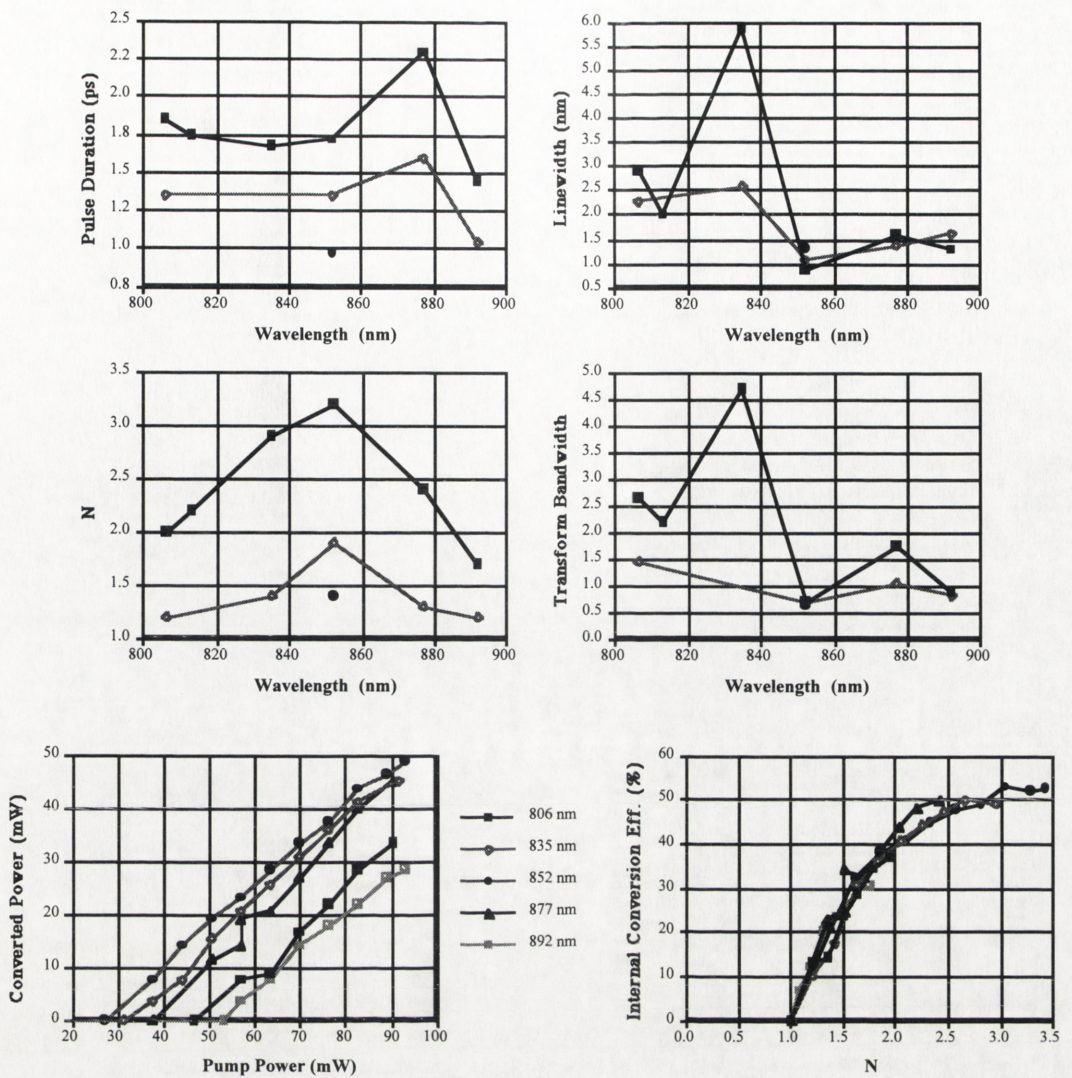
Figure 3-17 : The pulse durations, spectral bandwidths, the number of times above threshold (N) the measurements were taken and the time-bandwidth products of the signal pulses at various wavelengths from the dual-arm LBO OPO using the CVI mirror (see Figure 3-14) as an output coupler. The bottom figures show the variation in the converted power with the pump power at the focus in the LBO crystal and the internal conversion efficiency.
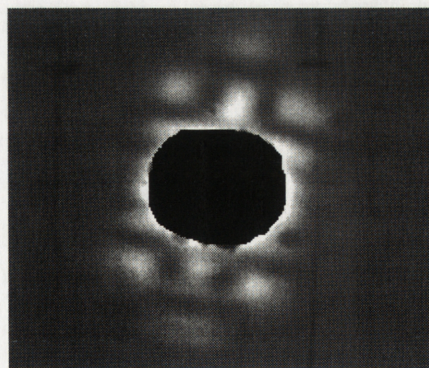

Figure 3-18 : An example of the high order multimode oscillation in the signal beam from the dual-arm LBO OPO. The centre of the image was obscured in order to view the higher modes.

without the InfAC signal periodically disappearing. The scanning rate of the InfAC could not be increased because the response time of the detector has to be faster than the variation in the InfAC signal, which is very fast at $\sim$ 5 μs. InfAC measurements of the signal pulses from the OPO running fully cw are presented later.

Data on the performance of the dual-arm OPO running with the chopped cw beam and using the CVI R=95% at 800 nm, 20^0 p-pol as the output coupler are shown in Figure 3-17. The Coherent mirror was no longer available for these measurements and was substituted by one from CVI which had a more restricted reflectivity range and lower transmission compared to the Coherent mirror. As a result the OPO operated over a narrower wavelength range and there was less output compared to the previous case with the one-arm OPO. The signal output power was near 5 mW or 300 W peak in 2 ps across the entire wavelength range of the OPO and the idler output power was between 15 mW to 20 mW or 900 W to 1.2 kW peak in 2 ps. As in the previous cases the pulse duration deceased substantially as the pump level dropped towards threshold and there was no real correlation between the pump level and the spectral bandwidth. The maximum pump level that could be achieved was 3.3 times above threshold at $\sim$ 850 nm. The internal conversion efficiency was around 30 % to 40 % at the edges of the wavelength range of the OPO and rose to above 50 % at $\sim$ 850 nm. One of the more important things to note is that, as in the previous cases, the signal pulses were generally not transform-limited and in some cases displayed very broad spectral bandwidths.

The IntAC and spectra of the signal pulses at 852 nm are shown in Figure 3-19. Typically the signal pulses had Gaussian like temporal profiles while the spectra were generally Gaussian-like, especially close to threshold. Although the spectra also displayed multiple peaks and sometimes oscillated on separate wavelengths, especially when the cavity length was detuned from the optimum.

It was noticed at this time that the signal beam could also oscillate on higher order spatial modes (see Figure 3-18). Care was taken when performing further measurements that the signal was oscillating only in the TEM_{00} mode. This was done by closing one of the pinholes in the OPO to increase the diffraction losses for the higher order modes. This could be achieved without decreasing the internal conversion efficiency of the OPO. It was found, however, that the higher order modes did not affect the properties of the spectrum or temporal profile of the signal pulse noticeably.

3.3.2.1.2 Full cw pump beam

When operating in the pure CW mode, it was found that the OPO threshold was about 25 % higher than in the chopped CW case. This was possibly due to mild thermal lensing, due the high average power, in the LBO SHG crystal, which would change the position and size of the pump focus in the OPO crystal. Figure 3-20 shows the variation in signal power with the pump power at the focus in the LBO OPO crystal and the internal conversion efficiency of the OPO for three separate wavelengths. Again the CVI mirror was used as the output coupler. The internal conversion efficiency exceeded 50 % around 3 times above threshold. The signal power coupled out of the OPO was typically 45 mW or 300 W peak in 2 ps: the same peak power as in the case of the chopped cw dual-arm OPO.

Figure 3-21, Figure 3-22 and Figure 3-23 show spectra, the temporal pulse profiles (as determined from the IntACs) and the InfACs of the signal pulses at 791 nm, 822 nm and at 851 nm at various pump levels. These data illustrate that the pulse characteristics can vary quite strongly for different tuning conditions.

Figure 3-21 shows the characteristics of the signal pulse oscillating at 791 nm at both 2 times and 1.4 times above threshold. The spectra are Gaussian, with the plots comparing the data with a Gaussian fit. The IntAC data was fitted to a Gaussian and the transform-limited temporal pulse shape is given for comparison. This was determined from a linear

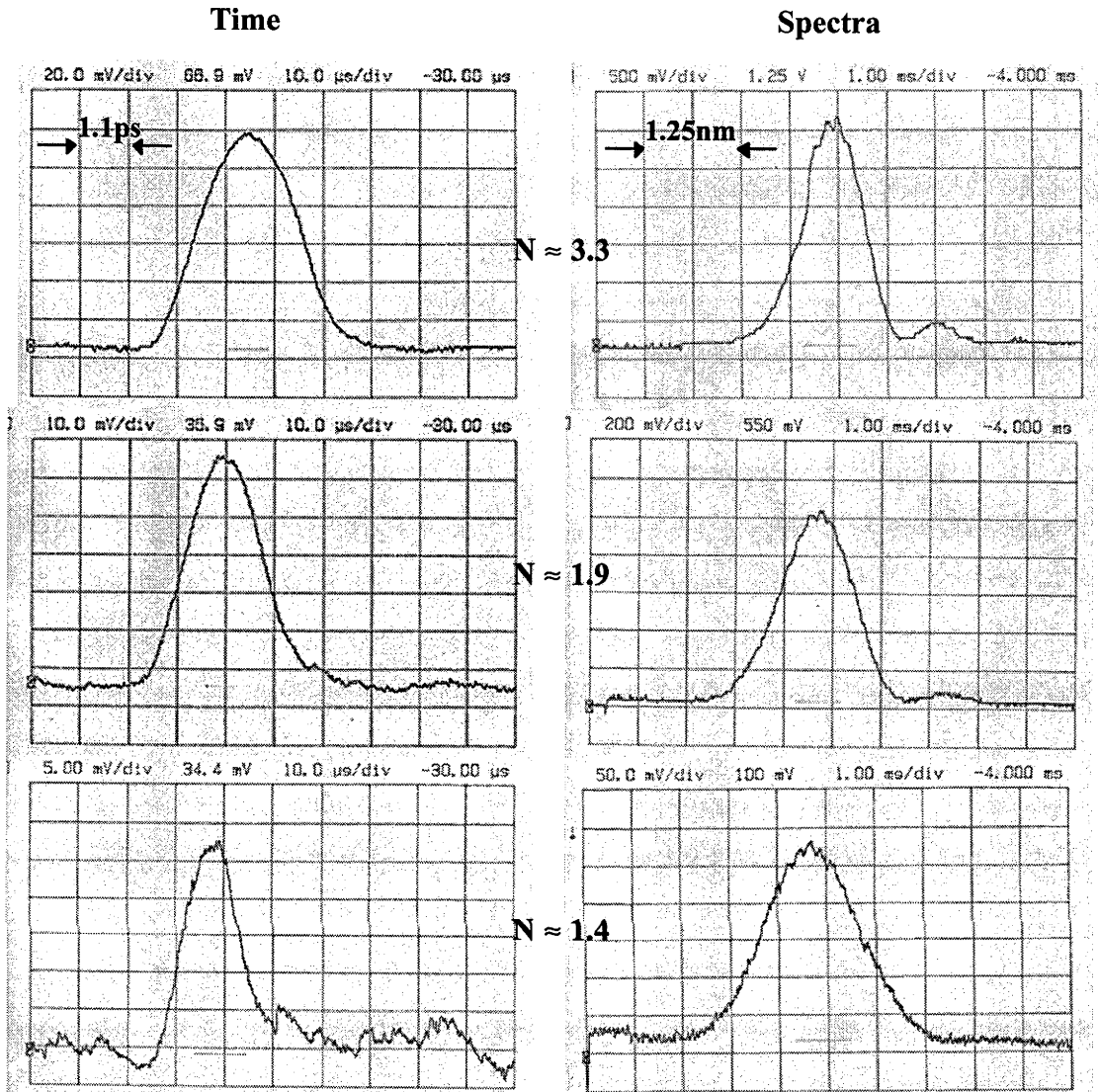**Time**   **Spectra**

Figure 3-19 : The intensity autocorrelations (left column) and the corresponding spectra (right column) of the signal pulse at 852 nm from the dual-arm LBO OPO with the CVI, R=95% output coupler mirror. The top row is at 3.3 times above threshold and the pulse duration is 1.8 ps±10% (Gaussian pulse shape) and the spectral bandwidth is 0.85±0.1nm. The middle row is at 1.9 times above threshold and the pulse duration is 1.4 ps±10% and the spectral bandwidth is 1.07±0.1nm. The bottom row is at 1.4 times above threshold and the pulse duration is 1.0 ps±10% and the spectral bandwidth is 1.3±0.1nm. Note that the spectrum at 3.3 times above threshold has a low side-peak that disappears as the pump level decreases. The structure in the intensity autocorrelation at 1.4 times above threshold is due to lack of signal to the detector and is not due to the signal pulse. The scale for the intensity autocorrelations is 1.1±0.1ps / 10μs and the scale for the spectra is 1.25nm / 2ms.
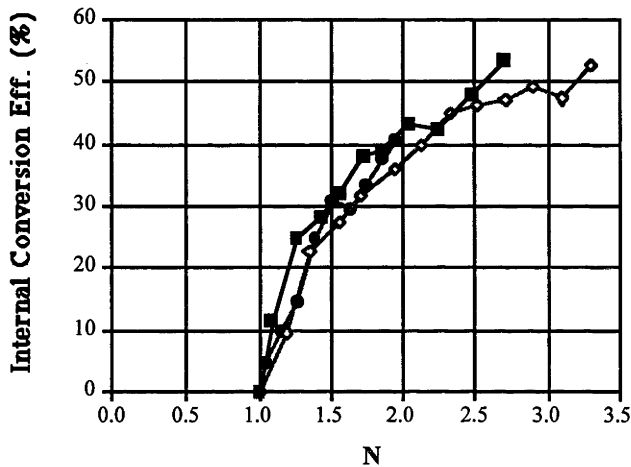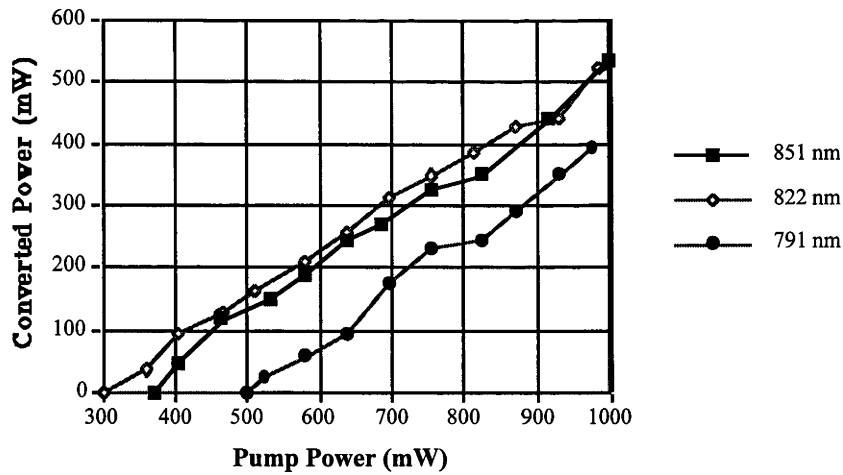
Figure 3-20 : The variation in the converted power with the pump power at the focus in the LBO crystal and the internal conversion efficiency at various wavelengths using the fully cw pump beam and the CVI output coupler mirror in the dual-arm LBO OPO.

interpolation of the Fourier transform of the spectral data (see Chapter 7 for more details). The time scale for the temporal pulse profile plots was determined by dividing the IntAC time scale by $\sqrt{2}$, which is the reduction factor between the autocorrelation width and the pulse width for a Gaussian pulse. This is a good assumption since the IntAC data fits a Gaussian profile very well. The InfAC plots show the interferometric data and the expected InfAC envelope of a Gaussian pulse with a pulse duration equal to that measured from the IntAC. The time scale is the time scale of the InfAC. As can be seen in the temporal pulse profile plots the IntAC is broader than the expected transform-limited pulse, ie. the signal pulse is not transform limited. Why the pulse is not transform-limited can be determined by close examination of the InfAC plots which reveals the presence of both linear and nonlinear chirp caused by dispersion and phase-modulation [21]. The presence of a frequency chirp, linear and nonlinear, will narrow the central portion of the InfAC because the change in frequency is greatest there. The leading and trailing edges of the pulse are not phase modulated and interference still occurs to delays as large as those for an unchirped pulse. An InfAC is sensitive to phase modulation, a frequency chirp that only broadens the spectrum of the pulse by 10 % will narrow the InfAC to 2/3 the width of an unchirped pulse. As the pump level decreased from 2 to 1.4 times above threshold the signal pulse became closer to being transform-limited.
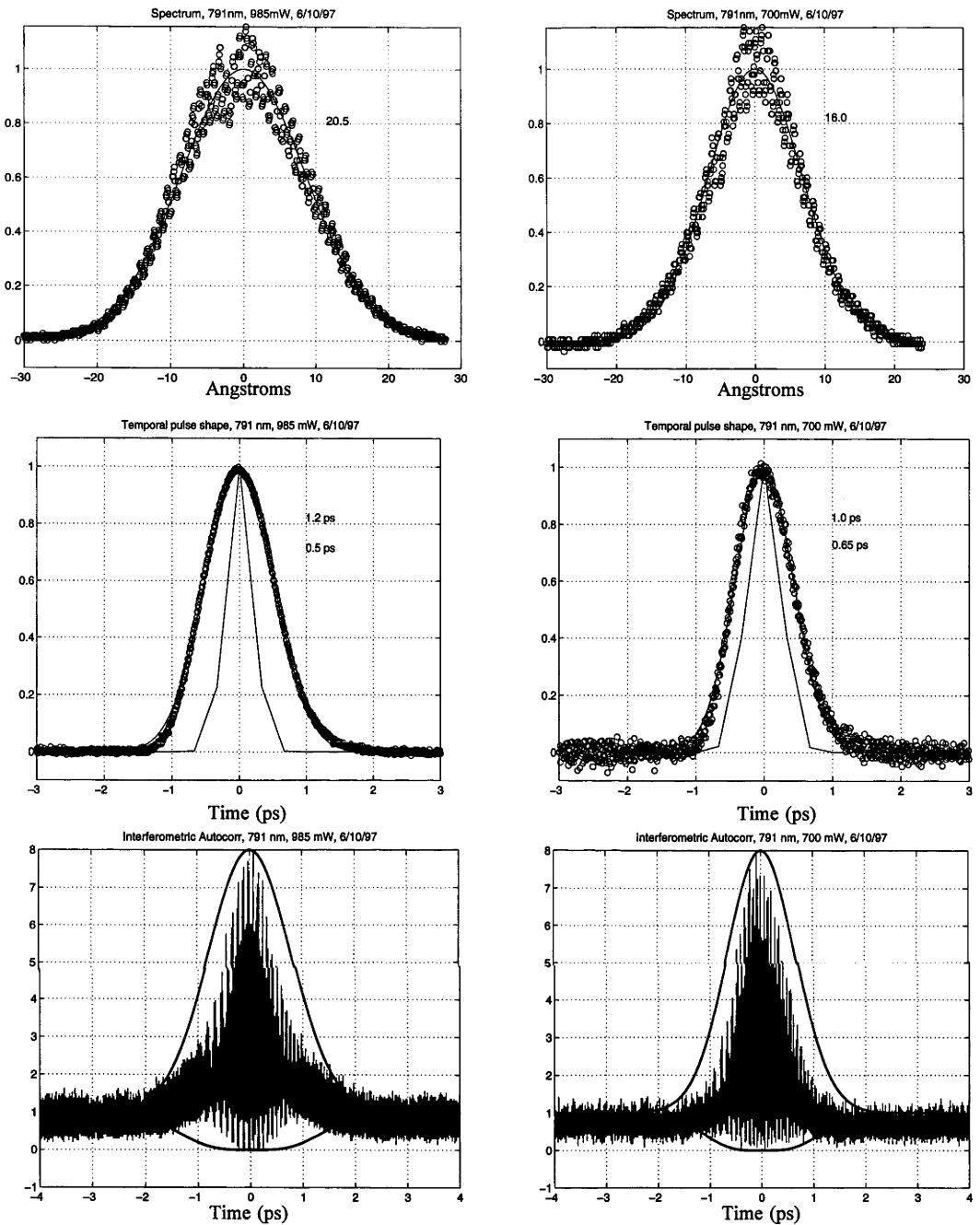
Figure 3-21 : The spectra, temporal pulse profiles determined from the intensity autocorrelations and the interferometric autocorrelations of the signal pulse at 791 nm from the dual-arm LBO OPO pumped by the fully cw pump beam and using the CVI mirror as the output coupler. The left column is for the maximum pump level of ~ 2 times above threshold and the right column is at ~ 1.4 times above threshold. The spectra data (circles) are fitted to a Gaussian profile (line) and the FWHM spectral bandwidth in Angstroms is shown in each figure. The intensity autocorrelation data (circles) is fitted to a Gaussian (line with circles) and the FWHM pulse duration is shown as the top number in each figure. The transform-limited pulse (line) as determined from the spectra and its corresponding pulse duration (lower number) is also shown in each figure. The interferometric plots show the data and the expected interferometric autocorrelation envelope for a Gaussian pulse with a pulse duration equal to that measured from the intensity autocorrelation.
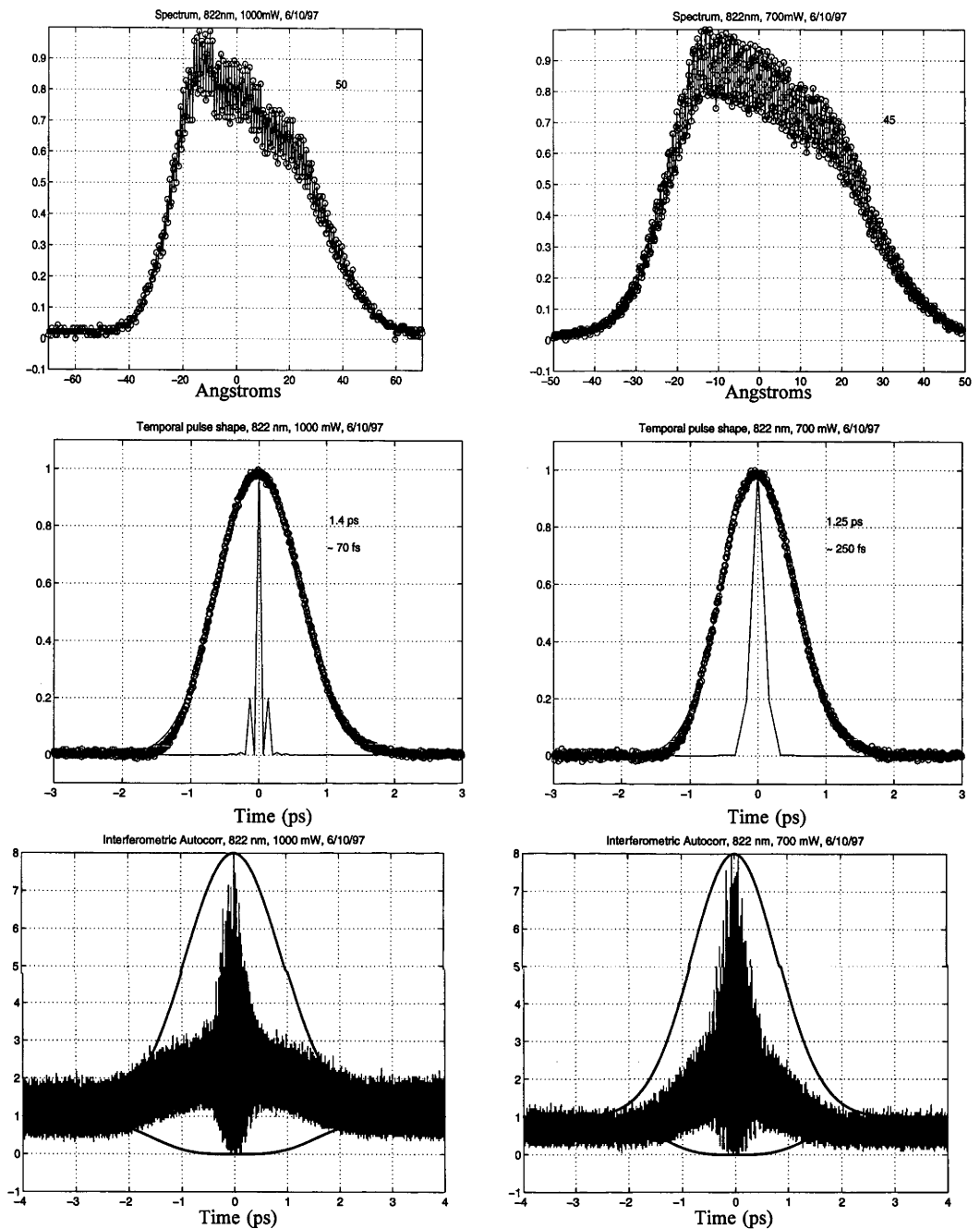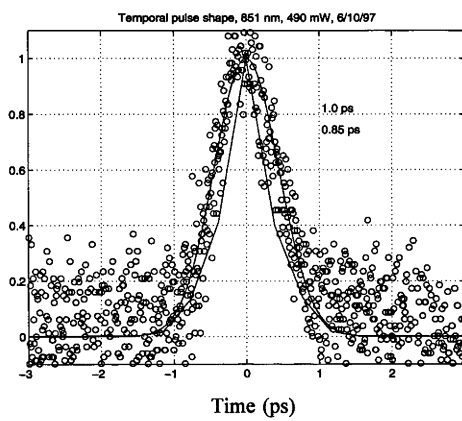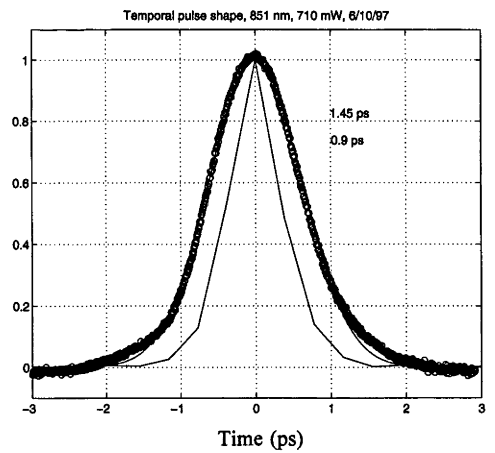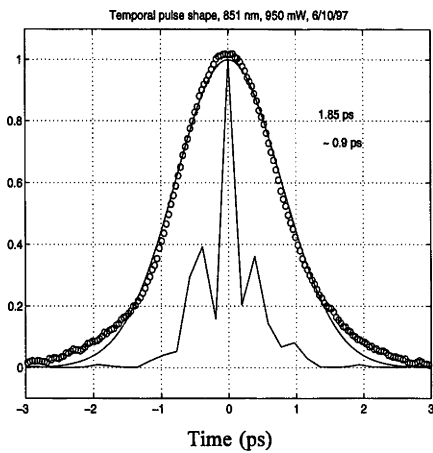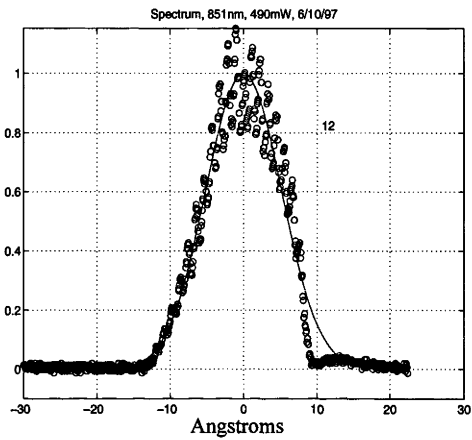
Figure 3-22 : The spectra, temporal pulse profiles determined from the intensity autocorrelations and the interferometric autocorrelations of the signal pulse at 822 nm from the dual-arm LBO OPO pumped by the fully cw pump beam and using the CVI mirror as the output coupler. The left column is for the maximum pump level of ~ 3.3 times above threshold and the right column is at ~ 2.3 times above threshold. The approximate FWHM spectral bandwidth in Angstroms is shown in each figure of the spectra. The intensity autocorrelation data (circles) is fitted to a Gaussian (line with circles) and the FWHM pulse duration is shown as the top number in each figure. The transform-limited pulse (line) as determined from the spectra and its corresponding pulse duration (lower number) is also shown in each figure. The interferometric plots show the data and the expected interferometric autocorrelation envelope for a Gaussian pulse with a pulse duration equal to that measured from the intensity autocorrelation.

68

Spectrum, 851nm, 950mW, 6/10/97

Spectrum, 851nm, 710mW, 6/10/97

Spectrum, 851nm, 490mW, 6/10/97

Temporal pulse shape, 851 nm, 950 mW, 6/10/97

Temporal pulse shape, 851 nm, 710 mW, 6/10/97

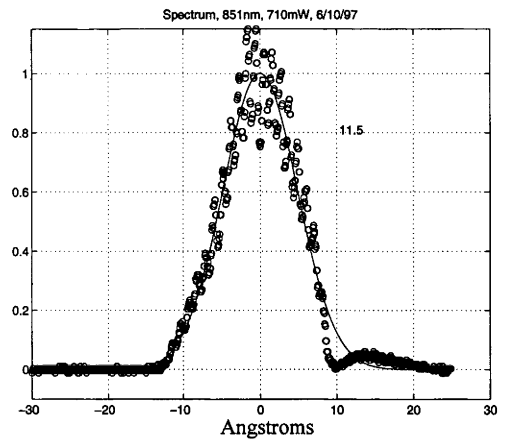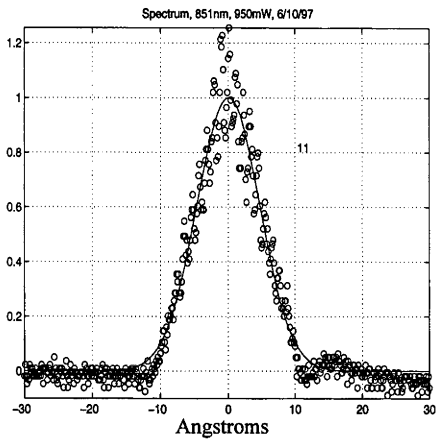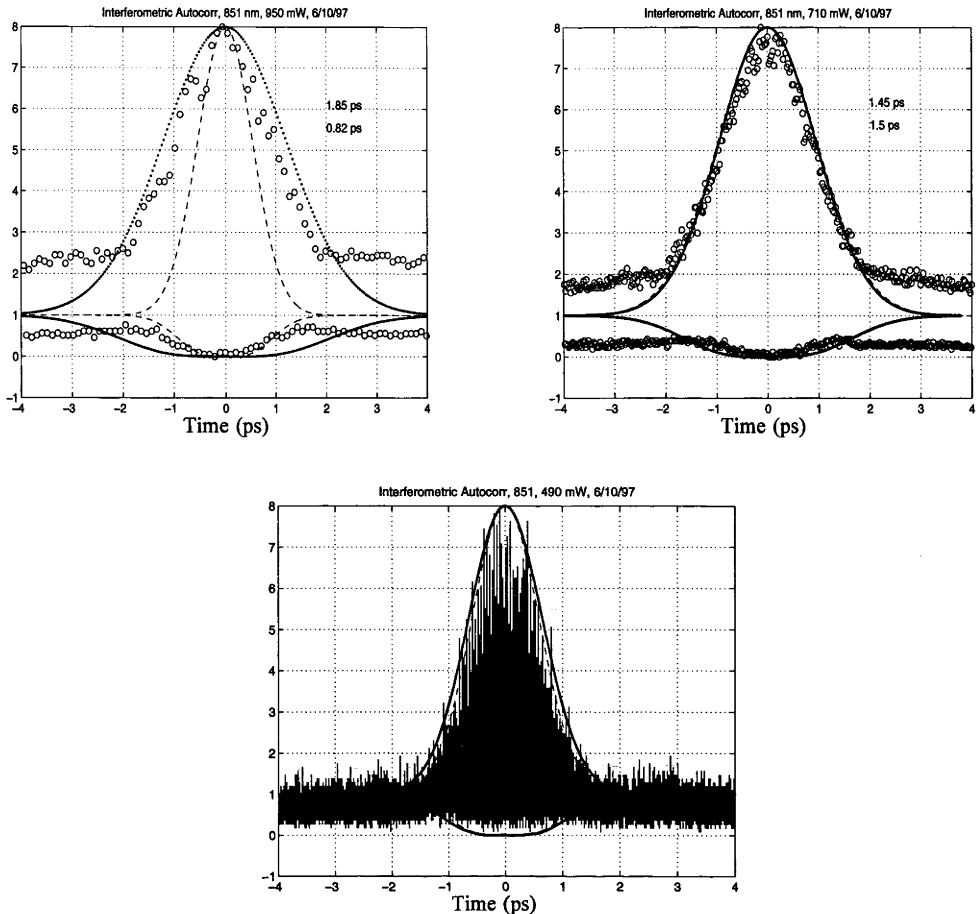Temporal pulse shape, 851 nm, 490 mW, 6/10/97

69

Figure 3-23 : The spectra, temporal pulse profiles determined from the intensity autocorrelations and the interferometric autocorrelations of the signal pulse at 851 nm from the dual-arm LBO OPO pumped by the fully cw pump beam and using the CVI mirror as the output coupler. Three sets of figures are shown for the case when the signal is oscillating at 851 nm, the first is for the maximum pump level of ~ 2.7 times above threshold, the next is at ~ 1.9 times above threshold and the last is at 1.3 times above threshold. For all spectra figures the spectra data (circles) are fitted to a Gaussian profile (line) and the FWHM spectral bandwidth in Angstroms are shown in each figure. For all temporal pulse shape figures the intensity autocorrelation data (circles) is fitted to a Gaussian (line with circles) and the FWHM pulse duration is shown as the top number in each figure. The transform-limited pulse (line) as determined from the spectra and its corresponding pulse duration (lower number) is also shown in each figure. For the first two interferometric autocorrelation figures the interferometric plots show the envelope of the data (circles), the expected interferometric envelope for a Gaussian pulse with a pulse duration equal to that measured from the intensity autocorrelation (dotted line) and the interferometric autocorrelation envelope of a Gaussian pulse fitted to the data (dashed line). The top number shows the pulse duration determined from the intensity autocorrelation and the bottom number shows the pulse duration of the Gaussian pulse fitted to the interferometric autocorrelation data. In the other interferometric autocorrelation figure the data is shown with the expected interferometric envelope for a Gaussian pulse with a pulse duration equal to that measured from the intensity autocorrelation.
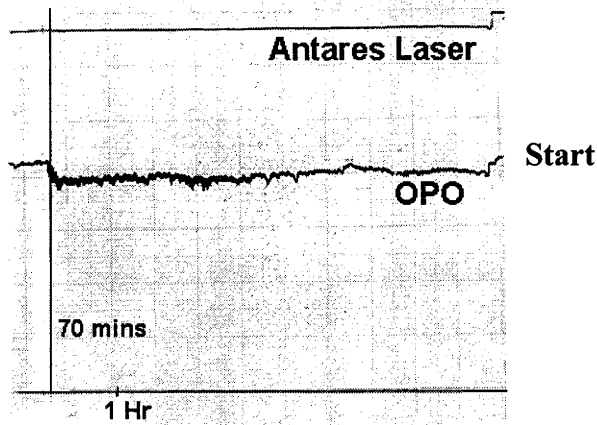
70

Figure 3-24 : The amplitude noise of the Antares Nd:YLF laser and the one-arm LBO OPO driven by the chopped cw pump beam as a function of time. The OPO output varies ± 5 % over a time scale of tens of minutes and varies a maximum of ± 3 % over a shorter time scale of a minute or less. The Antares laser varies less than 1 % in its power level over long periods of time. A quick adjustment of the Antares laser cavity length to regain optimum mode-locking eliminates the rapidly varying noise of the OPO. The other source of noise in the OPO is mainly due to air movements in the lab.

Figure 3-22 shows the characteristics of the signal pulse oscillating at 822 nm at both 3.3 times and 2.3 times above threshold. As in Figure 3-21, the pulses were not transform-limited. The spectra were very broad and square shaped, indicating a strong SPM. The InfACs show that the pulses were suffering from both dispersive broadening and phase-modulation, these effects diminishing the closer to threshold the OPO was operated. The lack of sidelobes in the predicted transform-limited temporal pulse shape at 2.3 times above threshold is due to the linear interpolation routine used to determine the transform-limited pulse shape from the spectrum.

Figure 3-23 shows the characteristics of the signal pulse oscillating at 851 nm at 2.7, 1.9 and 1.3 times above threshold. For oscillation at 851 nm, the spectra were Gaussian-like with a low side-peak: the same as the case with the dual-arm OPO using the chopped cw beam shown in Figure 3-19. The temporal pulse profiles showed that as the pump level decreased, the signal pulse became closer to being transform-limited as demonstrated by the InfAC plots. The first two InfAC plots show the data points with two fitted lines. The dotted line shows the expected interferometric autocorrelation envelope for a Gaussian pulse with a pulse duration equal to that measured from the IntAC, and the dashed line is the
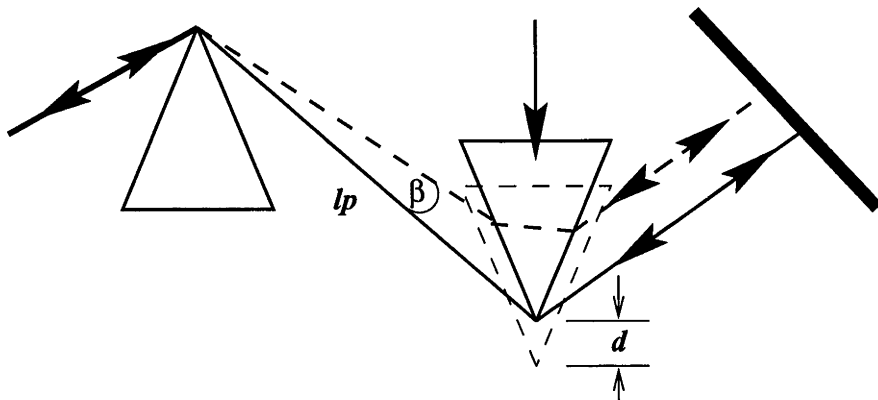
interferometric autocorrelation envelope of a Gaussian pulse fitted to the data. As can be seen from these plots, once the pump level fell to 1.9 times above threshold the expected Gaussian pulse shape matched the Gaussian pulse fitted to the data indicating that the pulse had very little frequency chirp.

One can conclude from these results that the signal pulses in the free running OPO were generally not transform-limited, especially when driven more than 2 to 3 times above threshold. They suffered from the effects of dispersion and phase modulation and furthermore oscillation on widely spaced, multiple frequencies also occurred in some conditions. The next section describes the measures taken to ensure single wavelength operation and the production of transform-limited signal pulses by using a prism pair to compensate for the effects of dispersion and phase-modulation in the LBO OPO.

3.4 Stabilised OPO

GVD and SPM / XPM were identified as major pulse shaping effects in the OPO. Both lead to the appearance of a frequency chirp in the circulating signal pulse whilst SPM / XPM also leads to spectral broadening. It was necessary to introduce elements into the cavity which provided an adjustable dispersion characteristic to counteract the intrinsic frequency chirp of the cavity. The sections below describe how this was done and the performance of the OPO with the dispersion compensating elements.

3.4.1 Dispersion compensating prism pair

Prism pairs or an array of four prisms have become a standard method of controlling dispersion in optical cavities resonating ultrashort pulses, especially for femtosecond pulses (see [22] for a general review). The prism pair uses angular dispersion to generate GVD in the circulating pulse. As shown in the figure on the previous page the beam incident on the first prism is spectrally dispersed, each spectral component of the beam is refracted at a different angle. The second prism corrects the beam's divergence and produces a collimated beam. Passing the beam back through the prism pair returns the dispersed spectral components into one beam again. However, since each spectral component has travelled a different path length the components have been shifted in time relative to one another. It has been shown that the angular dispersion causes GVD in the beam and is always negative [23]. The amount of negative GVD induced increasing with the separation between the prisms.

While negative dispersion is induced in the beam due to angular dispersion from the first prism, the material dispersion must be included in evaluating the overall affect of the prism pair. Since the material dispersion is positive, by inserting more of the second prism into the beam the overall amount of GVD can be adjusted from negative to positive. The negative dispersion, specifically the second derivative of phase with respect to frequency, introduced from a prism pair is [24, 25]

$$D_2^{prism} = \frac{d^2\phi_p}{d\omega^2} = \frac{\lambda^3}{2\pi^2 c^2} \frac{d^2 P}{d\lambda^2}$$

Eqn 3-4

where $\quad \dfrac{d^2 P}{d\lambda^2} = 4\left(\dfrac{d^2 n}{d\lambda^2} + \left(2n - \dfrac{1}{n^3}\right)\left(\dfrac{dn}{d\lambda}\right)^2\right)l_p Sin\beta - 8\left(\dfrac{dn}{d\lambda}\right)^2 l_p Cos\beta$

and where $\quad l_p Sin\beta = dTan\left(\dfrac{\alpha}{2}\right) \quad$ and $\quad l_p Cos\beta = l_p + dTan\left(\dfrac{\alpha}{2}\right)Tan\left(\dfrac{\varepsilon}{2}\right)$

P is the path length, l_p is the distance between the prism tips, n is the refractive index of the prism, β is the refracted ray angle relative to a reference ray that propagates between the tips of the prisms, α is the prism apex angle, ε is the deviation angle and d is the length of prism inserted into the beam, measured from the tip of the prism. The second order material dispersion is

$$D_2^{material} = \frac{d^2\phi_m}{d\omega^2} = \frac{\lambda^3 l_m}{2\pi c^2} \frac{d^2 n}{d\lambda^2}$$

Eqn 3-5

Where l_m is the length of material the ray passes through. Since the beam passes twice through the prism pair the dispersion is doubled.

Higher order terms can be taken into account but are neglected for our case since they only become important for very short pulses, below ≈ 100 fs.

Diffraction gratings can also be used to generate negative GVD through angular dispersion, however, the prism pair has the attraction of having low insertion loss since the prisms can be used at Brewster angle where the losses are generally < 1%.

Since the free running, dual-arm OPO has been examined in detail it is now possible to estimate the level of GVD and SPM/XPM in the cavity. Before estimating each contribution it is necessary to take into account how many passes the circulating signal pulse makes through the LBO crystal. The cavity lifetime of the signal wave can be estimated from the cavity losses. The total round trip cavity loss δ_c was around 8 % including the ~ 3 % transmission of the CVI output coupler mirror. The number of round trips a signal photon makes before being coupled out of the cavity or decaying away is approximately $1/\delta_c \approx 12$. The cavity enhancement factor is approximately $4 \delta_1/\delta_c^2$, where δ_1 is the transmission of the output coupler, and was around 30 times. With the OPO operating several times above threshold, where the pump depletion is around 50 %, the peak power of the signal pulse after one pass should be ~ 2.5 kW (in a 2 ps pulse). Through resonant enhancement the circulating peak power of the signal pulse should be ~ 75 kW.

The GVD from the material dispersion of LBO is double that shown in Figure 3-2 since the resonator was a standing wave cavity. Per round trip through the cavity the GVD should be ~ +1000 fs² at 780 nm down to ~ +700 fs² at 920 nm. The dispersion length L_D, or the length a pulse has to propagate through LBO before its pulse duration broadens by √2, is 17130 cm for a single round trip or 713 cm for a pulse resonated 12 times; assuming a pulse of 1.5 ps in duration and at a wavelength of 850 nm. For our case with a crystal length of 1 cm and the signal pulse passing through it twice per round trip the total propagation distance z is 24 cm and $z/L_D \approx 0.034$. The temporal broadening due to GVD alone is given by

$$\Delta t_B = \Delta t_0 \sqrt{1 + \left(\frac{z}{L_D}\right)^2}$$

where Δt_0 is the initial pulse duration. The GVD due to LBO will, therefore, not broaden the signal pulse significantly because the effective propagation distance of the circulating signal pulse is relatively small.

The nonlinear refractive index, n_2, of LBO has been reported to be 3.4±0.8 x 10^{-16} cm²/W [13]. The nonlinear phase shift due to SPM of the circulating signal pulse can be estimated as

$$\Delta\phi_{max} = \frac{2\pi n_2 I_0 L}{\lambda_0}\zeta$$

Where I_0 is the peak signal intensity, L is the propagation distance and ζ is the number of round trip in the cavity the signal photon makes and is equal to 12. In our case we can consider that $I_0 \approx 20$ GW/cm^2 (75 kW in a 15 μm radius) over the confocal parameter length, making L $\approx$ 4 mm (2 x confocal parameter). This gives $\Delta\phi_{max}$ = 2.4 or 0.75π (λ_o = 850 nm) radians . The nonlinear length L_{NL} due to SPM can be estimated as $L/\Delta\phi_{max}$ and is approximately 1.7 mm. L_{NL} is the distance over which $\Delta\phi_{max}$ = 1. $L_D \ll L_{NL}$, ie. SPM / XPM is the dominant effect which can affect the spectrum and lead to the appearance of chirp on the OPO pulses.

Despite SPM / XPM being the dominant effect it has been shown [15] that weak GVD can still play an important role in pulse shaping. As an example, Figure 2-5 shows the effect of GVD and SPM on the pulse shape and the instantaneous frequency chirp of a pulse propagating at 1064 nm through a single-mode optical fibre. Even the weak GVD of $z/L_D \approx$ 0.01 has a dramatic effect on the pulse shape and frequency chirp, broadening the pulse significantly and increasing the linear frequency chirp from a portion of the pulse to across the entire pulse. The reason for this has been explained in Chapter 2, Section 2.3.1.1. However, for the case of SPM / XPM and GVD in the OPO the effect of parametric gain and GVM must also be taken into account, as this also occurs every round trip. As was described in Section 3.2 to study these combined effects requires a numerical simulation of the OPO and even then it is not easy to separate each effect's contribution to the overall dynamics of the system. Overall, however, it is quite clear that SPM / XPM and GVD are quite strong enough in the LBO OPO to introduce frequency chirping, linear and nonlinear, in the circulating signal pulse.
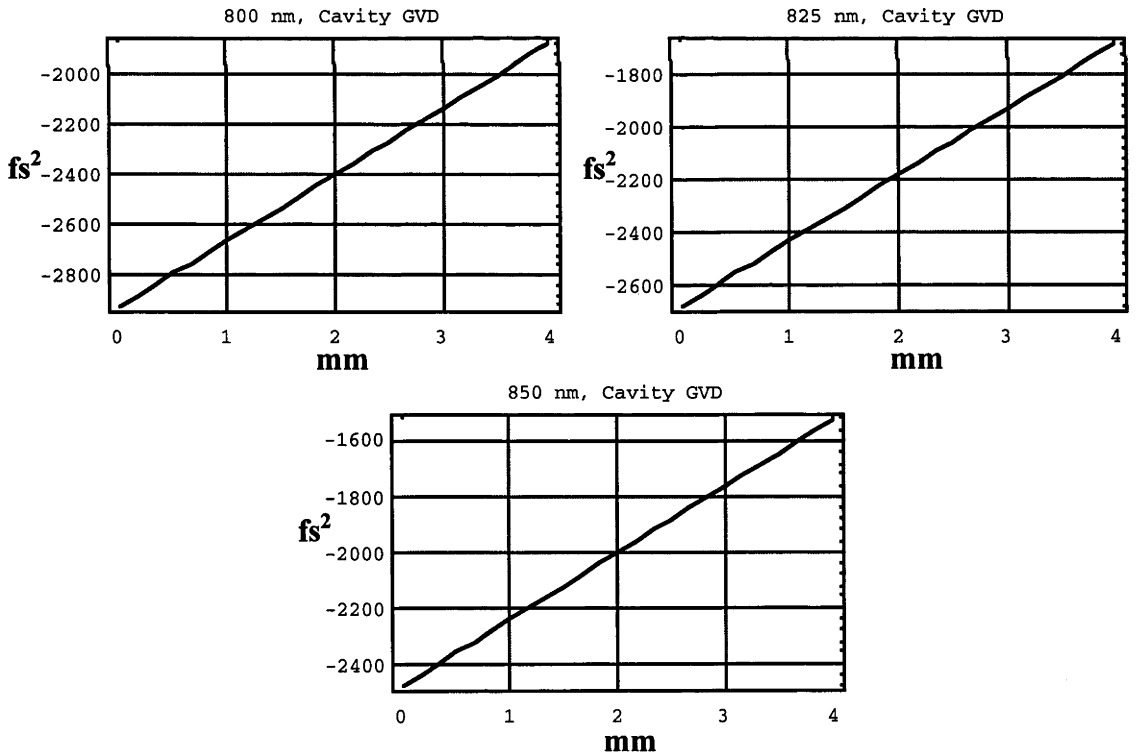

Figure 3-25 : The total GVD, in fs^2 , of the LBO OPO as a function of insertion depth of the second prism, d, in mm. The top left figure is for the signal wave at 800 nm, the top right figure is for the signal wave at 825 nm and the bottom figure is for the signal wave at 850 nm. The prism separation, l_p , is 300 mm.
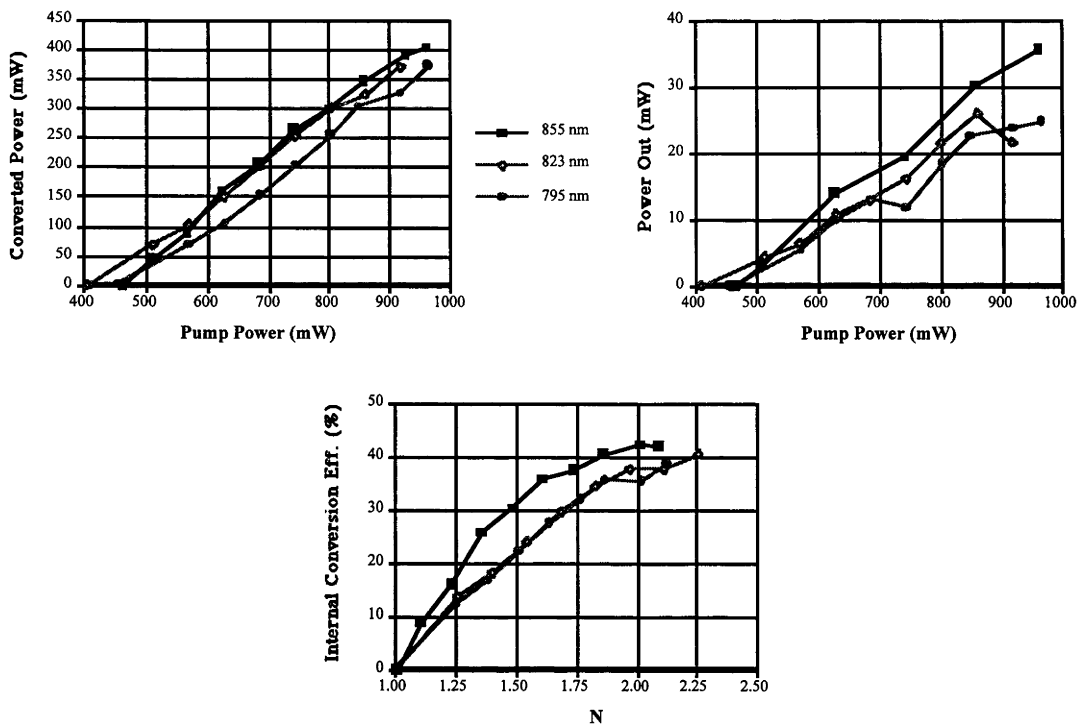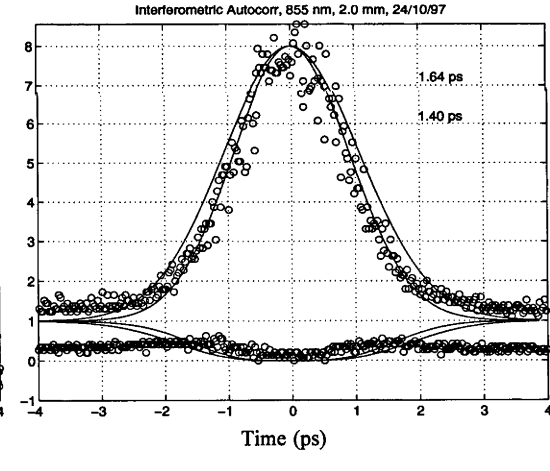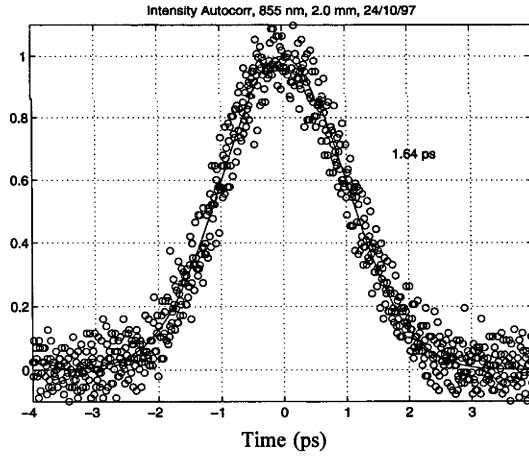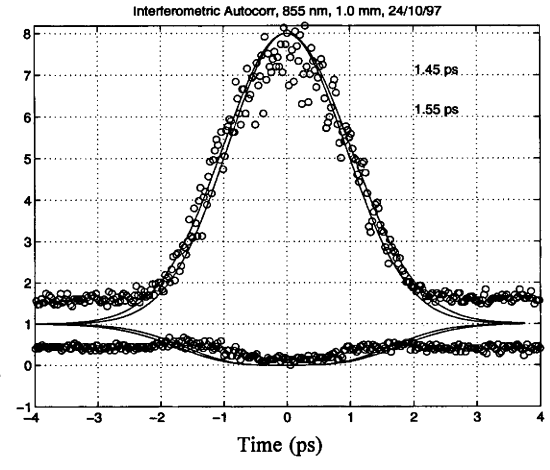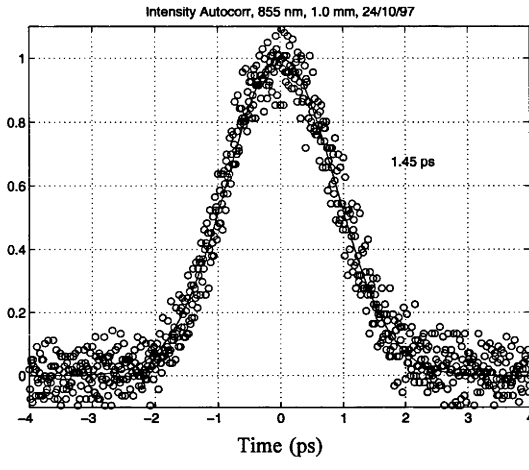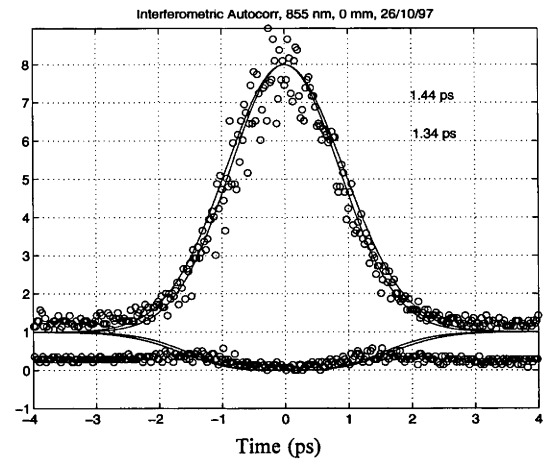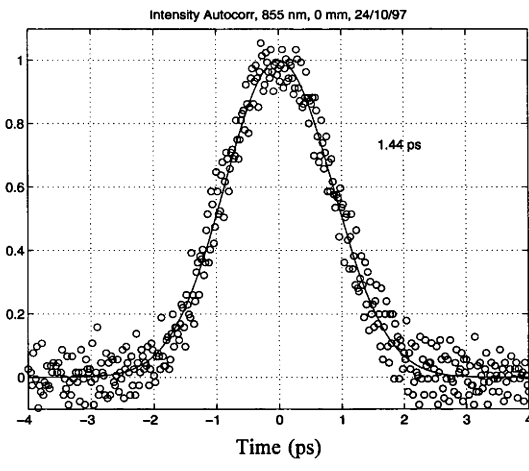
Figure 3-26 : **The variation in the converted power (top left) and the extracted signal power (top right) with the pump power at the focus in the LBO crystal plus the internal conversion efficiency (bottom figure) for the stabilised dual-arm LBO OPO operating with the CVI output mirror and the fully cw pump beam for various wavelengths.**

Figure 3-25 shows the total GVD (fs^2) of the OPO cavity with a pair of Brewster angled SF10 prisms separated 30 cm apart as a function of insertion depth of the second prism. The total GVD includes the negative GVD provided by the angular dispersion of the prism pair plus the positive material dispersion of the prisms themselves and the LBO crystal. As can be seen the net GVD is around -2000 fs^2 to -2500 fs^2 over a range of wavelengths. The net negative GVD is there to compensate for the extra frequency chirp that will result from the strong SPM / XPM in the cavity. The amount of frequency chirp that occurred in the OPO due to SPM /XPM and GVD was not estimated because no numerical simulation was carried out. The actual settings of the prism pair, the separation and insertion depth were optimised experimentally.

3.4.2 Characteristics and performance

To operate the OPO with the prism pair it was first necessary to align and run the free running OPO with the full cw pump beam. Then while the free running OPO was oscillating the first prism was slowly inserted into the signal beam until it deviated a portion of the signal beam without stopping oscillation. This deviated portion of the beam was used to align the position of the second prism and the end mirror. The angle of the end mirror was adjusted until the beam was reflected back through the prism pair and down the incoming beam axis. After that it was necessary to insert the first prism further until it deviated the entire beam. Oscillation was then started by adjusting the cavity length to obtain synchronisation. Fine tuning involved adjusting the angle of both end mirrors and the cavity length and fine tuning the Brewster angle setting of the prisms.

When operating with the prism pair the OPO was generally better behaved than for the case where it was free running. It had better amplitude stability and was more tolerant to variations in the alignment of the end mirror. Signal oscillation occurred only on one

75

Intensity Autocorr, 855 nm, 0 mm, 24/10/97

1.44 ps

Interferometric Autocorr, 855 nm, 0 mm, 26/10/97

1.44 ps
1.34 ps

Intensity Autocorr, 855 nm, 1.0 mm, 24/10/97

1.45 ps

Interferometric Autocorr, 855 nm, 1.0 mm, 24/10/97

1.45 ps
1.55 ps

Intensity Autocorr, 855 nm, 2.0 mm, 24/10/97

1.64 ps

Interferometric Autocorr, 855 nm, 2.0 mm, 24/10/97

1.64 ps
1.40 ps

Time (ps)

76
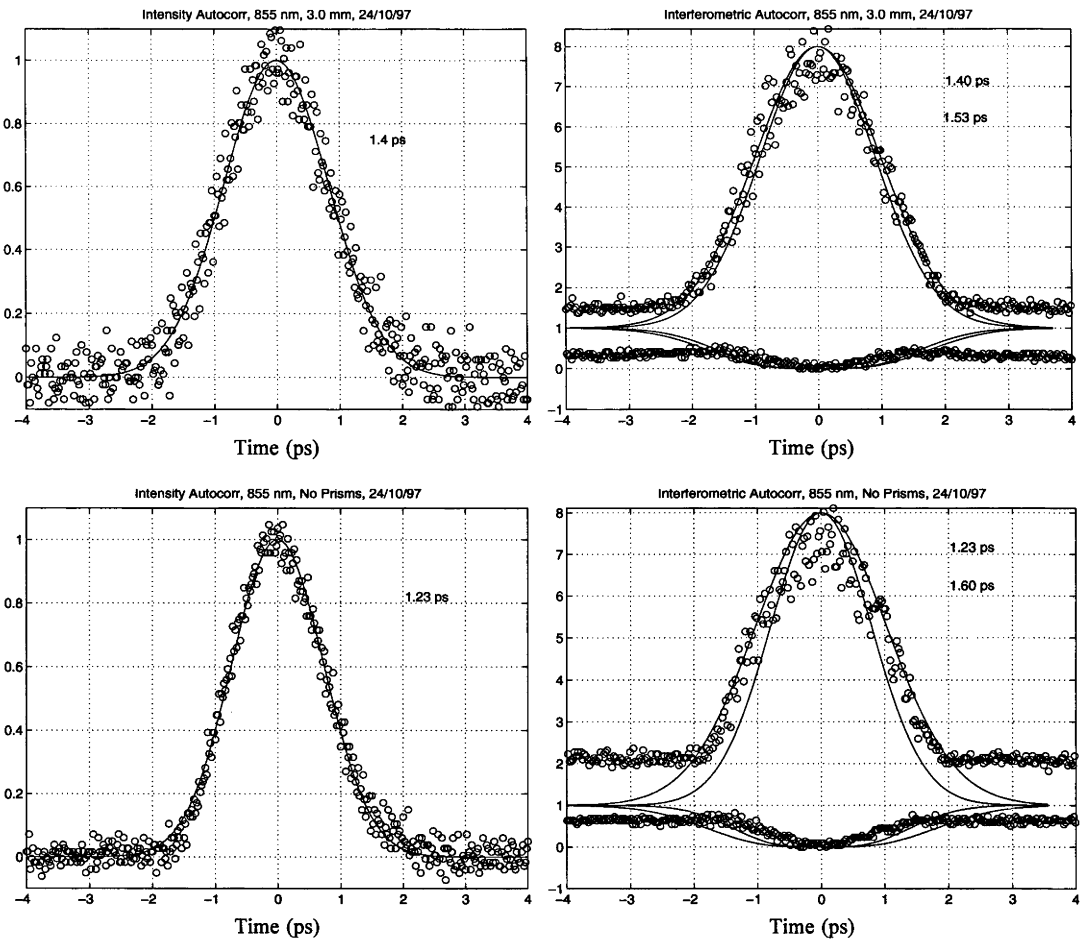
Figure 3-27 : The SHG intensity (left column) and interferometric (right column) autocorrelations of the signal pulse at 855 nm from the stabilised, fully cw LBO OPO at various prism insertion depths and without prisms. The intensity autocorrelation data (circles) is fitted with a Gaussian (line) and the FWHM pulse duration for this Gaussian fit is shown in each figure. The interferometric data (circles) is fitted with two Gaussians; one having a pulse duration equal to that from the intensity autocorrelation and the other is the best fit to the interferometric autocorrelation data. The two numbers in each figure are the FWHM Gaussian pulse durations of the intensity autocorrelation (top number) and the fit of the interferometric autocorrelation data (bottom number). The time scale is in picoseconds.

Intensity Autocorr, 825 nm, 0 mm, 26/10/97

Interferometric Autocorr, 825 nm, 0.0 mm, 26/10/97

Intensity Autocorr, 825 nm, 1.0 mm, 26/10/97

Interferometric Autocorr, 825 nm, 1.0 mm, 26/10/97

Intensity Autocorr, 825 nm, 2.0mm, 1.05 W, 26/10/97

Interferometric Autocorr, 825 nm, 2.0 mm, 1.05 W, 26/10/97
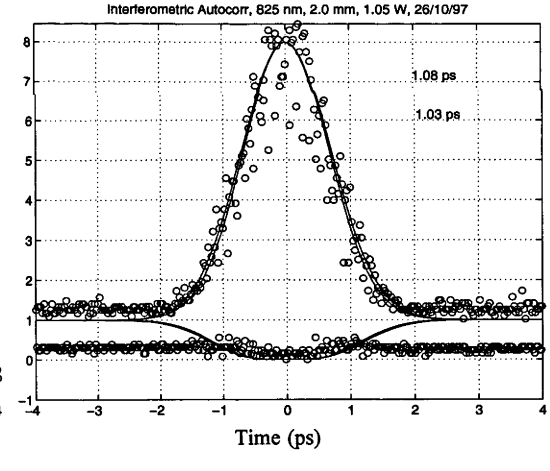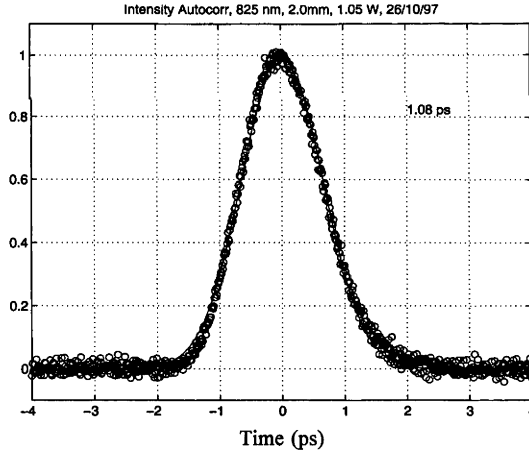
Figure 3-28 : The SHG intensity (left column) and interferometric (right column) autocorrelations of the signal pulse at 823 nm from the stabilised, fully cw LBO OPO at various prism insertion depths and without prisms. The intensity autocorrelation data (circles) is fitted with a Gaussian (line) and the FWHM pulse duration for this Gaussian fit is shown in each figure. For the me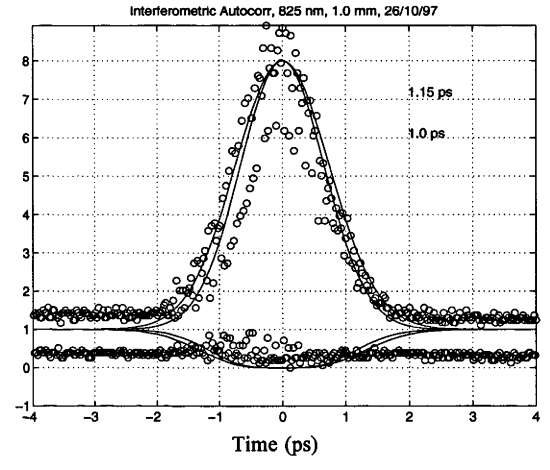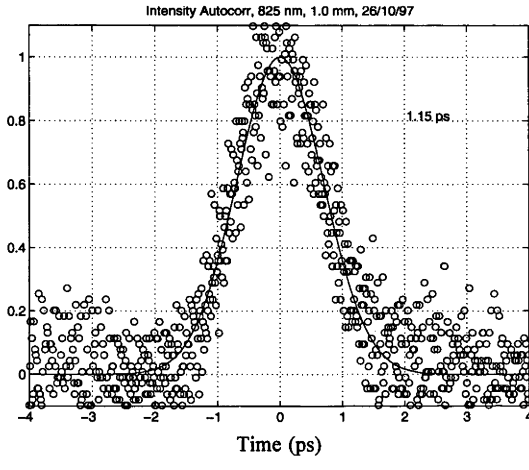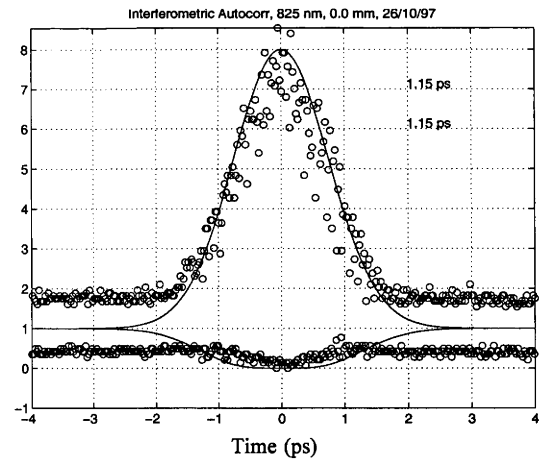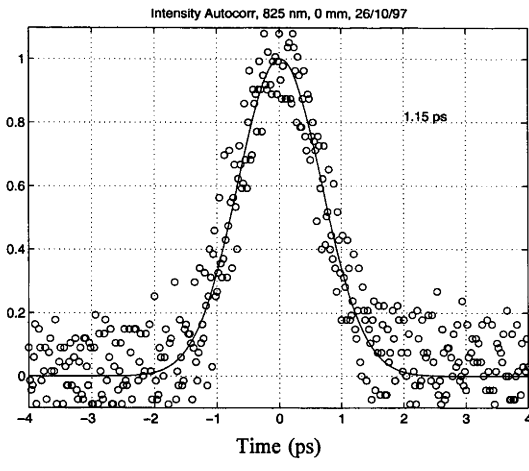asurements of the stabilised OPO the interferometric data (circles) is fitted with two Gaussians; one having a pulse duration equal to that from the intensity autocorrelation and the other is the best fit to the interferometric autocorrelation data. The two numbers in each figure are the FWHM Gaussian pulse durations of the intensity autocorrelation (top number) and the fit of the interferometric autocorrelation data (bottom number). For the measurement of the free running OPO the interferometric autocorrelation is shown with a Gaussian (line) of a pulse duration equal to that from the intensity autocorrelation. The time scale is in picoseconds.

79

Intensity Autocorr, 795 nm, 0.0 mm, 26/10/97

Interferometric Autocorr, 795 nm, 0.0 mm, 26/10/97

Intensity Autocorr, 795 nm, 1.0 mm, 26/10/97

Interferometric Autocorr, 795 nm, 1.0 mm, 26/10/97

Intensity Autocorr, 795 nm, 2.0 mm, 26/10/97

Interferometric Autocorr, 795 nm, 2.0 mm, 26/10/97

Interferometric Autocorr, 795 nm, 2.0 mm, 26/10/97
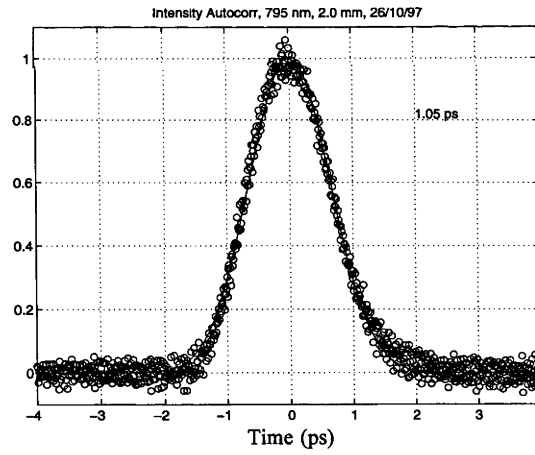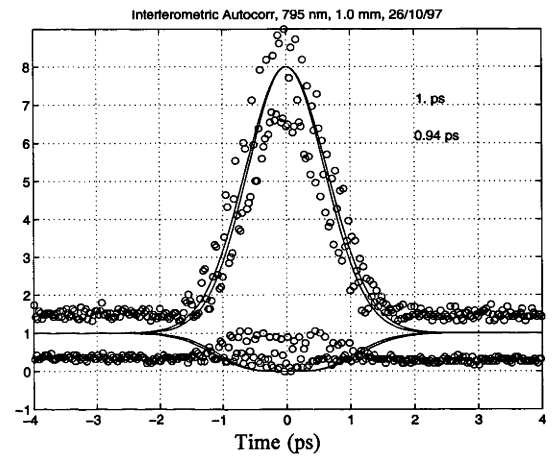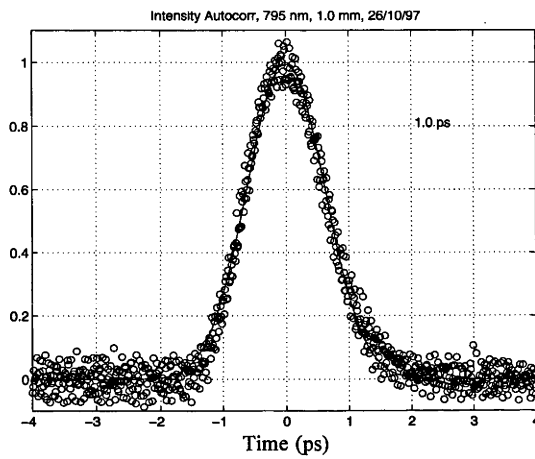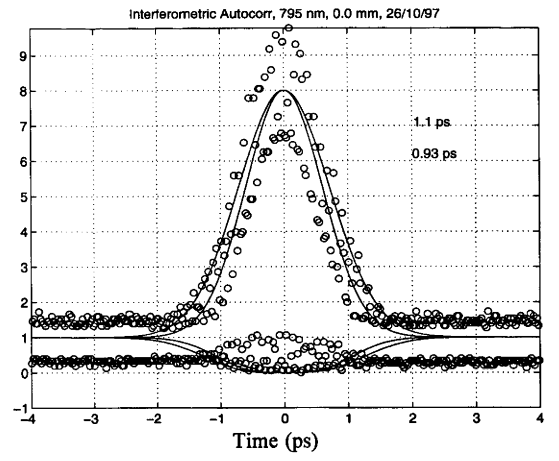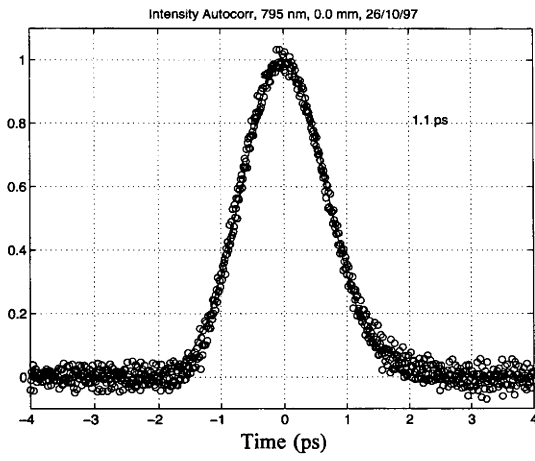
Figure 3-29 : The SHG intensity (left column) and interferometric (right column) autocorrelations of the signal pulse at 795 nm from the stabilised, fully cw LBO OPO at various prism insertion depths and without prisms. The intensity autocorrelation data (circles) is fitted with a Gaussian (line) and the FWHM pulse duration for this Gaussian fit is shown in each figure. For the measurements of the stabilised OPO the interferometric data (circles or line) is fitted with two Gaussians; one having a pulse duration equal to that from the intensity autocorrelation and the other is the best fit to the interferometric autocorrelation data. The two numbers in each figure are the FWHM Gaussian pulse durations of the intensity autocorrelation (top number) and the fit of the interferometric autocorrelation data (bottom number). For the measurement of the free r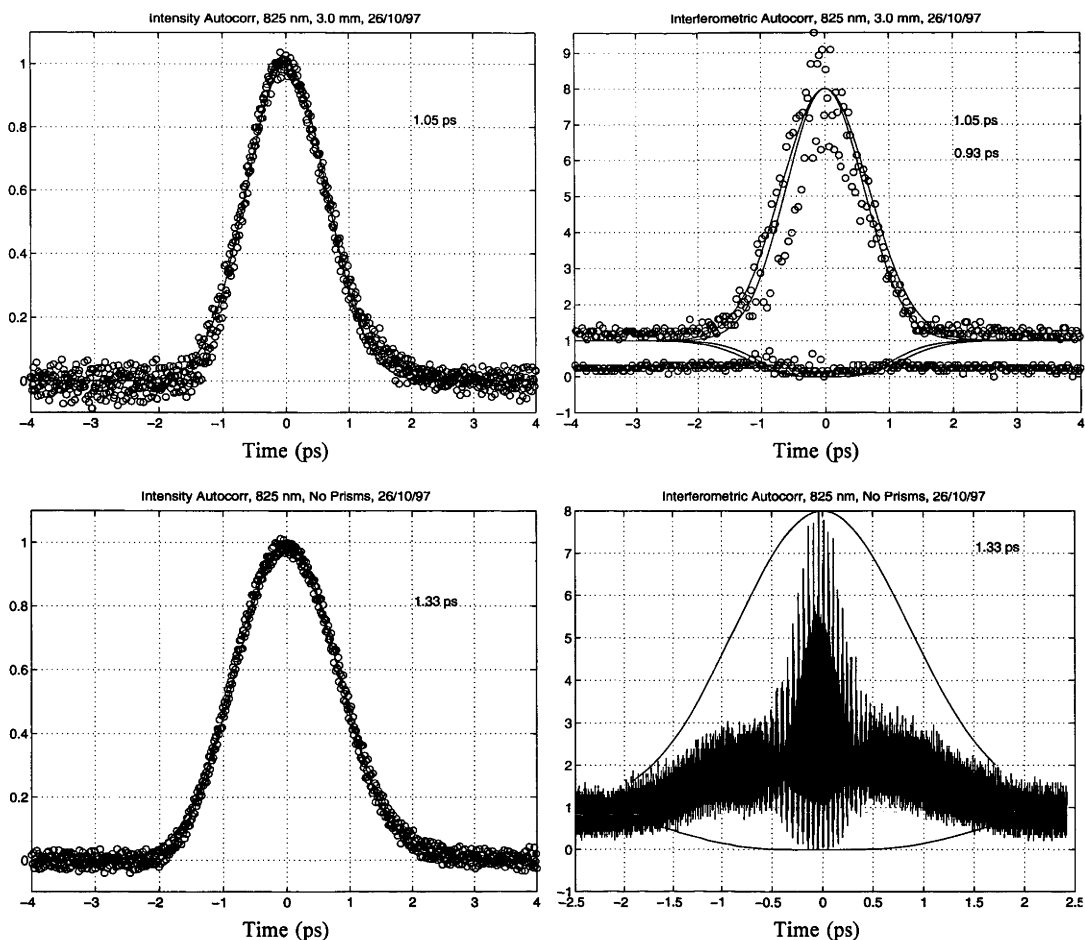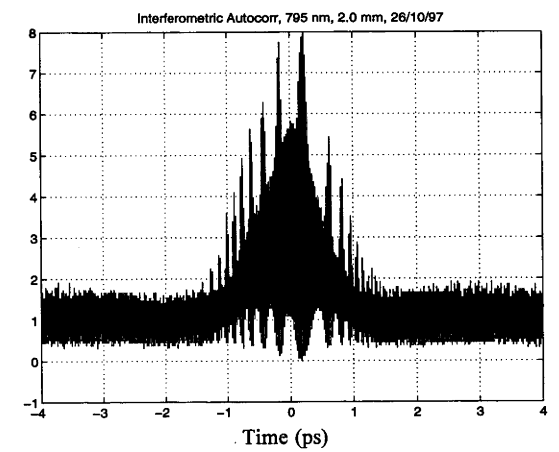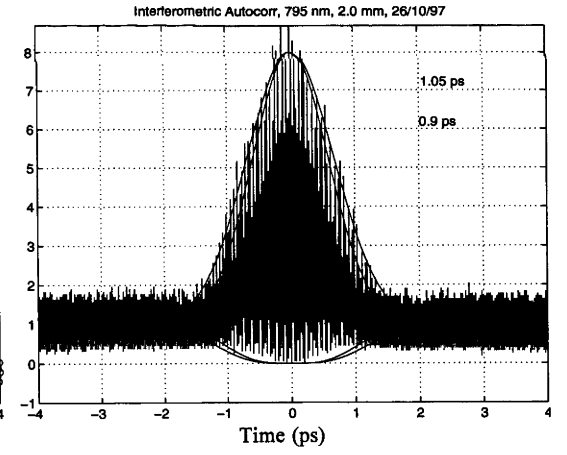unning OPO the interferometric autocorrelation is shown with a Gaussian (line) of a pulse duration equal to that from the intensity autocorrelation. It should be noted that the structure in the second interferometric autocorrelation at an insertion depth of 2 mm is due to the frequency instability described in the text . The time scale is in picoseconds.

81

frequency and the spectrum was Gaussian like. However, it was noted that the greater the insertion depth the more frequency unstable the OPO became. The spectrum of the signal started to shift around rapidly resulting in power fluctuations from the OPO. The optimum insertion depth was found to be around 0 to 1 mm where the OPO was generally well behaved and stable over long periods of time. The reason for this frequency instability may be due to the total cavity GVD becoming close to zero. It has been shown [26] that a LBO OPO is frequency unstable near zero GVD. In their case, at zero GVD the spectral bandwidth was much greater than at positive and negative net cavity GVD because all the spectral components could arrive in synchronisation with the pump pulse and experience gain, as opposed to negative or positive GVD where some spectral components would not be amplified by the pump pulse because they arrived too late or too early. At zero GVD the broadened spectrum is sensitive to cavity fluctuations since any shift in cavity length will mean spectral components moving out of synchronisation with the pump pulse resulting in large changes in the gain experienced by the resonated wave.

The internal conversion efficiency and the variation of the converted power and extracted signal power as a function of the pump power at the focus in the LBO crystal are shown in Figure 3-26. The addition of the SF10 prism pair increased the cavity losses. The OPO could be driven only about 2 times above threshold achieving an internal conversion efficiency of about 40 % compared to about 2.5 times above threshold and an internal conversion efficiency of 50 % in the free running, fully cw OPO. The extracted power was around 20 to 30 mW or 130 to 200 W peak power in 2 ps. The extraction efficiency was low, around 2 to 3 %. Despite the low output power of the OPO, good measurements of the temporal amplitude and phase characteristics of the signal pulse were obtained.
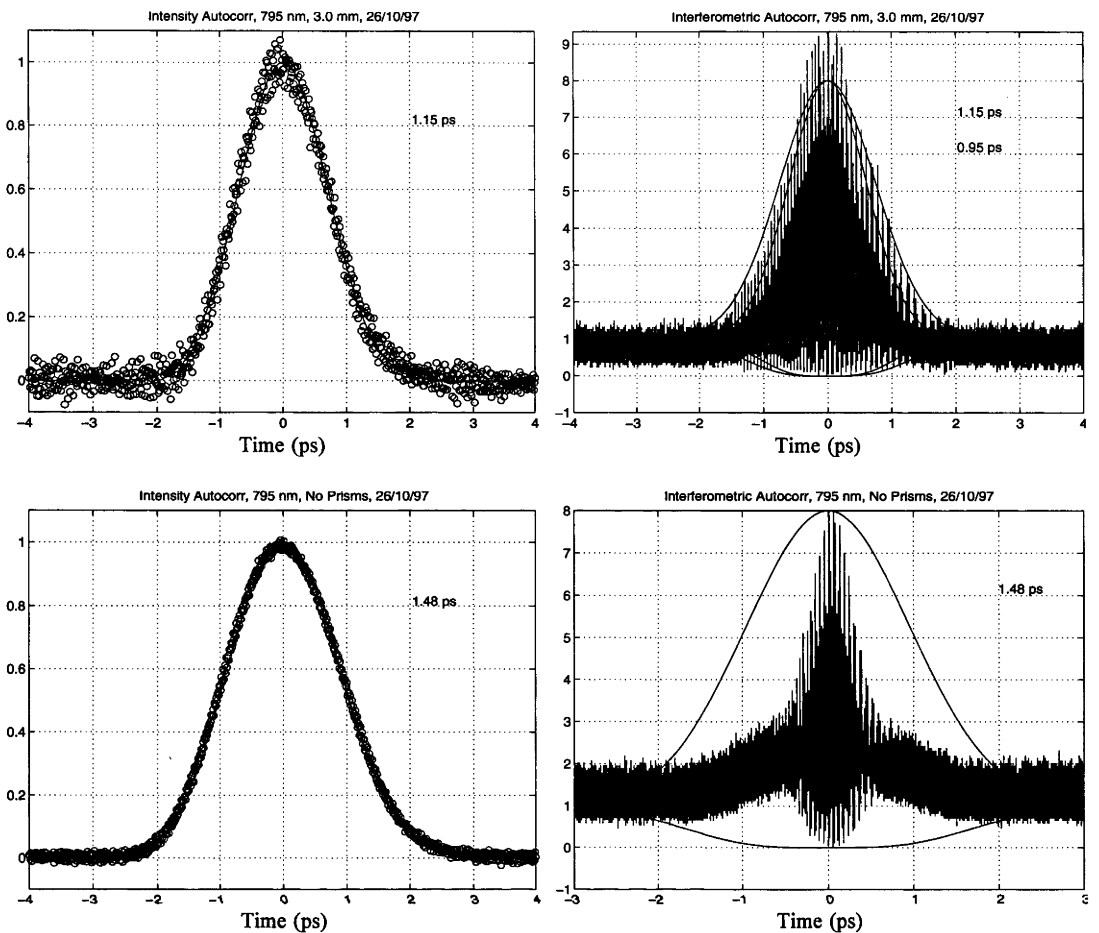
The SHG intensity and interferometric autocorrelations of the signal pulse at 855 nm, 823 nm and at 795 nm are shown in Figure 3-27, Figure 3-28 and Figure 3-29 respectively. The figures show the temporal characteristics of the signal pulse for prism insertion depths of 0 to 3 mm and, for comparison, the OPO running without prisms. All measurements were taken at maximum pump power.

The IntACs are fitted with a Gaussian pulse shape and the FWHM pulse duration of the fitted Gaussian is shown in each plot. The IntACs closely match the Gaussian pulse shape. For the measurements at 855 nm the pulse duration was 1.5±0.1 ps at all insertion depths and 1.2 ps without prisms. For the measurements at 823 nm the pulse duration is 1.1±0.05 ps at all insertion depths and 1.3 ps without prisms. For the measurements at 795 nm the pulse duration is 1.05±0.05 ps at all insertion depths and 1.5 ps without prisms. The InfACs are shown with the interferometric autocorrelation envelopes corresponding to two Gaussian pulses; one having a pulse duration equal to that of the IntAC and the other is the best fit to the InfAC data. For the measurements at 855 nm the pulse duration from the Gaussian fit to the InfAC data is 1.5±0.07 ps at all prism insertion depths. For the measurements at 823 nm the pulse duration from the Gaussian fit to the InfAC data is 1.0±0.04 ps at all prism insertion depths. For the measurements at 795 nm the pulse duration from the Gaussian fit to the InfAC data is 0.93±0.02 ps at all prism insertion depths. For the InfACs of the free running OPO at 823 nm and 795 nm only the Gaussian with a pulse duration equal to that of the IntAC is shown as the InfACs displayed significant frequency chirping.

At each insertion depth and for all three wavelengths the match between the pulse durations of IntAC and InfAC Gaussian fits are within 10 %. Whereas for the free running OPO measurements the InfAC at 823 nm and at 795 nm displayed significant frequency chirp and the measurement at 855 nm, where the free running measurement does not display significant chirp, the pulse durations of the two fits differ by 30 %. The free running result

at 855 nm is similar to results for the free running, fully cw OPO at 851 nm (see Figure 3-2?). An example of the frequency instability that arises with increasing insertion depth is show in the second InfAC at an insertion depth of 2 mm at 795 nm. When this measurement was taken the spectrum shifted in frequency, resulting in a rapid amplitude modulation in the SHG signal from the interferometric autocorrelator.

The match between the Gaussian fits of the IntACs and InfACs shows that the frequency chirping of the signal pulses evident in the free running OPO has been compensated for by the prism pair. It was also noticed that the OPO was more unstable with increasing insertion depth at 795 nm than at 823 nm and the most stable with increasing insertion depth at 855 nm. This is because the signal pulse at 795 nm displayed the greatest frequency chirp and the signal pulse at 855 nm displayed the least frequency chirp of the three measurements when the OPO was free running. This can be taken as further evidence that the frequency instability with increasing insertion depth is due to net cavity dispersion. Overall the OPO was the most stable at about 1 mm insertion depth. At 1 mm insertion depth the cavity GVD due to the LBO crystal and the net cavity GVD is +976 fs^2 and -2716 fs^2 at 795 nm; +909 fs^2 and -2448 fs^2 at 823 nm; and +833 fs^2 and -2208 fs^2 at 855 nm. This suggests that there is a significant contribution to the frequency chirping of the signal pulses is from SPM / XPM, as is suggested by the calculations in Section 3.4.1 and previous measurements. From the measurements all phase structure in the temporal pulse has been eliminated with the addition of the prism pair. It is very probably that the signal pulses from the stabilised OPO are close to transform-limited since the net negative cavity GVD introduced with the prism pair can not only remove the frequency chirp in the pulses but also the spectral broadening due to SPM / XPM [8, 13].

The idler pulses were not measured as the beam profiles still changed shape with cavity length detuning. Though the effect is much less than for the case where the OPO is free running but is still sufficient to warrant using the cavity constrained, signal pulses as the seed pulses for the OPAs. As will be shown in Chapter 6 the available peak power of the signal pulses is enough to provide seed pulses for the OPA.

3.5 Summary

This chapter described the theory, construction and operation of a cw, synchronously pumped, LBO OPO that produced signal and idler picosecond pulses that were wavelength tunable between 780 nm to 920 nm and between 1230 nm to 1620 nm using temperature tuned, type I, NCPM.

LBO had distinct advantages for this application over similar crystals such as BBO and KTP. Advantages included large angular, spectral and temperature acceptance angles; low group velocity mismatch between the pump and the signal and idler waves; no beam walk-off and ease of use experimentally.

The SRO OPO cavity was carefully designed to maximise the overall performance. Maximising cavity stability, the properties of the resonated signal wave and minimising astigmatism were carried out by modelling the cavity before construction. A successful alignment procedure that included mode-matching the pump beam into the cavity, setting the cavity length to maintain synchronisation between the signal and pump pulses and operating the cavity in the middle of the stability range were determined. After the alignment was carried out the OPO remained aligned for many days, simplifying routine operation. The effects of focusing on parametric gain was also taken into account; with the cavity constructed to be close to the optimum.

The pumping laser system provided enough peak power to drive the OPO up to 6 times above threshold with minimal cavity losses and up to 2.25 times above threshold in the dual-arm cavity with the dispersion compensating prism pair and an output coupler.

For the OPO operating without intracavity elements except the LBO crystal ("free running") and minimal losses, the internal conversion efficiency was up to 70 % and could be driven up to 6 times above threshold. In general the idler pulses coupled from the cavity were around 1 kW in peak power, 2 ps in duration and not transform limited. As predicted by theory the pulse duration of the idler pulses dropped to $\sim 0.5\ \Delta t_3$, becoming closer to transform-limited, as the pump level decreased. Using a variable transmission output coupler of 5 % to 10 % across the wavelength range of the OPO the signal pulses were studied. With this OPO configuration the internal conversion efficiency was up to 70 % at a maximum pump level of 4 times above threshold. The signal pulses had a pulse duration of 2 ps, similar to the pump pulse duration at pump levels well above threshold and a pulse duration of as small as 1.2 ps, about half the pump pulse duration, near threshold. The signal pulses also became closer to being transform limited the nearer to threshold the OPO was operated. Typically the signal and idler pulses had Gaussian-like temporal pulse profiles and spectra. However, it was possible for the signal and idler spectra to display multiple peaks or to be even comprised of widely space, multiple frequencies; especially when the OPO was driven well above threshold and the cavity length was detuned from optimum. While the spatial beam profile of the signal wave was close to TEM_{00} at all pump levels and with cavity length detuning, the idler beam profile displayed radical changes in its beam profile with cavity length detuning. This made the idler pulses unsuitable for use as seed pulses in the OPA. It was decided at this stage to use the signal wave as the seed pulses for the OPA. Since it was constrained by the cavity the beam profile was not susceptible to variations in pump levels and cavity length detuning.

The other problems associated with the pulses created by the LBO OPO, where they can oscillate on multiple frequencies and were not transform-limited, also makes them unsuitable as seed pulses for the OPA. From theory and other experiments it was known that GVD and SPM / XPM can play important pulse shaping roles in ps OPOs. To control the frequency of the oscillating signal wave and to compensate for any frequency chirp due to GVD and SPM / XPM in the cavity it was decided to include a prism pair and to change from a one-arm to dual-arm cavity so that the signal beam could be coupled from the cavity without being spectrally dispersed. At the same time the pump beam was made fully cw so that interferometric autocorrelations of the signal pulse could be carried out to specifically determine the cause of the pulses not being transform-limited.

The signal pulses from dual-arm OPO displayed similar characteristics to those from the one-arm OPO. However, when operating the dual-arm OPO with the fully cw pump beam the threshold was 25 % higher than for dual-arm OPO pumped by the chopped cw beam. The higher threshold may have been due to a weak thermal lensing in the SHG crystal when pumped by the fully cw beam or it may have been due to a slight depolarisation in the fully cw pump beam. Nevertheless the free running, fully cw, dual-arm OPO could be driven up to 3.5 times above threshold and had an internal conversion efficiency of 50 %.

From the interferometric autocorrelations of the signal pulses it was evident that there was strong frequency chirping in those signal pulses that were not transform-limited. This frequency chirping was due to SPM / XPM, as was evident from the spectral broadening and calculations, and GVD, as determined from the known GVD of LBO.

The total GVD due to the prism pair and the LBO crystal were calculated. It was also found that SPM and XPM were the dominant effects in the cavity. However, GVD was strong enough to have a significant influence. The net cavity GVD of the prism pair compensated for the material dispersion due to the LBO crystal and was sufficiently negative to compensate for the effect of SPM / XPM. The prism separation was optimised

experimentally as it was difficult to determine the combined effects of GVM, GVD, SPM / XPM and parametric gain of the frequency chirping of the signal pulses without a numerical simulation.

The OPO operating with the prism pair could be driven up to 2.25 times above threshold, reaching a internal conversion efficiency of 40 %. The OPO was well behaved and stable with prism insertion depths of around 1 mm. As the insertion depth increased the OPO became more unstable, especially if the signal pulse displayed significant frequency chirping when the OPO was free running. This instability may have been due to the net cavity GVD becoming close to zero; where it has been shown an OPO is intrinsically unstable. While accurate spectral information was not available it was also known that the spectra of signal pulses were Gaussian-like and with the prism insertion depth close to 1 mm they consisted of only one stable frequency. Despite this it was clearly evident from the intensity and interferometric autocorrelations that the addition of the prism pair compensated for the frequency chirping evident in the signal pulses in the free running OPO. It was expected that the pulses were close to transform-limited, especially if the net cavity GVD was negative.

3.6 References

[1]   J. D. Bierlein and H. Vanherzeele, "Potassium Titanyl Phosphate : properties and new applications," *JOSA B*, vol. 6, p. 622, 1989.

[2]   D. Eimerl, L. Davis, S. Velsko, E. K. Graham, and A. Zalkin, "Optical, mechanical, and thermal properties of barium borate," *J. Appl. Phys.*, vol. 62, p. 1968, 1987.

[3]   D. N. Nikogosyan, "Lithium Triborate (LBO). A Review of its properties and applications," *Appl. Phys. A*, vol. 58, p. 181, 1994.

[4]   R. L. Byer, *Optical Parametric Oscillators*, in Quantum Electronics: A Treatise, Ed. H. Rabin and C. L. Tang, vol. 1, pt B, p. 587: Acedemic Press, New York, 1975.

[5]   S. Lin, J. Y. Huang, J. Ling, C. Chen, and Y. R. Shen, "Optical parametric amplification in a lithium triborate tunable from 0.65 μm to 2.5 μm," *Appl. Phys. Lett.*, vol. 59, p. 2805, 1991.

[6]   H. Kogelnik and T. Li, "Laser Beams and Resonators," *Applied Optics*, vol. 5, p. 1550, 1966.

[7]   G. D. Boyd and D. A. Kleinman, "Parametric interaction of focused Gaussian light beams," *J. Appl. Phys.*, vol. 39, p. 3597, 1968.

[8]   M. Ebrahimzadeh, S. French, and A. Miller, "Design and performance of a singly resonant picosecond LBO optical parametric oscillator synchronously pumped by a self-mode-locked Ti:sapphire laser," *JOSA B*, vol. 12, p. 2180, 1995.

[9]   S. French, M. Ebrahimzadeh, and A. Miller, "High-power, high-repetition-rate picosecond optical parametric oscillator for the near- to mid-infrared.," *J. Modern Optics*, vol. 43, p. 929, 1996.

[10]   G. J. Hall, M. Ebrahimzadeh, A. Robertson, G. P. A. Malcolm, and A. I. Ferguson, "Synchronously pumped optical parametric oscillators using all-solid-state pump lasers.," *JOSA B*, vol. 10, p. 2168, 1993.

[11]   M. J. McCarthy, S. D. Butterworth, and D. C. Hanna, "High-power widely-tunable picosecond pulses from an all-solid-state synchronously-pumped optical parametric oscillator," *Optics Communs.*, vol. 102, p. 297, 1993.

[12]   M. J. McCarthy. D. C. Hanna, "All-solid-state synchronously pumped optical parametric oscillator," *JOSA B*, vol. 10, p. 2180, 1993.

[13]   S. D. Butterworth, S. Girad, and D. C. Hanna, "High-power, broadly tunable all-solid-state synchronously pumped lithium triborate optical parametric oscillator," *JOSA B*, vol. 12, p. 2158, 1995.

[14]   S. Guha, F. Wu, and J. Falk, "The effects of focusing on parametric oscillation," *IEEE J. Quant. Electronics*, vol. QE-18, p. 907, 1982.

[15]   G. P. Agrawal, *Nonlinear fiber optics*: Academic press, Inc., 1989.

[16] M. F. Becker, D. J. Kuizenga, D. W. Phillion, and A. E. Siegman, "Analytic expressions for ultrashort pulse generation in mode-locked optical parametric oscillators," *J. Appl. Physics*, vol. 45, p. 3996, 1974.

[17] E. C. Cheung and J. M. Liu, "Theory of a synchronously pumped optical parametric oscillator in steay-state operation," *JOSA B*, vol. 7, p. 1385, 1990.

[18] D. C. Edelstein, E. S. Wachman, and C. L. Tang, "Broadly tunable high repetition rate femtosecond optical parametric oscillator," *Appl. Phys. Lett.*, vol. 54, p. 1728, 1989.

[19] S. D. Butterworth, S. Girard, and D. C. Hanna, "A simple technique to achieve active cavity-length stabilisation in a synchronously pumped optical parametric oscillator," *Optics Communs.*, vol. 123, p. 577, 1996.

[20] C. Fallnich, B. Ruffing, T. Herrmann, A. Nebel, R. Beigang, and R. Wallenstein, "Experimental investigation and numerical simulation of the influence of resonator-length detuning on the output power, pulse duration and spectral width of a cw mode-locked optical parametric oscillator," *Appl. Phys. B*, vol. 60, p. 427, 1995.

[21] J.-C. M. Diels, J. J. Fontaine, I. C. McMicheal, and F. Simoni, "Control and measurement of ultrashort pulse shapes (in amplitude and phase) with femtosecond accuracy," *Applied Optics*, vol. 24, p. 1270, 1985.

[22] J.-C. Diels and W. Rudolph, *Ultrashort laser pulse phenomena*: Academic Press, Inc., 1996.

[23] R. L. Fork, O. E. Martinez, and J. P. Gordon, "Negative dispersion using pairs of prisms," *Optics Letters*, vol. 9, p. 150, 1984.

[24] R. L. Fork, C. H. Brito, P. C. Becker, and C. V. Shank, "Compression of optical pulses to six femtoseconds by using cubic phase compensation," *Optics Letters*, vol. 12, p. 483, 1987.

[25] Z. Zhang and T. Yagi, "Observation of group delay dispersion as a function of the pulse width in a mode locked Ti:Sapphire laser," *Appl. Phys. Lett.*, vol. 63, p. 2993, 1993.

[26] J. D. Kafka, M. L. Watts, and J. W. Pieterse, "Synchronously pumped optical parametric oscillators with LBO," *JOSA B*, vol. 12, p. 2147, 1995.

4. The effects of cavity length detuning in the OPO

4.1 Introduction

In Chapter 3 it was pointed out that the OPO can oscillate on multiple, widely spaced wavelengths and that the idler beam profiles can be ring shaped (see Figure 3-15), especially when the cavity length is detuned from optimum. This chapter presents more detailed observations of these effects and endeavours to find and explain the dominant mechanisms that cause these effects. This multiple wavelength oscillation was not due to four colour operation in the LBO OPO. Four colour operation occurs due to the retracing behaviour of the phase matching in non-critically phase matched LBO; it is possible to generate four colours, two for signal and two for the idler, simultaneously (see Figure 3-3).

The overall behaviour is complex. The appearance of the ring shaped idler beams was not necessarily associated with oscillation on widely spaced, multiple wavelengths. They could occur when the signal pulse was oscillating on one wavelength or on multiple wavelengths. In some cases, the signal pulse would start oscillating on multiple wavelengths while the idler beam profile remained close to Gaussian-like over the entire cavity length detuning range. One effect is not necessary to observe the other.

To the author's knowledge such phenomena have not been reported previously in synchronously pumped picosecond or femtosecond OPOs. The closest effect was reported by Chen, et. al. [1]. They found that in their KTP OPO, that was synchronously pumped by a frequency doubled, picosecond (4.5 ps), mode-locked Nd:YLF laser, the spectra of the signal and idler pulses split from a single into a double peaked spectrum when the cavity alignment was adjusted slightly. The single peaked signal spectra were around 1 nm wide whilst the peaks in the double peaked signal spectra were separated by ~ 2.5 nm. They explained the double wavelength oscillation as being due to noncollinear phase matching in the KTP crystal. The difference in the phase matching angle for two wavelengths separated by 2.5 nm was only 5 mrad. The signal beam profile and pulse duration did not alter with the change in the signal spectra. No mention was made of the idler beam profile.

As was mentioned in Chapter 3, Section 3.2, and first identified by [2], cavity length detuning causes the frequency of the oscillating pulse to shift. This is because any change in the cavity length causes the oscillating pulse to arrive early or late compared to the pump pulse. The resonated pulse experiences higher gain if it can shift wavelength to permit group velocity to compensate this timing error. In reality the wavelength shift is limited by the spectral gain bandwidth of the parametric process. The increase in gain obtained by shifting to a new wavelength to obtain improved pump overlap is balanced by the gain reduction induced through creating a phase mismatch. For the LBO OPO the spectral gain bandwidth (see Figure 3-1) is very broad and the group velocity mismatch between the signal and pump pulses (see Figure 3-2) changes slowly. Hence the signal wavelength can be shifted quite a long way by cavity length detuning. Figure 4-1 shows the change in wavelength needed to compensate the timing error between the pump and signal pulses due to detuning the cavity length at a phase matched signal wavelength of 850 nm.
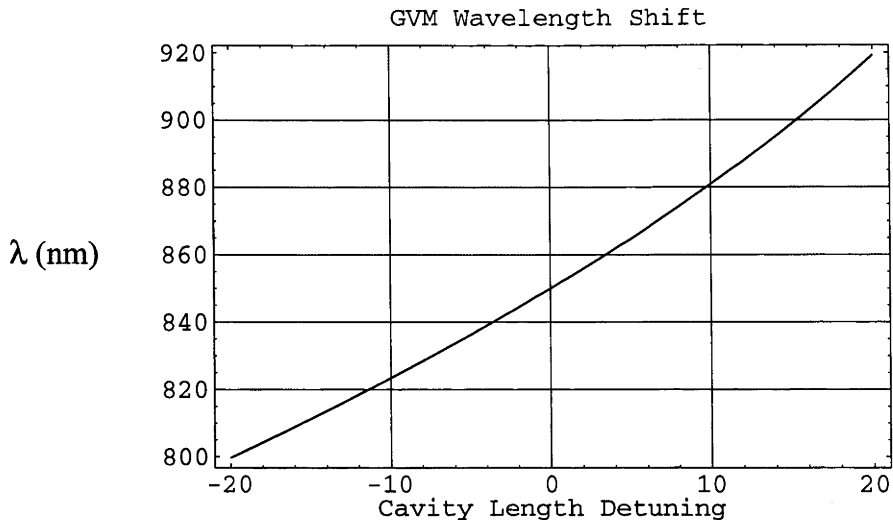
Figure 4-1 : The wavelength shift in the signal beam, in nm, to compensate for the timing error introduced by a cavity length detuning in microns. The phase matched signal wavelength is 850 nm.

4.2 The change in the idler beam profile

Some examples of the change in the idler beam profile as a function of cavity length detuning are shown in Figure 4-2. This displays "typical" behaviour of the idler beam profile, although it should be noted that the behaviour can also be much more complicated. The asymmetry in the ring shaped beams was caused by a slight misalignment of the OPO mirrors. The optimum, or zero point, of the cavity length detuning corresponded to maximum converted power (power converted from pump into signal and idler). At this zero point the idler beam profile was always Gaussian like. When the cavity length was increased the signal wavelength increased and the idler beam profile always remained Gaussian like until the OPO stopped oscillating. When the cavity length was reduced the signal wavelength decreased and the idler beam profile first remained Gaussian, then had a tendency to flatten and finally close to the edge of the oscillation range it expanded into a ring shaped beam profile.

This ring shaped idler beam profile appeared to be caused by non-collinear phase matching (Figure 4-3) in the LBO OPO. Non-collinear phase matching has previously been noted to result in ring shape beam profiles, though mainly for SHG [3-5]. Recently non-collinear phase matching has been used to create spectrally ultra-broad, ns pulses from a BBO OPO [6]. The idler and signal beam profiles were spatially dispersed in this OPO due to non-collinear phase matching.

Since the signal wavelength changed with cavity length detuning a phase mismatch, Δk, was introduced into the parametric process ($\Delta k = k_3 - k_2 - k_1 = 2\pi (n(\lambda_3)/\lambda_3 - n(\lambda_1)/\lambda_1 - n(\lambda_2)/\lambda_2$). If the cavity length was shortened it was possible for this mismatch to be compensated by non-collinear phase matching. This is because as the cavity length was decreased, the phase mismatch becomes negative, ie. the magnitude of the signal plus the idler momentum vector was greater than the pump momentum vector. The signal and idler beams can, therefore, experience higher gain by phase matching a few milliradians off the x-axis of the LBO
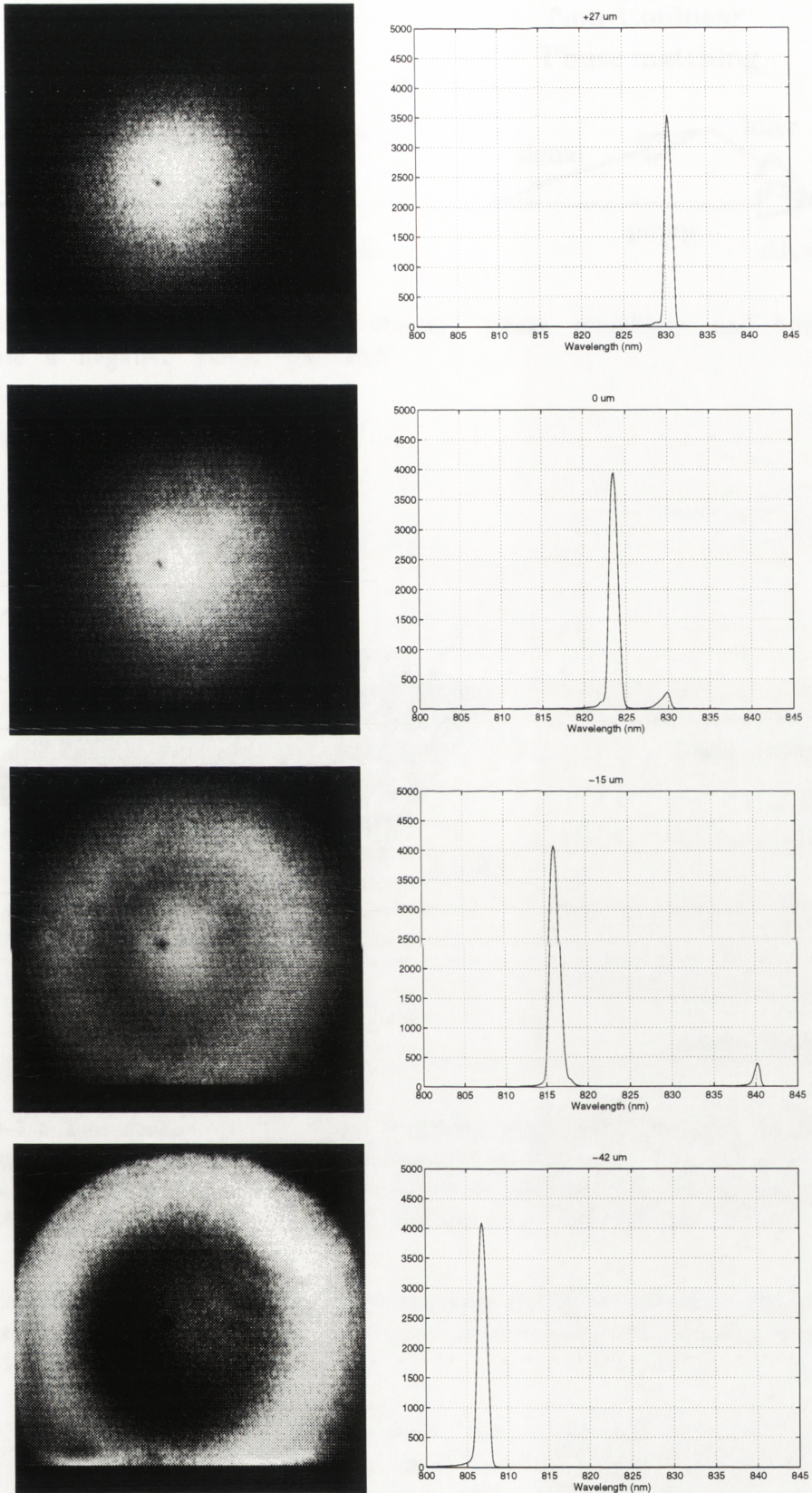
Figure 4-2 : An example of the change in the idler beam profile and signal wavelength with cavity length detuning.
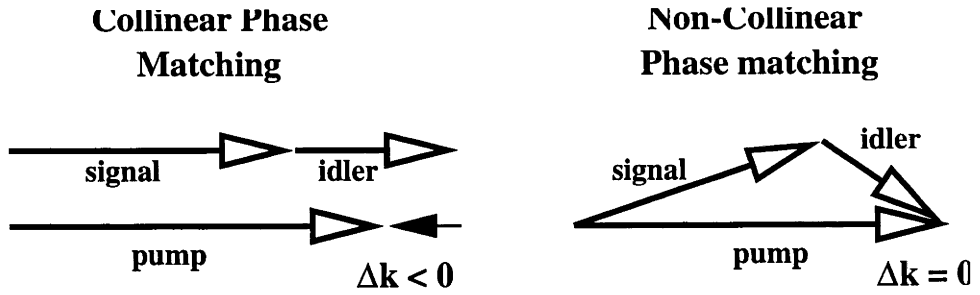
Figure 4-3 : The principle of non-collinear phase matching and how it can compensate a negative phase mismatch.
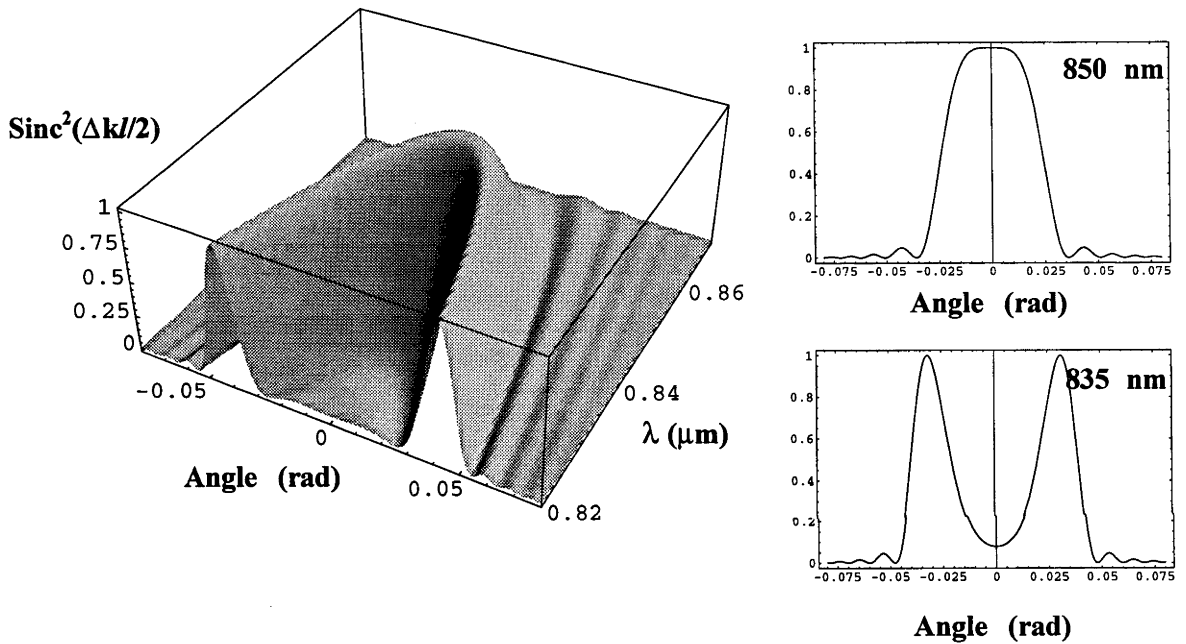
Figure 4-4 : The change in the phase matching angle with the shift in the signal wavelength from the phase matched wavelength of 850 nm. The 3D plot shows Sinc^2 ($\Delta k \, l/2$) with the angle from the x-axis in radians and the wavelength in μm. The 2D plots are cross sections at 850 nm (top) and 835 nm (bottom).

crystal. However, if the cavity length was increased the phase mismatch became positive and non-collinear phase matching could not compensate for the phase mismatch (see Figure 4-3).

Since the LBO crystal was non-critically phase matched the angular acceptance was very wide, ~ 47 mrad-cm$^{1/2}$. Terms up to the second order must be included to calculate the phase matching angle needed to compensate the phase mismatch. Using the analysis of [7], which can calculate the refractive index of a biaxial crystal for any arbitrary propagation direction and polarisation, the phase matching angle with wavelength and angle was calculated. To demonstrate that non-collinear phase matching occurred with decreasing cavity length, Figure 4-4 shows the phase matching factor Sinc^2 ($\Delta k \, l/2$) = Sin^2($\Delta k \, l/2$)/($\Delta k \, l/2$)^2 (l is the LBO crystal length) as a function of wavelength and angle. The efficiency of the parametric process was taken to be directly dependent on this Sinc^2 term. In this example the LBO crystal was at a temperature that was phase matched to produce a signal wavelength of 850 nm. As the cavity length was increased the signal wavelength increased,

introducing an increasing positive phase mismatch into the parametric process which reduced the OPO efficiency, ie. $Sinc^2 \rightarrow 0$. As the cavity length was shortened the signal wavelength decreased and the parametric process was no longer phase matched along the x-axis but at an increasing angle (for both θ and ϕ) from this axis. This would result in a ring shaped beam profile for both the signal and idler beams.

In the same way that the spectral gain bandwidth restricts the GVM induced wavelength shift, the OPO cavity and the spatial gain profile of the pump restricts the degree to which non-collinear phase matching can compensate for the phase mismatch introduced by the signal wavelength shift. Major points that restrict the non-collinear phase matching process are listed below.

- The OPO cavity has a Fresnel number [8] of at least 2.8. The resonator used in this work can support a signal beam expansion of only ~ 1.7 times above the TEM_{00} beam waist size before diffraction losses discriminate against further beam expansion. For a focussed TEM_{00} signal beam waist of ~ 15 μm in the LBO crystal, the beam divergence is ~ 18 mrads, hence the cavity can tolerate a beam divergence of ~ 30 mrads before diffraction losses become too great.

- Furthermore, if the beam divergence becomes too great the beam will not be periodically refocussed to the same position and size within the crystal. The cavity can support up to a ~ 2.5 change in the beam divergence while remaining stable (estimated from an ABCD calculation). Even then the beam will not be periodically refocussed to the same position and size.

- The picture is complicated further by the fact that the cavity acts as a Gaussian filter that shapes the signal beam's spatial profile during these multiple passes. This is why the signal beam profile always remains approximately Gaussian with cavity length detuning. The idler beam is not restricted directly by the cavity but indirectly through the gain experienced by the signal wave.

- Non-collinear phase matching will change the beam overlap between the signal and pump, reducing the gain. As the signal or the idler beam moves outside the pump volume it will experience decreasing parametric amplification. Once the noncollinear phase matching angle (in radians) from the x-axis exceeds the focal electric field beam waist radius of the signal the beam will expand to be greater than the pump beam within the pump confocal parameter length.

4.3 Multiple wavelength oscillation

This section presents results demonstrating the effects of cavity length detuning and pump power on the signal wavelength, focussing on the appearance of simultaneous oscillation on multiple signal wavelengths. Multiple wavelength oscillation is a novel effect that is dependent on many factors occurring simultaneously in the OPO.

The synchroresonance curves of the OPO, showing the average power of the signal pulses coupled from the cavity, and the spectra of the signal pulses were recorded for different pump powers and at different phase matching temperatures. The behaviour of the synchroresonance curves were sensitive to both pump power and whether the signal was oscillating at multiple wavelengths or not. The synchroresonance curves were recorded for the one arm OPO operating with the chopped cw pump beam. To obtain the data, the end mirror of the long arm of the OPO cavity was mounted on a Newport programmable motion translation stage with its axis carefully aligned so that it travelled parallel to the
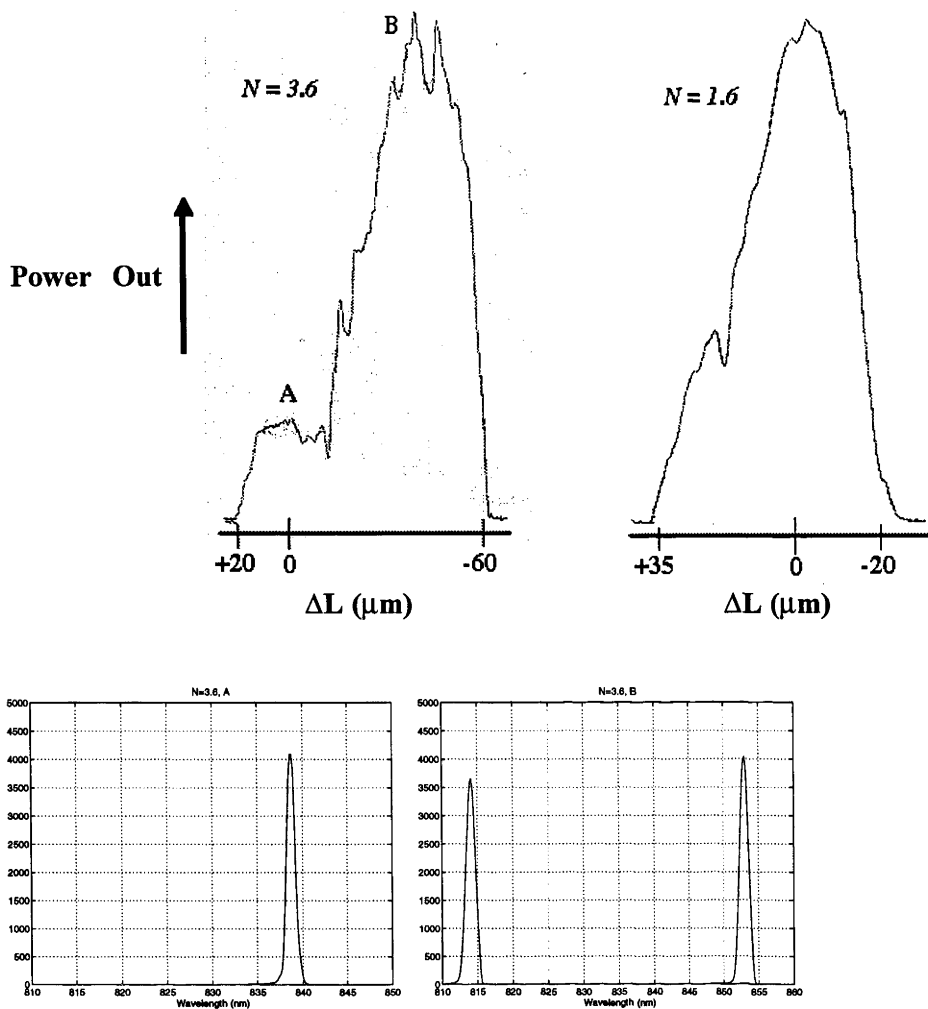
Figure 4-5 : Synchroresonance curves, signal output power versus cavity length, for the LBO OPO at 3.6 times above threshold and 1.6 times above threshold. The signal spectra corresponding to points A and B are also shown. The zero point in the synchroresonance curve is taken to be the cavity length at which maximum pump depletion occurs.

signal beam axis. The translation distance was quite small as the OPO typically oscillated over a distance of only ~ 70 μm. The signal power coupled out of the end mirror was less than 3 mW cw (175 W peak) and was monitored by a reverse-biased Si:PIN detector. The detected signal was sent through a Lock-In amplifier and recorded on a chart recorder. The spectrum of the signal beam was simultaneously recorded by the Lamda CCD spectrometer and stored on a PC. The spectrometer has a resolution of ~ 1 nm (Chapter 7).

Some examples of synchroresonance curves are show in Figures 4-5 to 4-7. In all the figures the zero point was taken to be the position where the pump depletion was maximised in the OPO, ie. where there was a minimum of cw depleted pump power. Please note that this is a different definition than the one used previously, where the zero point was taken to be the point near maximum converted power. Since the synchroresonance curves were measured quickly only the point where maximum pump depletion was noted. The previously used definition of the zero point would always occur near the peak of the synchroresonance curves in Figures 4-5 to 4-7.
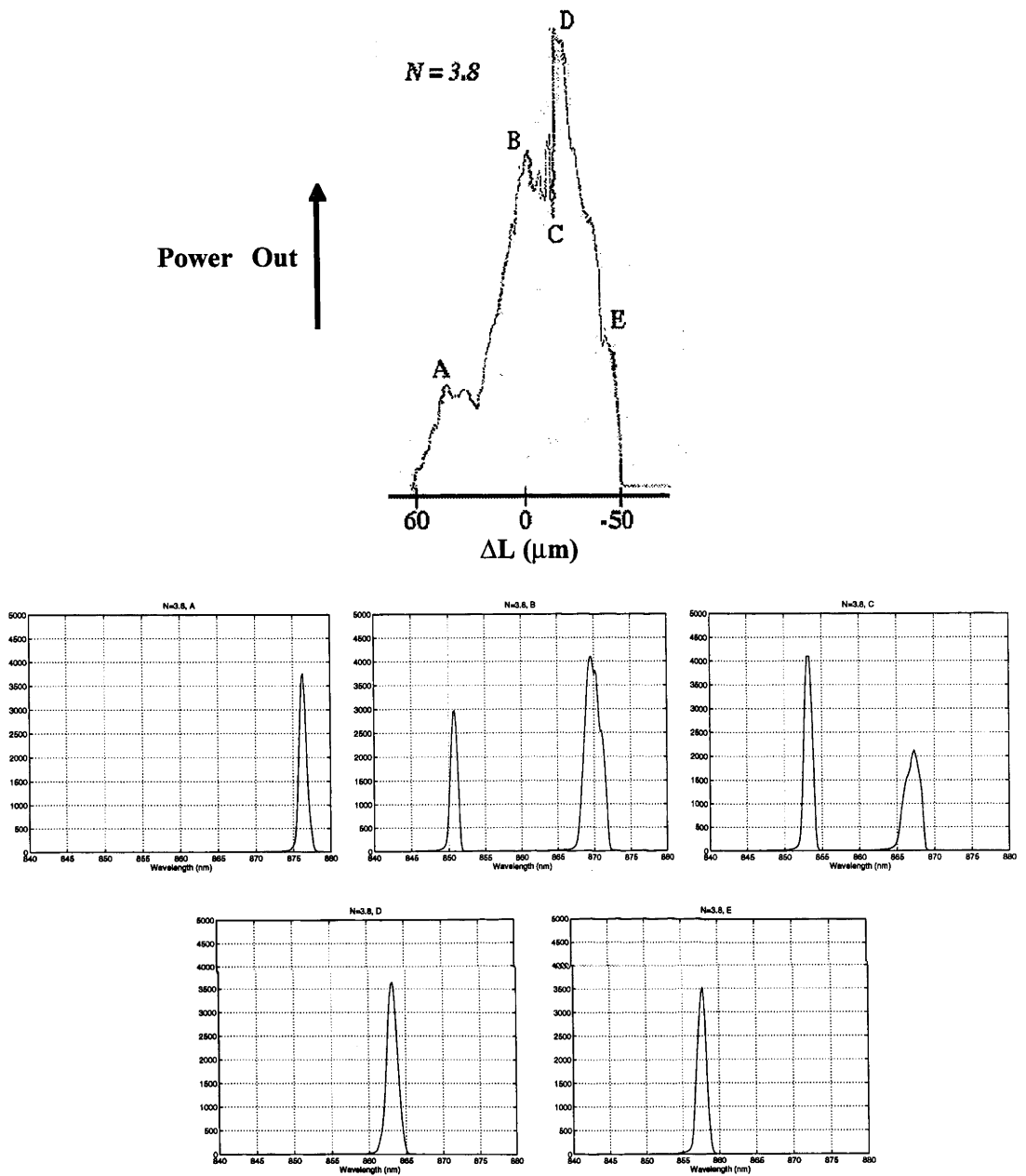
Figure 4-6 : A synchroresonance curve for the LBO OPO at 3.8 times above threshold. The signal spectra corresponding to points A to E are also shown. The zero point in the synchroresonance curve is taken to be the cavity length at which maximum pump depletion occurs.

Maximum pump depletion does not usually correspond to the maximum output power of the signal beam, ie. maximum converted power, when the OPO is driven at more than ~ 2.5 times above threshold. This can be understood by looking at Figure 4-8 which shows experimental measurements of the depleted pump power and the power converted into signal and idler waves as a function of the pump power at the focus of the LBO crystal. In a the figure maximum pump depletion would occur near ~ 2.5 times above threshold or 45 mW. As the incident pump power was increased, reconversion occurred creating more pump power. However, the power of the signal and idler pulses still increased. By choosing cavity length where there was maximum pump depletion the OPO was effectively operating at a point close to ~2.5 times above threshold where there would not be as much signal output power as from a cavity length which maximised the converted power.
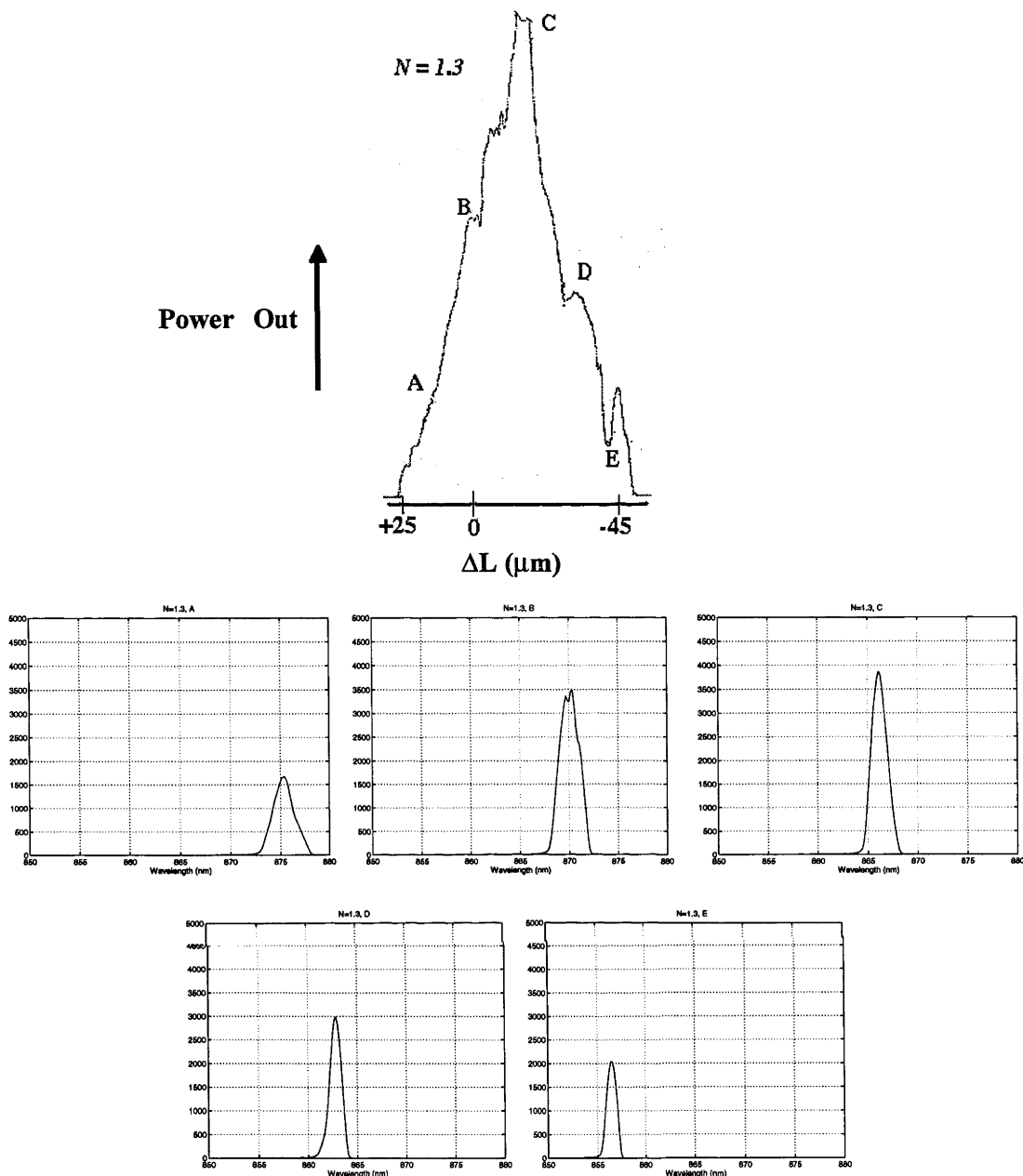
Figure 4-7 : A synchroresonance curve for the LBO OPO at the same phase matching temperature as the curve shown in Figure 4-6 but at 1.3 times above threshold. The signal spectra corresponding to points A to E are also shown. The zero point in the synchroresonance curve is taken to be the cavity length at which maximum pump depletion occurs.

In Figure 4-5, for the OPO operating well above (3.6x) threshold, maximum pump depletion occurred at a single signal wavelength of 839 nm. When the cavity length was increased oscillation quickly stopped but when the cavity length was decreased the single signal wavelength split into two with one wavelength slowly increasing and the other more rapidly decreasing until oscillation ceased. When the pump power was reduced (1.6x threshold) only one signal wavelength appeared and that decreased with decreasing cavity length.

In Figure 4-6 the OPO was tuned to a longer wavelength and operated well above threshold (3.8x). Maximum pump depletion occurred in conditions when two signal wavelengths

94
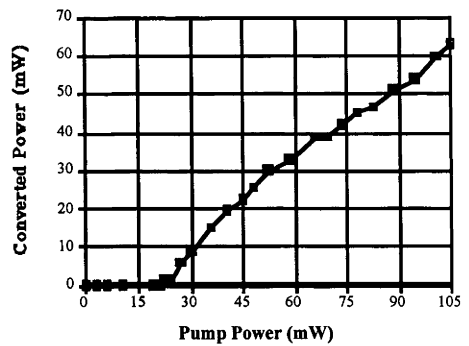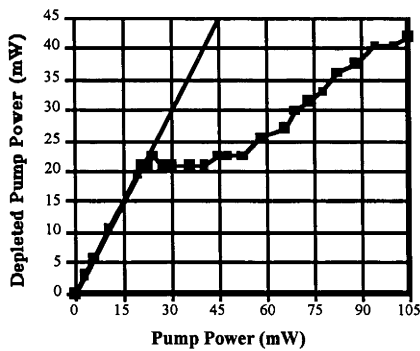
Figure 4-8 : The depleted pump power and the power converted into signal plus idler as a function of the chopped cw pump power at the focal point in the LBO crystal of the one-arm OPO.

existed simultaneously. Increasing the cavity length caused the lower wavelength to die away and the upper wavelength to increase until oscillation ceased. Decreasing the cavity length caused the two signal wavelengths to coalesce into a single wavelength at roughly the average wavelength of the two; the cavity length for maximum converted power. Then the single wavelength slowly decreased with decreasing resonator length until oscillation ceased.

For the same case but with lower pump power, Figure 4-7, the OPO always emitted a single signal wavelength which moves downwards in wavelength with decreasing cavity length.

The gain experienced at the edges of the oscillation range was quite low, equivalent to the gain near threshold and always resulted in the oscillation of a single wavelength.

These examples were chosen to display the typical signal wavelength behaviour of the LBO OPO with cavity length detuning and pump power, although in some instances even more complex behaviour was observed. However, the general behaviour can be summarised as follows. For pump powers that drove the OPO up to ~ 2.5 times above threshold the tuning behaviour was similar to that of previously reported synchronously pumped, ps LBO OPOs. Oscillation occurred at a single signal wavelength the value of which decreased with decreasing cavity length.

This tuning behaviour can be explained, as mentioned previously, by the wavelength shift induced GVM compensation of the timing error between the pump and signal. With the synchroresonance curve generally having a asymmetric triangular shape across the whole detuning range.

When the pump power was increased the behaviour of the LBO OPO changed markedly. The synchroresonance curve generally developed a double humped shape, with one peak being much smaller than the other. The smaller peak always lay on the positive detuning side of the curve and the larger one was always on the negative detuning side. The maximum pump depletion occurred at a cavity length usually located somewhere between these two peaks. Maximum converted power occurred at the cavity length near the highest peak. On the positive detuning side the signal spectra typically consisted of a single wavelength peak while on the negative detuning side the signal spectra can consist of multiple wavelengths. When the signal was oscillating at multiple wavelengths there were usually just two wavelengths present, but sometimes there were three or four, especially near the longer wavelength reflectivity edge of the OPO cavity. As would be expected the OPO operated over a longer cavity length range with increased pump power. It should be noted that ring shape idler beams were generally seen towards the edge of the negative detuning range and
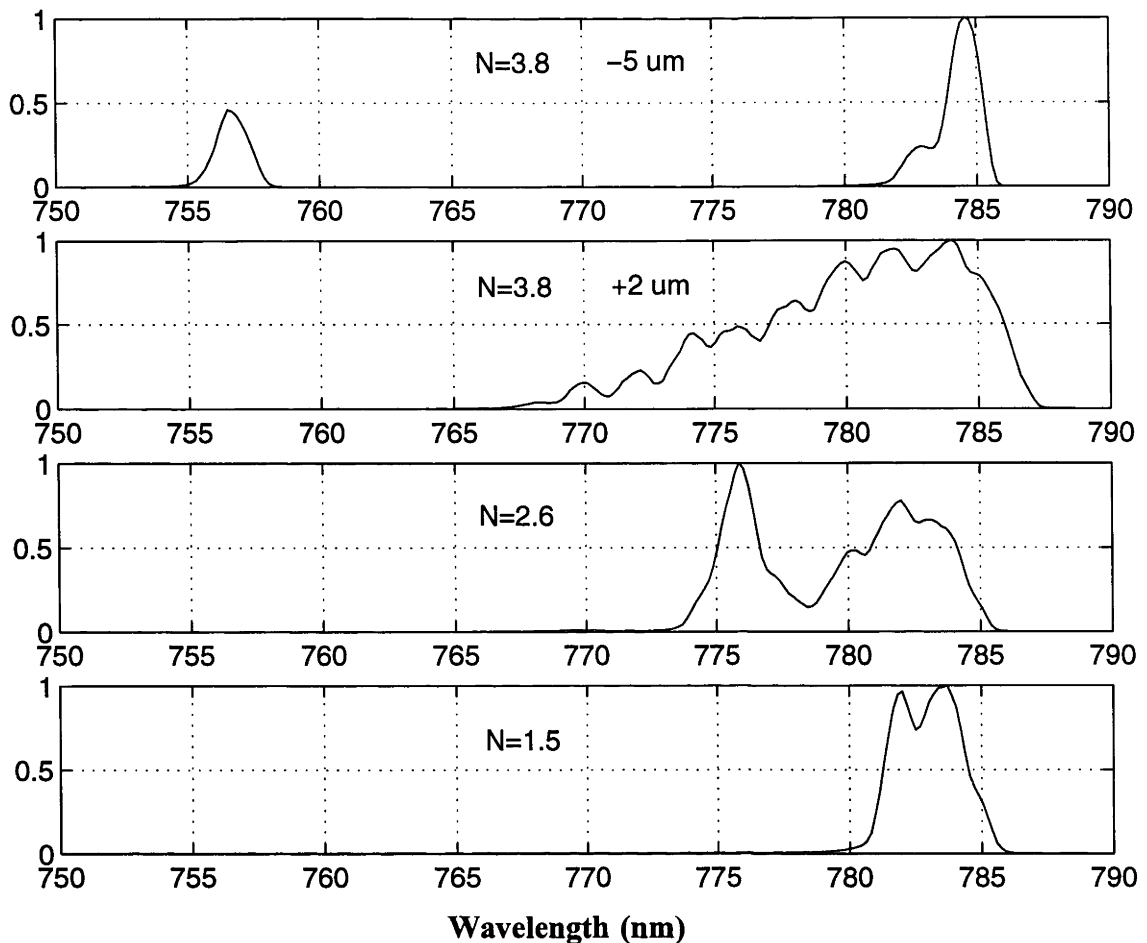
Figure 4-9 : An example of the change in the signal spectra with increasing pump power. The number of times above threshold is shown in each figure. The two top figures show spectra at a cavity length -5 μm and + 2 μm from the position where the bottom two spectra were measured.

can be associated with appearance of several oscillating wavelengths. However, as mentioned previously, the ring shaped idler beams do not always appear and it proved difficult to correlate the observed idler beam behaviour and the appearance of multiple signal wavelength. In some cases the idler beam remained Gaussian-like over the entire detuning range.

This complex behaviour does not appear to be explained by invoking any single straightforward process within the OPO in the way that non-collinear phase matching explained the ring shaped idler beams. It is known from the interferometric autocorrelations of the signal pulses presented in Chapter 3, that there was significant phase modulation due to both SPM and XPM on the pulses, as well as a contribution due to GVD in the cavity. These effects combined with parametric gain and GVM play a major role in the shaping the signal pulse in time and in frequency.

SPM symmetrically broadens the spectrum of the signal pulse whilst XPM, which can be stronger than SPM, can make the spectrum asymmetric with the presence of GVM [9]. Since phase modulation of the signal pulse was an accumulative process in the LBO OPO (ie. it occurs over several round trips), the spectral shaping process due to SPM and XPM can not be simply be thought of as due to an initially un-phase modulated, high intensity pulse propagating through a known length of material equivalent to the total number of passes through the LBO crystal. A pulse with an initial phase modulation will, for example,

96

produce a very different SPM spectrum than a pulse with no initial phase modulation. Parametric gain and GVM complicate the pulse shaping process since all the waves are coupled through these effects. It is postulated that the multiple frequency oscillation originates from an interplay between these various effects in conditions where large phase modulation occurs in the cavity, ie. at high pump powers.

Figure 4-9 shows a typical example of the evolution of the signal spectrum with increasing pump power and for small cavity length variations. In this example the mirrors of the one arm, chopped cw OPO were changed for ones that reflected from 700 to 900 nm. The end mirror in the long arm had a transmission of less than 1 % to achieve the highest possible signal power. At low pump power (1.5x threshold) the OPO only oscillated over a range of 12 μm. For these conditions, the maximum pump depletion occurred at the peak of the asymmetric triangular synchroresonance curve. The bottom plot in
Figure 4-9 shows the signal spectra at this zero point. It consists of a double-peaked spectrum at 783 nm. As the peak power was increased to ~ 2.6 times above threshold the signal spectrum broadened and these two peaks separated until they lay at 776 nm and 783 nm respectively. As the pump power was increased further the signal spectrum became unstable, sometimes it was a single wavelength and then it quickly changed to two, widely spaced, separate wavelengths and then back again into a single wavelength. Examples of the two extremes the signal oscillated between are shown in the top two figures of
Figure 4-9. The double wavelength signal spectrum was stabilised by applying a -5 μm change to the cavity length, whilst the single, broad signal spectrum occurred for a +2 μm adjustment from the zero point position. This fine cavity length adjustment was achieved with a piezoelectric transducer mounted on the translation stage of the end mirror. The single, broad signal spectrum at + 2 μm is quite characteristic of a strongly phase modulated pulse due to XPM.

It is evident from measurements that as the pump power increased the phase modulation in the OPO increased proportionally. The parametric gain process appears to preferentially amplify the peaks in the signal spectra to produce widely spaced, separate frequencies. The OPO must be driven with enough pump power so that there is sufficient phase modulation in the signal pulse before this spectral splitting occurs. The OPO only oscillated on multiple frequencies for pump powers above 2.5 to 3 times above threshold (~ 2.5 kW to ~ 3 kW peak power). LBO in particular, as opposed to a crystal like KTP, has a broad spectral gain bandwidth that would allow oscillation on widely separated multiple frequencies.

A question that arises is that when there was multiple frequency oscillation in the OPO what was temporal profile of the generated signal and idler pulses?

Previously, slow scan SHG intensity autocorrelation and SHG FROG measurements were taken of the idler pulse from the one arm LBO OPO pumped by the chopped cw beam. The measurements were taken at maximum pump power, which corresponded to operation ~ 5 times above threshold. The slow scan SHG LBO intensity autocorrelator is described in Chapter 7. The SHG FROG traces of the idler pulse involved measuring its spectrum while scanning the autocorrelator in time. The SH spectrum was measured with the Lamda CCD spectrometer since it can record up to 100 consecutive spectra. However, the Lamda spectrometer only has a 1 nm resolution so the FROG trace does not contain much fine spectral information about the pulse. This was not seen as a great disadvantage as temporal information about the pulse was desired. The intensity autocorrelation and FROG traces were taken simultaneously. The SHG intensity autocorrelations were taken of the idler pulse instead of the signal pulse because the spectral gain bandwidth for the LBO autocorrelator crystal is very large (> 100 nm) near 1.3 μm. This allowed autocorrelation measurements of widely separate frequencies. The spectral gain bandwidth for the signal wavelength region was much narrower, around 15 nm at 850 nm for a 2 mm thick LBO crystal (Chapter 7),
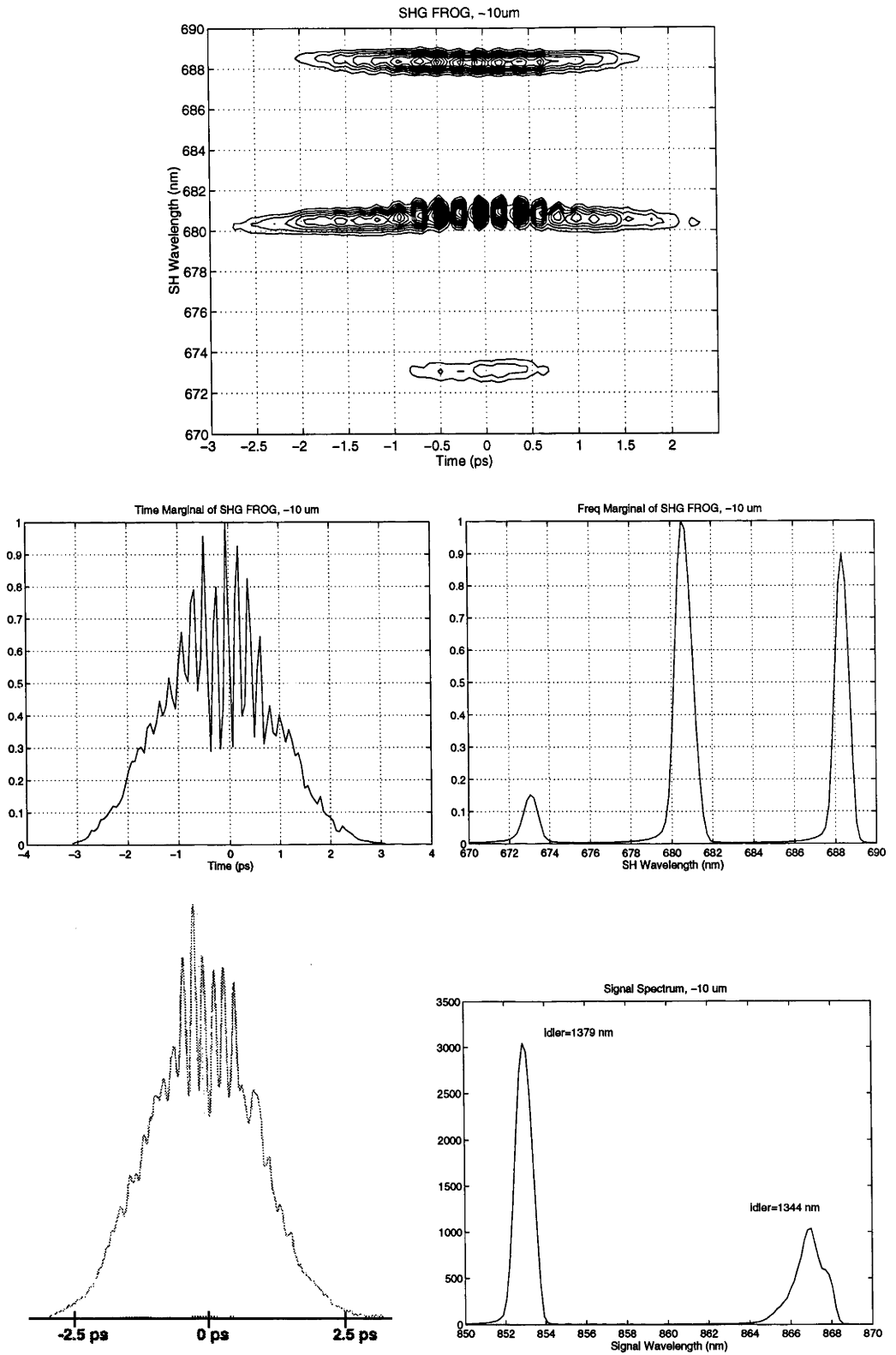
Figure 4-10 : The SHG FROG trace, the time and frequency marginals from the SHG FROG trace and the SHG intensity autocorrelation of the idler pulse emitted from the one arm LBO OPO at a cavity length detuning of -10 μm. The corresponding signal spectrum is also shown. The vertical axis of the signal spectrum is arbitary.
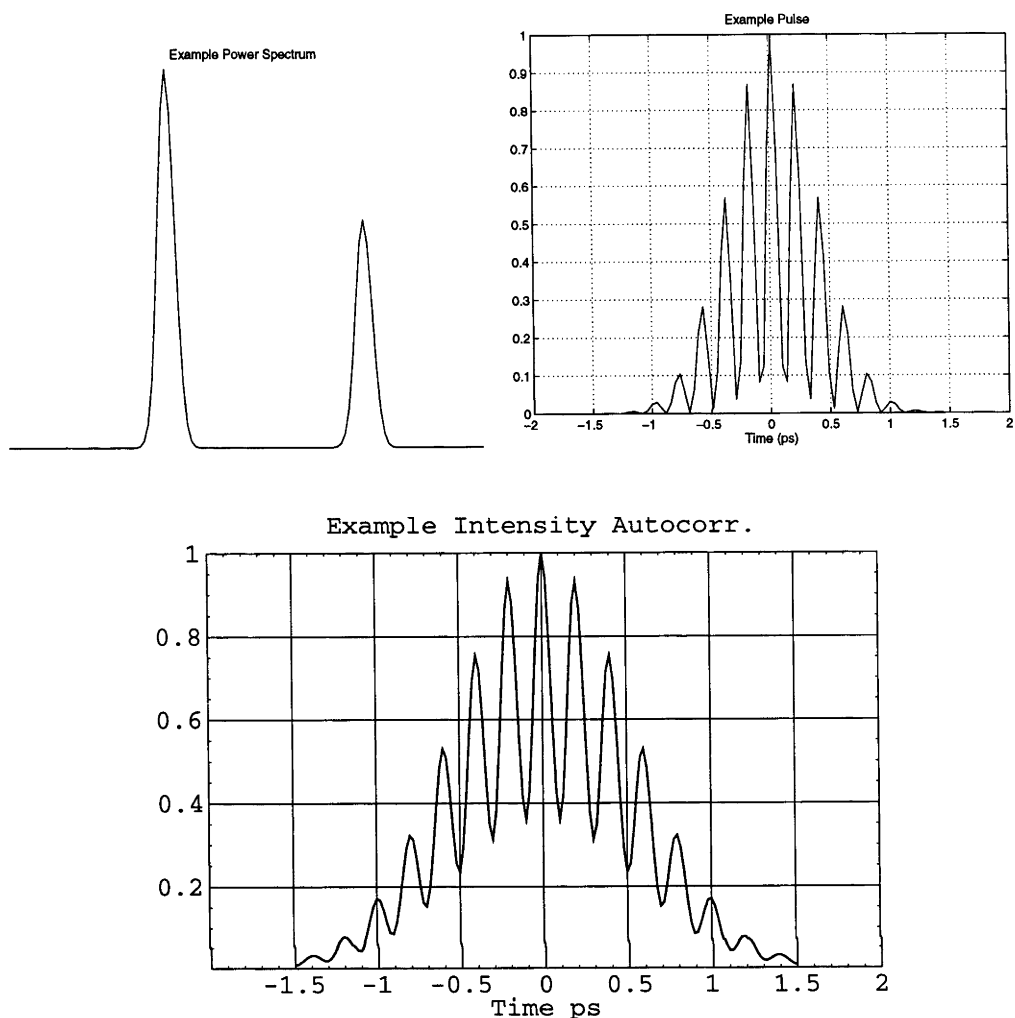
Figure 4-11 : A theoretical example of the intensity temporal profile of a pulse with the power spectrum shown in the top left hand figure and the expected SHG intensity autocorrelation of this pulse. Refer to the text for more details.

and this would have prevented meaningful measurements when the signal spectrum consisted of multiple, widely spaced wavelengths.

The SHG FROG of a idler pulse is shown in Figure 4-10. In this particular case the cavity length was detuned - 10 μm from the zero point. In this case, the zero point was taken to be the cavity length at which maximum pump depletion occurred at low pump power (N ≈ 1). At maximum pump power (N ≈ 4.5) the OPO oscillated over a range from + 40 μm to - 50 μm. For this measurement the signal was oscillating at 853 nm and at 867 nm, which corresponded to idler wavelengths of 1379 nm and 1344 nm respectively. The SHG FROG trace shows three wavelengths. A primary spectral peak at 681 nm, a less intense sideband at 689 nm and another very low power sideband at 673 nm. The central spectrum was strongly amplitude modulated in time with a modulation period around 230 fs. Both sidebands were modulated to a lesser degree. The central spectrum was caused by sum frequency generation of the two idler wavelengths at 1379 nm and 1344 nm : ie, 1379 + 1344 → 681 nm . The two sidebands were caused by frequency mixing between the sum frequency generation and second harmonic generation of the original idler wavelengths. The separation between the sidebands and the central wavelength should be equal to one quarter

the separation between the idler wavelengths, ie. 8.75 nm. The sidebands were actually at $\pm$ 8 nm from the central wavelength at 681 nm, quite close to expectations. One sideband was much more intense than the other due to the difference in power between the original two idler wavelengths. The amplitude modulation was due to interference between the two idler wavelengths and the period of modulation should be equal to the beat frequency : $\Delta\lambda = 35$ nm $\Rightarrow \Delta v = 5.66$ x 10^{12} Hz $\Rightarrow \Delta t_{mod} = 180$ fs. Close to the measured value of ~ 230 fs.

The time marginal from the SHG FROG trace, which is the integration of the FROG trace in the wavelength direction, is shown in Figure 4-10 and is equivalent to the SHG intensity autocorrelation (also shown in Figure 4-10). Both show that the idler pulse was Gaussian-like with a strong amplitude modulation. The depth of the modulation is not as strong in the intensity autocorrelation because of the Lock-In detection used. The frequency marginal, the integration of the FROG trace over all time, is also shown in Figure 4-10. It shows the relative amplitudes of the SH spectra. Since the intensity autocorrelation shape was complex it was not easy to deconvolve the actual intensity temporal profile of the idler pulse. To find out the likely shape of the temporal pulse an example, transform-limited, pulse was constructed from a double wavelength spectrum. The spectrum, the resulting temporal profile and the SHG intensity autocorrelation of this pulse are shown in Figure 4-11. Qualitatively the sample intensity autocorrelation and the measured intensity autocorrelations of the idler pulse agree quite closely. As already mentioned, the period of the amplitude modulation being controlled by the relative wavelength spacing of the two idler wavelengths. It was expected the idler pulse and the oscillating signal pulse had temporal pulse shapes similar to the example pulse shape shown in Figure 4-11.

For the two signal wavelengths shown in Figure 4-10 the difference in time due to GVM was only 30 fs (~ 1.5 % of the pulse duration). This strongly modulated pulse can be thought of as two, almost synchronised, interfering pulses, each one with a single, distinct wavelength. It was also expected that the phase of the signal and idler pulses were strongly modulated in time.

4.4 Summary and conclusions

This chapter presented novel experimental results related to the effect of detuning the cavity length of the LBO OPO on the idler beam profile and the resonated signal spectrum. It was found that sometimes the idler beam profiles changed from a Gaussian like shape to become ring shaped when the cavity length was shortened. It was also found that the OPO frequently oscillated on two or more, separate signal wavelengths when the OPO was driven more that 2.5 to 3 times above threshold, especially when the cavity length was simultaneously detuned. No correlation between the two effects was evident.

The ring shaped idler beam profiles were due to non-collinear phase matching in the LBO crystal. When the cavity length was adjusted the signal wavelength shifted to one with a group velocity that partially compensated for the induced timing error between the pump and the signal. Since the LBO crystal was phase matched to produce only one signal and idler wavelength, a shift in the signal wavelength introduced a phase mismatch between the three waves reducing the parametric gain. For negative cavity length detuning this phase mismatch can be compensated by non-collinear phase matching a few milliradians off the beam axis. This process was limited by the constraints of the cavity and the pump gain volume in the LBO crystal. Both constraints did allow non-collinear phase matching up to $\sim$ 1.5° (~ 30 mrad) off axis, more than enough to see ring shaped beam profiles. The signal beam profile did not display any change because it was directly constrained by the cavity.

The multiple frequency oscillation was due a number of dynamic effects that occurred simultaneously within the LBO OPO. Normally, the multiple signal wavelengths consisted

of two, separate wavelengths but there were sometimes three or four wavelengths. The multiple frequency oscillation only occurred when the OPO was driven more than 2.5 to 3 times above threshold. Since it was evident that as the pump power increased the degree of phase modulation increased as well the multiple frequency oscillation was tied to the level of phase modulation in the cavity. The parametric process appeared to preferentially amplify the peaks of the phase modulated signal spectrum. Above some pump power the single wavelength split into two or more separate wavelengths. The temporal pulse profile of the signal and idler pulses, when the spectra of each pulse consists of two separate wavelengths, was a very strongly amplitude modulated, Gaussian-like pulse where the amplitude modulation period was equal to the 1/ beat frequency between the two separate wavelengths. This strongly modulated Gaussian-like pulse shape can be thought of as being caused by two coherent pulses, of separate, single wavelengths that were coincident in time and interfering with each other.

This hypothesis on multiple frequency oscillation was based on an interpretation of the experimental results. To accurately model the LBO OPO, to try and reproduce these experimental results theoretically, would require a simulation that modelled the amplitude and phase of all three waves, in time and frequency, including parametric gain, GVM, GVD, SPM, XPM, the effect of cavity length detuning and including the spatial beam profiles of all three waves (since it has been shown that non-collinear phase matching can occur in this OPO). This would be difficult to perform (see [10] for an example) and was left for future work.

4.5 References

[1]   L. P. Chen, Y. Wong, and J. M. Liu, "Singly resonant optical parametric oscillator synchronously pumped by frequency-doubled additive-pulse mode-locked Nd:YLF laser pulses," *JOSA B*, vol. 12, p. 2192, 1995.

[2]   D. C. Edelstein, E. S. Wachman, and C. L. Tang, "Broadly tunable high repetition rate femtosecond optical parametric oscillator," *Appl. Phys. Lett.*, vol. 54, p. 1728, 1989.

[3]   R. Trebino, "Second-harmonic-generation rings and refractive-index measurement in uniaxial crystals," *Appl. Optics*, vol. 20, p. 2090, 1981.

[4]   J. A. Giordmaine, "Mixing of light beams in crystals," *Phys. Rev. Letts.*, vol. 8, p. 19, 1962.

[5]   S. X. Dou, D. Josse, and J. Zyss, "Noncritical properties of noncollinear phase-matched second-harmonic and sum-frequency generation in 3-methyl-4-nitropyridine-1-oxide," *JOSA B*, vol. 8, p. 1732, 1991.

[6]   J. Wang, M. H. Dunn, and C. F. Rae, "Polychromatic optical parametric generation by simultaneous phase matching over a large spectral bandwidth," *Optics Letters*, vol. 22, p. 763, 1997.

[7]   M. A. Dreger and J. H. Erkkila, "Improved method for calculating phase-matching criteria in biaxial nonlinear materials," *Optics Letters*, vol. 17, p. 787, 1992.

[8]   A. Siegman, *Lasers*. Mill Valley: University Science Books, 1986.

[9]   G. P. Agrawal, *Nonlinear fiber optics*: Academic press, Inc., 1989.

[10]   C. Fallnich, B. Ruffing, T. Herrmann, A. Nebel, R. Beigang, and R. Wallenstein, "Experimental investigation and numerical simulation of the influence of resonator-length detuning on the output power, pulse duration and spectral width of a cw mode-locked optical parametric oscillator," *Appl. Phys. B*, vol. 60, p. 427, 1995.

5. The pump laser system for the OPA

5.1 Introduction

The OPA system requires a low power seed pulse and an amplifying pump pulse. The seed pulses were provided by the LBO OPO and the pump pulses by amplification of single pulses from the Antares laser to high energy using a pair of Nd:YLF amplifiers. The amplifier output was then frequency doubled using a novel second harmonic generator in a geometry known as group velocity mismatched second harmonic generation (GVMSHG). From the simulations of the OPA it was determined that the 527 nm pump pulses should have an energy of at least 1.25 mJ and a pulse duration of 500 fs or less, ie. a peak power of at least 2.5 GW. The work to create pump pulses which fulfil these requirements will be outlined in this chapter. This includes a description of the experimental apparatus; a description of GVMSHG and theoretical simulation of the expected SHG efficiency; and measurements of performance of the overall system. As will become evident, it proved difficult to obtain performance close to the predicted level, and an extensive study was undertaken to track down the source of this deficiency.

The Nd:YLF amplifier chain was developed by Prof. Barry Luther-Davies and Dr. Yanjie Wang as part of earlier research. This amplifier chain consisted of a Nd:YLF regenerative amplifier and a Nd:YLF single-pass amplifier. The input to the amplifier was a single pulse from the Coherent Nd:YLF Antares laser, which also provides the pulses for the OPO pump system. The use of Antares seed pulses meant that it was straightforward to synchronise the OPO output pulses with the OPA pump pulse. The amplifier system was developed from a chirped pulse amplification (CPA) system using Nd:glass which had been developed previously [1] to test the GVMSHGconcept. The use of Nd:YLF was intended to extend GVMSHG to a high repetition rate laser.

Originally this GVMSHGsystem was designed to be used with 1054 nm pulses ~ 1.5 ps in duration. The ~ 6 ps pulse from the Nd:YLF amplifier chain were to be compressed using a grating pulse compressor after they had been passed through a multipass nonlinear optical delay line, where the pulse undergoes SPM to develop a linear frequency chirp [16]. Unfortunately this system did not prove stable enough to be used routinely. New simulations were therefore completed as part of this thesis to determine the performance of this doubling system using the longer pulses obtained straight from the amplifier chain. These new simulations showed that even for a predelay less than the pulse duration and a crystal length less than optimum significant advantages can still be obtained from the GVMSHG process over the case where there is no predelay.

GVMSHG is a particularly effective process for the creation of ultra-short frequency doubled pulses from a Nd laser system [2]. It not only generates the second harmonic of the 1054 nm pulse but compresses the SH pulse relative to the pump pulse by making use of the group velocity mismatch which exists between the e and o rays at the fundamental wavelength and the e-ray second harmonic (ie. for a type II interaction). The frequency doubling crystal was Potassium Dihydrogen Phosphate (KDP) [3]. GVMSHG in KDP is possible because the group velocity of the e-ray second harmonic is almost equal to the average group velocity of the o and e-ray fundamentals. As a result, if the slowest (o-ray) fundamental pulse enters the KDP doubler before the e-ray fundamental then during propagation the e-ray fundamental overtakes the o-ray pulse. Maximum second harmonic generation always occurs at a point mid-way between these two pulses. This point moves through the crystal at a velocity equal to the mean of the group velocities of the o- and e-ray fundamentals: a velocity that is nearly the same velocity as the generated SH pulse. As a result, the second harmonic energy only grows in a region whose duration is much shorter than the pump pulses. Energy flow to the second harmonic is maintained in the face of pump depletion due

to inflow of undepleted fundamental energy arising from the relative velocity between the pumps and the second harmonic. During propagation the fast e-ray fundamental actually overtakes the slow o-ray fundamental and consequently all time points in both fundamental pulses interact with a single time point in the second harmonic. Thus the energy transfer to the short second harmonic can be very efficient. In fact GVMSHG is more complex than described above since reconversion from second harmonic to pump radiation also occurs enhancing the pulse compression process. This will be evident from the simulations presented later in this chapter.

GVMSHG works best when the difference in transit time through the crystal for the o and e-ray fundamentals approximately equals the pulse duration. For ps duration pulses this means that the crystal thicknesses are quite large: typically 3-5 cm. The angular acceptance of KDP then places a limitation on the beam diameter that can be used with these long doubling crystals. Since the Nd:YLF amplifier system produces a longer pulse duration and lower pulse energy that the Nd:glass system on which the GVMSHG process was developed, the angular acceptance of KDP limits the maximum achievable fundamental intensity and, therefore, the overall performance. To minimise this problem it was planned to use a pair of KDP crystals, rather than a single crystal. They were orientated so that their crystalline c-axes were not parallel but orientated as mirror images: ie. in the so-called alternating-Z configuration. In this configuration any angular dephasing of the SHG process caused by the beam divergence in the first crystal is compensated for by the second crystal. For a total crystal length of L the effective angular acceptance angle is that of a crystal of length L/2.

The resulting experimental parameters were significantly different from those used in previous work using the Nd:glass system and hence it was necessary to perform a range of numerical simulations of the GVMSHG process to obtain an optimum design.

A similar GVMSHG system was constructed by Umbrasas, et. al. , [4] using a variable predelay and a 4 cm long KDP crystal. Using a Nd:YAG based amplifier system the fundamental pulse had a pulse duration of 12 ps and a maximum energy of 20 mJ. Using predelays roughly equal to the pulse duration, a ratio between the fundamental o and e rays intensities of $I_o/I_e = 1.3$ and a total fundamental intensity of 4.2 GW/cm^2 they were able to compress the generated SH pulse down to 360 fs. The compressed pulse shape consisted of a narrow central peak with large sidelobes. Their system will be discussed in further detail in Section 5.4.1.

5.2 Theory of group velocity mismatched SHG

Originally the theory and experiments done with GVMSHG concentrated on pulses between 1 and 2.5 ps in duration and the use of a single KDP frequency doubling crystal. The pulse compression mechanism depends on having sufficient fundamental intensity in the crystal so that pump depletion and reconversion of the fundamental occurs, sufficient group velocity mismatch and short enough pulse durations that the e and o rays can pass through each other while propagating through the crystal. When the e-ray is delayed with respect to the o-ray at the crystal input, by an amount approximately equal to the fundamental pulse duration (Δt_ω) , the SH is generated in the first part of the KDP crystal where the e and o rays overlap. As the e-ray catches up to the o-ray the SH grows until it reaches a similar magnitude to the fundamental waves and maximum pump depletion occurs. In the later part of the crystal the e-ray overtakes the o-ray and the two fundamental pulses separate. As a consequence, the leading edge of the SH pulse overlaps with an intense e-ray and weak o-ray. Reconversion from the SH back into an o-ray fundamental then occurs, removing energy from the front of the second harmonic pulse. The trailing edge of the SH, overlaps with an intense o-ray and weak e-ray and again reconversion occurs to create an e-ray fundamental wave. These combined processes result in removal of energy preferentially from the leading and trailing edges of the SH pulse, leaving only a narrow, central peak.

With a correct choice of predelay between e and o-pulses; crystal length; and fundamental intensity; the SH pulse duration can be narrowed by an order of magnitude below the input pulse durations ~ 2.5 ps whilst the overall second harmonic energy conversion efficiency remains at high levels (35-45%). From the previous simulations and experiments it is known that to achieve maximum pulse compression for short pulses of between 1 to ~ 2.5 ps the optimum KDP crystal length is around 25 mm, the optimum predelay of the e-ray is around ~ 2 ps, $I_o/I_e = 1$ and fundamental intensity is around 6 GW/cm^2.

At lower intensities than this optimum the introduction of the predelay dramatically increases the energy conversion from the fundamental into SH compared to the case where there is no predelay [5]. Without predelay the e and o rays will separate after propagating through ~ 1 cm of KDP for pulses of ~ 2 ps or less. This limits the energy conversion to a maximum of around 40 %. For type II (e + o ↔ e) SHG of 1 μm radiation in KDP the group velocity mismatch between the fundamental o-ray and the SH, δt_{o2} , is 0.55 ps/cm and between the e-ray and the SH, δt_{e2}, is -0.77 ps/cm at a fundamental wavelength of 1054 nm. Thus a predelay of approximately Δt_ω can approximately double the interaction length, improving the maximum energy conversion to around 80 % for pulses ~ 1 ps in duration. At intensities higher than the optimum value, greater reconversion and stronger SH pulse compression occurs in the presence of the predelay and additionally substructure develops on the pulse. For most applications this is quite undesirable.

The experiments conducted previously on GVMSHG closely matched theoretical simulations. Since the YLF laser used in these experiments provided quite different operating parameters compared with this earlier work, additional numerical studies were warranted to define the best operating point for GVMSHG when using longer 5 - 8 ps duration pulses.

These simulations modelled the temporal interaction of all three waves as they propagated through the SHG crystal. They included the effects of gain,; pump depletion; reconversion; phase mismatch ($\Delta k \neq 0$); group velocity mismatch; and absorption. The simulations did not include the phase of the interacting waves only their amplitude. They therefore neglected higher-order effects such as GVD, SPM and cross-phase modulation (XPM). The simulations assumed that the fundamental pulse was transform-limited and there was no GVD or SPM/XPM in the SHG crystal. Assuming that the electric fields of the interacting waves are monochromatic, infinite plane waves the electric field, ξ, for each wave is

$$\xi_i(z,\tau) = \tfrac{1}{2}\left[E_i(z,\tau)\exp\left(i(\omega_i\tau - k_i z)\right)+c.c.\right]$$

In the slowly varying envelope approximation, the equations that describes the SHG process including the second-order nonlinearity, phase mismatch, GVM and absorption are

$$\frac{\partial E_o}{\partial z} = iK_o E_e^* E_2 \exp(i\Delta kz) - \delta t_{o2}\frac{\partial E_o}{\partial \tau} - \frac{1}{2}\alpha_o E_o$$

$$\frac{\partial E_e}{\partial z} = iK_e E_o^* E_2 \exp(i\Delta kz) - \delta t_{e2}\frac{\partial E_e}{\partial \tau} - \frac{1}{2}\alpha_e E_e$$

$$\frac{\partial E_2}{\partial z} = iK_2 E_o E_e \exp(-i\Delta kz) - \frac{1}{2}\alpha_2 E_2$$

Eqn 5-1

where z is the propagation distance through the crystal and $\tau = t - z/v_{g2}$ is the time frame relative to the second harmonic pulse propagating through the crystal. $K_j = \dfrac{2\pi d_{eff}}{n_j\lambda_j}$ is the nonlinear coupling coefficient; where the j subscript refers to the o-ray (o), e-ray (e)

and the SH (2) waves; n is the refractive index and d_{eff} is the effective nonlinear coefficient. α is the absorption coefficient, δt_{ij} is the group velocity mismatch between the waves and $\Delta k = k_2 - k_o - k_e$ is the phase mismatch between the waves. The first term on the RHS describes the interaction of each wave through the second-order nonlinearity of the crystal, ie. SHG and parametric amplification. The growth of each wave depends on the magnitude and phase of the other two waves. The effect of a small phase mismatch is incorporated as a loss in the exponential expression. The effect of group velocity is included in the second terms. Absorption is included as the last term.

Assuming that there is perfect phasematching, ie. $\Delta k = 0$, then Eqn 5-1 becomes

$$\frac{\partial E_o}{\partial z} = K_o E_e E_2 - \delta t_{o2} \frac{\partial E_o}{\partial \tau} - \frac{1}{2}\alpha_o E_o$$

$$\frac{\partial E_e}{\partial z} = K_e E_o E_2 - \delta t_{e2} \frac{\partial E_e}{\partial \tau} - \frac{1}{2}\alpha_e E_e$$

$$\frac{\partial E_2}{\partial z} = -K_2 E_o E_e - \frac{1}{2}\alpha_2 E_2$$

Eqn 5-2

The above equations are readily simulated numerically.

If there is a phase mismatch, ie. $\Delta k \neq 0$ then Eqn 5-1 can be numerically simulated by expanding the equations into real and imaginary parts to form six coupled equations.

The parameters used in the simulation are shown in Table 5-1.

The numerical simulation was carried out with a Fortran program that calls an IMSL partial differential equation solving library routine named DMOLCH. DMOLCH can numerically solve the equations using the characteristic method of lines, representing the solutions as cubic Hermite polynomials. The IMSL DMOLCH routine is a refinement on the original PDECOL routine of Madsen and Sincovec [6].

Table 5-1 : The parameters used to simulate type II, GVMSHG in KDP at a fundamental wavelength of 1054 nm. Data derived from [7] and [8]

Phase matching angle (degrees)	$\theta_m = 59.2$
Nonlinear coefficient (pm/V)	$d_{36} = 0.38$
Effective nonlinear coefficient (pm/V)	$d_{eff} = -d_{36} \sin(2\theta_m) = 0.34$
Nonlinear coupling coefficient (V^{-1})	$K_o = 1.36943 \times 10^{-6}$ $K_e = 1.393109 \times 10^{-6}$ $K_2 = 2.762336 \times 10^{-6}$
Refractive index	$n_o = 1.494099$ $n_e = 1.468703$ $n_2 = 1.481401$
Group velocity mismatch (ps/cm)	$\delta t_{o2} = 0.55274$ $\delta t_{e2} = -0.76733$
Absorption (cm^{-1})	$\alpha_o = 0.058$ $\alpha_e = 0.02$ $\alpha_2 = 0.0$

5.2.1 The Alternating-Z configuration

To explain how the use of two SHG crystals in an alternating-Z configuration compensates for the angular dephasing of the SHG process caused by beam divergence, as well as, Poynting vector beam walk-off it is necessary to investigate the symmetry properties of the KDP crystal. KDP is a negative uniaxial crystal that belongs to the $\bar{4}2m$ symmetry group. The induced second-order polarisation wave for SHG is [9, 10]

$$P_i(2\omega) = \sum_{j,k=x,y,z} \left(\sum_{lmn=a,b,c} \left(\alpha_{li} d_{lmn}(-2\omega,\omega,\omega)\alpha_{mj}\alpha_{nk} \right) \right) E_j(\omega)E_k(\omega)$$

where i = x, y or z. The subscripts x, y and z refer to the laboratory frame of reference and the subscripts a, b and c refer to the principle crystalline axes. The relationship between the two frames of reference are related by the direction cosines α_{li}.

$$\begin{pmatrix} a \\ b \\ c \end{pmatrix} = \alpha_{li} \begin{pmatrix} x \\ y \\ z \end{pmatrix} = \begin{pmatrix} Cos\varphi Cos\theta & Sin\varphi & Cos\varphi Sin\theta \\ -Sin\varphi Cos\theta & Cos\varphi & -Sin\varphi Sin\theta \\ -Sin\theta & 0 & Cos\theta \end{pmatrix} \begin{pmatrix} x \\ y \\ z \end{pmatrix}$$

For KDP $\varphi = 0$, simplifying the direction cosines. Using the nonvanishing nonlinear coefficients for the $\bar{4}2m$ symmetry group $d_{lmn} = d_{14} = d_{25} = d_{36} \neq 0$ the induced nonlinear polarisation wave for type II, SHG in KDP becomes

$$P_e(2\omega) = d_{eff}(2\omega)E_e(\omega)E_o(\omega)$$

where the e-ray is parallel to the laboratory x-axis and the o-ray is parallel to the laboratory y-axis. Propagation is along the laboratory z-axis. The effective nonlinear coefficient d_{eff} is

$$d_{eff} = (d_{14} + d_{36})\alpha_{ax}\alpha_{by}\alpha_{cx} = -d_{36} Sin(2\theta)$$

where θ is the angle between the z axis and the crystalline c-axis.

By rotating the second KDP SHG crystal 180^0 with respect to one of the laboratory axes it is possible to reverse the sign of the effective nonlinear coefficient and to compensate for beam walk-off [11, 12]. Figure 5-1 shows the three different orientations for the two crystals. In the first case the second crystal is rotated 180^0 around the x-axis. With respect to the propagating beam the direction of the b-axis inverted, ie. $\alpha_{by} \rightarrow - \alpha_{by}$. d_{eff} of the second crystal becomes $+d_{36} Sin(2\theta)$. The inverse of the first crystal. In the second case the second crystal is rotated 180^0 around the z-axis. With respect to the propagating beam the direction of the b-axis is also inverted, ie. $\alpha_{by} \rightarrow - \alpha_{by}$. d_{eff} of the second crystal becomes $+d_{36} Sin(2\theta)$. The inverse of the first crystal. In the last case the second crystal is rotated 180^0 around the y-axis. With respect to the propagating beam the direction of the a and c axes are inverted, ie. $\alpha_{ax} \rightarrow - \alpha_{ax}$ and $\alpha_{cx} \rightarrow -\alpha_{cx}$. d_{eff} of the second crystal becomes $-d_{36} Sin(2\theta)$. The same as the first crystal. Reversing the sign of d_{eff} causes a π phase shift in the induced nonlinear polarisation wave and, therefore, between the SH wave and the fundamental waves. For those orientations where the effective nonlinear coefficient is reversed the second crystal compensates for angular dephasing caused by beam divergence and walk-off, (see Figure 5-2). The direction of the Poynting vector walk-off is always orthogonal to the phase matching index surface at the phase matching point. Since this
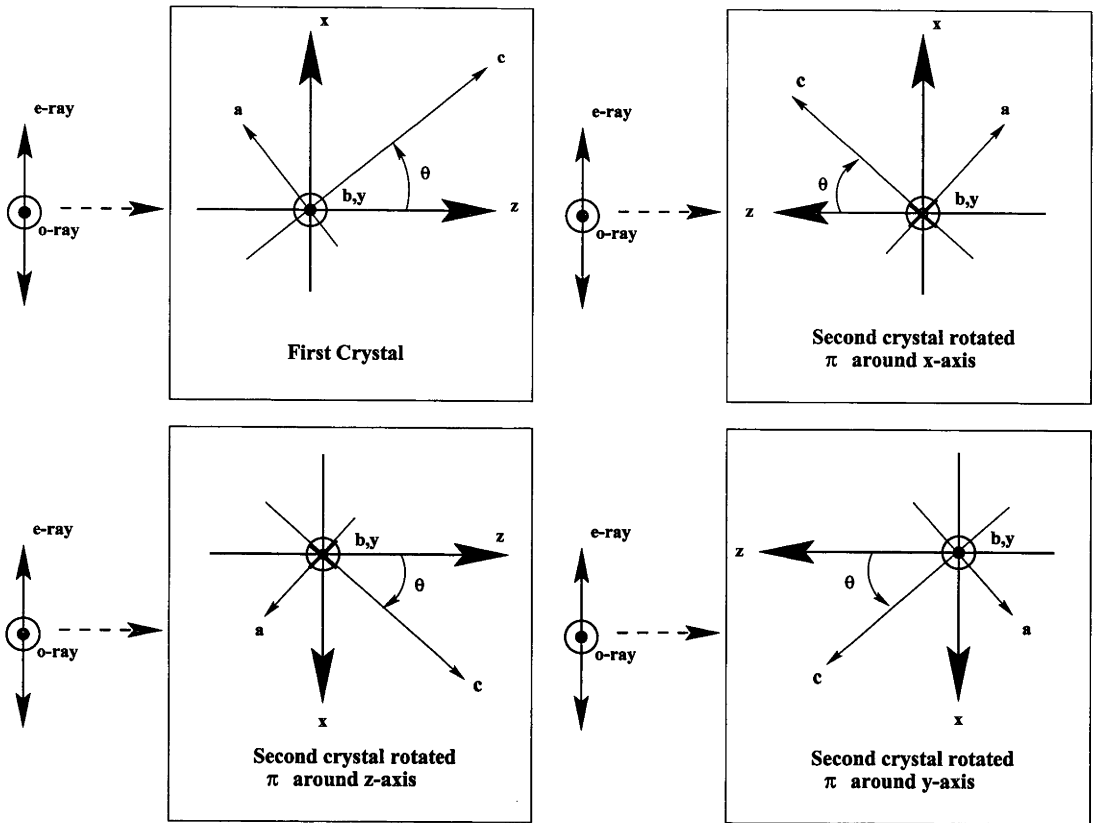
Figure 5-1 : The relationship of the crystallographic and laboratory axes relative to the propagating beams for various orientations of the second KDP SHG crystal relative to the first KDP SHG crystal.
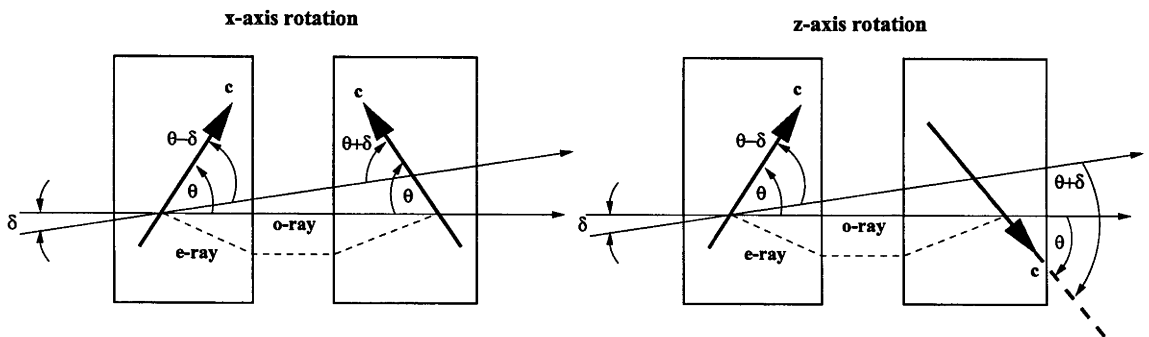

Figure 5-2 : The two orientations for a pair of identical KDP SHG crystals that compensate for any angular dephasing of the SHG process due to the beam divergence δ and the Poynting vector beam walk-off of the e-rays.

index surface in reversed for the cases where the second crystal has been rotated 180^0 around the x and z axes the fundamental e-ray and the SH beam propagate back towards the fundamental o-ray. As long as the two crystal are identical (cut at the same crystal angle and length) the walk-off is corrected.

The FWHM acceptance angle for type II SHG in KDP at ~ 1 μm is 3.24 mrad-cm [13]. This provides a measure of how sensitive the SHG process is to changes in the phasematching angle θ.

107

Predelay crystal
25 mm KDP (II)

GVMSHG crystals
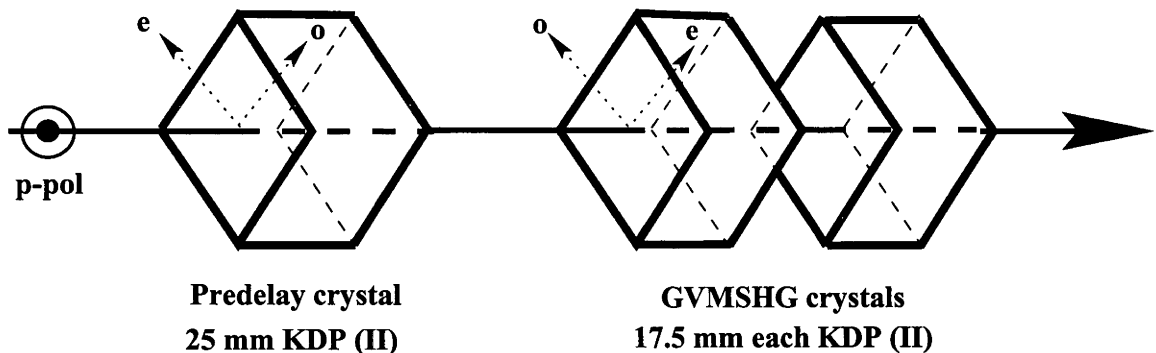**17.5 mm each KDP (II)**

Figure 5-3 : The experimental layout for group velocity mismatched second harmonic generation (GVMSHG).

Since the phase mismatch $\Delta k = \Delta k(\theta) = 2\pi/\lambda \ (\ 2n_2(\theta) - n_e(\theta) - n_o \ )$ detuning the crystal will introduce a phase mismatch and decrease the efficiency of the SHG process. This acceptance angle is the FWHM of the small-signal conversion efficiency curve, which is proportional to $[Sin(\Delta k(\theta)l/2)/(\Delta k(\theta)l/2)]^2$, as a function of angle. Since the divergence of the fundamental beam introduces an effective change in the crystal angle, beam divergence introduces a phase mismatch into the SHG process. This phase mismatch or dephasing can be expressed as $\delta_\theta = 1/2 \ \Delta k \ l_x = \beta_\theta \ \Delta\theta \ l_x$; where $\beta_\theta = \partial\Delta k/\partial\theta = 2.56$ $(mrad-cm)^{-1}$ is the angular sensitivity for KDP (type II) [13, 14], $\Delta\theta$ is the difference between the propagation angle and the phasematching angle (δ in Figure 5-2) and l_x is the length of the crystal. If we assume that the beam divergence causes the angular dephasing, $\Delta\theta = \lambda/\pi w_0$, where w_0 is the 1/e electric field beam radius. To maintain a high conversion efficiency the angular dephasing δ_θ must be less than $\pi/10$ [14]. Since the two KDP SHG crystals are used in a angular dephasing compensating configuration any angular dephasing is only due to the first crystal, ie. l_x is equal to the thickness of the first crystal not the combined length of both crystals.

The spectral acceptance bandwidth of type II phase matching in KDP is 13.8 nm-cm for frequency doubling light at ~ 1 μm. It is broad enough not to restrict the SHG process.

As has been explained above, when the two KDP crystals are in an alternating-Z configuration there is a 180^0 phase shift in the SH beam relative to the fundamental beams in the second crystal. Hence if the two crystals were simply butted together, this would result in any SH generated in the first crystal being converted back into fundamental after propagating through the second crystal. As a result, for efficient SHG, the phase of the SH wave from the first crystal must be rotated 180^0 to compensate the 180^0 rotation in the induced SH polarisation wave before entering the second crystal. This can be done by taking advantage of the dispersion in an air space introduced between the two crystals. The amount of phase change between the SH and fundamental waves can be determined from the coherence length of air l_c . $l_c = \lambda/2\pi\Delta n$, where Δn is the difference between the refractive index of air at 527 nm and at 1054 nm and λ is the fundamental wavelength of 1054 nm. For air at STP and λ=1064 nm, $l_c = 13.1$ cm [15]. After propagating a coherence length the phase of the SH wave has rotated 2π relative to the fundamental waves. Hence the distance between the two KDP SHG crystals should be set to 6.6±0.3 cm to rotate the SH 180^0 relative to the fundamental. Since the KDP crystals used in these experiments had Sol-Gel AR coatings, this of course assumes that the did not add introduce any additional relative phase shifts between the propagating beams. In most instances, the crystal spacing was adjusted to obtain maximum conversion efficiency thereby eliminating such uncertainties.
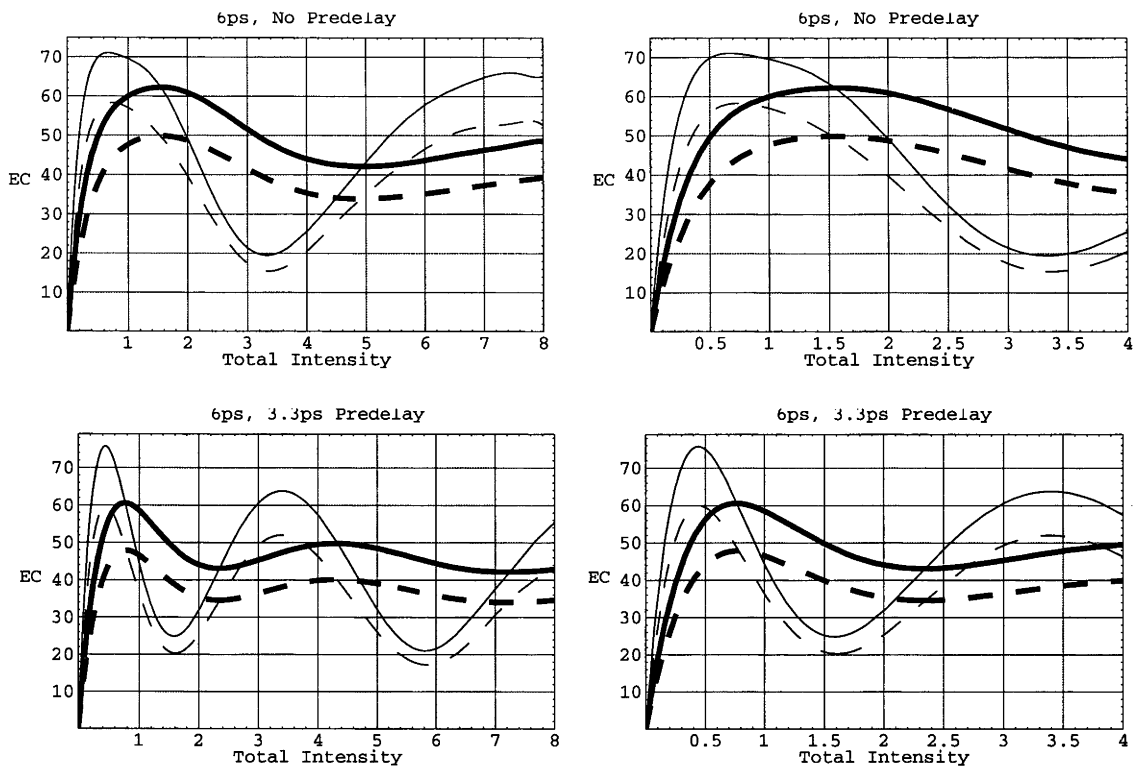
108

Figure 5-4 : The energy conversion (EC) in percent of fundamental into second harmonic with total fundamental intensity in GW/cm^2 for type II SHG in 3.5 cm of KDP with and without predelay. The fundamental pulse duration is 6 ps (FWHM) and the predelay is 3.3 ps. The thin lines are for a plane wave and the thick lines are an average for a Gaussian beam profile with an 1/e electric field beam radius of 8 mm , ie. area = 1 cm^2. The full lines correspond to a 0 μrad beam divergence and the dashed lines to a 150 μrad beam divergence.

5.2.2 Numerical simulation results

The numerical simulation models the arrangement of KDP crystals shown in Figure 5-3. The length of each of the KDP SHG crystals was 1.75 cm, with the first crystal having Sol-Gel AR coatings for 1054 nm on the entrance face and for 700 nm on the exit face and the second has Sol-Gel AR coatings for 700 nm on the entrance face and for 527 nm on the exit face. Using an AR coating for 700 nm minimises the losses for both the fundamental and the SH. Each crystal was cut at the phase matching angle for type II SHG, $\theta = 59.2^0$. As will be shown below, the pulse from the amplifier chain was ~ 6 ps in duration and had a maximum energy of ~ 18 mJ. The 1/e electric field radius of the collimated fundamental beam at the KDP crystals was nominally taken to be 8 mm for the simulations, giving a beam area of 1 cm^2. This gives a maximum peak intensity for the fundamental beam of 3.0 GW/cm^2 and a beam divergence of 40 μrad ($\delta_\theta = 0.18 \approx \pi/18$). The ratio of the power of the fundamental e to o rays was taken to be 1:1.

The predelay was created by assuming the linearly polarised beam from the laser passed initially through an additional 2.54 cm long KDP crystal cut for type II, SHG at 1054 nm. This crystal had a Sol-Gel AR coating for 1054 nm on the entrance face and another for 527 nm on the exit face. The predelay crystal was orientated so that the axes of the e-ray and o-ray were orthogonal to those of the GVMSHG KDP crystals. The angle of the crystal
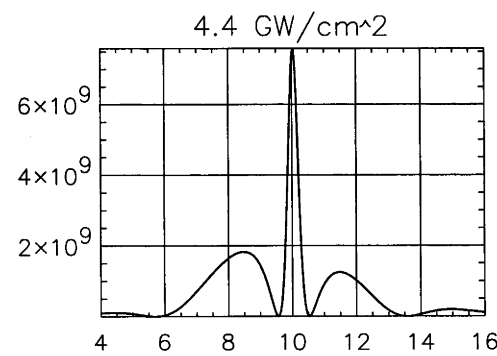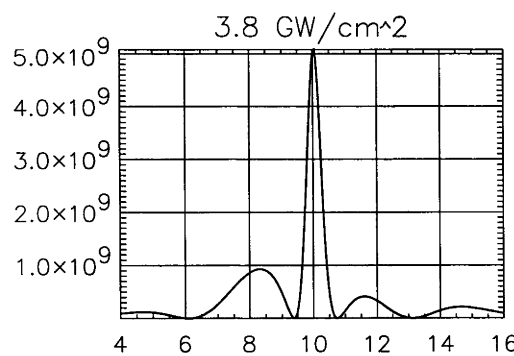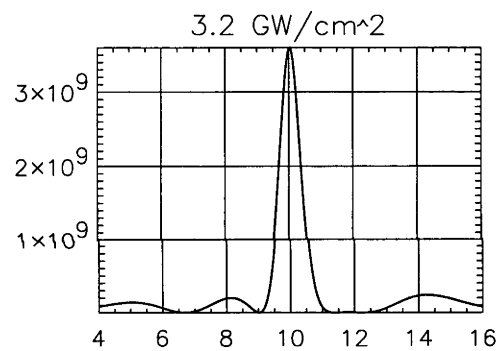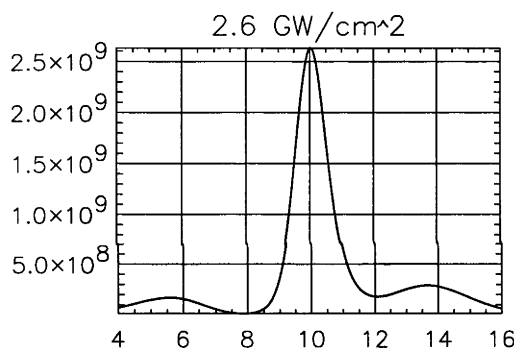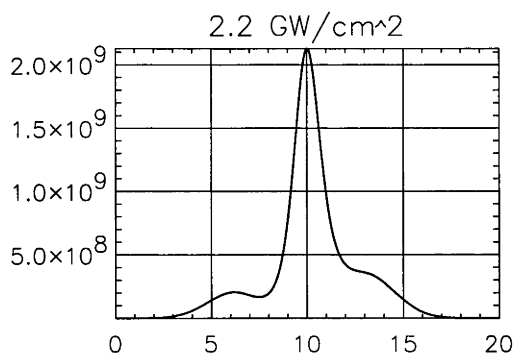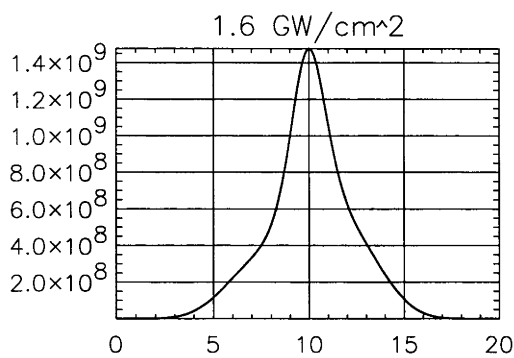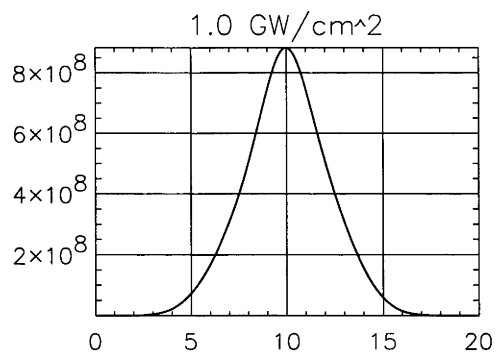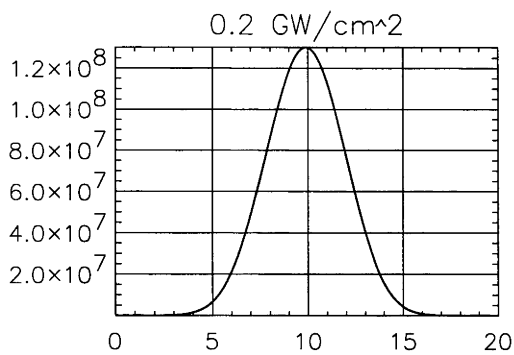
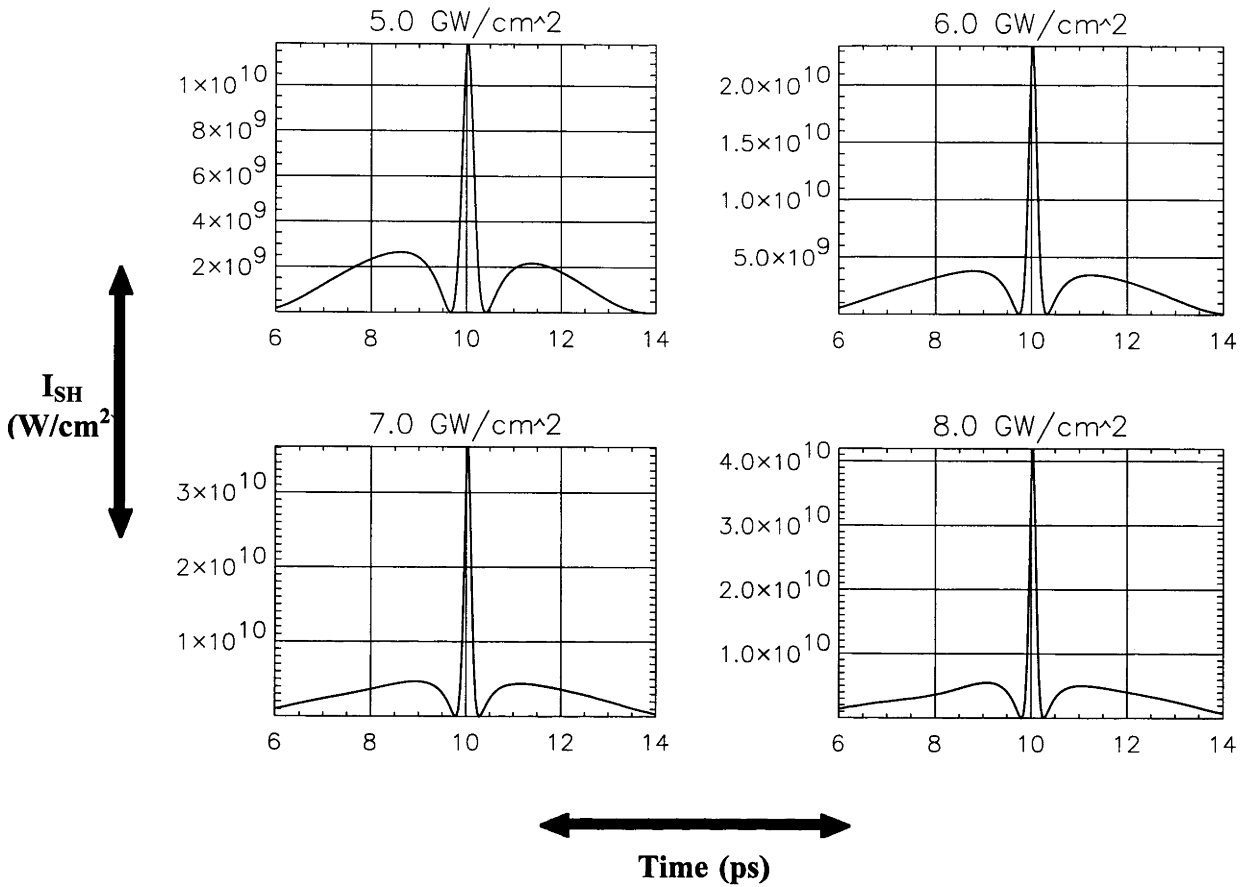**Figure 5-5 : The temporal pulse profiles of the second harmonic at various total fundamental intensities for the case of no predelay. The results are for type II SHG in 3.5 cm of KDP assuming perfect phase matching and monochromatic, infinite plane waves. The vertical scale is the second harmonic intensity in W/cm² and the horizontal scale is time in picoseconds.**

was also detuned slightly so that it did not generate any SH. After propagating through the birefringent KDP crystal the o-ray was delayed by 3.3 ps relative to the e-ray. Since the axes were reversed in the GVMSHG crystals the e-ray became the o-ray and the o-ray became the e-ray. The e-ray at the input to the SHG pair was thus delayed 3.3 ps with respect to the o-ray. Even though this predelay was smaller than the pulse duration of the fundamental it will be shown that substantial pulse compression was still theoretically possible.

The results of these simulations are show in Figures 5-4 to 5-7.

Figure 5-4 shows the energy conversion of fundamental into second harmonic as a function of the total intensity of the fundamental beam incident on the KDP crystals with and without a 3.3 ps predelay. The intensity of the e-ray and o-ray fundamental pulses was taken to be half the total intensity of the fundamental pulse, ie. $I_T = I_o + I_e$ where $I_o/I_e = 1$. The thin lines are the energy conversions for an infinite plane wave and the thick lines are the energy conversions for a fundamental pulse with a Gaussian beam profile and an area of 1 cm². Since the intensity varies across a Gaussian beam, the energy conversion also varies across the beam profile. The full lines were calculated for perfect phase matching, ie. $\Delta k=0$; and the dashed lines include the phase mismatch introduced by a 150 μrad beam divergence. As can be seen from these figures, the predelay causes pump depletion and reconversion of the SH back into fundamental at much lower intensities than when there is no predelay.
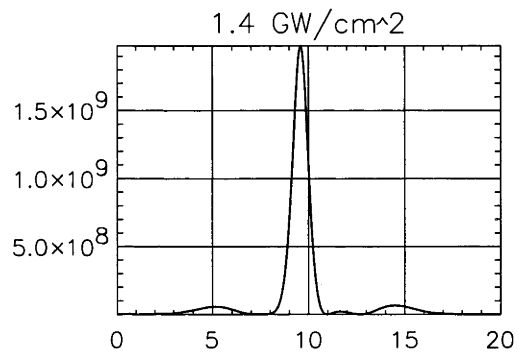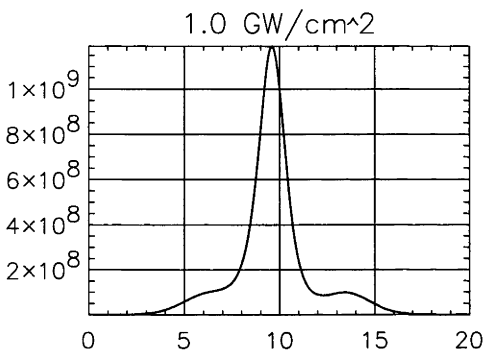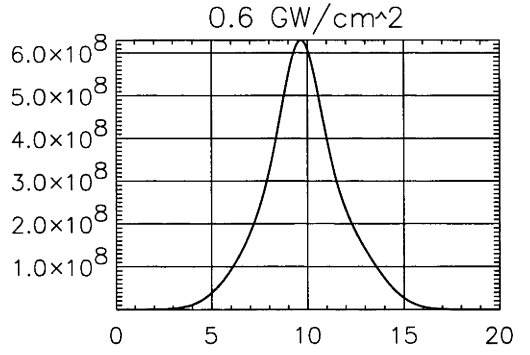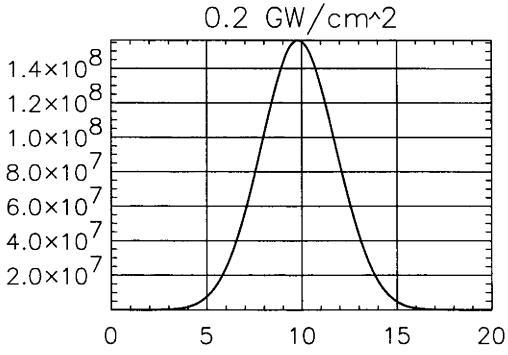
Time (ps)
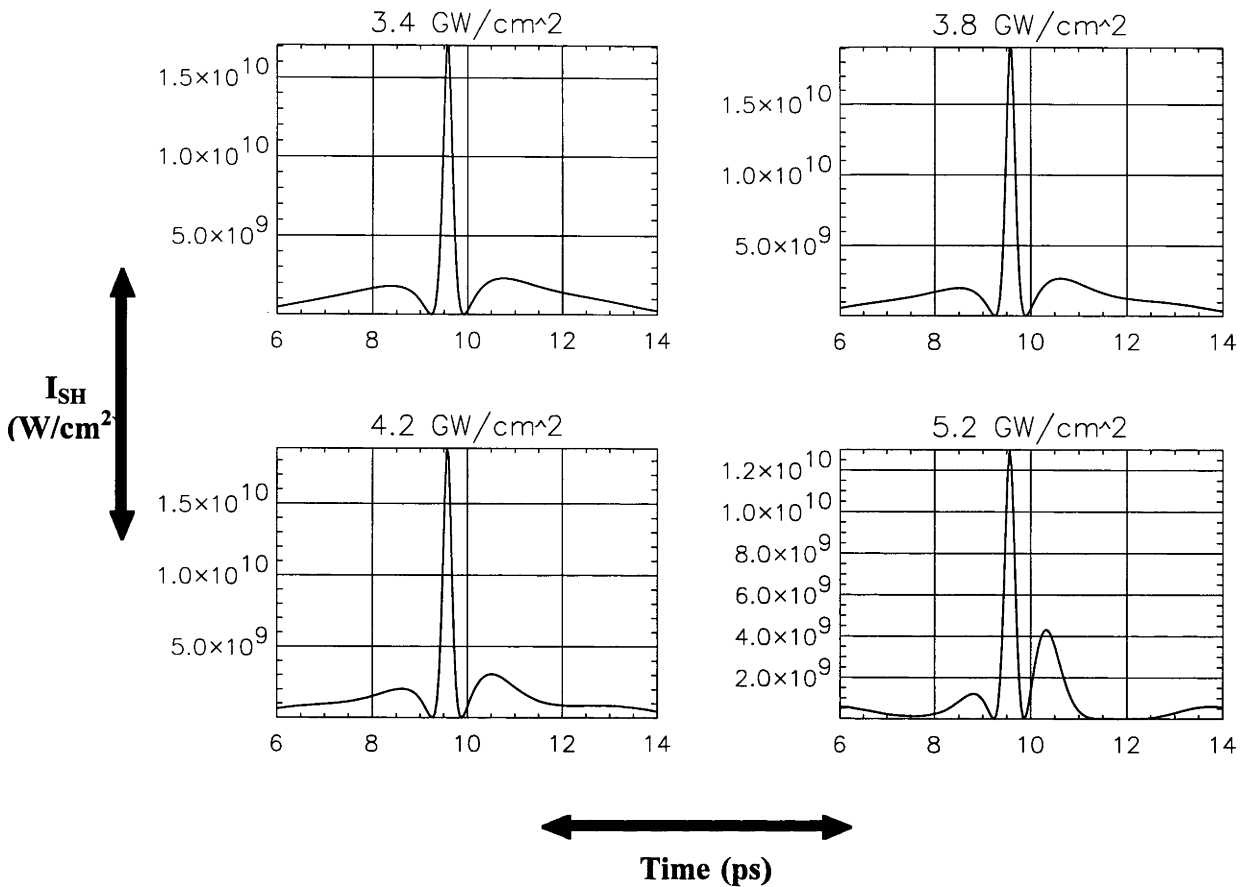
Figure 5-6 : The temporal pulse profiles of the second harmonic at various total fundamental intensities for the case of a predelay of 3.3 ps. The results are for type II SHG in 3.5 cm of KDP assuming perfect phase matching and monochromatic, infinite plane waves. The vertical scale is the second harmonic intensity in W/cm^2 and the horizontal scale is time in picoseconds.
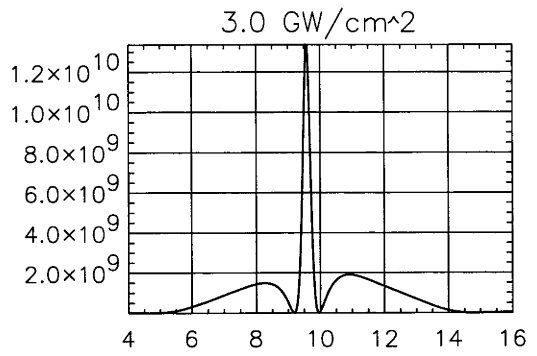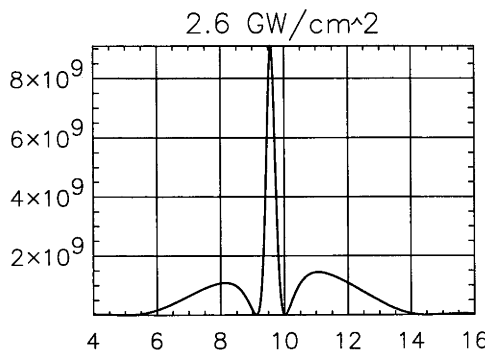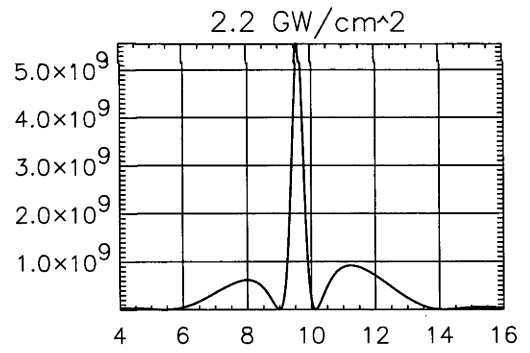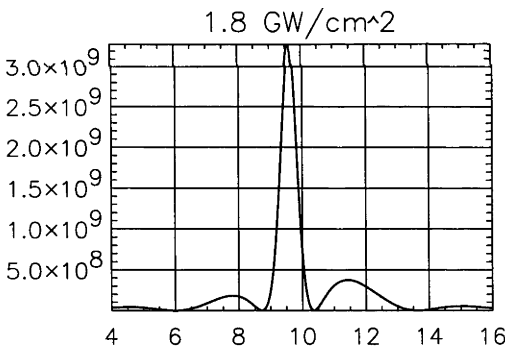
The temporal pulse profiles of the second harmonic pulse are shown in Figure 5-5 and Figure 5-6, without and with predelay, respectively. As the fundamental intensity is increased, pump depletion occurs and eventually the SH starts to reconvert into the fundamental waves. In both cases the GVM between the e and o rays causes reconversion of the wings of the SH pulse, rather than the central peak, leading to significant SH pulse compression. As indicated by the energy conversion curves, this reconversion and pulse compression occurs at lower intensities in the presence of the predelay. With predelay the maximum reconversion of the SH pulse occurs at half the intensity compared with the case of no predelay. The compressed SH pulse consists of a central peak ~ 200 fs in duration and low intensity wings that stretch for several picoseconds on either side of the pulse. To achieve the shortest central spike with smallest sidelobes it is desirable to drive the GVMSHG system between 2 GW/cm^2 and 4.5 GW/cm^2 when using 3.3 ps predelay and between 4 GW/cm^2 and 8 GW/cm^2 when using no predelay. The sidelobes or wings in the compressed SH pulse are generally lower in intensity when using a predelay, around 14 % of the peak intensity over the entire desired intensity range. The shape of the sidelobes stays the same over this intensity range compared to the sidelobes for the compressed SH pulse with no predelay, which vary between 30 % to 12 % of the peak intensity between 4 GW/cm^2 and 8 GW/cm^2 .

Figure 5-7 shows data extracted from the temporal profiles. From these plots the following points can be made. When GVMSHG is driven with fundamental intensities necessary to achieve the best compressed SH pulse, the energy in the central peak is ~ 30 % of the total
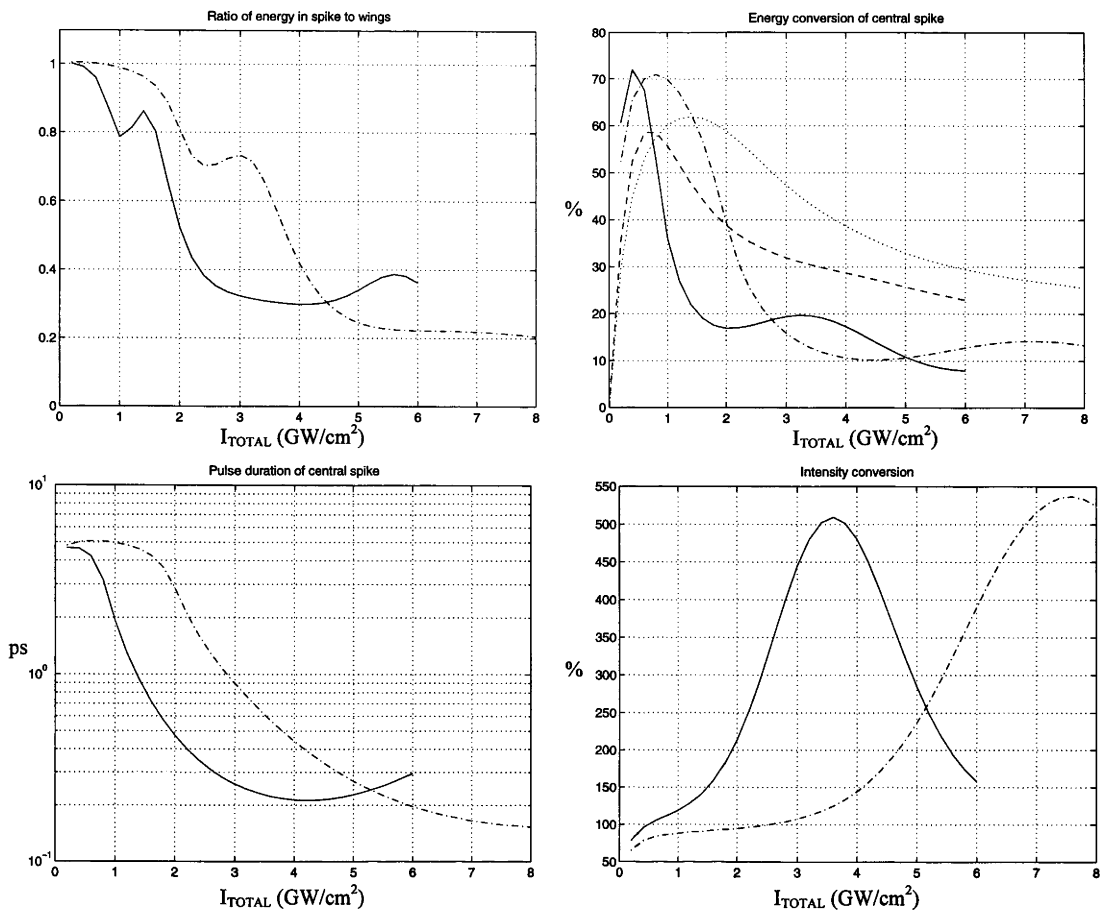
Figure 5-7 : The top left figure shows the ratio of energy in the central peak to that in the rest of the SH pulse. The top right figure shows the energy of the central peak as a percentage of the total energy of the incident fundamental pulse. The bottom left figure shows the FWHM pulse duration in picoseconds of the central peak of the SH pulse. The bottom right figure shows the peak intensity of the SH pulse as a percentage of the total fundamental intensity. The full line is for 3.3 ps predelay and the dash-dot line is for no predelay. In the energy conversion figure the dashed and dotted lines are an average for a Gaussian beam profile with an 1/e electric field beam radius of 8 mm, with and without predelay, respectively. The horizontal axis in all plots is the total fundamental intensity in GW/cm^2.

energy of the SH pulse for the case of the predelay, compared with 20 % without predelay. The actual energy of the central peak is around 19 % of the total energy of the fundamental pulse when a predelay is used compared with 12 % when there is no predelay. The shortest pulse duration that can be theoretically achieved is close to 200 fs when using a predelay and 150 fs without a predelay. The peak intensity of the compressed SH pulse is up to 5 to 5.5 times that of the total fundamental intensity for both cases. Note that these calculations apply for conversion from an infinite plane wave.

Simulations were also conducted varying the fundamental pulse duration and the predelay. They showed that the results presented above are not particularly sensitive to the fundamental pulse duration for values between ~ 4.5 to greater than 8 ps. As would be anticipated, however, as the fundamental pulse duration approaches the value of the predelay (3.3 ps), the dynamics of energy conversion and SH pulse compression become more sensitive to variations in the fundamental pulse duration. Varying the predelay shifts the total fundamental intensity at which maximum reconversion of the SH pulse occurs. It
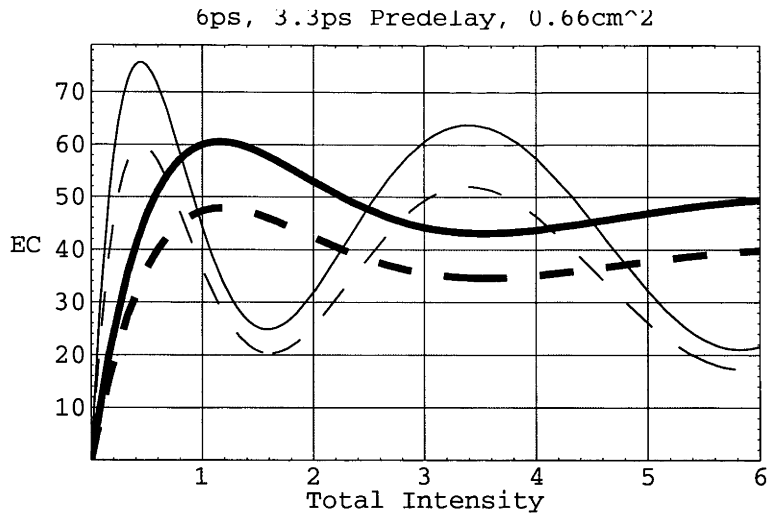
Figure 5-8 : **The energy conversion in percent (EC) of fundamental into second harmonic with total fundamental intensity in GW/cm^2 with a 3.3 ps predelay and for a fundamental pulse duration of 6 ps. The thin lines are for a plane wave and the thick lines are an average for a Gaussian beam profile with an 1/e electric field beam radius of 6.5 mm , ie. area = 0.66 cm^2. The full lines correspond to a 0 μrad beam divergence and the dashed lines to a 150 μrad beam divergence.**

was generally found that predelay always aided compression of the SH pulse, for the case where the fundamental pulse duration was longer than the predelay and the crystal length was less than the GVM separation distance, l_{GVM} , between the e and o fundamental rays.

The maximum obtainable peak power of the fundamental pulse in the conditions assumed above was ~ 3.0 GW/cm^2 (~ 18 mJ in 6 ps). This is less than the optimum for the GVMSHG system with a 3.3 ps predelay where an intensity of ~ 4.5 GW/cm^2 is needed to achieve the best compressed SH pulse. It was, therefore, necessary to reduce the beam area to ~ 0.66 cm^2 which is equivalent to a 1/e electric field radius, w_o , of ~ 6.5 mm. The energy conversion curves averaged over this beam profile are shown in Figure 5-8. The beam divergence for w_o = 6.5 mm is 50 μrad which gives an angular dephasing $\delta_\theta \approx 0.22 \approx \pi/14$. If we were not to use any predelay then we would require a beam radius of ~ 4.5 mm, or an area of 0.32 cm^2, to reach intensities of ~ 9 GW/cm^2. This would give a beam divergence of 75 μrad or an angular dephasing of $\delta_\theta \approx 0.34 \approx \pi/9$ which exceeds the dephasing threshold set earlier of $\pi/10$. From all considerations it would be better to use the predelay.

In summary, the use of a predelay with 4 - 8 ps duration fundamental pulses has the advantage of requiring about half the fundamental intensity compared to the case of no predelay to obtain the best SH compressed pulse. It also converts more of the fundamental energy into the central peak of the SH compressed pulse. Approximately the same pulse compression and peak intensity conversion could be obtained with or without the predelay. Using a 3.3 ps predelay compresses the SH pulse from ~ 6 ps down to ~ 200 fs in duration, with the central peak having around ~ 20 % of the total energy of the fundamental pulse near the optimum fundamental intensity of 4.5 GW/cm^2.

It would be preferable to use a flat beam profile so that all the energy in the fundamental pulse is close to one intensity. If this were the case all the pulse could be compressed. For a Gaussian beam profile different parts of the beam undergo a different degree of pulse compression. However, since the pulse duration of the central peak is less than 500 fs for intensities between ~ 2 GW/cm^2 up to the maximum of 4.5 GW/cm^2 approximately two

115

thirds of the fundamental pulse energy will be converted to a sub-500 fs pulse for a Gaussian beam profile. As a result more than 2 mJ of sub-500 fs SH pulse energy should be obtained for an 18 mJ, 6 ps input pulse with a Gaussian beam profile. This gives a peak power around 4 GW which is more than is required to pump the OPA.

5.3 Experiments

5.3.1 The Nd:YLF amplifier chain

The experimental layout of the Nd:YLF amplifier chain is shown in Figure 5-9. The system consisted of three major elements: the mode-locked, cw Nd:YLF (Coherent 76-YLF Antares) laser; the regenerative Nd:YLF amplifier; and the single pass Nd:YLF amplifier.

Part of the beam from the Antares laser used to pump the OPO was used as the source of seed pulses for the amplifier chain. As mentioned previously the beam from the Antares was chopped at 160 Hz to reduce the cw power by 8.8 times. About 1/3 of the Antares output was focussed into a second single mode fibre with a waveplate and a thin-film polarising beamsplitter used to vary the coupled power. Generally the cw power coupled into the fibre was less than 1 W, or 220 W peak power in a 13 nJ pulse. After propagating through 50 m of single mode fibre the spectrum was broadened by SPM increasing from 0.27 Angstroms at the laser output to around 15 to 17 Angstroms. SPM introduces a frequency chirp across the pulse (see Chapter 2). A pulse is then "sliced" from the train of pulses from the Antares by the two Pockel cells in tandem to provide a contrast ratio of better than 10^5 for the switch. The rejected beam was monitored using a spectrometer which recorded the SPM spectrum. A waveplate before the first Pockel cell was used to correct for any polarisation rotation in the fibre and to optimise the SPM spectrum.

The single output pulse was injected into a ring regenerative Nd:YLF amplifier (RA) which boosted the pulse energy to a maximum of 1.5 mJ. Gain narrowing in Nd:YLF simultaneously reduces the pulse duration from 60 ps to around 6 ps. The process is as follows. The linewidth of the lasing transition in Nd:YLF is sufficiently narrow that it will only amplify the central frequency components in the SPM spectrum. However, since the pulse is frequency chirped, ie. the different frequency components in the spectrum correspond to different time points within the pulse, gain narrowing affects not only the spectrum but also reduces the pulse duration. As will be shown later, measurements indicated that the output pulse from the RA were close to the transform-limit assuming a 6 ps Gaussian profile.

The pulse from the RA was then passed through a single pass amplifier using a 6 mm diameter, 10 cm long Nd:YLF rod where the energy is roughly increased by an order of magnitude to a maximum of around 18 mJ. This pulse was then used as the fundamental pulse to drive the GVMSHG system.

The timing control signals for the pulse slicer and the flashlamps powering the amplifiers were derived from the Antares laser itself, the chopper and by monitoring the fluorescence from the Nd:YLF rod in the RA. The repetition rate of the amplifiers was 20 Hz and was determined by a 8 times divider operating on the 160 Hz reference signal from the chopper. The clock signal from the Antares laser mode-locker was used to synchronise switching of the Pockel cells used in the pulse slicer and within the RA.
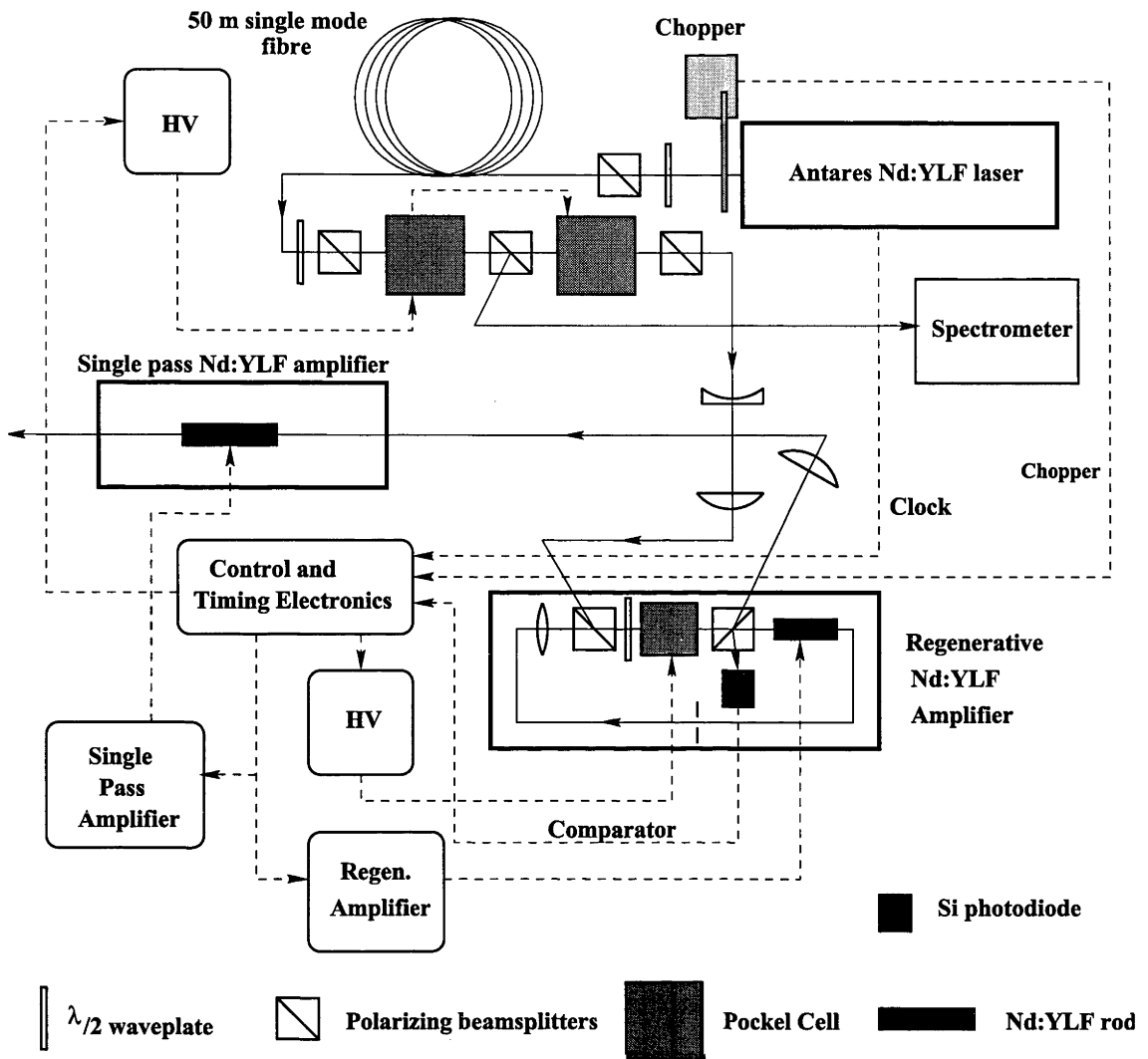
Figure 5-9 : The experimental layout of the Nd:YLF amplification chain operating at 1054 nm.

Since the gain of the RA is very high, it was desirable to stabilise it against jitter in the gain induced by flashlamp fluctuations, etc. This was achieved by monitoring the fluorescence from the Nd:YLF rod in the RA using a Si photodiode, and controlling the command pulses sent to the pulse slicer and Pockels cell in the RA so that they occurred at a time when the fluorescent intensity fell to a pre-determined level. Since the fluorescence intensity is directly related to the gain in the laser material, this in effect clamps the RA gain. By this process the shot-to-shot jitter in the RA output was reduced to a few %. Firing of the RA and single pass amplifiers was synchronised.

5.3.2 Characteristics of the amplified 1054 nm pulse

The amplified 1054 nm pulse was measured by SHG intensity autocorrelation and the McPherson spectrometer and was found to have a Gaussian like temporal and spectral shape with a pulse duration around 6 ps, assuming a Gaussian pulse, and spectral bandwidth of around 3 Angstroms for pulse energies from 2.5 mJ to 18 mJ (see Figure 5-10 for an example). The intensity autocorrelator used a 1 mm thick KDP (type I, $\theta=90^0$) as the SHG crystal and was measured using a Si PIN detector and a Boxcar integrator, averaging over 10 shots (see Chapter 7 for more details).
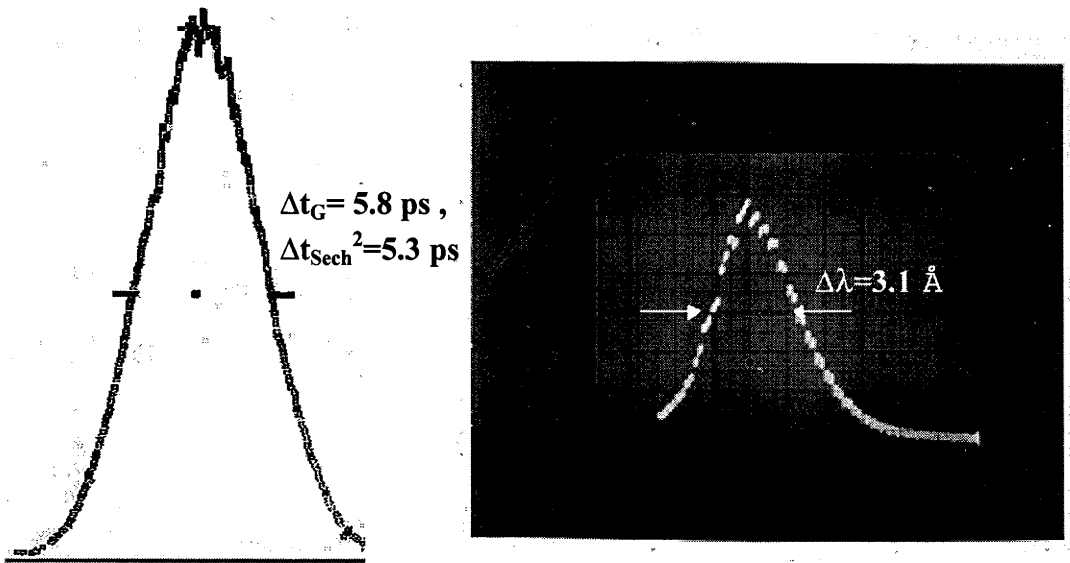
Figure 5-10 : The SHG intensity autocorrelation and spectrum of the amplified 1054 nm pulse where the pulse energy is 10 mJ. The FWHM pulse duration determined from the intensity autocorrelation is 5.8±0.6 ps for a Gaussian pulse shape and 5.3±0.5 ps for a $Sech^2$ pulse shape. The spectrum has a FWHM bandwidth of 3.1±0.6 Angstroms. The transform bandwidth product is 0.48 for a Gaussian pulse (1.1 times above the transform limit) and 0.44 for a $Sech^2$ pulse (1.4 times above the transform limit). The scale for the photo of the spectrum is 1.25 Angstroms per division.

The time-bandwidth product of the pulse is within 10 to 15 % of the transform limit if one assumes a Gaussian pulse shape, and within 40 to 50 % of the transform-limit if a $Sech^2$ pulse shape is assumed; remaining unchanged for pulse energies up to 18 mJ. The fact that the time-bandwidth product was close to the transform limit was taken to indicate that there was little phase distortion on the pulse. It was assumed for subsequent work that the amplified 1054 nm pulse was essentially transform limited. Later this assumption will be shown to be erroneous and the cause of the failure to achieve strong pulse compression of the SH pulse through GVMSHG.

5.3.3 The GVMSHG system

The 1054 nm beam from the amplifiers was expanded and collimated by a telescope before passing through a thin-film polariser, to ensure the polarisation state of the beam, and into the GVMSHG crystals. The beam after the single pass amplifier had a 1/e electric field beam radius, w_o, of ~ 4 mm. and this was increased to $w_o \approx 6.5$ mm using the telescope which used two, 2 inch diameter, AR coated plano-convex lenses with focal lengths of 500 mm and 800 mm. To align the telescope a small portion (< 10 %) of the 1054 nm beam was reflected back down the beam axis. At a point about halfway along the beam path between the RA and the single pass amplifier the outgoing beam forms a waist of less than 1 mm in diameter. The separation between the two lenses in the telescope was adjusted until the reflected beam was also focussed at the same point indicting a beam waist existed at the position of the reflecting mirror.

Since KDP is hydroscopic the GVMSHGcrystals and the predelay crystal were kept in an enclosure which was flushed with heated, dry nitrogen gas. All the crystals were evenly heated to about 25°C.

118

With the GVMSHG crystals correctly orientated and their separation between the two KDP doubling crystals set to 6.6 cm, the energy conversion from the fundamental into the SH was measured as a function of the total fundamental intensity. Based on previous experience with the Nd:glass laser system, it was expected that the energy conversion curve would be quite close to the theoretical predictions. However, this was not the case. The conversion efficiency was less than 40 % at an intensity were it was expected to be near 60 %. There were a number of potential causes of this observation, the most likely was initially believed to be a problem with the alternating-Z configuration of the SHG crystals and then it was believed due to excess divergence in the output beam due to thermal lensing in the amplifiers. As was shown in the simulated energy conversion curves, any increase in beam divergence drops the SH energy conversion quite substantially.

5.3.4 Characterisation of the Beam divergence

In an attempt to locate the intensity needed for maximum conversion the telescope was changed to 1:1 magnification (using two 500 mm focal length plano-convex lenses) to obtain higher beam intensity. The beam waist size, w_o, was then 4.3 mm, giving a beam area of 0.29 cm^2 and a maximum intensity of 10 GW/cm^2. This allowed experiments to be carried out not only using the pair of 17.5 mm crystals in the alternating-Z geometry (which might itself have been introducing some errors affecting the conversion) but also other combinations of predelays and lengths of SHG crystals. Conversion measurements were made, for example, using a single 17.5 mm crystal with a 3.3 ps predelay. In these conditions the maximum energy conversion for a Gaussian beam with w_o = 4.3 mm should occur at 8 to 9 GW/cm^2. In this case there was a similar discrepancy between the predicted and measured energy conversion efficiency, and hence it did not appear that the alternating-Z configuration was responsible for the problem. Other crystal and delay combination reinforced the notion that the discrepancy was not due to the doubling system itself, rather it was attributable to some beam or pulse property.

The spatial beam profile of the amplified pulse was re-measured, this time at different large distances from the telescope. Previously the beam had only been measured a short distance (~ 2 m) after the telescope where the profile was a good fit to a slightly elliptical Gaussian profile. When measurements were made up to 20 m from the telescope it was found that the beam diverged quite strongly in one plane, and became quite elliptical after 5 m, however, the beam remained collimated in the orthogonal plane. In the description that follows the direction of strong divergence will be referred to as the long axis and the orthogonal direction, the short axis of the beam. Figure 5-11 (top row) shows an example of the beam at 1.56 m and at 10.57 m after the telescope. With the divergence being around 600 μrad ($\delta_\theta \approx 2.72 \approx 0.85\,\pi$) in the direction of the long axis, it is not surprising that the SH energy conversion was lower than expected.

This increased divergence may have been due to thermal loading in the single pass amplifier Nd:YLF rod. To test this the repetition rate of the amplifiers was decreased down to 5 Hz by changing the chopper frequency from 160 Hz to 40 Hz. The beam sizes in the long and short axis directions was re-measured. The beam divergence along the long axis dropped significantly at the lower repetition rate (see Figure 5-11). By measuring the beam sizes it was possible to calculate the beam divergence at different repetition rates. The results are shown in Figure 5-12. Decreasing the repetition rate to 5 Hz dramatically improved the spatial beam quality. The divergence in the long axis at 20 Hz was about 8 times the diffraction limit ($M^2 \approx 8$) or 600 μrads. While this drops to about 3 times diffraction limit or 240 μrads when the repetition rate was reduced to 5 Hz. The divergence along the short axis was always near the diffraction limit of 80 μrads ($M^2 \approx 1$).

1.56 m	10.57 m
20 Hz	

1.56 m	10.57 m
5 Hz	
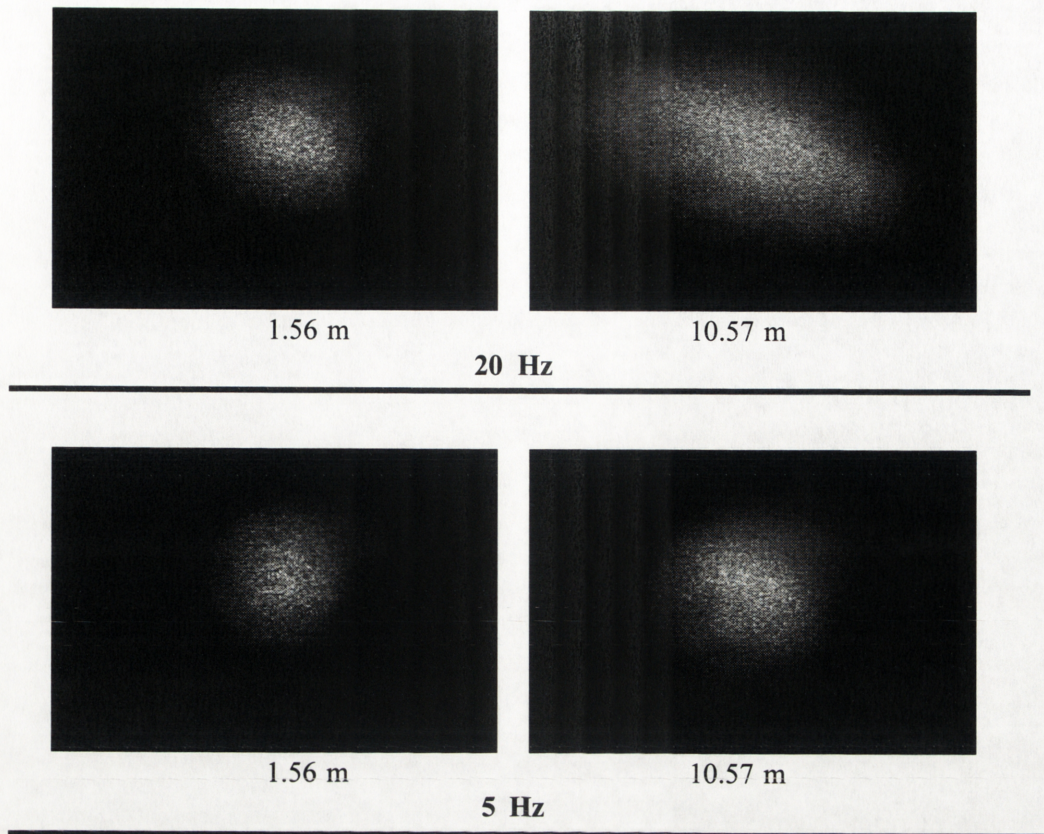
Figure 5-11 : Images of the 1054 nm amplified beam. The pulse energy is 15 mJ, 1.5 mJ of which is from the Regen amplifier. The top row of images were taken with the amplifiers operating at 20 Hz and the bottom row were taken with the amplifiers operating at 5 Hz. The images in the left column were taken 1.56 m from the telescope and those in the right column were taken 10.57 m from the telescope. As can be seen from these images decreasing the repetition rate of the amplifiers improves the beam divergence.
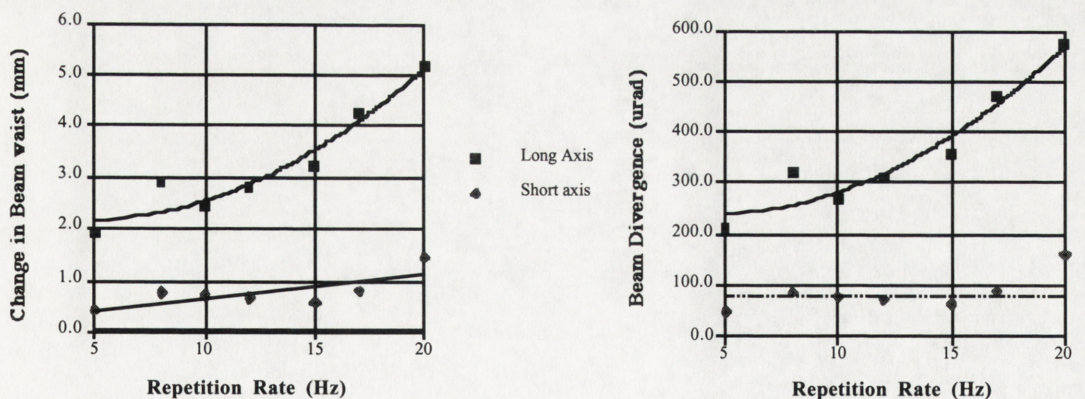
Figure 5-12 : The figure on the left shows the change in the beam waist size for the beam between 1.56 m and 10.57 m from the telescope with repetition rate . The right hand figure shows the beam divergence as a function of the repetition rate. The beam waist size at 1.56 m from the telescope is around 4.3 mm (1/e electric field waist). The dashed line shows the diffraction limit of 80 μrad for the 4.3 mm beam waist. The beam diffracts mainly in one plane, with this plane referred to as the long axis and the orthogonal plane referred to as the short axis. The initial pulse energy was 15 mJ at 20 Hz.
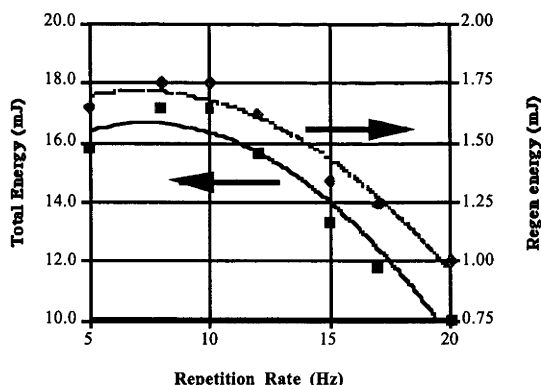
Figure 5-13 : The variation in pulse energy after both amplifiers and just the Regen amplifier with repetition rate.

It was also found that the pulse energy improved with a lower repetition rate (see Figure 5-13). This indicates that the single pass amplifier was being driven too hard, with thermal loading limiting the pulse energy and causing lensing in the polarisation sensitive plane of the Nd:YLF rod.

While reducing the repetition rate of the amplifiers improved the beam divergence and pulse energy it still left the beam with a divergence of ~ 240 μrads along one axis. It was also found that the divergence changed with increasing pulse energy; roughly doubling for both axes as the pulse energy changed from 1 mJ to above 15 mJ (ie. from 80 μrads to ~ 150 μrads in the short axis and from ~ 200 μrads to ~ 400 μrads in the long axis) for the case when the telescope was aligned at low pulse energies. This posed a problem since it implied that a different telescope alignment was needed for each pulse energy.

A partial solution was introduced which involved orientating the two KDP crystals so that their o-ray axis was aligned with the long axis of the beam. The o-ray direction is less sensitive to beam divergence because the refractive index, n_o , and hence the wave vector, k_o , does not depend on the propagation direction in the KDP crystal. Hence excess divergence in the long axis direction could be tolerated. Because increased divergence was observed at high pulse energy in the short axis direction, which was aligned with the angle sensitive e-ray axis in the KDP crystals, a divergence of 150 μrads was assumed for further calculations (see Figure 5-8).

After fixing the beam divergence problem the energy conversion curves were again measured for the GVMSHGsystem, as well as for other different crystal combinations and compared with theoretical expectations. While the SH energy conversion reached theoretical expectations it occurred at much higher total fundamental intensities. The excess beam divergence can not account for this discrepancy.

5.3.5 Measurements of the second harmonic pulse

After identifying and minimising the problems associated with excess beam divergence and seeing that good energy conversion into SH was occurring (even though it was at higher than expected intensities), measurements were made of the temporal pulse profile of the SH pulse to see if any pulse compression was occurring. Disappointedly there was only minor pulse compression of the SH pulse and this occurred at intensities much higher than predicted. The best compressed SH pulse achieved is shown in Figure 5-14. The central portion of SH beam was compressed to approximately 2 ps at intensities above 5.5 GW/cm^2, in significant disagreement with the simulations.

121
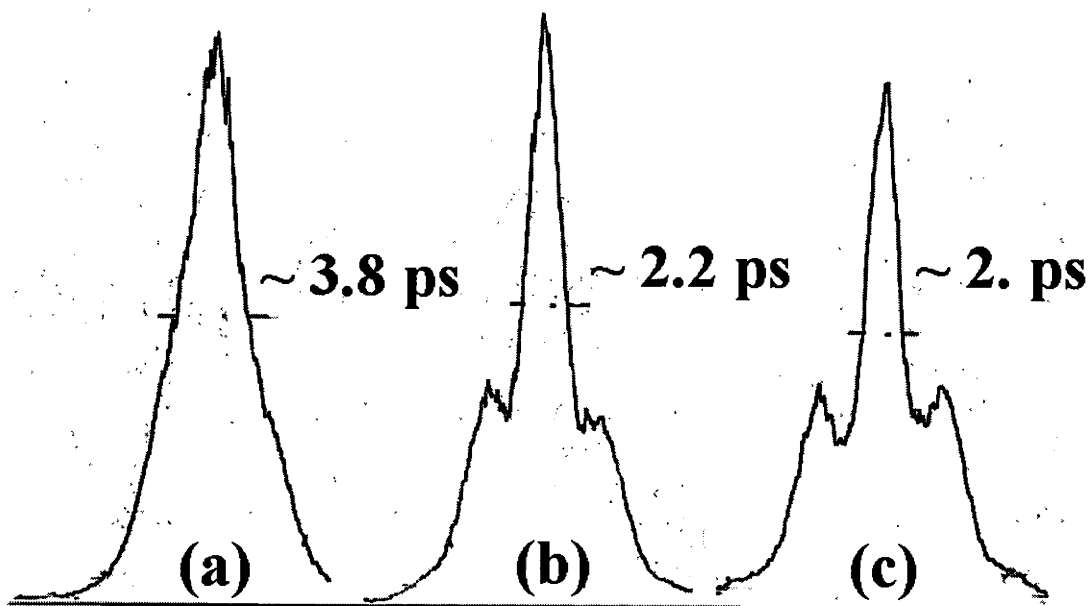
Figure 5-14 : SHG intensity autocorrelations of the 527 nm pulse from the GVMSHG system. The total fundamental intensity is around 6 GW/cm^2 and the 1/e electric field beam radius, w_o = 4.3 mm. (a) is the autocorrelation of the whole SH beam. (b) is the autocorrelation of the central portion of the SH beam within a radius of 0.6 w_o . (c) is the autocorrelation of the central portion of the SH beam within a radius of 0.25 w_o .
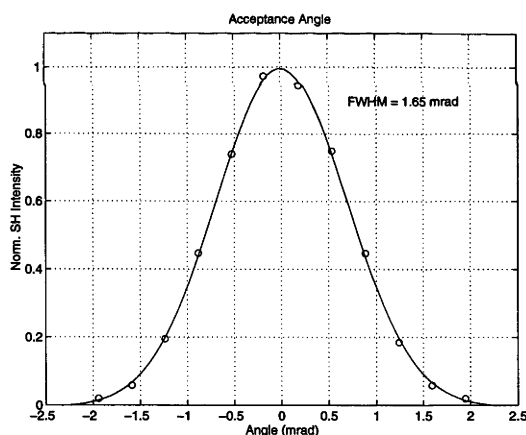
Figure 5-15 : The type II SHG angular acceptance angle for the second 17.5 mm KDP crystal measured with a 3 mJ, 6 ps 1054 nm pulse. The experimental acceptance angle is 1.65 mrad and compares well with the theoretical value of 1.85 mrad.

Again it was suspected that there was something wrong with the SHG crystals; so the acceptance angles were measured of the two KDP SHG crystals and the predelay KDP crystal to see if they were correct. If the measured acceptance angle deviate from the theoretical values, it would indicate that the crystals were of poor quality and unsuitable for high gain SHG. The acceptance angles of each crystal was measured using the short 6 ps amplified 1054 nm pulse, as well as, using a long ~ 60 ps amplified 1054 nm pulse. It is possible to bypass the single mode fibre and to directly amplify the 60 ps pulse from the Antares laser. The 60 ps pulse was used to prevent GVM affecting the measurements of SH power.
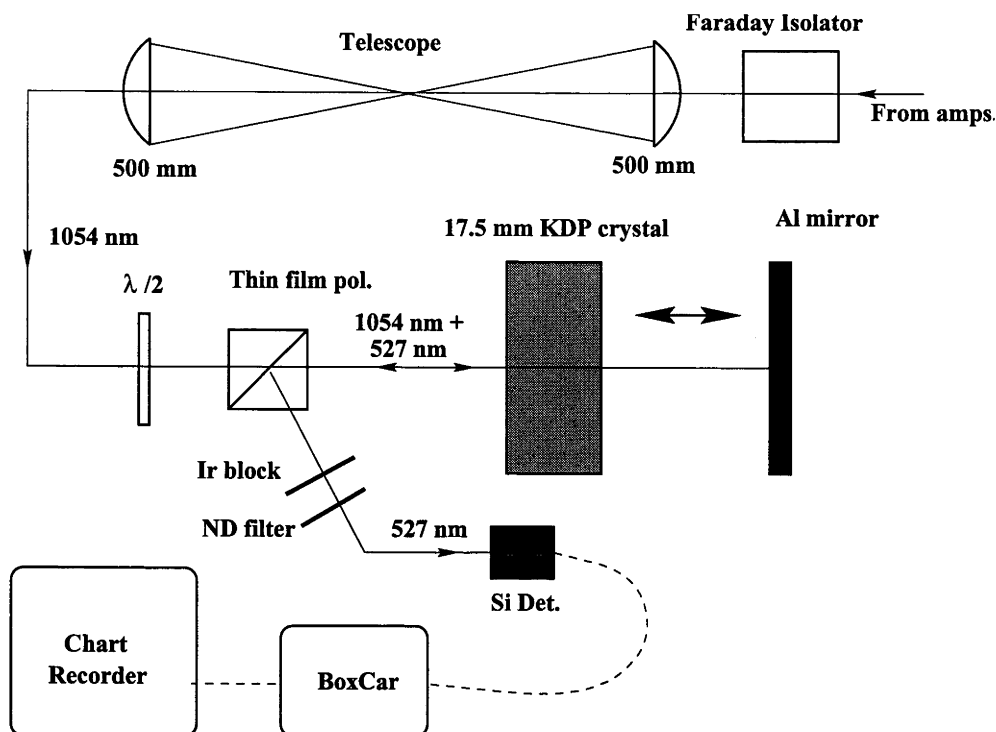
Figure 5-16 : The experimental layout for measuring the coherence length of 1054 nm radiation in air near STP.

The acceptance angles were measured by recording the generated SH power as a function of crystal angle. In each case type II SHG was used with the ratio of intensities between the e and o rays being 1:1. The measured acceptance angles were within 10 % of the theoretical values for the two 17.5 mm KDP crystals for both the long and short pulse (see Figure 5-15). For the 25 mm KDP predelay crystal the experimental value was within 12 % with the theoretical value for the long pulse and within 30 % for the short pulse. The large error of 30 % is probably due to GVM affecting the SH power rather than a poor quality crystal. The experimental error was estimated to be around 10 to 15 %. This agreement of the experimental and theoretical acceptance angles suggests that all the crystals used in the GVMSHG system were performing correctly.

The relative phases of the 1054 nm and 527 nm radiation after propagation through air was also measured to ensure the pulses entered the second SHG crystal with the correct relative phase difference. Using a low fundamental intensity and one of the 17.5 mm KDP crystals, the fundamental and SH beams were reflected back along the beam path by a mirror, passing through the KDP crystal twice. The experimental layout is shown in Figure 5-16. The fundamental intensity was less than 600 MW/cm^2 and the repetition rate was 5 Hz. The KDP crystal was aligned so that the SH power was maximised on the first pass. The Aluminium coated mirror reflected both the fundamental and SH beams back down the beam axis. The SH power after the second pass through the crystal was monitored by using the partial reflection of the SH beam off the thin film polarising beamsplitter. As the distance between the crystal and the mirror increases from zero the phase of the SH rotates relative to the fundamental due to the dispersion of the air. When the phase of the SH rotates by exactly π relative to the fundamental then all the SH power generated in the forward pass will be reconverted to the fundamental in the backward pass through the crystal, assuming no pump depletion or reconversion of the SH beam on either pass through the crystal. To maximise the SH power there should be no phase shift between the SH and the fundamental

123

due to propagation between the crystals. It was found that the distance between the point of maximum and minimum SH power, equivalent to half the coherence length l_c, was 6.5 cm. This agrees well with the calculated value of 6.6 cm. It was also found that for any separation of the crystal and mirror the SH could be maximised by detuning the crystal angle slightly. However, the period between maximum or minimum SH power was always close to 13 cm. Detuning the crystal angle introduces a constant phase mismatch in the SHG process which can compensate for the phase mismatch introduced by the dispersion of air.

5.3.6 Phase distortion in the fundamental pulse

At this stage it was suspected that there was some phase distortion on the fundamental pulse which could be affecting the GVMSHG. This could arise due to SPM in the amplifier chain if it was operated at too high an intensity. To determine whether this was likely, a simple estimation of SPM in the single pass amplifier was made.

The Nd:YLF rod in the single pass amplifier is 6 mm in diameter and 10 cm long. Taking the beam waist $w_o = 3/1.5 = 2$ mm. The peak intensity of the 1054 nm pulse from the RA at the entrance face of the rod is 2.6 GW/cm^2 to 3.9 GW/cm^2, corresponding to pulse energies of 1 to 1.5 mJ. This leads to a phase shift $\Delta\phi$ due to SPM of 0.46 to 0.69 rads over the entire rod if there is no amplification of the pulse. However, since there is an amplification gain of about 10 dB the phase modulation will be worse than this.

A usual criterion for measuring the nonlinear distortions in high-gain laser amplifiers is the B integral. This is a measure of the overall distortion, due to the optical Kerr effect, suffered by a pulse through propagating through a laser amplifier rod. To keep phase distortions to a minimum the B integral should be less than 3 to 5 [17].

$$B = \frac{2\pi n_2}{\lambda} \int_0^l I(z)\,dz = \frac{2\pi n_2}{\lambda} I(0) \int_0^l e^{gz}\,dz$$

where g is the unsaturated gain of the amplifier, l is the length of the rod and n_2 is the nonlinear refractive index. Taking $g = G_{dB}/(4.34\ l) = 0.23$ where $G_{dB} = 10$ and $l = 10$ cm, $n_2 = 3 \times 10^{-16}$ cm^2/W and $I(0) = 2.6$ to 3.9 GW/cm^2 gives B = 1.8 to 2.7. While less then the usual tolerance level the B integral, it is still high enough to indicate that some phase modulation will occur.

Measuring the intensity autocorrelation and spectrum of the pulse does not yield specific information about the phase of the pulse. The best that can be done is to compare the time-bandwidth product and the transform-limited value with any deviation indicating that phase distortion may exist. However, small amounts of phase distortion are difficult to detect by this means, yet it can have a strong effect on SHG. The next section outlines a phase sensitive method of measuring the pulse.

5.4 Self diffraction frequency resolved optical gating (SD FROG)

Frequency resolved optical gating (FROG) is a relatively new technique [18] that allows the measurement of both the amplitude and phase of the electric field of an optical pulse. A number of experimental geometries and nonlinear processes can be used to measure the FROG trace. In our case self diffraction (SD) using the optical Kerr effect was employed. When two identical replicas of a pulse are crossed at an angle in a Kerr medium they interfere creating an intensity grating (see Figure 5-17). Through the optical Kerr effect, this intensity grating creates a refractive index grating from which the pump beams can
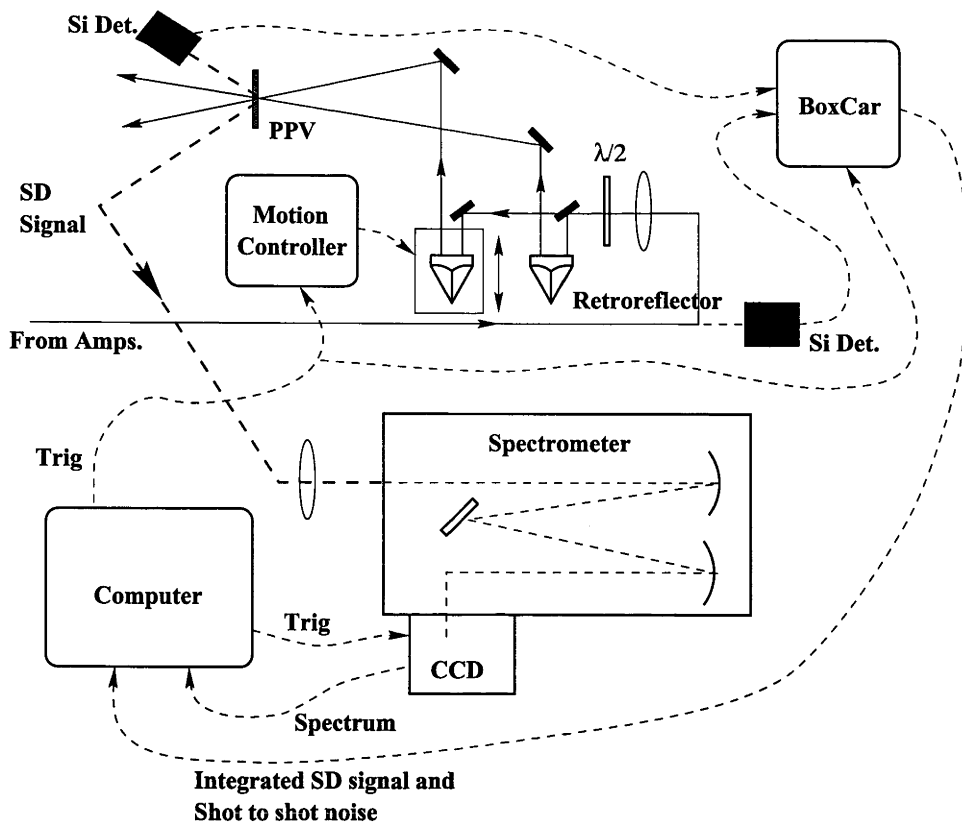
Figure 5-17 : The experimental layout for the SD FROG measurements of the amplified 1054 nm pulse.

self-diffract. Generally self-diffraction leads only to a symmetric interchange of photons between the pump beams since diffraction into higher orders is not phase matched. However, if the medium is thin enough (less than the coherence length of the process), and the induced grating very strong, higher order diffraction is readily observable. To measure the FROG trace of the pulse using SD the spectrum of the SD beam is measured by a suitable spectrometer. By scanning one of the pump beams through the other in time, the complete spectrogram (time vs frequency) of the pulse can be measured. To extract amplitude and phase information about the pulse from this spectrogram is difficult but by visually inspecting the spectrogram or FROG trace valuable information about any phase distortion in the pulse can be found [19]. Figure 5-18 shows typical SD FROG traces and the corresponding instantaneous frequencies of a transform-limited pulse and pulses that have a linear frequency chirp and SPM. Because of the sensitivity of SD FROG to phase distortions visual inspection of a FROG trace provides a strong indication of the magnitude and the type of the phase distortion in a pulse.

The medium used in this experiment was a film of conjugated polymer called poly(p-phenylenevinylene) or PPV. It has a very high n_2 up to 2×10^{-12} cm^2/W allowing the use of quite thin films to produce enough signal to be used in FROG. It has been previously used in the Laser Physics Centre for SD FROG measurements of $\sim$ 100 fs pulse from an amplified Ti:Sapphire system [20]. The film was around 10 μm thick and was deposited on a glass slide.

The amplified 1054 nm pulse was split into two identical replicas using a 50 % reflectivity beamsplitter and the two beams were focussed to overlap on the PPV film to a spot less than 100 μm in diameter. The energy of the pulse was greatly reduced (OD > 2) by neutral density filters to protect the film from burning. One beam was delayed relative to the other

125
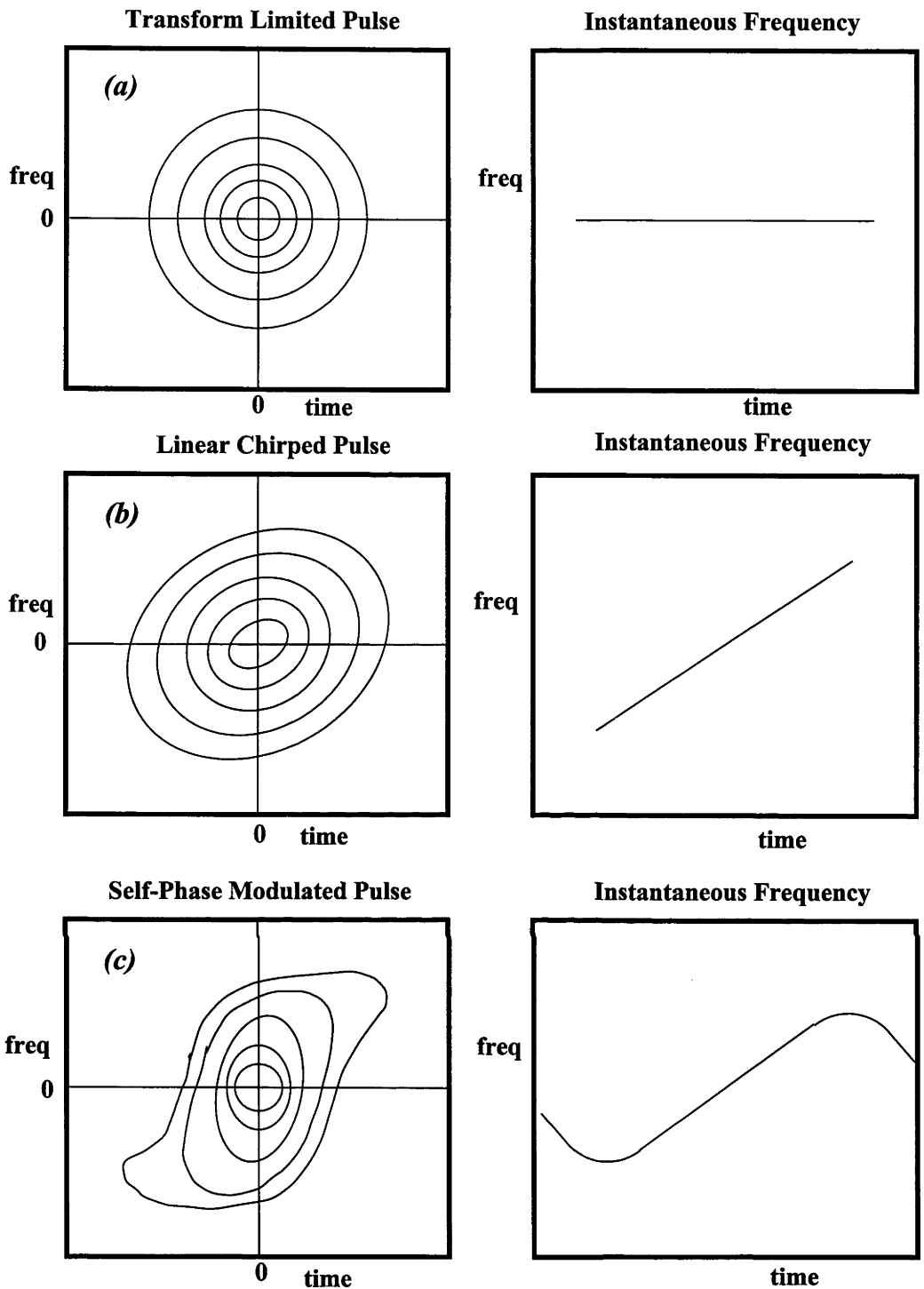
Figure 5-18 : Typical examples of the self-diffaction FROG traces and the corresponding instantaneous frequencies of, (a), a transform-limited pulse, (b), a pulse with a linear frequency chirp and (c), a self-phase modulated pulse.

by a computer controlled translation stage that moved one of the retroreflectors. The zero position, where both beams were coincident in time at the focal point, was set by using a KDP SHG crystal. The SD signal was sent to a McPherson 1m scanning spectrometer fitted with the Lamda spectrometer's 2048 channel CCD array. The spectrometer resolution was 0.6 Angstroms. The CCD array measured the spectrum of the SD pulse and was controlled by a computer. The computer was able to store 100 successive exposures from the CCD array. This allowed the FROG trace to be constructed from spectra measured from 100 steps in time.

Each scan was averaged over 10 shots to reduce the effect of shot to shot variation in energy. Also the average shot to shot variation in the pulse energy was monitored by a Si detector positioned before the pulse entered the beamsplitter. The second Si detector measured the intensity of the SD signal and integrated the SD signal in time, ie. it produced a third order intensity autocorrelation of the pulse. Again the data from both detectors was averaged over 10 shots.

To control the timing of the data capture system the trigger pulse used to fire the laser amplifiers was also used to trigger the computer. The computer then triggered the BoxCar integrator, moved the translation stage and started an exposure of the CCD array. The translation stage was triggered before the BoxCar and the CCD array to take into account the travel time in moving to a new position. The measurements were taken at 10 Hz.

To prevent distortion of the pulse from SPM in the PPV film, the SD signal was restricted to less than 0.1 % of the pump power [21]. The time direction was sampled at 333 fs per step and the wavelength range was sampled at 0.008 nm per pixel. According to [21] the time step should lie between 0.27 ps and 2.2 ps and the entire pulse, down to 0.01 % of the peak intensity, should lie within FROG trace.

To check that the data was correct, the frequency marginal or the integration of the FROG trace in the time delay direction was compared with the expected frequency marginal, which is the convolution of the spectrum of the pulse and its second harmonic.

$$M_{SD}(\omega) = \int_{-\infty}^{\infty} I_{FROG}(\omega, t) dt$$

$$M_{SD}(\omega) = I_{\omega}(-\omega) * I_{2\omega}(\omega)$$

The comparison of the two is shown in Figure 5-19. The match is close indicating that the data is relatively free from systematic errors.
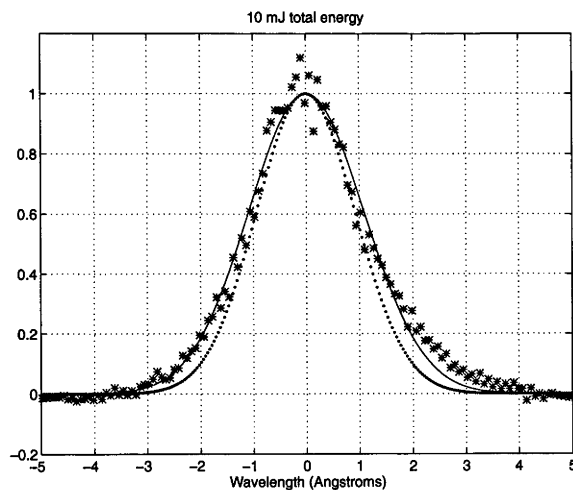
Figure 5-19 : The frequency marginal of the FROG trace for the 10 mJ, 1054 nm pulse compared to the expected frequency marginal. The stars are the data of the frequency marginal and the solid line is the best fit of a Gaussian to the data. The dotted line is the expected frequency marginal.
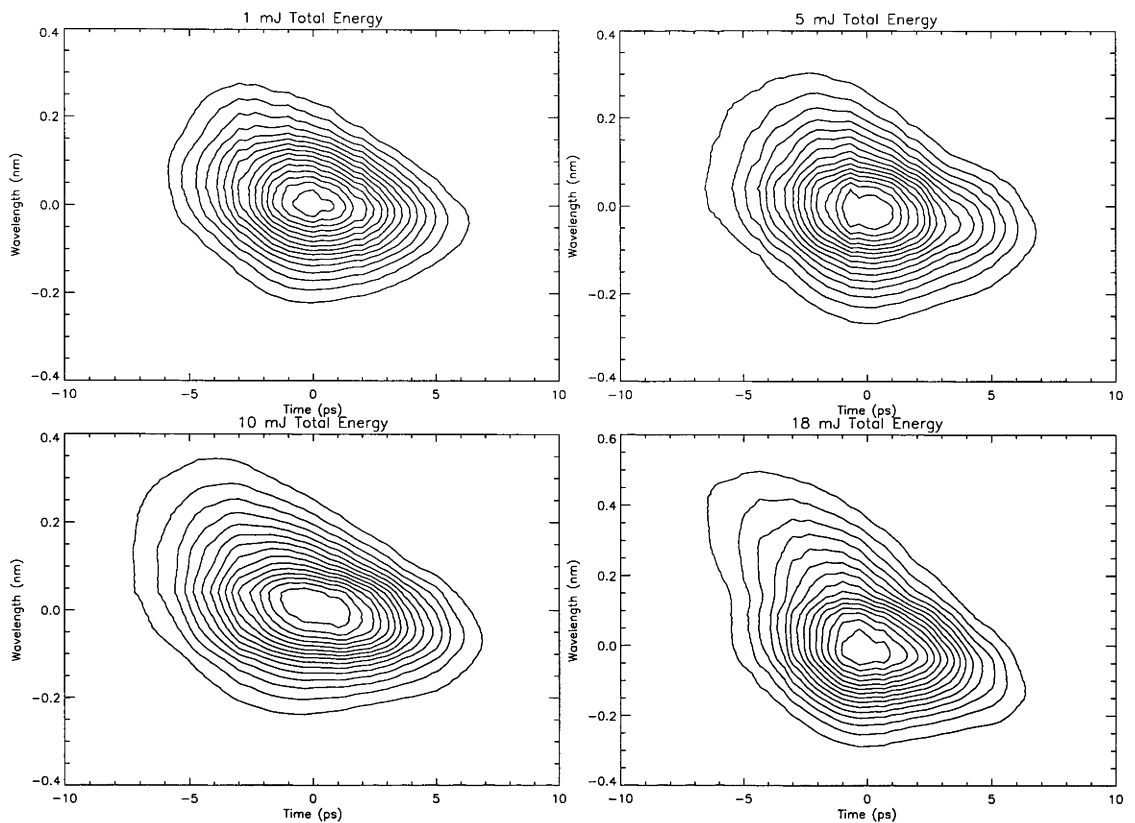
Figure 5-20 : Experimental self diffraction FROG traces of the amplified 1054 nm pulse for various pulse energies. The repetition rate of the amplifiers was 10 Hz. Please note the change of the wavelength scale for the 18 mJ FROG trace.

To eliminate the effects of shot to shot noise in the FROG trace, the data from each SD FROG trace was normalised against the integrated SD scan taken with the second Si detector. This happens as follows. The mean energy of the pulse over the entire scan time was found from the data taken by the first Si detector. For each data point the percentage deviation from this mean energy was found. This was then used to eliminate noise in the integrated SD scan. Since the SD signal responds as I_0^3, where I_0 is the incident intensity, the error due to variation in pulse energy is 3 times worse in the SD signal. Each data point in the integrated SD scan was corrected for this error and then a Gaussian was fitted to the data (see Figure 5-23). The agreement between the data and the Gaussian was generally good. This corrected integrated SD scan was then used to normalise the FROG trace by scaling every spectra by the difference between the fitted Gaussian and the data point in the integrated SD scan.

This did not remove all experimental noise in the FROG trace. To remove small scale structure the data were smoothed using an IDL function which applies a specified box averaging over the entire trace. Care was taken that the inherent shape of the FROG trace was not distorted by this process but that noise on the FROG trace was removed as efficiently as possible.

The FROG measurements of the amplified 1054 nm pulse are shown in Figure 5-20. Also shown in Figure 5-21 are the FROG traces for a 6 ps and a 4 ps transform-limited Gaussian pulse.
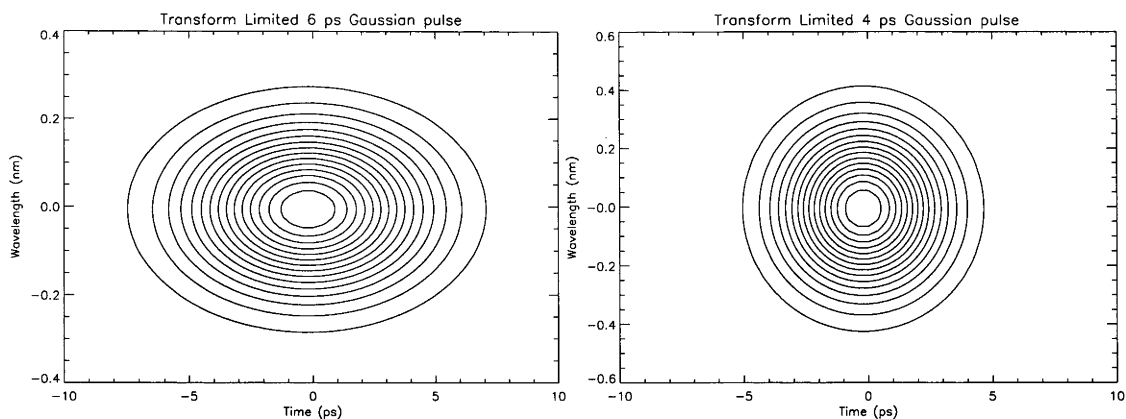
Figure 5-21: Simulated self diffraction FROG traces for transform-limited Gaussian pulses that are 6 ps and 4 ps in duration, respectively. Please note the change of the wavelength scale between traces.
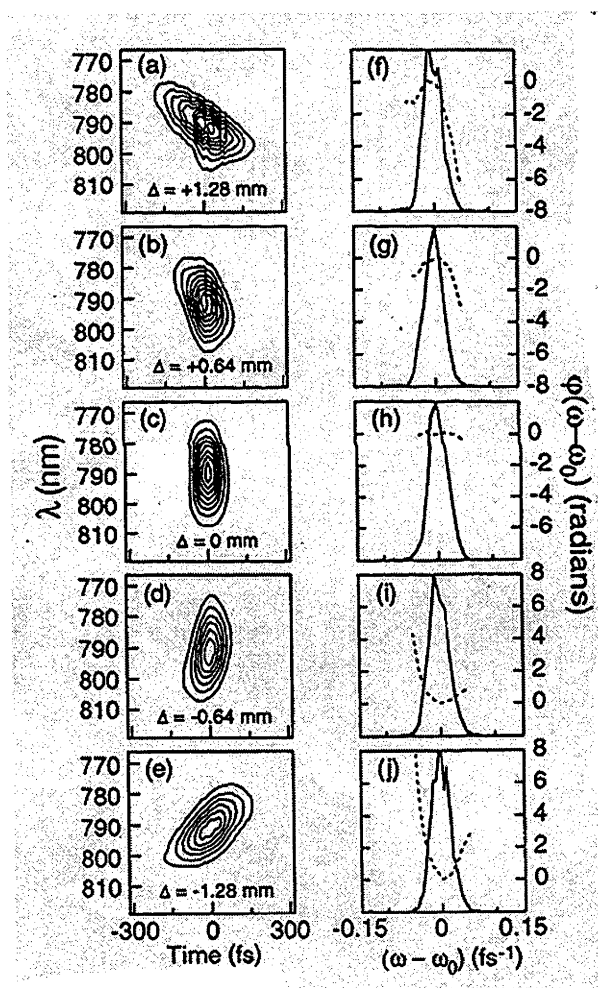
Figure 5-22 : (a) - (e) are polarisation gate FROG traces of pulses from a chirped-pulse amplification Ti:Sapphire laser system for different grating separations. (f) - (j) are the retrieved amplitude and phase of the spectra of the pulse. Trace (c) and plot (h) show the pulse from the optimal grating separation. Reproduced from [22].

129
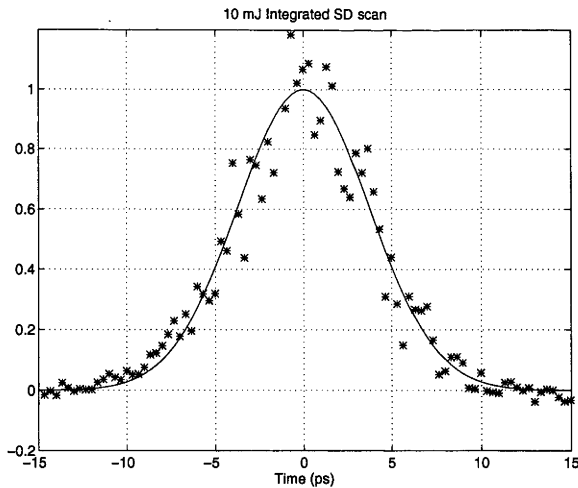
Figure 5-23 : The corrected integrated self diffraction scan for the 10 mJ, 1054 nm pulse.

As is evident from the resulting FROG traces, the 1054 nm pulses do suffer from phase distortion which becomes worse with increasing pulse energy. The first plot in Figure 5-20 shows the pulse from the RA with an energy of 1 mJ. This indicates that while the single-pass amplifier added significantly to the phase distortion, especially at high energies, the pulse from the RA was already distorted.

The exact amplitude and phase of the electric field in time and frequency were not extracted from the FROG traces. However, a major advantage of FROG analysis is that a qualitative evaluation of the phase distortion is often evident from visual inspection of the traces. It is apparent that the higher wavelength side of all the FROG traces displays a negative linear frequency chirp. The lower wavelength side has a more complex phase structure which could result from competition between SPM and a linear frequency chirp. Similar FROG traces have been reported before. Figure 5-22 shows a series of FROG traces and the retrieved power spectra and corresponding spectral phases of the pulses from a CPA Ti:Sapphire laser for different diffraction grating pulse compressor separations. The figure is reproduced from [22] and the FROG traces were taken using the polarisation gate (PG) geometry. The FROG traces from PG and SD are very similar since they are both based on the third order nonlinear, optical Kerr effect [19], especially for low levels of phase distortion. The FROG trace (a) in Figure 5-22 is qualitatively very similar to the FROG traces taken of the 1054 nm pulse particularly the sloping upper edge; the square-like lower, right-hand edge; and the "pinched" central peak. Figure 5-22(f) shows the retrieved power spectrum and the spectral phase from Figure 5-22(a). Since there is a qualitative match between the FROG traces in Figure, especially for the 10 mJ and 18 mJ traces, and the FROG trace in Figure 5-22(a) it is reasonable to expect that the spectral phase characteristics of the 1054 nm pulse are the same as those shown in spectrum in Figure 5-22(f). The spectral phase of Figure 5-22(f) shows that lower wavelength portion of the pulse has a linear frequency chirp (quadratic spectral phase) while the rest of the pulse has a relatively flat, cubic spectral phase.

The linear frequency chirp evident in the FROG traces in Figure 5-20 indicates that the pulse could be compressed after amplification. At the time of writing this thesis, Prof. B. Luther-Davies had constructed a 4 pass diffraction grating, pulse compressor and succeeded in compressing the pulse the RA from 6 ps down to ~ 4 ps. The pulse durations were measured using degenerate four-wave mixing (DFWM) in glass in the same apparatus used to take the SD FROG traces. While glass has a very low n_2 , DFWM is a phase matched process making the process much more efficient. The fact that the pulse can be compressed confirms a substantial linear frequency chirp existed on the pulse from the RA.

130

5.4.1 GVMSHG with a phase distorted fundamental pulse.

Since the fundamental pulse was not transform-limited it became important to understand how phase distortion affects the GVMSHG process Because of the existence of, for example, a linear chirp, the phase mismatch for SHG is no longer constant but varies in time, frequency and position within the crystals. To model this is beyond the scope of the numerical simulation presented earlier. However, the following discussion provides a qualitative understanding of how significant phase distortion is to the GVMSHGprocess and how it actually affects SH pulse compression.

Sources of phase modulation in the GVMSHGprocess are the beam divergence, the group velocity mismatch between the waves and any phase mismatch due to phase distortion in the fundamental pulse.

The phase mismatch due to the beam divergence has already been discussed and is generally kept as low as possible. For a beam divergence, $\Delta\theta$, of 150 μrad, such as in the experiment, gives a phase mismatch $|\Delta k| = \beta_\theta \Delta\theta = 0.38$ cm^{-1}.

The group velocity mismatch introduces an effective phase mismatch into the SHG process because the pulses walk away from each other changing the dynamics of the interaction and hence the phase difference between the waves. The predelay in the GVMSHG process changes this effective phase mismatch to alter the relative phase difference of the waves so that there is efficient compression of the SH pulse. By changing the GVM between the pulses through a predelay the interaction can be altered. The ideal predelay balances the phase modulation of the SH pulse so it experiences equal phase modulation on both sides of the central peak. Without predelay the SH pulse experiences an uneven phase modulation over its temporal profile resulting in the SH pulse breaking up into a number of peaks through pump depletion and reconversion. The effective phase mismatch due to GVM can be roughly estimated by considering the GVM and the pulse duration of the interacting waves. The phase mismatch due to GVM (see Section 3.2) is

$$\Delta k = \left(\frac{1}{v_g^o} - \frac{1}{v_g^e}\right)\delta\omega = 1.32[ps/cm]\delta\omega$$

For a Gaussian pulse the bandwidth $\delta\omega \approx 4 \ln(2)/\Delta t$, where $\Delta t = 6$ ps gives $\delta\omega \approx 0.46$ ps^{-1} and $|\Delta k| \approx 0.62$ cm^{-1} . Again this is quite a low phase mismatch.

The phase mismatch due to a phase distortion in the fundamental pulse was not modelled in the numerical simulation as it was assumed that the pulse was transform-limited. The phase mismatch due to a phase distortion can be hard to model if the distortion is of a complex nature. To provide a simple estimate of the level of phase mismatch it was assumed the phase distortion was due to a linear frequency chirp. A number of estimates will be used to find the magnitude of the frequency chirp in the fundamental pulse.

To be able to compress the 1054 nm pulse from 6 ps down to ~ 4.5 ps, a compression of ~ 1.3 times, requires a chirp parameter b of 0.8 [23] where the compression of a Gaussian pulse of pulse duration Δt_0 (FWHM) due to a linear frequency chirp is

$$\Delta t_{min} = \frac{\Delta t_0}{\sqrt{1+b^2}}$$

The expansion factor $\sqrt{1+b^2}$ can be looked on as the excess bandwidth of the time-bandwidth product. So, the spectrum of the pulse is $\sqrt{1+b^2}$ larger than the transform-limited value. In this case the excess frequency due to the linear frequency chirp is $\Delta\omega = (1 - \sqrt{1+b^2}$

) $\Delta\omega_0$ where $\Delta\omega_0 = 4 \ln(2)/\Delta t_0$. This excess frequency bandwidth corresponds to a phase mismatch $\Delta k = \Delta\omega/c$. This phase mismatch is due to the difference in frequency between components in the pulse. For an expansion factor $\sqrt{1+b^2} = 1.3$ this means a phase mismatch $\Delta k = 4.6$ cm^{-1}. This is large compared to the interaction phase mismatch due to GVM and the phase mismatch due to the beam divergence.

Another estimate of the phase mismatch due a linear frequency chirp was taken from the SD FROG trace of the 10 mJ, 1054 nm pulse. The slope of the central portion of the FROG trace (by taking a line along the long axis of the trace, see Figure 5-24) and accounting for the fact that a SD FROG trace indicates a linear frequency chirp that is 4/3 greater than the real linear frequency chirp [19] the chirp parameter, b, was taken to be between 0.6 to 0.75, giving a expansion factor $\sqrt{1+b^2}$ between 1.15 to 1.25. The upper limit is quite close to the chirp parameter estimated from the achieved pulse compression. For a chirp parameter b = 0.6 the phase mismatch is still large at $\Delta k = 2.3$ cm^{-1} . As can be seen even a small linear frequency chirp introduces a large phase mismatch into the SHG process.

The parametric gain coefficient for OPA is $\Gamma^2 = (2/n \, \varepsilon_0 \, c) \, K_0 \, K_e \, I_2$ and $\Gamma^2 = (2/n \, \varepsilon_0 \, c) \, K_0 \, K_2 \, I_e$ (in our case $I_e = I_o = I_{Total}/2$) is the gain coefficient for SHG (degenerate sum frequency generation) and where K_j is the nonlinear coupling coefficient, n is the refractive index of the material and ε_0 is the permeability of free space. Taking the total fundamental intensity $I_{Total} = 6$ GW/cm^2 and, for this example, the SH intensity also reaches 6 GW/cm^2, gives a parametric gain coefficient $\Gamma = 2.4$ cm^{-1} for type II, SHG in KDP and is the same for both SHG and OPA. Immediately one can see that there is going to be problems in the GVM SHG process if the large phase mismatch due to a linear frequency chirp in the fundamental pulse is taken into account. The large phase mismatch due to the frequency chirp will dominate over the effect of parametric gain and GVM in the SHG process.

At the entrance to the crystal, where the e and o ray fundamental intensities are equal and the SH intensity is zero, the relative phase difference between the fundamental and SH radiation should be $-\pi/2$. As the waves interact within the crystal the SH pulse grows in intensity with the interaction causing a shift in the phase of all three waves at different time points. This can be seen from the three coupled PDEs in Eqn 5-1 and the analysis of Bakker, *et. al.* [24]. Bakker, *et. al.*, analysed the effect of a phase mismatch and an initial phase difference on the second-order nonlinear processes of parametric amplification and SHG. They included the effects of group velocity mismatch and pump depletion, building on the previous work of [25] and [26]. The phase of each of the three coupled PDEs in Eqn 5-1 is [24]

$$\arg\left(dE_o/dz\right) = \frac{\pi}{2} - \arg(E_e) + \arg(E_2)$$

$$\arg\left(dE_e/dz\right) = \frac{\pi}{2} - \arg(E_e) + \arg(E_2)$$

$$\arg\left(dE_2^{int}/dz\right) = \frac{\pi}{2} + \arg(E_o) + \arg(E_e)$$

$$\arg\left(dE_2^{ph}/dz\right) = \frac{\pi}{2} + \arg(E_2)$$

<div align="right">**Eqn 5-3**</div>
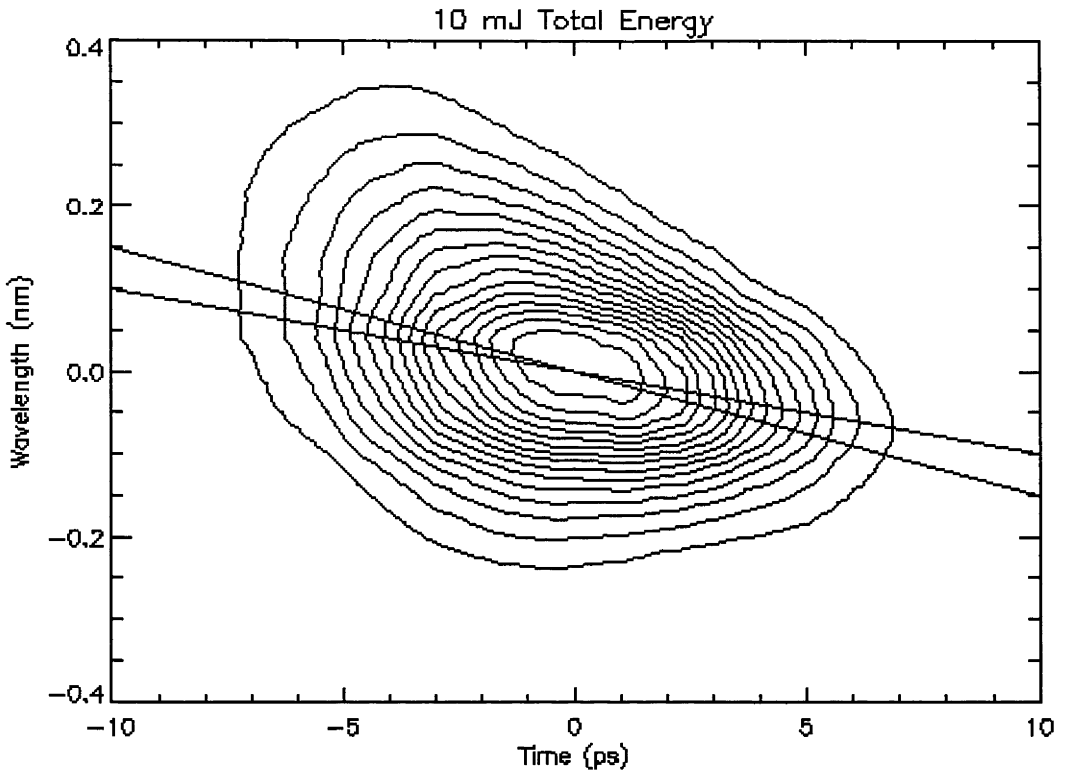
Figure 5-24 : The SD FROG trace of the 10 mJ, 1054 nm amplified pulse. The two lines in the trace show the upper and lower estimates of the linear frequency chirp used in the text.

where $arg(E_j)$ is the phase of the complex electric field E_j for each of the three waves, j = o, e, 2. The important fact about these equations is that the phase of the differential of the SH has two parts: the superscript "int" refers to the phase due to the nonlinear interaction, which can include GVM, and the other superscript "ph" refers to the phase from an initial phase mismatch between the waves, such as that from a linear frequency chirp. The dynamics of the SHG process are dominated by a phase modulation generated by the parametric interaction if the initial phase mismatch is small. If the initial phase mismatch is large, or the phase modulation due to the interaction becomes small at any stage, then the process is dominated by the initial phase mismatch. Since $E_j = E_j$ (z,t) the pulse can acquire different phases at different time points along the pulse just from the interaction alone.

Without the effect of the phase mismatch due to a linear frequency chirp the GVMSHG process is dominated by the phase modulation created through the SHG process, ie. GVM and SHG/parametric gain. However, since the phase mismatch due to the linear frequency chirp is greater than or equal to both effects it will dominate, or at the least severely affect, the SHG process and the compression of the SH pulse.

However, in the central portion (in time) of the fundamental pulse the phase mismatch due to any phase distortion like a linear frequency chirp is smaller than when considering the phase mismatch across the entire pulse. It likely that in the central portion of the pulse there could still be some pulse compression of the SH pulse as long as the phase mismatch due to the interaction and GVM dominated over any phase mismatch due to a frequency chirp in the fundamental. This could be the possible reason why some mild pulse compression is still seen in the central portion of the SH beam from the GVMSHG system.

In the paper by Umbrasas, *et. al.,* [4], they too had problems with phase modulation on the fundamental pulse. Their 12 ps, 20 mJ pulse had a time-bandwidth product of 0.7. They

used strong spatial filtering and apodized apertures that selected an area at the centre of the fundamental beam to provide a useable quality beam. As a result, with roughly half the original peak power available after filtering, they were limited in their achievable total fundamental intensity. They needed to use small beam areas to achieve intensities up to 4.2 GW/cm^2, limiting energy conversion through beam walk-off and beam divergence. The chirped fundamental pulse had the effect of increasing the power of the sidelobes on the compressed SH pulse and limiting the achievable compressed pulse duration. The higher the phase modulation and fundamental intensity, the higher the sidelobes and the smaller the compression. In our GVMSHG experiment the fundamental pulse had a time-bandwidth product of ~ 1.3; nearly two times worse than in the case in Umbrasas, *et. al.*, while using a similar length crystal (3.5 cm total compared to 4 cm in Umbrasas, *et. al.*) . This is further evidence that the chirped fundamental pulse was the probable cause of the lack of a suitably compressed SH pulse from the GVMSHG system.

5.5 Summary and conclusions

This chapter presents work done to model and efforts to experimentally realise an efficient SHG system that compresses the SH pulse in time through the effect of GVM. Despite having a non-optimum predelay and crystal length the theoretical simulations suggest that the SH pulse can be compressed from 6 ps down to ~ 200 fs in duration, assuming an ideal, plane-wave interaction, at half the intensity required for SHG without predelay. This process is efficient enough that the resulting peak power of the compressed SH pulse should be more than enough to drive the LBO OPA.

The SHG system used two KDP crystals in an alternating-Z configuration to help alleviate the problem of the small angular acceptance angle of KDP limiting the SHG conversion efficiency.

A Nd:YLF amplifier chain consisted of a mode-locked, cw Nd:YLF laser; a ring regenerative amplifier and a single pass amplifier providing the fundamental pulses for the GVMSHG system. The amplifiers boosted the pulse energy from the oscillator from ~ 10 nJ to ~ 18 mJ while compressing the pulse from 60 ps down to 6 ps in duration. To achieve this pulse compression, a 50 m length of single mode optical fibre was used to chirp the output pulse from the Nd:YLF laser oscillator via SPM. In the regenerative amplifier only those frequency components falling within the gain narrowed linewidth of the system received high gain, and this lead to the amplification of only a part of the pulse in time, strongly reducing the output pulse duration.

Intensity autocorrelations and spectral measurements of the amplified 1054 nm pulse indicated that the pulse was close to transform-limited, within the experimental uncertainties. Unfortunately, when the energy conversion of fundamental into SH via GVMSHG was measured it was found to be less than expected from the numerical simulations.

The beam from the amplifier chain was found to be excessively divergent in one plane due to distortions introduced by the single pass amplifier, resulting from thermal loading of the Nd:YLF rod. Reducing the repetition rate of the amplifier helped improve the beam quality. However, the beam still had a divergence three times greater than the diffraction limit in one plane and as the pulse energy is increased the beam divergence changed, roughly doubling from 1 mJ to 15 mJ. To compensate for the higher beam divergence in one plane, the o-ray axis, which is less sensitive to beam divergence, of the SHG crystals was aligned with the highly divergent plane of the fundamental beam. Nevertheless, the minimum beam divergence remained as roughly twice the diffraction limit.

Intensity autocorrelation measurements were then taken of the SH pulse. The SH pulse displayed only mild pulse compression, with the pulse being compressed down to ~ 2 ps in duration at an intensity much higher than expected. The angular acceptance angles of the predelay and SHG crystals were measured and found to agree with the theoretical values, indicating that the crystals were of high quality and not responsible for the problems with GVMSHG. The separation between the two KDP SHG crystals was also checked and found to be correct.

At this stage it was suspected that there must something wrong with the fundamental pulse that had so far eluded detection. Phase sensitive measurements of the pulse were taken using self diffraction FROG. These indicated that the pulse suffered from a complex phase distortion. The phase distortion primarily consisted of a linear frequency chirp, due to a quadratic spectral phase, with higher order phase terms as well.

It was argued that the frequency chirp over the fundamental pulse has a substantial effect on the GVMSHG. The argument was based on estimates of the relative magnitude of the various effects in the GVMSHG process. The beam divergence is a minor effect and does significantly alter the evolution of the SH pulse. The evolution of the SH pulse is controlled by an interplay between the parametric gain, due to the three wave interaction, and the GVM between the pulses. This is what was modelled by the numerical simulation in the beginning of the chapter. To estimate the effect of a frequency chirp on this process the interaction was described in terms following the analysis of [24]. The SHG process can be thought of as being controlled by the change in the phase difference between the three interacting waves. The parametric gain and GVM affect this phase difference to alter the evolution of the SH pulse and the dynamics of the SHG process. A frequency chirp or phase distortion can also affect the phase difference between the waves since the SHG process is also sensitive to an initial phase mismatch. It was estimated that if the phase distortion in the amplified 1054 nm beam was purely due a linear frequency chirp then the phase distortion would probably dominate, or at the least significantly affect, the SHG process because its effect is at least as great as that of the parametric gain and the GVM. It is expected that this is the cause of the lack of significant SH pulse compression. The small, measured pulse compression may be due to a temporal portion of the pulse were the phase distortion is not that great compared to the rest of the pulse.

At this time a four-pass, diffraction grating pulse compressor has been constructed by Prof. B. Luther-Davies that corrects for the inherent frequency chirp in the pulse from the regenerative amplifier. The fundamental pulse has been successfully compressed from 6 ps down to ~ 4.5 ps in duration. It is expected that this will improve the achievable SH pulse compression by removing the frequency chirp in the pulse.

5.6 References

[1] Y. Wang, "Development of a high contrast Nd:Glass laser using chirped pulse amplification," PhD, *Laser Physics Centre, RSPhySE*: Australian National University, 1993.

[2] Y. Wang and B. Luther-Davies, "Frequency-doubling pulse compressor for picosecond high-power neodymium laser pulses," *Optics Letters*, vol. 17, p. 1459, 1992.

[3] D. Eimerl, "Electro-optic, linear, and nonlinear optical properties of KDP and its isomorphs," *Ferroelectrics*, vol. 72, p. 95, 1987.

[4] A. Umbrasas, J.-C. Diels, J. Jacob, G. Valiulis, and A. Piskarskas, "Generation of femtosecond pulses through second-harmonic compression of the output of a Nd:YAG laser," *Optics Letters*, vol. 20, p. 2228, 1995.

[5] Y. Wang, B. Luther-Davies, Y. H. Chuang, R. S. Craxton, and D. D. Meyerhofer, "Highly efficient conversion of picosecond Nd laser pulses with the use group-velocity-mismatched frequency doubling in KDP," *Optics Letters*, vol. 16, p. 1862, 1991.

[6] N. K. Madsen and R. F. Sincovec, "Algorithm 540 : PDECOL, General collocation software for partial differential equations," *ACM Trans. Mathematical Software*, vol. 5, p. 326, 1979.

[7] F. Zernike, "Refractive indicies of Ammonium Dihydrogen Phosphate and Potassium Dihydrogen Phosphate between 2000 Angstroms and 1.5 microns," *JOSA*, vol. 54, p. 1215, 1964.

[8] R. C. Eckardt, H. Masuda, Y. X. Fan, and R. L. Byer, "Absolute and relative nonlinear optical coefficients of KDP, KD*P, BBO, LIO$_3$, MgO:LiNbO$_3$ and KTP measured by phase-matched second harmonic generation," *IEEE J. Quant. Electronics*, vol. QE-26, p. 922, 1990.

[9] S. K. Kurtz, "Measurement of Nonlinear Optical Susceptibilities," in *Quantum Electronics : A treatise*, vol. 1, H. Rabin and C. L. Tang, Eds. New York: Academic Press, 1975.

[10] S. Singh, *CRC Handbook of laser science and technology*, vol. 3, pt 1: CRC Press Inc., 1986.

[11] M. A. Norton, D. Eimerl, C. A. Ebbers, S. P. Velsko, and C. S. Petty, "KD*P frequency doubler for high average power applications," *SPIE, Solid State Lasers*, vol. 1223, p. 75, 1990.

[12] J. J. Zondy, M. Abed, and S. Khodja, "Twin-crystal walk-off-compensated type II second-harmonic gerenration: single-pass and cavity-enhanced experiments in KTP," *JOSA B*, vol. 11, p. 2368, 1994.

[13] R. S. Craxton, S. D. Jacobs, J. E. Rizzo, and R. Boni, "Basic properties of KDP related to the frequency conversion of 1 micron laser radiation," *IEEE J. Quant. Electronics*, vol. QE-17, p. 1782, 1981.

[14] D. Eimerl, "High average power harmonic generation," *IEEE J. Quant. Electronics*, vol. QE-23, p. 575, 1987.

[15] S. P. Velsko and D. Eimerl, "Precise measurements of optical dispersion using a new interferometric technique," *Applied Optics*, vol. 25, p. 1344, 1986.

[16] Y. Wang, B. Luther-Davies, and H. Giordano, "Generation of energetic picosecond optical pulses from Nd:Doped crystal lasers," presented at IQEC, Sydney, 1996.

[17] A. Siegman, *Lasers*. Mill Valley: University Science Books, 1986.

[18] D. J. Kane and R. Trebino, "Characterization of arbitary femtosecond pulses using frequency-resolved optical gating," *IEEE J. Quant. Electrons*, vol. 29, p. 571, 1993.

[19] K. W. DeLong, R. Trebino, and D. J. Kane, "Comparison of ultrashort-pulse frequency-resolved-optical-gating traces for three common beam geometries," *JOSA B*, vol. 11, p. 1595, 1994.

[20] B. Luther-Davies, M. Samoc, J. Swiatkiewicza, A. Samoc, M. Woodruff, R. Trebino, and K. W. DeLong, "Diagnostics of femtosecond laser pulses using films of poly(p-phenylenevinylene)," *Optics Communs.*, vol. 131, p. 301, 1996.

[21] K. W. DeLong, D. N. Fittinghoff, and R. Trebino, "Practical issues in ultrashort-laser-pulse measurement using frequency-resolved optical gating," *IEEE J. Quant. Electrons.*, vol. QE-32, p. 1253, 1996.

[22] B. Kohler, V. V. Yakovlev, K. R. Wilson, J. Squier, K. W. DeLong, and R. Trebino, "Phase and intensity characterization of femtosecond pulses from a chirped-pulse amplifer by frequency-resolved optical gating," *Optics Letts.*, vol. 20, p. 483, 1995.

[23] G. P. Agrawal, *Nonlinear fiber optics*: Academic press, Inc., 1989.

[24] H. J. Bakker, P. C. M. Planken, L. Kuipers, and A. Lagendijk, "Phase modulation in second-order nonlinear-optical processes," *Phys. Rev. A*, vol. 42, p. 4085, 1990.

[25] R. C. Eckardt and J. Reintjes, "Phase matching limitations of high efficiency second harmonic generation," *IEEE J. Quant. Electrons.*, vol. QE-20, p. 1178, 1984.

[26] Y. N. Karamzin and A. P. Sukhorukov, "Limitation on the efficiency of frequency doublers of picosecond light pulses," *Sov. J. Quant. Electron.*, vol. 5, p. 496, 1975.

6. High gain optical parametric amplification

6.1 Introduction

This chapter outlines numerical studies of high gain optical parametric amplification for several nonlinear crystals. With high gain optical parametric amplification it is possible to efficiently produce broadly tunable, ~ GW, sub-500 fs near-transform-limited pulses from 780 nm to 900 nm for the signal and from 1270 nm to 1625 nm for the idler. However, numerical work was conducted to optimise the performance of the optical parametric amplification system against the detrimental effects of group velocity mismatch (GVM) and variation in the intensity and pulse duration of the pump and seed signal pulses.

Since optical parametric amplification is a nonlinear process, sensitive to factors such as GVM, when used with short pulses, and the input power of the seed pulse, an important factor in designing the OPA system is to obtain a linear or sub-linear transfer function for the power of the output pulses. The transfer function being the relationship between the power of output pulses with the variation in the power of the pump pulses. Figure 6-1 shows a transfer function with three relationships. The line with a gradient > 1 would produce output pulses with peak powers that were very sensitive to variations in the pump power and, therefore, should be avoided. The line with a gradient of 1 means that any amplitude noise is not amplified by the OPA. The last line with a gradient < 1 means the peak power of the output pulses is relatively insensitive to variations in the pump power, making it the more desirable transfer function of the three.

As will be shown in the section on the first OPA, using one OPA to amplify low power seed pulses to high powers usually results in output pulses that are sensitive to variations in the pump power or the input power of the seed pulse since the transfer function is super-linear (gradient > 1) up to the point of maximum pump depletion. This is because for an undepleted pump pulse the parametric gain is proportional to $\exp(\sqrt{I_{pump}})$. In this case, to amplify Gaussian-like seed pulses up to power levels where pump depletion and reconversion occurs, to maximise the energy conversion and peak power of the output pulses, would result in the pulses experiencing a very different amount of gain at different spatial points if
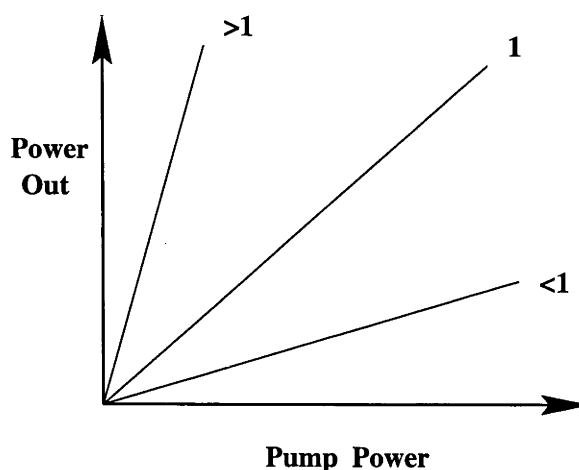

Figure 6-1 : An example transfer function; the power of the output pulse as a function of the power of the pump pulses.

the pulse has a Gaussian beam profile. This will inevitably lead to the high intensity centre of the pulse undergoing reconversion and "breaking" up into a series of narrow peaks while the rest of the pulse undergoes little gain at all. It is not possible to successfully amplify all of the pulse evenly with very high gains $> \sim 1 \times 10^4$. With lower gains it is possible to make Gaussian profile pulses less sensitive to variations in the input parameters.

For this reason the modelled optical parametric amplification system consisted of two, travelling wave Optical Parametric Amplifiers (OPA). The first OPA was designed to use a small portion of the compressed 527 nm pulse from the GVMSHG (Chapter 5) to amplify the low power signal pulse from the OPO (Chapter 3) by up to $\sim 1 \times 10^5$ times while simultaneously reducing the pulse duration of the signal pulse. This amplified signal pulse was then intended for use as the seed pulse in the second OPA which was to be pumped by the remainder of the compressed 527 nm pulse. The seed signal and the generated idler pulse were amplified by ~ 1000 times, to provide better control of the properties of the output pulses, to reach similar power levels as the pump pulse. Several nonlinear crystals were investigated, including KD*P, LBO and BBO, to examine the differences between their performances as high gain OPAs.

While the first OPA uses a very high gain and the peak power of the output pulses will be shown to be sensitive to the peak power of the pump pulses (super-linear transfer function), the second OPA was designed with a low gain so that the peak power of the output pulses would be generally insensitive to variations in the pump power and input power of the seed pulses (sub-linear transfer function).

Perhaps the closest OPA system to the one modelled in this chapter was a triple-pass, 4 mm long, type II, BBO OPA that was pumped by a 1.1 mJ, 200 fs, compressed 527 nm pulse from a GVMSHG system and that produced wavelength tunable, 200 fs signal and idler pulses between 635 nm to 3000 nm [1]. The energy conversion into the signal and idler pulses was less than 8 % (10s of microjoules). The gain on the first pass was 10^7 at a pump intensity of 115 GW/cm^2 , 10^4 at 50 GW/cm^2 on the second pass and 200 at 25 GW/cm^2 on the last pass. The signal and idler pulses exhibited a high contrast of $\sim 4 \times 10^4$ compared to the wings on the pump pulse.

Most of the work detailed above and in the introduction chapter focused on experimental work rather than numerical or theoretical work (see [2-5]). The numerical simulations presented in this chapter looked at the influence of predelay, variation in the initial pump and signal pulse durations, as well as, how tuning the wavelength of the signal and idler wavelengths affected the performance of the OPAs.

6.2 Theory

The equations which govern the parametric amplification or SHG of short optical pulses has been shown before in Eqn 5-1, Chapter 5. The equations for optical parametric amplification, including GVM are :

$$\frac{\partial E_o}{\partial z} = iK_o E_e^* E_2 \exp(i\Delta kz) - \delta t_{o2} \frac{\partial E_o}{\partial \tau} - \frac{1}{2}\alpha_o E_o$$

$$\frac{\partial E_e}{\partial z} = iK_e E_o^* E_2 \exp(i\Delta kz) - \delta t_{e2} \frac{\partial E_e}{\partial \tau} - \frac{1}{2}\alpha_e E_e$$

$$\frac{\partial E_2}{\partial z} = iK_2 E_o E_e \exp(-i\Delta kz) - \frac{1}{2}\alpha_2 E_2$$

For perfect phase matching, ie. $\Delta k=0$, transform-limited input pulses and neglecting absorption the equations simplify to :

139

$$\frac{\partial E_1}{\partial z} = K_1 E_2 E_3 - \delta t_{13} \frac{\partial E_1}{\partial \tau}$$

$$\frac{\partial E_2}{\partial z} = K_2 E_1 E_3 - \delta t_{23} \frac{\partial E_2}{\partial \tau}$$

$$\frac{\partial E_3}{\partial z} = -K_3 E_1 E_2$$

Eqn 6-1

where the subscripts i=1,2,3 refer to the signal, idler and pump waves respectively. $K_i = 2\pi d_{eff}/n_i\lambda_i$ is the nonlinear coupling coefficient and $\delta t_{ij} = (1/vg_i - 1/vg_j)$ is the inverse group velocity mismatch between waves i and j. The above equations show the temporal development of all three infinite plane waves in a time frame relative to the pump, $\tau = t - z/vg_3$, as they propagate through a nonlinear crystal.

Since perfect phase matching was assumed in the simulation the dephasing due to processes such as beam divergence must be kept low for the simulations to be accurately applied to experimental conditions. Other limitations apart from the angular acceptance of a nonlinear crystal are the spectral acceptance bandwidth; Poynting vector beam walk-off; GVM walk-off between the pulses; and self- or cross-phase modulation (SPM/XPM). The spectral acceptance bandwidth must be large enough to support ~ 200 fs pulses otherwise energy will be lost in the parametric conversion process. Generally, the walk-off angle is 1^0 to 2^0 in most crystals and does not pose a problem with short crystal lengths and beam sizes more than a millimetre. The GVM between the waves generally poses a greater problem for frequency conversion of pulses less than a picosecond in duration because the pulses can separate from each other within the crystal length, reducing the interaction length and limiting the conversion efficiency. To control the phase modulation effects from third order nonlinear effects the pump intensity must be kept low enough that there is sufficient parametric gain without causing too much phase distortion of the generated signal and idler waves.

There are many nonlinear optical crystals that can be used as an OPA pumped by light at ~ 530 nm. KDP [6] has a limited transparency range in the near-IR, with the absorption edge for an o-ray at 1200 nm and at 1400 nm for an e-ray. This makes it unsuitable for generating idler pulses wavelength tunable from 1200 nm to above 1600 nm as absorption is very strong for both type I and type II interactions. KD*P [6] on the other hand has a greater transparency range, with the absorption edge for an o-ray at 1600 nm and at 1700 nm for an e-ray making it suitable for type I (e ↔ o+o) and type II (e ↔ o+e, where the o ray is the signal) interactions. BBO [7] is also suitable, using type I and II interactions, for use as an OPA. Another crystal that can be used is LBO [8], but only with a type I (e ↔ o+o) interaction as the type II interaction requires angle tuning over 30^0 to cover the desired wavelength range which would cause problems experimentally. The same reason was used to discount the use of KTP [9] as a useful OPA. Figure 6-2 shows the phase matching curves for the various crystals and phase matching interactions.

The various properties of the most suitable OPA crystals are shown in Tables 6-1 to 6-5. In general the data shown are relevant to the production of signal wavelengths between 780 nm and 920 nm. KD*P has a low nonlinear coefficient, although the type I interaction has a broad spectral acceptance bandwidth and small angular acceptance angle whilst the type II interaction has a broad angular acceptance and a moderate spectral acceptance bandwidth. LBO has a higher nonlinear coefficient than KD*P and very broad angular and spectral acceptance bandwidths. BBO has the highest nonlinear coefficient but a small acceptance angle and a broad spectral acceptance bandwidth for type I interaction but a wide acceptance angle and small acceptance bandwidth for the type II interaction. Assuming a pump beam

waist of 2 mm the crystal length over which walk-off separates the pump and OPA beams in BBO II (which has the greatest walk-off angle of 3.65^0) is 5.5 cm; much greater than the crystal length required for use as an OPA. Assuming a beam waist size of 2 mm which corresponds to a beam divergence of 84 µrad, and limiting any angular dephasing to less than $\pi/10$ implies the angular acceptance angle for the OPA crystal must be greater than 1 mrad. To be able to support short ~ 200 fs pulses at ~ 850 nm the spectral acceptance bandwidth of a particular crystal must be much greater than 5 nm.

Table 6-6 shows standard figures of merit (a measure of how good the crystal is at parametric or SHG generation) for the crystals under investigation. BBO and LBO are much better than KD*P at parametric generation. The low effective nonlinear coefficient of KD*P means that long crystal lengths would have to be used in comparison with BBO and LBO. This would limit the usefulness of KD*P as a high gain OPA.

Table 6-7 shows the nonlinear coupling coefficients and inverse group velocity mismatch parameters for amplifying a signal wave at 800 nm, 850 nm and 900 nm for each OPA. These were the parameters used in the simulations. It is desirable for the nonlinear coupling coefficients and the GVM between the waves to vary as little as possible across the entire tuning range. In that way the OPA is insensitive to variation in the seed signal wavelength. Both KD*P I and LBO I have the lowest GVMs for both the signal and idler of all the potential OPAs examined. They also vary the greatest amount because of this. The BBO I and II crystals have large GVMs, with the inverse GVM for the idler and pump being ~ -1.6 ps/cm for BBO II. This large GVM may affect the overall efficiency of the process, if the crystal length was quite long, due to the signal and idler pulses walking away from the pump pulse. This will be examined in greater detail when the results of the numerical simulations are presented.

Numerical simulations were performed of an OPA system consisting of two crystals; from now on referred to as OPA1 and OPA2. A two crystal OPA system has the added advantage, to the one discussed previously, of keeping the SPM and XPM introduced from the high pump intensities to a minimum. The pump intensity in both OPAs was kept to less than 30 GW/cm^2. For LBO and KD*P, $n_2 \approx 3.2$ x 10^{-16} cm^2/W, while for BBO, $n_2 \approx 4.9$ x 10^{-16} cm^2/W; so the XPM[1] modulation between the waves in OPA2 (where all three waves reach similar power levels) is ~ 0.15 rads/mm for LBO or KD*P and ~ 0.23 rads/mm for BBO at a pump intensity of 20 GW/cm^2. The signal pulse from OPA1 was used as the seed for OPA2. As will be shown, the peak power of the signal pulse from OPA1 was kept much lower than the peak power of the pump pulse so it would not suffer phase modulation, and can be considered a near transform-limited pulse. To amplify the seed signal pulses with one OPA requires pump intensities up 100 GW/cm^2 which would introduce considerably phase modulation on the output pulses.

The pump pulse was assumed to be a Gaussian pulse between 500 fs and 1 ps in duration with up to 2.5 GW peak power. A Gaussian pulse was chosen for simplicity. Even though the compressed SH pulse from the GVMSHGsystem was only approximately Gaussian in the central peak, however, it is this central peak rather than the wings of the pulse which contributes to the optical parametric amplification process. The signal pulse from the stabilised, dual arm OPO was assumed as the seed pulse for OPA1. It was assumed that this signal pulse was tunable between 780 nm to 900 nm (1625 nm to 1272 nm for the idler); was a Gaussian pulse 1.5 ps to 2 ps in duration; and had a peak power between 25 W and 125 W. This covers the performance of the stabilised, dual-arm OPO which produced near transform-limited, Gaussian like pulses that were 1.5 ps to 2 ps in duration with peak powers from 150 W to 200 W.

---

[1] The phase modulation due to XPM is 2 times greater than that due to SPM for waves of different frequencies and similar power levels.

Table 6-1 : Properties of a KD*P I OPA

Nonlinear Coefficient	$d_{eff} = d_{36} \sin \theta = 0.25$ pm/V
Walk-off angle	$\rho = 1.6^0$
Acceptance Angle (FWHM)	$\Delta\theta_{accept.} \approx 1.1$ mrad-cm
Spectral Acceptance Bandwidth (FWHM)	$\Delta\lambda_{accept.} \approx 5$ nm-cm@780 nm - 30 nm-cm@920 nm

Table 6-2 : Properties of a KD*P II OPA

Nonlinear Coefficient	$d_{eff} = d_{36} \sin 2\theta \approx 0.35$ pm/V
Walk-off angle :- idler :- pump	$\rho \approx 1.1^0$ $\rho \approx 1.6^0$
Acceptance Angle (FWHM)	$\Delta\theta_{accept.} \approx 5 - 11$ mrad-cm
Spectral Acceptance Bandwidth (FWHM)	$\Delta\lambda_{accept.} \approx 2.5$ nm-cm

Table 6-3 : Properties of a LBO I OPA

Nonlinear Coefficient	$d_{eff} = d_{32} \cos \phi = 1.2$ pm/V
Walk-off angle	$\rho \approx 0.2^0$
Acceptance Angle (FWHM)	$\Delta\theta_{accept.} \approx 11$ mrad-cm
Spectral Acceptance Bandwidth (FWHM)	$\Delta\lambda_{accept.} \approx 21 -34$ nm-cm

Table 6-4 : Properties of a BBO I OPA

Nonlinear Coefficient	$d_{eff} = d_{22} \cos \theta - d_{31} \sin \theta = 1.6$ pm/V
Walk-off angle	$\rho \approx 3.2^0$
Acceptance Angle (FWHM)	$\Delta\theta_{accept.} \approx 0.5$ mrad-cm
Spectral Acceptance Bandwidth (FWHM)	$\Delta\lambda_{accept.} \approx 5 -14$ nm-cm

Table 6-5 : Properties of a BBO II OPA

Nonlinear Coefficient	$d_{eff} = d_{22} \cos^2 \theta \approx 1.35$ pm/V
Walk-off angle :- idler :- pump	$\rho \approx 3.4^0$ $\rho \approx 3.65^0$
Acceptance Angle (FWHM)	$\Delta\theta_{accept.} \approx 6 - 10$ mrad-cm
Spectral Acceptance Bandwidth (FWHM)	$\Delta\lambda_{accept.} \approx 1.5 - 2.1$ nm-cm

Table 6-6 : Relative figure of merit for the above crystals.

Crystal	KD*P I	KD*P II	LBO I	BBO I	BBO II
Figure of Merit, F= $\| d_{eff}/n^3 \|^2$	5.9×10^{-27}	1.2×10^{-26}	8.6×10^{-26}	1.5×10^{-25}	1.1×10^{-25}
Relative figure of merit	0.07	0.14	1	1.74	1.28
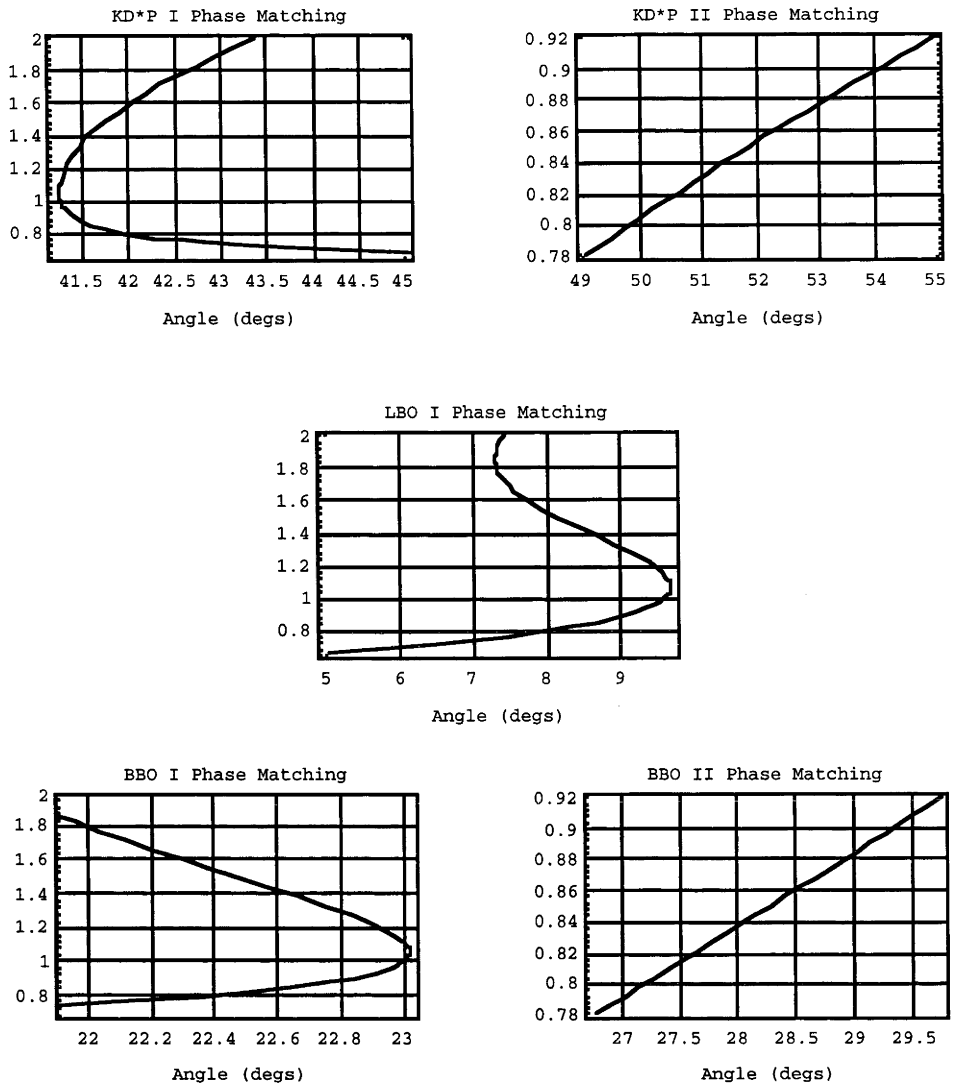
Figure 6-2 : The phase matching curves for KD*P I and II, LBO I and BBO I and II for optical parametric amplification with a 527 nm pump wave. The vertical axis is the wavelength in μm.

6.3 The first optical parametric amplifier

A 3 mm to 4 mm long LBO crystal was modelled as OPA1. A LBO crystal was chosen because a suitable crystal was already available in the laboratory; it had a low GVM; and wide angular acceptance angles and spectral bandwidths. It had a higher nonlinearity than KD*P and was similar to BBO. BBO could have been used as well but no available crystal was available and, as will be shown in Section 6.4, there are no distinct advantages in using BBO over LBO for high gain optical parametric amplification except the higher nonlinearity. Both can achieve similar performances as an OPA.

Experimentally, it was assumed that the pump pulse was a small portion of the compressed pulse from the GVMSHGsystem, which was predicted to be 500 fs in duration or less, and had a peak power of 320 MW. The Gaussian pump pulse was also assumed to form a waist with a 1/e electric field beam radius w_0 of 1 mm in the LBO crystal, giving a peak intensity of 20 GW/cm^2. For a 4 mm long LBO crystal the acceptance angle is ~ 27.5 mrad and the spectral acceptance bandwidth is greater than 52.5 nm. Neither one will restrict the parametric process.

143

800 nm	KD*P I	KD*P II	LBO I	BBO I	BBO II
K_1 (V^{-1})	1.291e-6	1.907e-6	5.786e-6	7.564e-6	6.657e-6
K_2 (V^{-1})	0.679e-6	1.015e-6	3.026e-6	3.954e-6	3.532e-6
K_3 (V^{-1})	1.970e-6	2.922e-6	8.812e-6	11.517e-6	10.186e-6
δt_{13} (ps/cm)	0.1018	0.3252	-0.2565	-0.5666	-0.2594
δt_{23} (ps/cm)	0.4257	-0.5078	-0.3565	-0.9582	-1.605

850 nm	KD*P I	KD*P II	LBO I	BBO I	BBO II
K_1 (V^{-1})	1.209e-6	1.771e-6	5.449e-6	7.109e-6	6.148e-6
K_2 (V^{-1})	0.749e-6	1.112e-6	3.363e-6	4.385e-6	3.854e-6
K_3 (V^{-1})	1.959e-6	2.882e-6	8.812e-6	11.494e-6	9.998e-6
δt_{13} (ps/cm)	0.061	0.3481	-0.3122	-0.6466	-0.2813
δt_{23} (ps/cm)	0.2478	-0.6178	-0.4228	-0.9618	-1.608

900 nm	KD*P I	KD*P II	LBO I	BBO I	BBO II
K_1 (V^{-1})	1.140e-6	1.638e-6	5.150e-6	6.709e-6	5.695e-6
K_2 (V^{-1})	0.812e-6	1.186e-6	3.662e-6	4.769e-6	4.120e-6
K_3 (V^{-1})	1.952e-6	2.823e-6	8.813e-6	11.478e-6	9.811e-6
δt_{13} (ps/cm)	0.036	0.3872	-0.3550	-0.7123	-0.2843
δt_{23} (ps/cm)	0.1464	-0.6840	-0.4480	-0.9449	-1.590

Table 6-7 : The nonlinear coupling coefficients for the signal, idler and pump beams, as well as, the inverse group velocity mismatch parameters for optical parametric amplification of a signal wave at 800 nm, 850 nm and 900 nm with a pump wave at 527 nm in various crystals.

The power of the signal and idler from a 3 mm, 3.5 and 4 mm long LBO I crystal as a function of pump power and seed signal power are shown in Figure 6-3. The pump pulse duration was 500 fs and the seed signal had a pulse duration of 2 ps and a wavelength of 850 nm. The seed signal peak power was varied between 25 W to 125 W. At a pump intensity of 20 GW/cm^2 and a seed signal of 125 W the 3 mm long crystal produced a 0.6 MW signal pulse and a 0.4 MW idler pulse; the 3.5 mm crystal produced a 3 MW signal pulse and a 2 MW idler pulse; and the 4 mm long crystal produced a 15 MW signal pulse and a 9 MW idler pulse. For the 4 mm long crystal, the gain experienced by a 125 W, 2 ps signal pulse was 1.2 x 10^5, whereas the idler was generated from quantum noise. The peak power of the signal and idler increased linearly with the seed signal peak power (see Figure 6-4) and with signal wavelength.

Interestingly the final pulse duration of the signal and the generated idler pulses were found to be independent of the seed signal peak power (see Figure 6-5). This was because of the high gain of the OPA. The temporal development of the pulses was dictated by the shape of the pump pulse, not the initial signal pulse. Also it should be noted from Figure 6-5 that for the 4 mm long LBO OPA the pulse duration was less than 300 fs for pump powers greater than 70 MW. Since in experiments the interacting beams would not be infinite plane waves but have Gaussian spatial beam profiles, Figure 6-5 indicates we can still expect that the signal and idler pulse durations would remain short even after averaging over the intensity distribution of the beam and lie in the range of 300 fs or less, for a 500 fs, 320 MW Gaussian pump pulse. For other combinations of pump and seed signal pulse duration the final signal and idler pulse durations for a 320 MW (20 GW/cm^2) pump pulse in a 4 mm long LBO crystal are shown in Table 6-8. The final pulse duration of both the signal and
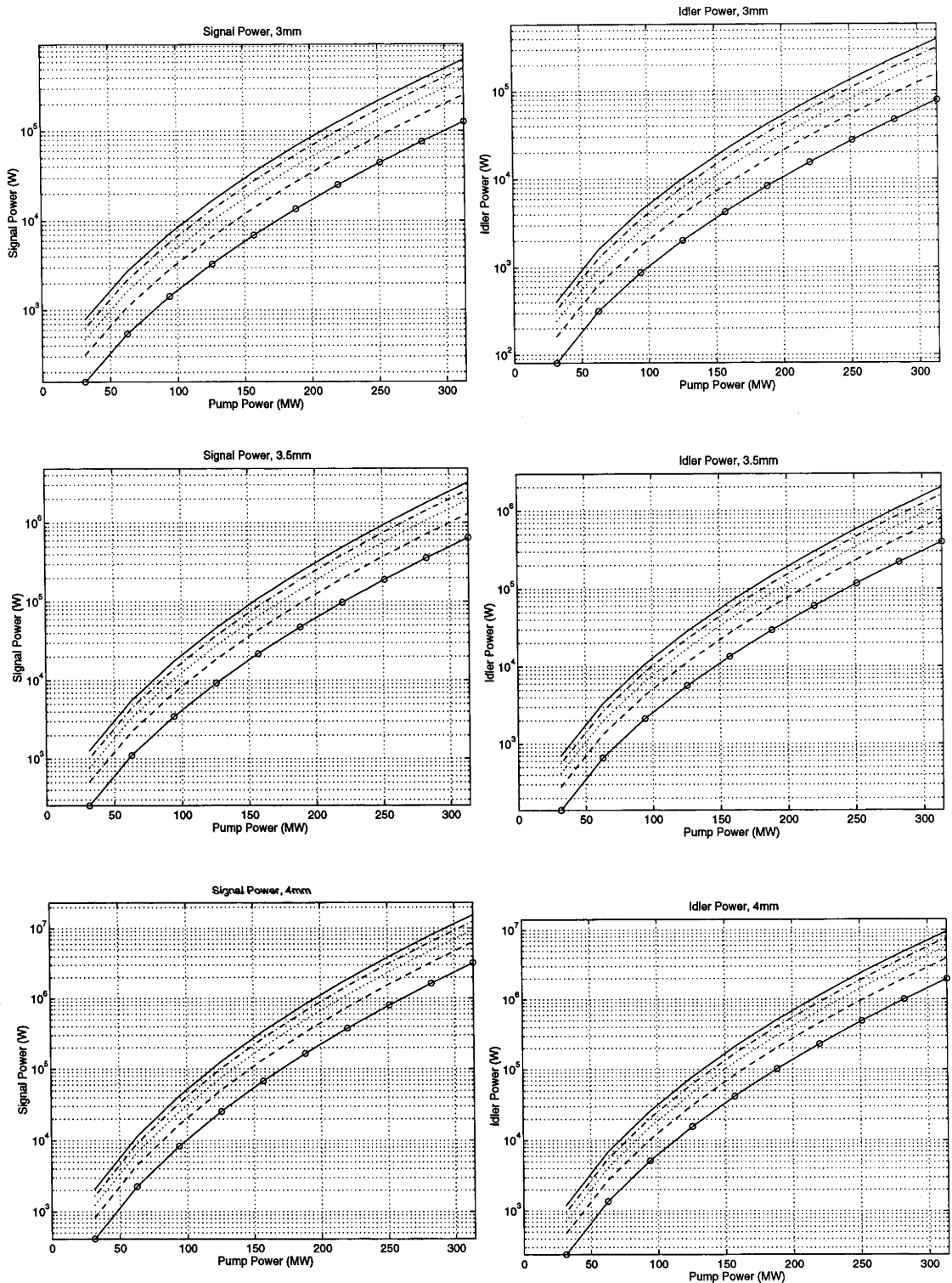
Figure 6-3 : The signal and idler power from a 3 mm, 3.5 mm and 4 mm long LBO I OPA pumped by a 320 MW, 500 fs, 527 nm Gaussian pulse. The seed signal pulse is at a wavelength of 850 nm, has a duration of 2 ps and has a peak power of 25 W (solid line with circles), 50 W (dashed line), 75 W (dotted line), 100 W (dash-dotted line) and 125 W (solid line).
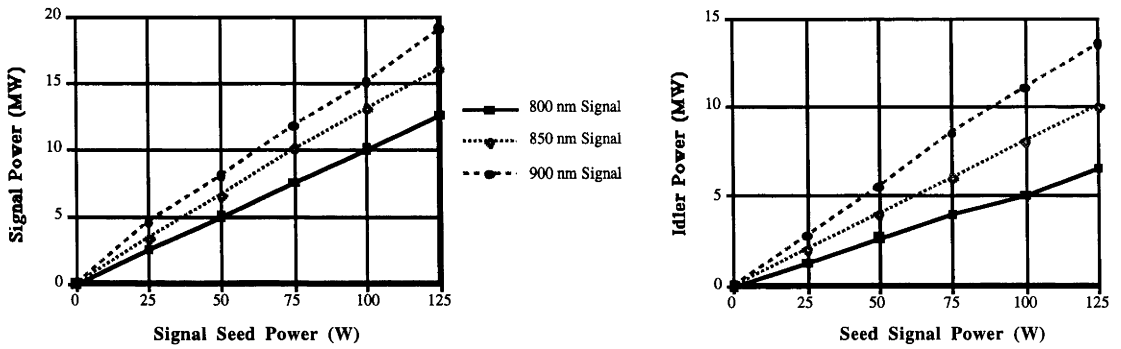
Figure 6-4 : The variation in the peak power of the signal and idler pulses from a 4 mm LBO I OPA pumped by a 500 fs, 320 MW (20 GW/cm^2) pump pulse with the seed signal wavelength and peak power.
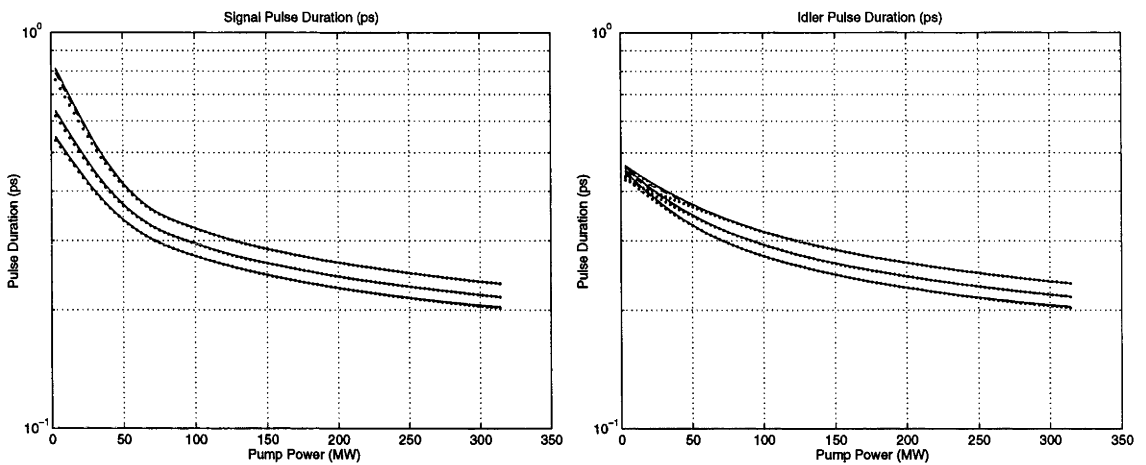
Figure 6-5 : The pulse durations of the signal and idler pulses from a 3 mm (top line), 3.5 mm (middle line) and 4 mm (bottom line) long LBO I OPA pumped by a 320 MW, 500 fs, 527 nm Gaussian pulse. The input seed signal is at a wavelength of 850 nm, has a duration of 2 ps and has a peak power of 25 W to 125 W. The final pulse duration is independent of the initial peak power of the seed signal pulse.

Table 6-8 : The pulse duration's of the signal and idler pulses from a 4 mm long LBO I OPA at a pump intensity of 20 GW/cm^2 for various input seed signal and pump pulse durations and at different seed signal wavelengths.

Initial Pulse Duration		800 nm		850 nm		900 nm	
Δt_{signal}	Δt_{pump}	*Signal*	*Idler*	*Signal*	*Idler*	*Signal*	*Idler*
1.5 ps	500 fs	204 fs	204	203	203	203	202
"	750 fs	303	303	300	300	300	299
"	1 ps	400	399	396	396	393	394
2 ps	500 fs	204	204	203	203	202	202
"	750 fs	300	300	297	298	296	297
"	1 ps	390	393	390	390	389	388

146

idler were also independent of the initial seed signal pulse duration and wavelength. For a 1 ps pump pulse the signal and idler pulse durations were 400 fs, 300 fs for a 750 fs pump pulse and 200 fs for a 500 fs pump pulse at an intensity of 20 GW/cm^2.

The pulse duration of the pump pulse and the seed signal pulse did not have a strong effect on the peak power of the signal and idler pulses from OPA1. The peak power varied ± 10 % with changes in the pump duration from 500 fs to 1 ps and for the seed signal pulse duration from 1.5 ps to 2 ps.

As has been mentioned above, in actual experiments the interacting beams would not be infinite planes waves but have Gaussian spatial beam profiles so we can not expect the peak power of the signal and idler pulses from the OPA to be as high as indicated by the simulations. For this reason it is better to use the longer 4 mm LBO crystal which produced higher peak power pulses. Figure 6-6 shows the peak power of the signal pulse from a 4 mm long OPA averaged over a Gaussian spatial beam profile with a 1 mm beam waist. As expected the peak power was much lower for the Gaussian average than for the plane wave case and was very sensitive to variation in the pump power (super-linear). For a 50 W to 100 W, 2 ps seed signal we can expect the signal peak power to be between 1 to 2 MW.

In conclusion, the numerical simulations of a 4 mm long LBO I OPA produced a 1 to 2 MW, 300 fs to 500 fs Gaussian signal pulse when pumped by a 320 MW, 500 fs to 1 ps pump pulse and seeded by a 1.5 ps to 2 ps, 25 W to 125 W signal pulse tunable between 800 nm to 900 nm. The maximum pump intensity was taken to be 20 GW/cm^2. The peak power of the signal and idler pulses from the OPA varied linearly with variation in the seed signal peak power and wavelength. The pulse duration's of the signal and idler pulses from the OPA were independent of the seed signal peak power and wavelength but were dependent on the pump pulse duration and weakly dependent of the pump peak power. This Gaussian signal pulse is ideal for use as a seed pulse for the second OPA. The linear transfer function of the peak power of the output signal and idler pulses with seed signal power means that any amplitude noise in the seed signal pulse is not amplified.

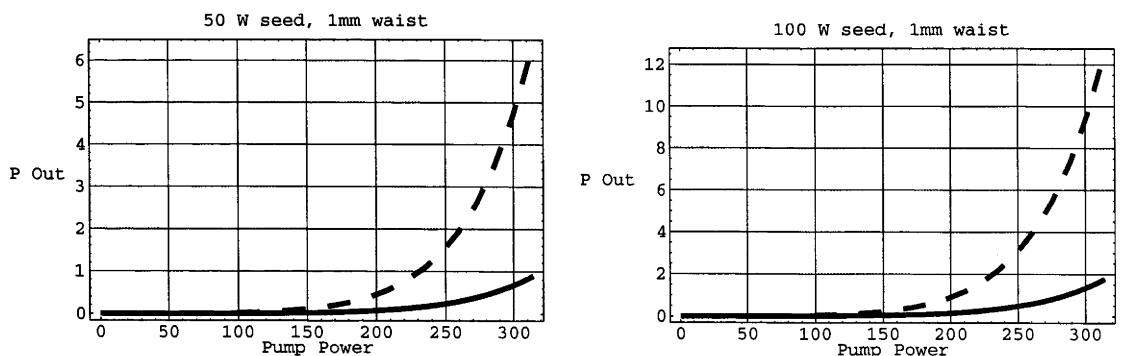Figure 6-6 : The peak power of the signal pulse from a 4 mm long LBO I OPA as a function of the pump power for a 50 W and a 100 W peak power, 850 nm, 2 ps seed signal pulse. The dashed line is the calculation of a infinite plane wave and the solid line is the average over a Gaussian beam profile with a 1/e electric field beam radius of 1 mm. The pump power and the signal power are in MW. The pump pulse is 500 fs in duration.

6.4 The second optical parametric amplifier

For OPA2 it was assumed that the Gaussian pump pulse had a peak power of 2.5 GW and was 500 fs to 1 ps in duration. The seed signal pulse was from OPA1 and had the properties described above. It was also assumed that the pump beam formed a 2 mm beam waist on the OPA crystal, giving a peak pump intensity of 32 GW/cm^2.

Initial simulations were done to find the best crystal length for each of the crystals and interactions shown in Tables 6-1 to 6-5 using a 500 fs, 2.5 GW pump pulse and a 300 fs, 1 MW Gaussian seed signal pulse at 850 nm. For KD*P I the optimum crystal length was ~ 12 mm, for KD*P II it was ~ 10 mm, for LBO I it was 2.5 mm to 3 mm, for BBO I it was 2 mm to 2.5 mm and for BBO II it was 2.5 mm to 3 mm.

For a 12 mm long KD*P I OPA the acceptance angle is 0.92 mrad and the spectral acceptance bandwidth is between 4.2 nm to 25 nm. While the acceptance angle is just acceptable the spectral bandwidth is quite low near 780 nm and would pose problems for short signal pulses. For a 10 mm long KD*P II OPA the acceptance angle is 5 - 11 mrad and the spectral acceptance bandwidth is around 2.5 nm. Again the narrow spectral bandwidth would create problems in amplifying short signal pulses. For this reason the KD*P II was discarded for use as a suitable OPA2. The KD*P I crystal was still kept for comparison with other shorter crystals. A 3 mm long LBO I crystal has very broad angular and spectral acceptance angles; an angular acceptance angle of 16.5 to 36.5 mrad and a spectral acceptance bandwidth above 70 nm. A 2 mm long BBO I crystal has an angular acceptance angle 2.5 mrad and a spectral acceptance bandwidth above 25 nm. A 2.5 mm long BBO II has an angular acceptance angle above 24 mrad and a spectral acceptance bandwidth between 6 nm to 8.4 nm. The spectral bandwidth is quite low for a BBO II OPA but is still just broad enough to amplify 200 fs signal pulses from 800 nm to 900 nm.

For each different chosen OPA (12 mm KD*P I, 3 mm LBO I, 2 mm BBO I and 2.5 mm BBO II) the 300 fs, 1 MW seed signal pulse was delayed relative to the 500 fs pump in the simulations to see if it had any effect on energy conversion. For KD*P I the optimum predelay was found to be near + 100 fs and for LBO and BBO OPAs it was found to be near - 100 fs. Figure 6-7 shows

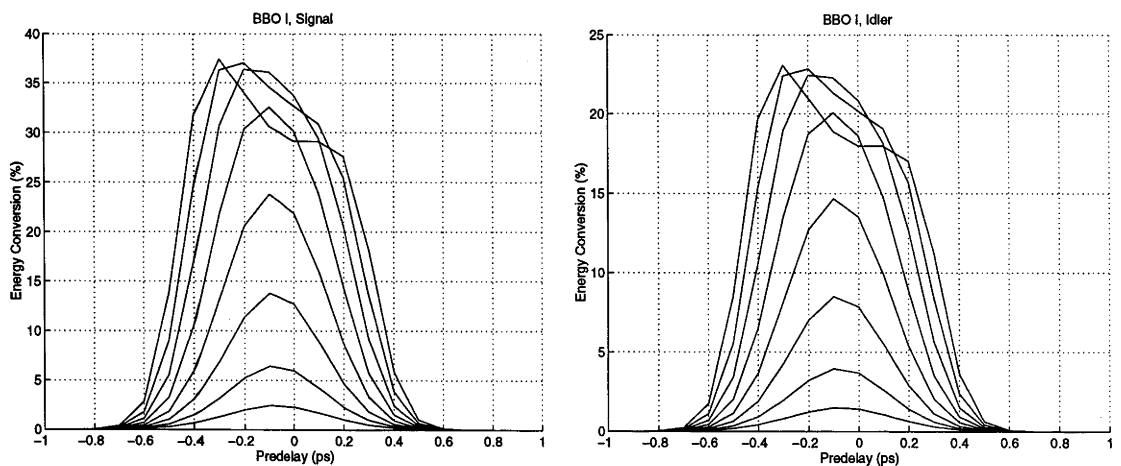**Figure 6-7 :** The energy conversion of a 500 fs pump pulse into a signal pulse at 850 nm and an idler pulse at 1387 nm in a 2 mm long BBO I OPA with a 300 fs, 1 MW seed signal pulse as a function of signal predelay relative to the pump beam and pump intensity. The pump intensity increases from 5 to 40 GW/cm^2 in 8 steps. The optimum predelay is - 100 fs for both the signal and idler pulses.
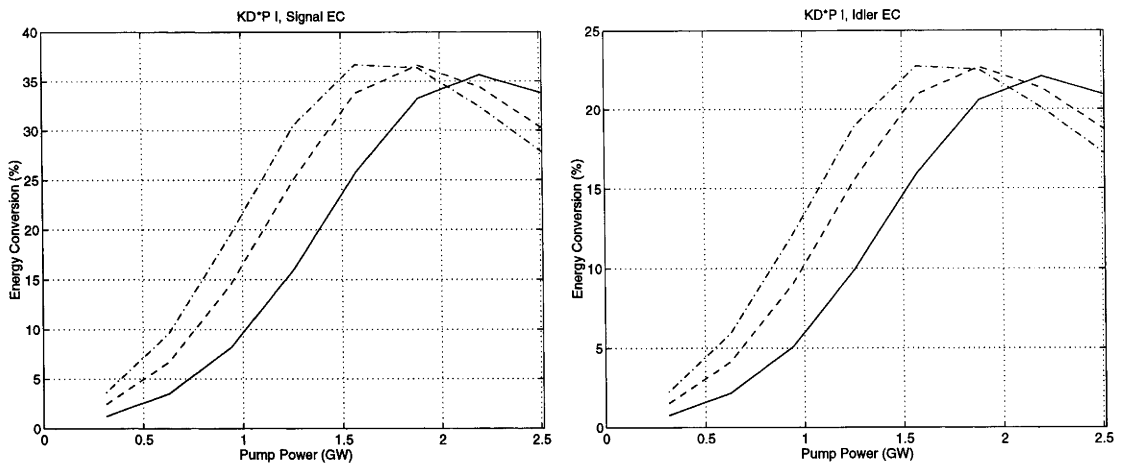
Figure 6-8 : The energy conversion of a 500 fs pump pulse into signal and idler pulses as a function of pump power for a 12 mm long KD*P I OPA. The 300 fs seed signal pulse at 850 nm has a peak power of 0.5 MW (solid line), 1 MW (dashed line) and 1.5 MW (dash-dotted line).
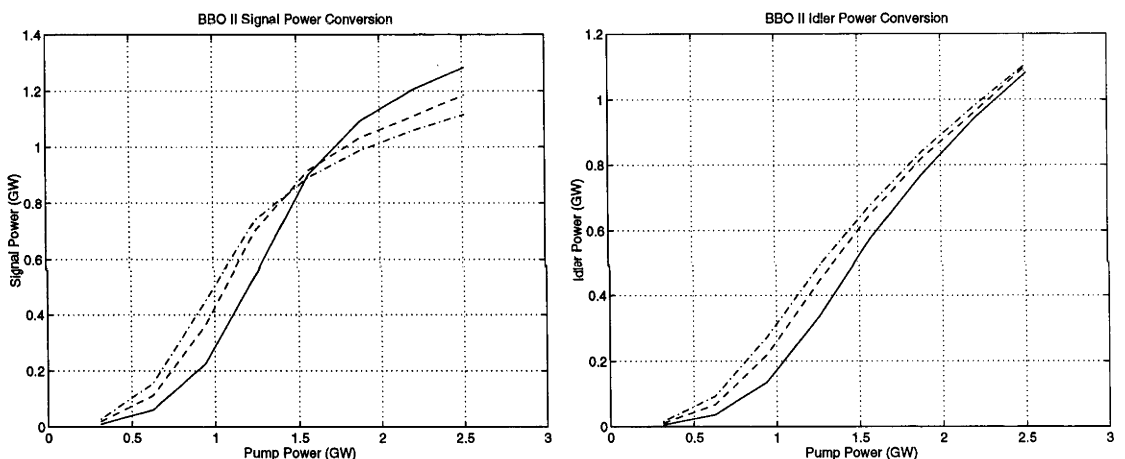
Figure 6-9 : The power of the signal and idler pulses from a 2.5 mm long BBO II OPA pumped by a 500 fs pump pulse as a function of pump power. The 300 fs seed signal pulse at 850 nm has a peak power of 0.5 MW (solid line), 1 MW (dashed line) and 1.5 MW (dash-dotted line).

the case for the 2 mm long BBO I OPA. In every case predelay only marginally increased the energy conversion. Experimentally, if the short pump and seed signal pulses were coincident in time within ± 100 fs of the optimum predelay energy conversion would be near optimum. From now on the optimum predelays will be used in further simulations.

Varying the peak power of the seed signal pulse had a similar effect for all the OPAs. Figure 6-8 shows the energy conversion curve of the signal and idler pulses for a 0.5 MW, 1 MW and 1.5 MW, 300 fs seed signal pulse at 850 nm for the 12 mm long KD*P I OPA. The peak energy conversion was near 35 % for the signal and near 23 % for the idler for all OPAs but occurred at a pump power from 1.5 GW to 2.2 GW (24 - 35 GW/cm^2) for the KD*P I OPA and BBO I OPA; from 1.3 GW to 1.6 GW (21 - 25 GW/cm^2) for the LBO I OPA; and from 1.5 GW to 2 GW (24 - 32 GW/cm^2) for the BBO II OPA. Figure 6-9 shows the power of the signal and idler pulses from the 2.5 mm long BBO II OPA under the
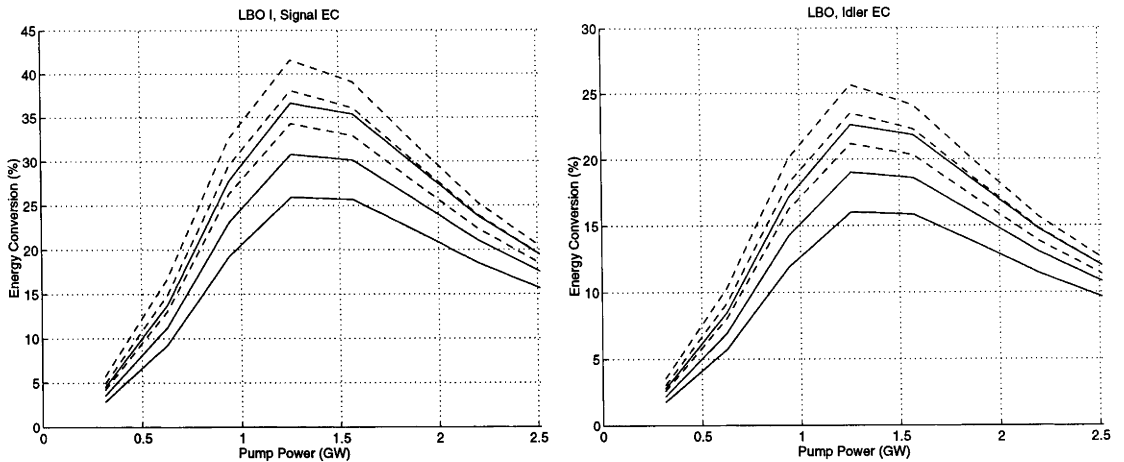
Figure 6-10 : The energy conversion into signal and idler pulses as a function of pump power for a 3 mm long LBO I OPA. The solid lines are for a 300 fs, 1 MW seed signal at 850 nm and the dashed lines are for a 500 fs, 1 MW seed signal at 850 nm. For each set of 3 lines the top line is for a 500 fs pump pulse, the middle line is for a 750 fs pump pulse and the bottom line is for a 1 ps pump pulse. The energy conversion is maximised when the pump and signal pulse durations are equal.

Figure 6-11 : The peak power of the idler pulse from a 2.5 mm long BBO II OPA and a 3 mm long LBO I OPA as a function of pump power. The solid lines are for a 300 fs, 1 MW seed signal at 850 nm and the dashed lines are for a 500 fs, 1 MW seed signal at 850 nm. For each set of 3 lines the top line is for a 500 fs pump pulse, the middle line is for a 750 fs pump pulse and the bottom line is for a 1 ps pump pulse.

same conditions as the energy conversion curves in Figure 6-8. The BBO I and II OPAs produced higher power signal pulses (~ 1 GW), near the maximum energy conversion pump powers, than the KD*P I OPA (~ 0.8 GW) and the LBO I OPA (~ 0.9 GW). The power of the idler pulses was around 0.8 GW for all the OPAs near the maximum energy conversion pump powers, except for the LBO I OPA which produced 0.6 GW idler pulses near a 1.5 GW pump power. Considering that the seed signal power changes from 0.5 MW to 1.5 MW in the cases above, a variation of ± 50 % for a 1 MW seed signal pulse, all the OPAs are not very sensitive to variation in the seed signal power. The BBO OPAs

performed better than the KD*P I OPA or the LBO I OPA in this case where the seed signal power varies. They produced higher peak power signal and idler pulses. For all OPAs the signal and idler pulse durations remained between 200 fs to 300 fs for all pump powers up to the pump powers required for maximum energy conversion.

The effect of varying the pump and seed signal pulse durations on each of the OPAs was investigated. In all cases the energy conversion into the signal and idler pulses was improved when the pump and seed signal pulse durations were roughly equal (Figure 6-10). The same levels of energy conversion are reached by all the OPAs. As expected, the shorter the pump and seed signal pulse, the greater the peak power of the signal and idler pulses from all the OPAs. Figure 6-11 shows the peak power of the idler pulses from the 2.5 mm long BBO II OPA and the 3 mm long LBO I OPA. In general, the BBO II OPA produced higher peak power signal and idler pulses of all the OPAs, with LBO being the worst. While all the OPAs displayed very similar behaviour with variation in the pump and seed signal pulse durations for the idler pulse (Figure 6-11); the behaviour changed considerably between the different OPAs for the signal pulse. The BBO II OPA and KD*P I OPA displayed almost no change in the signal peak power with variation in the pump and seed signal pulse durations up to pump powers of 2.5 GW (40 GW/cm^2) but the LBO I OPA and the BBO I OPA showed a range of signal peak powers with different pulse durations when the pump power exceeded the power needed for maximum energy conversion (see Figure 6-12).

Generally the pulse durations of the signal and idler pulses were similar with variation in the pump and seed signal pulse durations and are shown in Table 6-9 and Table 6-10. The range of pulse durations cover those pump powers up to where maximum energy conversion occurred. Above these pump powers the signal and idler pulses became distorted through reconversion. For a 300 fs seed signal the signal and idler pulse durations rose from ~ 250 fs to ~ 330 fs as the pump pulse increased from 500 fs to 1 ps. For a 500 fs seed signal the signal and idler pulse durations rose from ~ 300 fs to ~ 450 fs as the pump pulse increased from 500 fs to 1 ps. This indicates that the signal and idler pulse durations were relatively insensitive to variation in the pump pulse duration or the seed signal pulse duration. The peak power of the signal and idler pulses was determined to a greater degree by the energy conversion of the pulses.

Variation in the wavelength of the signal and idler pulses, between 800 nm to 900 nm for the signal, had little effect on the signal pulse from the LBO and BBO OPAs. It did have a bigger effect on the signal pulse from the KD*P I OPA. This was due to the large relative change in the GVMs for the signal and idler beams which would have changed the optimum predelay value, which was kept constant in this simulation, and therefore the energy conversion. For the KD*P I OPA the signal energy conversion was maximised at 1.8 GW for 850 nm and 900 nm signal wavelengths; and at 2.1 GW for a 800 nm signal wavelength. For the other OPAs the maximum energy conversion occurred at the same pump power. The behaviour of the idler energy conversion was similar between all the OPAs except the KD*P I OPA at the 800 nm seed signal wavelength (see Figure 6-13).

The signal and idler peak power from all the OPAs was similar for all three test wavelengths, except for the 800 nm signal wavelength in the KD*P I OPA. The signal power decreased (the idler power increased) as the signal wavelength increased from 800 nm to 900 nm for all the OPAs (idler decreased from 1544 nm to 1272 nm), reflecting the change in the photon energy of the pulses. An example of the behaviour of the idler peak power for the KD*P I OPA and BBO I OPA are shown in Figure 6-14.

The durations of the signal and idler pulses did not change to a great degree with the change in wavelength. Again the power of the signal and idler pulses was determined by the energy conversion. An example of the temporal pulse profiles from the 2 mm long BBO I OPA are shown in Figure 6-15.
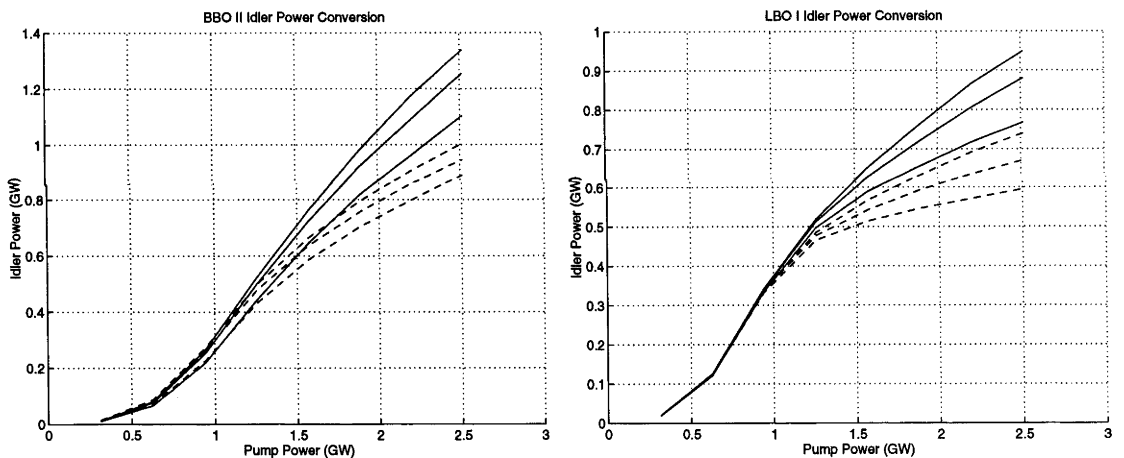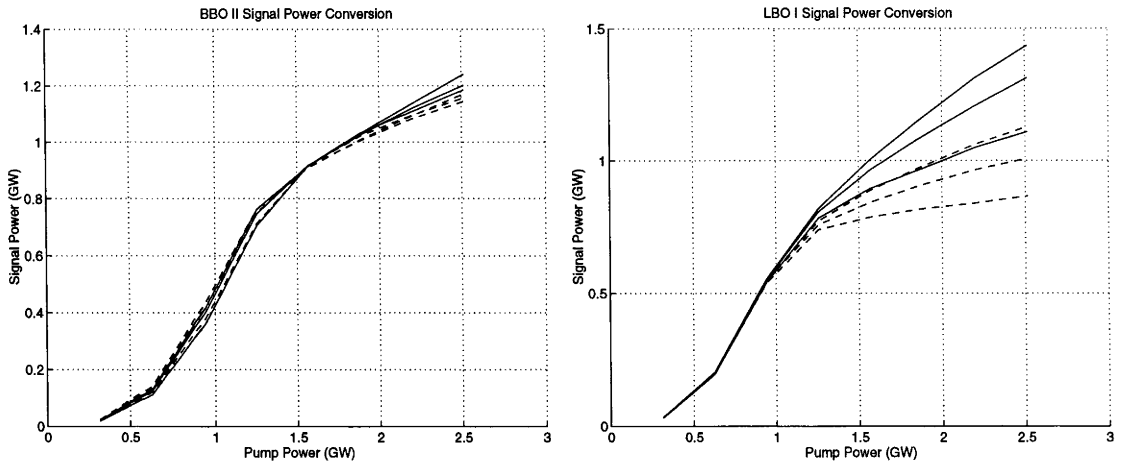
151

Figure 6-12 : The peak power of the signal pulse from a 2.5 mm long BBO II OPA and a 3 mm long LBO I OPA as a function of pump power. The solid lines are for a 300 fs, 1 MW seed signal at 850 nm and the dashed lines are for a 500 fs, 1 MW seed signal at 850 nm. For the LBO I OPA for each set of 3 lines the top line is for a 500 fs pump pulse, the middle line is for a 750 fs pump pulse and the bottom line is for a 1 ps pump pulse. For the BBO II OPA the various cases cannot be distinguished.

Table 6-9 : The range of pulse durations of the signal pulse from the OPAs with different pump and seed signal pulse durations.

Δt_{signal}	Δt_{pump}	KD*P I	LBO I	BBO I	BBO II
300 fs	500 fs	230-250 fs	230-270	230-250	240-300
"	750 fs	270-330	270-330	270-330	270-400
"	1 ps	300-370	270-370	270-370	400-530
500 fs	500 fs	270-300	270-330	270-330	270-350
"	750 fs	350-400	350-430	350-400	350-450
"	1 ps	400-500	400-530	400-500	400-600

Table 6-10 : The range of pulse durations of the idler pulse from the OPAs with different pump and seed signal pulse durations.

Δt_{signal}	Δt_{pump}	KD*P I	LBO I	BBO I	BBO II
300 fs	500 fs	~ 250	230-270	~ 230	250-300
"	750 fs	270-330	280-400	260-300	300-350
"	1 ps	290-370	280-400	270-300	300-400
500 fs	500 fs	270-310	270-350	260-300	290-350
"	750 fs	350-430	350-450	350-400	350-450
"	1 ps	400-500	400-550	400-500	410-550

152
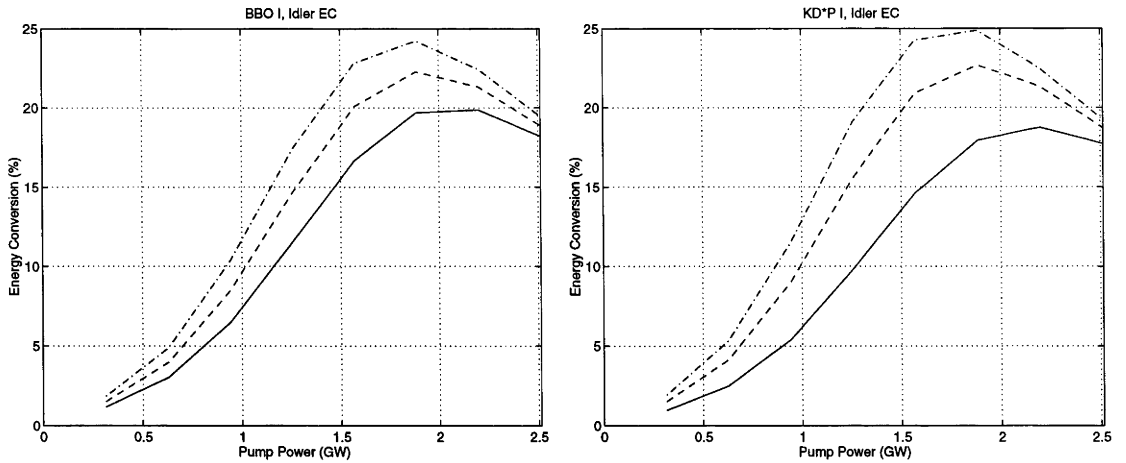
Figure 6-13 : The energy conversion of the idler pulse from a 2 mm long BBO I OPA and a 12 mm long KD*P I OPA as a function of pump power. The solid line is for a 800 nm seed signal wavelength; the dashed line is for a 850 nm seed signal wavelength and the dash-dotted line is for a 900 nm seed signal wavelength. The pump pulse is 500 fs in duration and the seed signal is 300 fs in duration with a peak power of 1 MW.
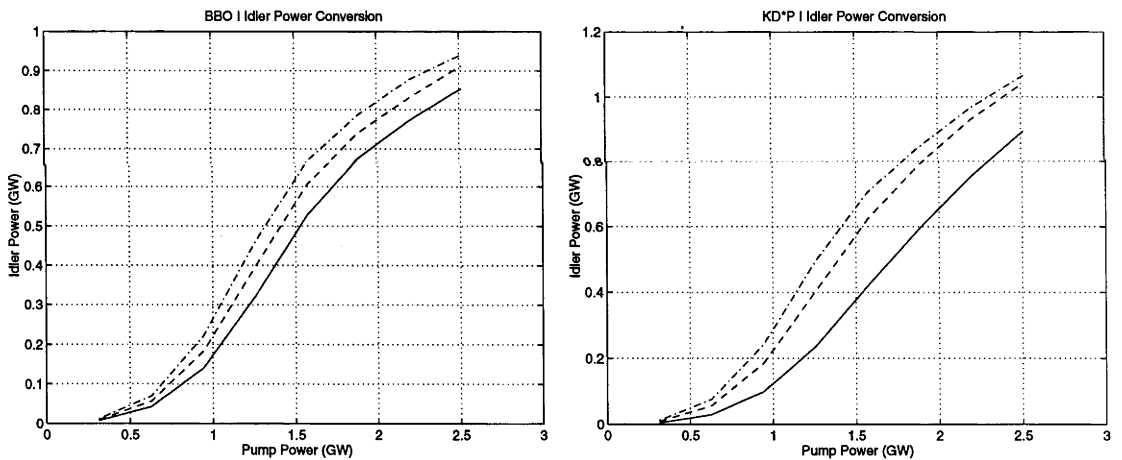
Figure 6-14 : The idler peak power from a 2 mm long BBO I OPA and 12 mm long KD*P I OPA as a function of pump power. The solid line is for a 800 nm (1544 nm idler) seed signal wavelength; the dashed line is for a 850 nm (1387 nm idler) seed signal wavelength and the dash-dotted line is for a 900 nm (1272 nm idler) seed signal wavelength. The pump pulse is 500 fs in duration and the seed signal is 300 fs in duration with a peak power of 1 MW.

153

Figure 6-15 : The temporal pulse profiles of the pump (dotted line), idler (dashed line) and signal (solid line) from a 2 mm long BBO I OPA. The left hand column is at a pump power of 1.26 GW (20 GW/cm^2) and the right hand column is at a pump power of 1.6 GW (25 GW/cm^2). The initial pump pulse was 500 fs in duration and the 300 fs, 1 MW seed signal pulse is at a wavelength of 800 nm (top row), 850 nm (middle row) and 900 nm (bottom row). The vertical axis is in units of 100 MW and the horizontal axis is in ps.
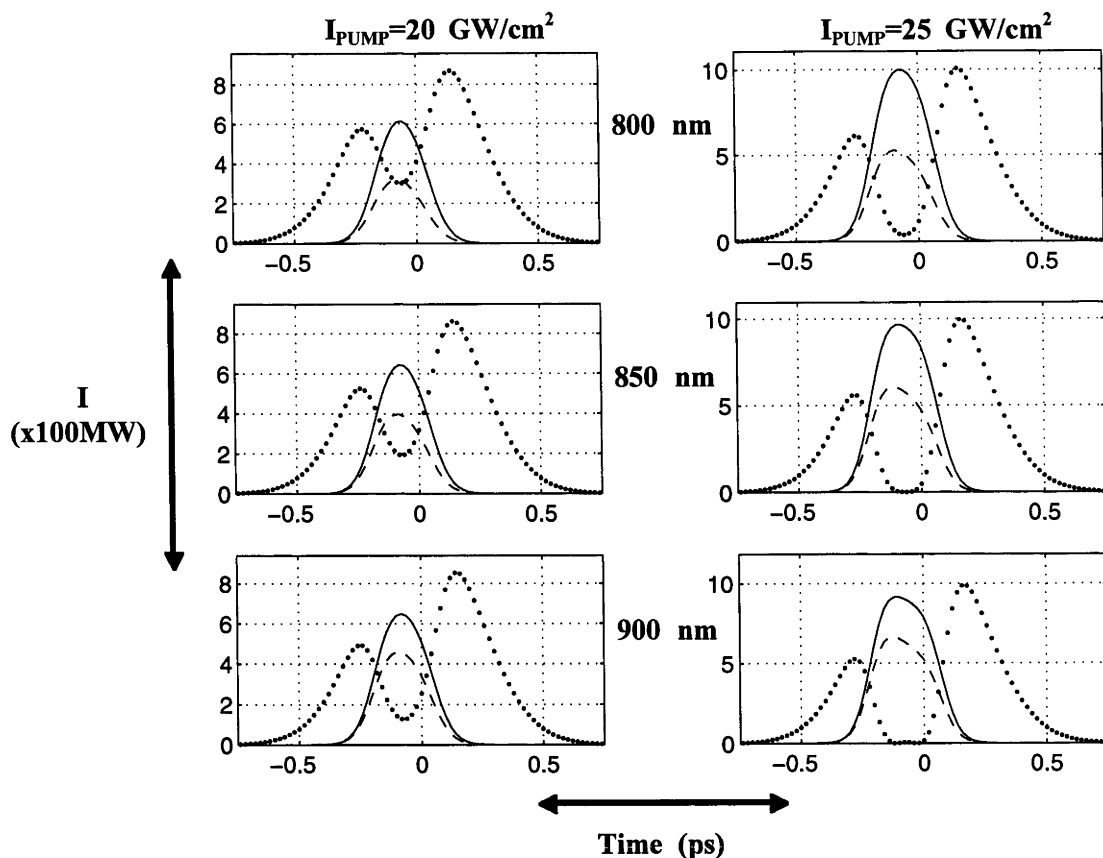
Figure 6-16 shows the Gaussian averaged energy conversion for typical signal and idler energy conversion curves for the BBO I OPA and the LBO I OPA. The Gaussian averaged energy conversion saturates at ~ 23 % for the signal and at ~ 14 % for the idler for all OPAs and for a 500 fs pump pulse duration and a 300 fs seed signal pulse duration. For the LBO I OPA the energy conversion saturated above 1.8 GW (29 GW/cm^2) and above 2.5 GW (40 GW/cm^2) for the others. In experiments, the most stable operating position would be at or above these pump intensities. The higher pump intensities required of the BBO and KD*P OPAs could be alleviated by using a higher power seed signal, slightly longer crystals or using more pump power if it were available. The pulse duration of the signal and idler with spatially Gaussian beams was expected to still be near to or below the seed signal pulse duration since the pulse duration of both waves has been shown to only be weakly dependent on pump power up to where reconversion occurs.

In summary, the simulated KD*P I OPA should be used with a predelay of ~ + 100 fs while the other simulated OPAs should be used with a ~ -100 fs predelay (for a 300 - 500 fs signal pulse and ~ 500 fs pump pulse) to maximise energy conversion for the signal and idler pulses. To maximise the energy conversion and peak power the pump and seed signal pulse durations should be equal and as short as possible. Energy conversions of ~ 40 % for the signal and ~ 25 % for the idler were predicted with a pump and seed signal pulse duration of 500 fs each for all OPAs. The simulated OPAs were generally not sensitive to variations in the seed signal power or to variations in the signal and idler wavelength. The pulse durations of the signal and idler did not change strongly with pump powers up to those required for maximum conversion efficiency and with variations in seed pump power; pump and seed

signal pulse duration; and wavelength. They were below the seed signal pulse duration for pump pulse durations from 500 fs to 1 ps and for all pump powers up to those required for maximum conversion efficiency. For all the simulated OPAs the maximum energy conversion, for both the signal and idler, occurred at a pump intensity of ~ 30 GW/cm^2 (~ 2 GW), except for the LBO I OPA where it occurred at ~ 20 GW/cm^2 (~ 1.3 GW). The lower pump intensity of the LBO I OPA would account for the lower peak powers of the signal and idler pulses from this OPA.

It is expected that Gaussian-like ≥ 600 MW, 300 fs to 400 fs signal and ≥ 300 MW, 300 fs to 400 fs idler pulses should be produced by all the simulated OPA2s when pumped by a 500 fs, ≥ 2 GW, 527 nm pulse and seeded by a 300 fs to 500 fs, ~ 1 MW signal pulse. This estimate takes into account the Gaussian spatial beam profile of the interacting beams; the variation in the seed signal power; the variation in the pump and seed signal pulse durations (though the shorter and the more equal the better); and the variation in the wavelengths of the signal and idler pulses.

6.5 Summary and conclusions

This chapter presented results of simulations carried out to model a high gain optical parametric amplification system consisting of 2 crystals. The simulations modelled the temporal interaction of the three waves as they propagated through a nonlinear crystal. It included parametric gain, pump depletion, reconversion, and the group velocity mismatch between the waves.
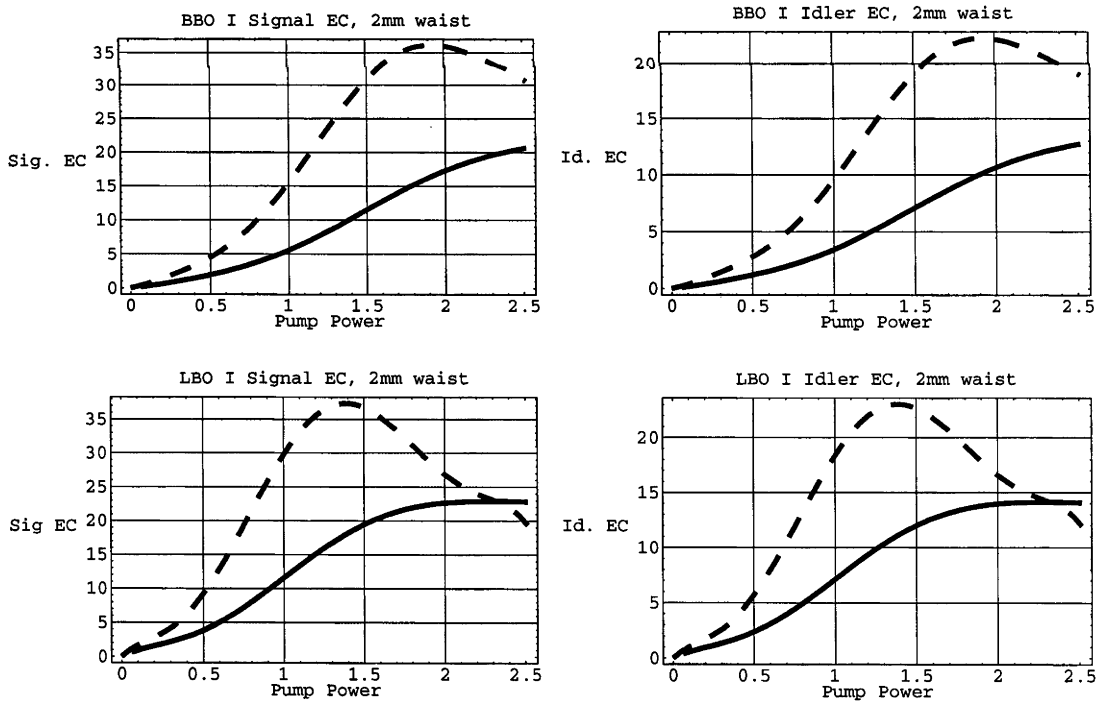

Figure 6-16 : The plane wave (dashed) and Gaussian averaged signal (solid) and idler energy conversions for a 2 mm long BBO I OPA and a 3 mm long LBO I OPA as a function of the 500 fs pump pulse power. The Gaussian average is over 1/e electric field beam radius of 2 mm. The seed signal has a duration of 300 fs and a peak power of 1 MW.

155

A two crystal optical parametric amplification system was chosen to avoid using very high gains in amplifying the seed pulse to power levels similar to the pump. Using a single stage OPA with the very high gain of $\sim 1 \times 10^7$ would result in a poorly performing OPA because of the high sensitivity of the output pulses to variations in pump power and input power of the seed pulses.

The first OPA was chosen to be a 3 to 4 mm long LBO I crystal pumped by a $\sim$ 500 fs, 320 MW pulse and seeded by a 1.5 ps to 2 ps, 25 W to 125 W signal pulse from the OPO. The power of the signal and idler pulses scaled linearly with the seed signal power and with a change in wavelength. The pulse duration was found to be independent of the seed signal power and only weakly dependent on the pump pulse duration. It was found that the 4 mm OPA produced $\sim$ 300 fs, $\sim$ 1 MW Gaussian-like signal pulses when the Gaussian spatial beam profile of the interacting beams were taken into account.

The second modelled OPA consisted of 4 possible crystals and phase matching interactions. It was seeded by the signal pulse from the first OPA. Initial calculations were done to chose an appropriate crystal length. A 12 mm long KD*P I OPA, a 3 mm LBO I OPA, a 2 mm BBO I OPA and a 2.5 mm BBO II OPA were chosen. It was found that the performance of all the OPAs were similar. The energy conversion from the $\sim$ 500 fs, 2 - 2.5 GW Gaussian pump pulse into signal and idler pulses was improved when a predelay of + 100 fs for the KD*P I OPA and - 100 fs for the others was used, as well as, equal pump and seed signal pulse durations. The peak power of the signal and idler pulses was improved when energy conversion was maximised, when the pulse duration's of the pump and seed signal were as short as possible, and when operating at longer signal wavelengths (900 nm). The pulse duration's of the signal and idler pulses were not greatly influenced by changing parameters of the pump or seed signal pulses. They remained the same as, or below, the seed signal pulse duration. Taking into account the Gaussian spatial beam profiles of the interacting beams, OPA2 was expected to amplify the $\sim$ 300 fs, $\sim$ 1 MW seed signal pulse to be a 300 - 400 fs, $\geq$ 600 MW signal pulse, for all wavelengths between 800 nm to 900 nm, and to generate a 300 - 400 fs, $\geq$ 300 MW idler pulse.

It is important to maintain fairly constant pump and signal pulse durations. Variation in the pulse duration would lead to improvements or degradations in the energy conversion, even for a Gaussian averaged beam, and lead to a variation in the peak power of the signal and idler pulses. This would be ultimately dependent on the temporal stability of the compressed SH pulse from the GVMSHG system. Overall small variations ($\pm$ 10 - 20 %) in the pump and seed signal peak power would not have a great effect on the final signal and idler pulses if one operated OPA2 at pump powers where the energy conversion was saturated. From the plane wave calculations it is known that these variations did not change the amount of energy conversion just the pump power level at which it occurred. For a Gaussian beam, at the pump powers where saturation occurs, there will be little change in the energy conversion of the signal or idler; and since their pulse durations are weakly dependent on the pump power, the peak power of the signal and idler pulses will be fairly constant. The moderate gain of OPA2 has resulted in a transfer function for the signal and idler output pulses that is generally insensitive to variation in the pump power.

The best OPA2 would not be the KD*P I OPA as SPM / XPM would be much stronger in this OPA than in the LBO and BBO OPAs. For a 12 long KD*P crystal pumped by 30 GW/cm^2 the nonlinear phase shift due to XPM would be $\sim$ 2.7 rads $\approx$ 0.85 π. For a 3 mm long LBO and a 2 mm long BBO crystal the nonlinear phase shift would be $\sim$ 0.68 rads $\approx$ $\pi/5$. Of the remanding OPAs only the BBO II OPA has the disadvantage of having a narrow spectral acceptance bandwidth. It can not support signal pulses below $\sim$ 200 fs in duration. Though this could be used in restricting excessive spectral bandwidth in the amplified signal and generated idler pulses. Either the LBO I OPA or BBO I OPA would serve best as the second OPA.

The experimental investigation of these numerical simulations was left for future work because of the lack of a suitably compressed SH pulse from the GVMSHG system (see Figure 5-14, Chapter 5). The central peak of the compressed SH pulse had a pulse duration > 2 ps.

6.6 References

[1]   R. Danielius, A. Dubietis, G. Valiulis, and A. Piskarskas, "Femtosecond high-contrast pulses from a parametric generator pumped by the self-compressed second harmonic of a Nd:Glass laser.," *Optics Letters*, vol. 20, p. 2225, 1995.

[2]   Y. Wang and B. Luther-Davies, "Optical-parametric-amplification-based prepulse eliminator for a chirped-pulse-amplification Nd:glass laser," *JOSA B*, vol. 11, p. 1531, 1994.

[3]   R. A. Baumgartner and R. L. Byer, "Optical Parametric Amplification," *IEEE J. Quant. Electron.*, vol. QE-15, p. 432, 1979.

[4]   F. Huang and L. Huang, "Picosecond optical parametric generation and amplification in LBO and BBO," *Appl. Phys. Lett*, vol. 61, p. 1769, 1992.

[5]   J. M. Liu, G. Zhou, and S. J. Pyo, "Parametric gain of the generation and the amplification of ultrashort optical pulses," *JOSA B*, vol. 12, p. 2274, 1995.

[6]   D. Eimerl, "Electro-optic, linear, and nonlinear optical properties of KDP and its isomorphs," *Ferroelectrics*, vol. 72, p. 95, 1987.

[7]   D. Eimerl, L. Davis, S. Velsko, E. K. Graham, and A. Zalkin, "Optical, mechanical, and thermal properties of barium borate," *J. Appl. Phys.*, vol. 62, p. 1968, 1987.

[8]   D. N. Nikogosyan, "Lithium Triborate (LBO). A Review of its properties and applications," *Appl. Phys. A*, vol. 58, p. 181, 1994.

[9]   J. D. Bierlein and H. Vanherzeele, "Potassium Titanyl Phosphate : properties and new applications," *JOSA B*, vol. 6, p. 622, 1989.

7. Diagnostic tools

7.1 Introduction

This chapter explains in detail the various diagnostic tools used to measure the temporal pulse profiles and the spectra of the pulses. To measure the temporal characteristics of a pulse a number of methods were used : SHG intensity autocorrelations, which measure the amplitude of a pulse; SHG interferometric autocorrelations and self diffraction frequency resolved optical gating (SD FROG), which reveal information about the amplitude and phase of a pulse. To measure the spectral characteristics of a pulse two types of spectrometers were used.

At various stages throughout this thesis the reader has been referred to this chapter for details on how actual measurements were taken. Please refer to the section in this chapter that covers the instrument used to take the measurements. This chapter only describes the actual devices. The context in which they were used has already been described in the referring chapters.

7.2 SHG intensity autocorrelation

In a SHG intensity autocorrelator, such as those shown in Figure 7-1, the pulse that was to be measured was split into two equal intensity, replicas of the original pulse. When the pulses were focussed into a SHG crystal they generated a SH signal that was dependent on the square of the original intensity (as long as the conversion efficiency was small). By delaying one pulse relative to the other, through changing its propagation distance through the autocorrelator, the SH signal changed in magnitude. The normalised variation in the intensity of the SH signal with time delay, τ, can be described as [1, 2]

$$I_2(\tau) = G_2(\tau) = \frac{\int\limits_{-\infty}^{\infty} \left|E^2(t)E^2(t-\tau)\right| dt}{\int\limits_{-\infty}^{\infty} \left|E^2(t)\right|^2 dt} = \frac{\int\limits_{-\infty}^{\infty} I(t)I(t-\tau) dt}{\int\limits_{-\infty}^{\infty} I(t)^2 dt}$$

where I(t) is the temporal intensity profile of the pulse to be measured and $G_2(\tau)$ is the second-order intensity autocorrelation function. It is assumed that the recorded signal does not respond to varying phase factors in the electric field of the pulse. As can be seen from this equation, by measuring the shape of the SH signal the original time-dependent intensity profile of the pulse can be estimated. The SH signal is normally referred to as an intensity autocorrelation signal.

The intensity autocorrelation function does not unambiguously define the shape of the original pulse. As a result it is usual to compare the measured function with that for a known pulse profile, such as a Gaussian or a $Sech^2$ profile. For these pulse shapes the relation between the FWHM duration of the normalised intensity autocorrelation, $\Delta\tau$, and the FWHM duration of the actual pulse, Δt, are known. For a Gaussian pulse $\Delta t = \Delta\tau/\sqrt{2}$ and for a $Sech^2$ $\Delta t = 0.645 \Delta\tau$. [2] contains the relationships for different pulse shapes. It is normal practice to use the measured pulse duration and the measured spectral FWHM bandwidth, Δf, to determine the time-bandwidth product. Depending on what pulse was assumed for the intensity autocorrelation the time-bandwidth can be compared with the transform-limited value to gain an estimate of how much phase modulation the pulse contains. For a Gaussian
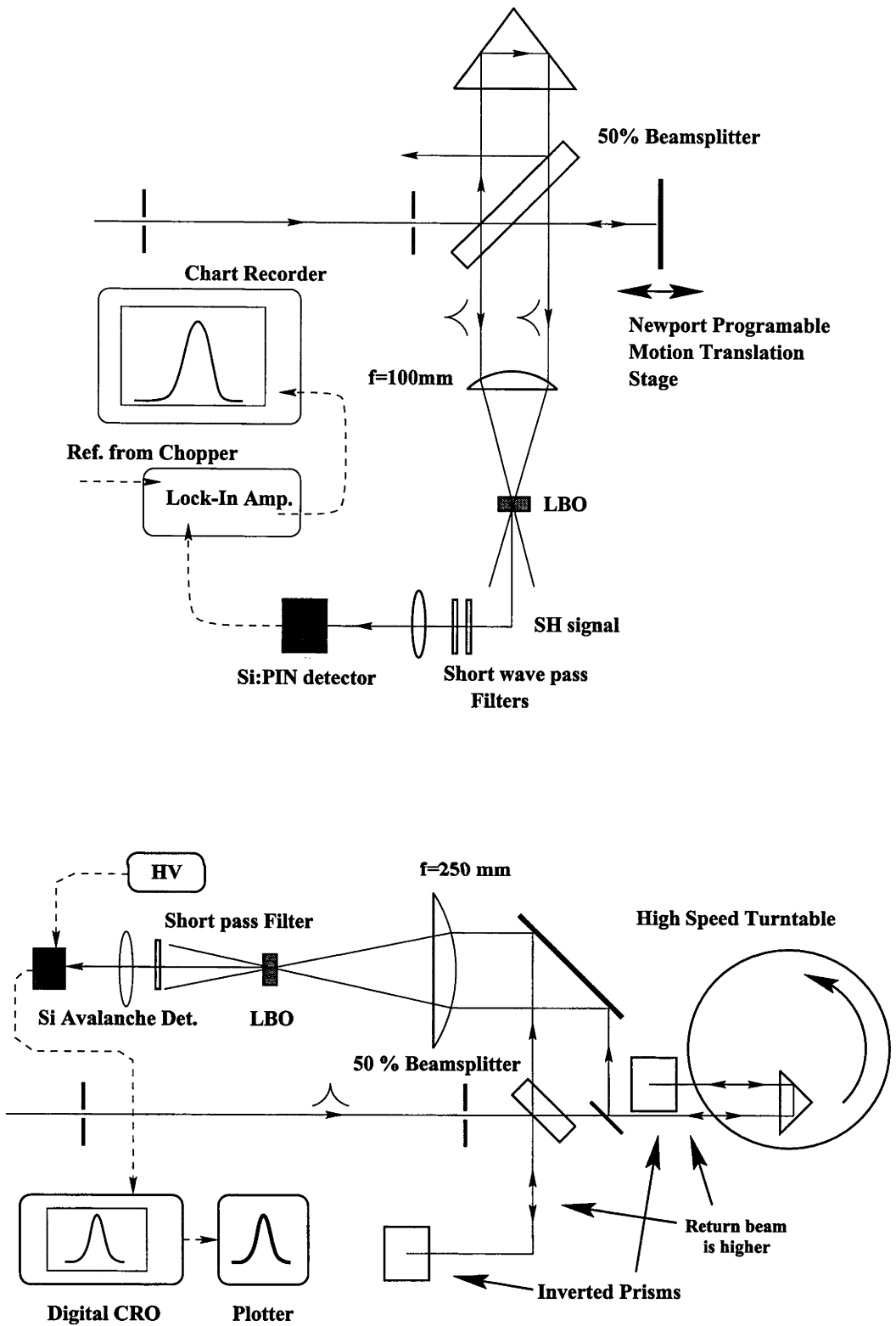
Figure 7-1 : The experimental layout of two LBO SHG intensity autocorrelators. The top autocorrelator is used for slow scans and the lower autocorrelator is used for fast scans. Please refer to the text for more details.

pulse $\Delta f \Delta t = 2 \ln(2)/\pi = 0.441$ and for a Sech^2 pulse $\Delta f \Delta t = 0.315$ for transform-limited pulses. However, the accuracy of this method in evaluating phase modulated pulses which are close to the transform limit is usually poor due to experimental error.

For complex pulse shapes, such as the compressed 1054 nm pulse, the transform limited pulse shape was determined from the power spectrum of the pulse, $I(\omega)$. Taking $\sqrt{I(\omega)}$ gives $|E(\omega)|$, the absolute value of the spectrum of the electric field. Taking the Fourier transform of $|E(\omega)|$ gives $|E(t)|$ and therefore $I(t)$. This allows the transform-limited intensity autocorrelation for any pulse with a known power spectrum to be determined.

Normally the SH intensity autocorrelation signal was measured using non-collinear phase matching. Two pulses cross at an angle inside the crystal such that the SH was usually generated at an angle which bisected the angle between the two input beams. In this way the SH intensity autocorrelation signal was free from any background. The contrast ratio was therefore higher than for the case were the pulses are collinear. The background second-order intensity autocorrelation has a contrast ratio of 3:1, whereas, it is infinite for a background free intensity autocorrelation.

The following sections describe in detail the various intensity autocorrelators used in the experiments. The autocorrelators were based on two SHG crystals, LBO and KDP. Since the SHG crystal is the most important part of the intensity autocorrelator the description of each autocorrelator is divided under each crystal.

7.2.1 Intensity autocorrelators based on Lithium Triborate

LBO has been described previously in connection with the optical parametric oscillator. For angle-tuned, critically phase matched, type I (o + o $\leftrightarrow$ e) SHG, LBO displays different behaviour than when used in the OPO. Information about important parameters are summarised in Figure 7-2 and Figure 7-3.

Using the Sellmeier equations from [3] the phase matching curve for type I SHG in LBO was determined and is shown in Figure 7-2. With a 20^0 change in crystal angle LBO can frequency double any wavelength between 0.75 to above 1.6 μm. For wavelengths below 1.21 μm and above 1.38 μm phase matching occurs in the principle XY plane where $\theta = 90^0$ and ϕ varies. Between these two wavelengths phase matching occurs in the orthogonal XZ plane where $\phi = 0^0$ and θ varies.

Since the phase matching becomes non-critical at 1.21 and 1.38 μm, the retracing wavelength points, the derivative $\partial \Delta k / \partial \lambda = 0$ and the SHG efficiency becomes relatively insensitive to variation in crystal angle. In what follows, the acceptance angle was defined to be the angle at which the SHG gain dropped by half. The plot of the angular acceptance angle for LBO I SHG is shown in Figure 7-3. The acceptance angle goes to infinity at the retracing wavelength points since the acceptance angle was only calculated to first order with λ. Generally the acceptance angle is very broad for wavelengths above 1 μm, reaching up to 40 to 60 mrad-cm at the retracing points [4]. Between 0.8 to 0.9 μm, where SHG intensity autocorrelations of the signal pulse from the OPO were measured, the acceptance angle is between 1 to 2 mrad-cm.

The FWHM spectral acceptance bandwidth is very broad for type I SHG in LBO. Since the group velocity mismatch between the SH and the fundamental beam drops to zero near 1.3 μm the SHG process is spectrally non-critically phase matched at this point, ie. $\partial \Delta k / \partial \lambda = 0$. The spectral bandwidth has been experimentally measured to be 155 nm-$\sqrt{}$cm at this point [4].
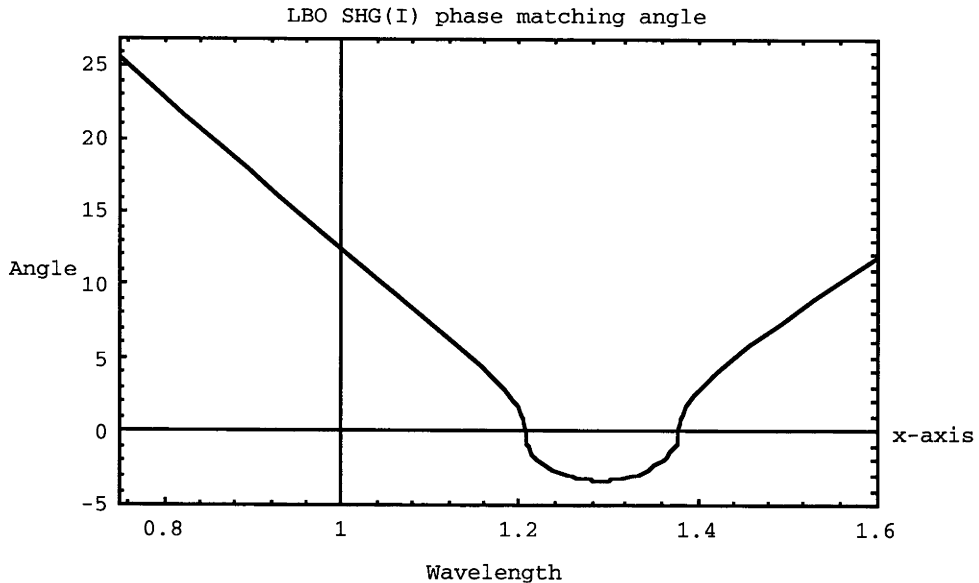
Figure 7-2 : The phase matching angle for type I, SHG using LBO. Phase matching is in the principle XY plane ($\theta = 90°$, ϕ varies) for those angles above the x-axis and phase matching is in the principle XZ plane ($\phi = 0°$, θ varies) for those angles below the x-axis. The angle is in degrees and the wavelength is in microns.

The walk-off angle is quite low across the entire wavelength region of interest. Generally it is around 0.2 $°$ for wavelengths above 1.1 μm and up to 0.8$°$ at 800 nm.

The LBO crystal used for the SHG intensity autocorrelation measurements was an uncoated 3 mm x 3 mm x 2 mm long crystal cut at $\theta = 90°$ and $\phi = 8°$. Using this crystal to measure the signal pulses from the OPO meant an angular acceptance angle of 5 to 10 mrad and that the beams would separate by up to 30 μm over the 2 mm crystal length, which precluded using beam waists smaller than ~ 100 μm. For wavelengths above 1 μm the acceptance angle posed no restrictions. The spectral acceptance bandwidth and GVM posed no problems in the measurement of pulses longer than a picosecond within the specified wavelength range.

Two examples of the intensity autocorrelators used in experiments are shown in Figure 7-1.

The autocorrelator in the top figure was typical of the autocorrelator used to take slow scans of the signal and idler pulses from the OPO, as well as, the 1054 nm pulse from the fibre-diffraction grating pulse compressor and Antares laser. The pulse from the OPO was aligned through two pinholes and then split into two equal intensity beams by a 50% reflectivity beamsplitter mirror. To measure the idler pulses from the OPO a CVI mirror with a 50 % reflectivity between 1200 nm to 1600 nm for s-polarised light was used. A similar mirror with a 50 % reflectivity between 700 nm to 900 nm was used to measure the signal pulses. To change the p-polarised pulses from the OPO into s-polarised pulses an out of plane rotation was used before the pulses were sent to the autocorrelator. One of the split beams passed through an AR-coated 1 inch right-angle prism and the other was reflected off a protected Aluminium mirror mounted on a Newport motion controlled translation stage that provided the variable time delay. The right-angle prism returned the beam shifted roughly 15 mm to the left of the beam reflected from the Al mirror. The two beams were then focussed into the 2 mm thick LBO and the generated SH beam then detected by a reverse-biased Si:PIN detector with a rise-time of 2 ns. The crossing angle was quite small,

161
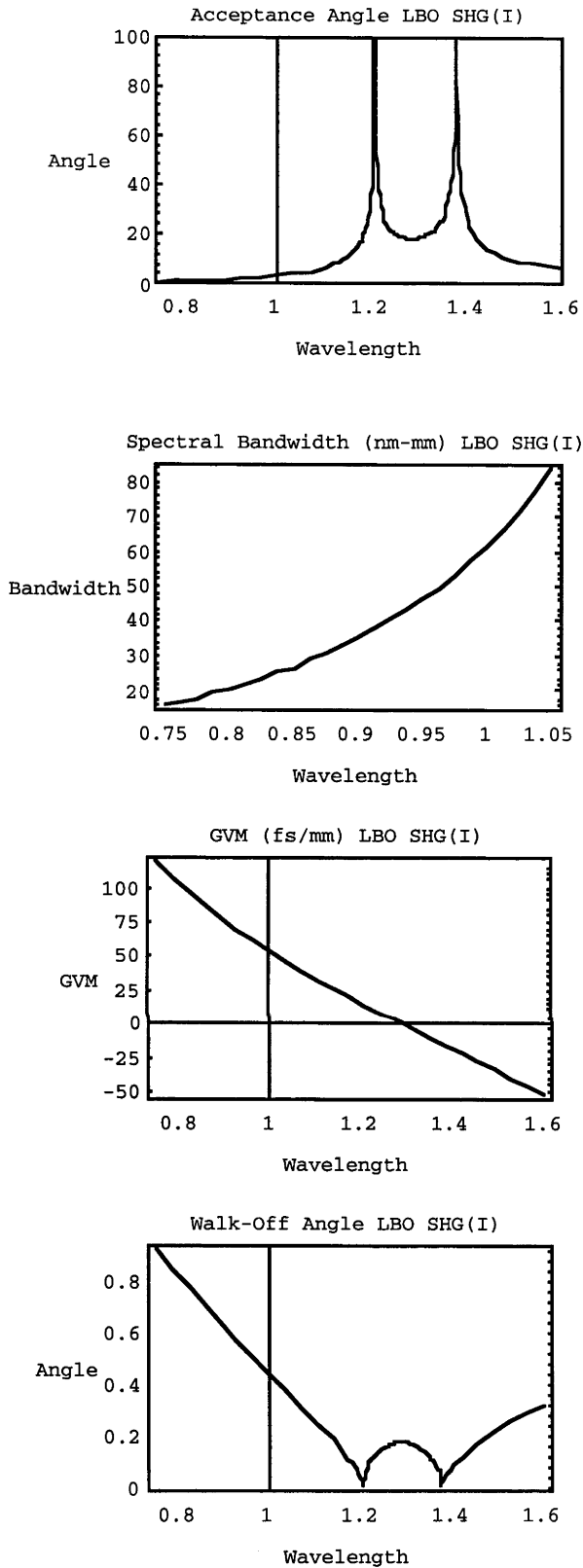
Figure 7-3 : These figures show the FWHM angular acceptance angle in mrad-cm, the FWHM spectral acceptance bandwidth in nm-mm, the group velocity mismatch (GVM) between the SH and the fundamental in fs/mm and the Poynting vector beam walk-off angle in degrees for critically phase matched, type I, SHG in LBO at wavelengths between 0.75 μm to 1.6 μm. Please note that the acceptance angle and spectral bandwidth are only first order calculations.

162

less than 10^0, allowing the two beams to interact over the entire crystal length. The focussed beam size was greater than 100 μm. The SH intensity was kept much lower than the fundamental intensity to prevent pump depletion affecting the measurement and to prevent the detector signal saturating. The detected SH signal was then sent to a Lock-In amplifier which took the reference signal from the chopper. The Lock-In detection allowed the signal to noise ratio to be increased. The signal from the Lock-In was recorded by a chart recorder. To align this autocorrelator the 1054 nm pulse from the Antares Nd:YLF laser was used. Since it was 60 ps in duration and was much higher in power than the pulses from the OPO, it simplified the alignment of the autocorrelator. If the original pulse was low in intensity, such as the signal pulses from the OPO, the autocorrelator was modified so that the returning beams from the Al mirror and right-angle prism did not return through the beamsplitter.

For experimentally simplicity the crossing angle of the beams was kept constant and the crystal angle was adjusted to maximise the non-collinear phase matched SH autocorrelation signal. As long as the actual crystal angle was greater than the phase matching crystal angle, the angle could be tuned to maximise the SH autocorrelation signal for a particular crossing angle.

To calibrate this autocorrelator involved inserting a piece of glass into one of the arms of the autocorrelator. This changed the propagation distance and introduced a known time delay between the pulses. This known time delay depended on the thickness and refractive index of the piece of glass.

The second type of autocorrelator, which is also shown in Figure 7-1, measured the SHG intensity autocorrelations at a ~ 200 Hz rate. The setup was very similar to the slow scan autocorrelator. The beam was split into two equal intensity beams by an appropriate 50 % reflectivity mirror. One of the beams passed through an inverted right-angle AR coated prism making the return beam 15 mm higher than the incoming beam. The return beam passed over the beamsplitter and was focussed into the LBO crystal by an AR coated 250 mm focal length lens. The other beam was delayed relative to the other by a high speed turntable that rotated at ~ 200 Hz. The beam passing through the beamsplitter entered an AR coated right-angle prism on the turntable and then another inverted right-angle prism which raised the return beam about 10 mm higher than the incoming beam. The return beam passed through the prism on the turntable and was then reflected off a Al mirror and focussed into the LBO crystal. The prisms and beam were aligned so that when the moving prism on the turntable did not deviate the beam. The SH autocorrelation signal was detected by a Si Avalanche photodiode that was biased by 400 to 420 V. This detector was much more sensitive and had a faster risetime that the other Si:PIN detector. The signal from the detector was displayed on a digital CRO, with the CRO being triggered from the line signal. This displayed signal was then plotted or stored on a floppy disk.

This autocorrelator was harder to calibrate than the slow scan autocorrelator. The alignment and calibration was carried out with the compressed pulse from the fibre-diffraction pulse compressor. A 25 mm long KDP crystal cut for type II SHG of 1054 nm radiation (the same crystal used as the predelay crystal for GVMSHG) was inserted into the beam between the two pinholes. The crystal was detuned slightly in angle to prevent SHG occurring. By suitably aligning the o and e ray axes of the crystal to be at 45^0 to the incoming s-polarised 1054 nm beam the 1054 nm pulse was spilt into two pulses polarised at 45^0 to the beam axis, with one pulse 3.3 ps ahead of the other pulse. To correct for the polarisation rotation of each of the pulses the beam passed through a polarising beamsplitter cube aligned to pass s-polarised light. This gave two, s-polarised pulses that were separated in time by 3.3 ps. Since the compressed pulse was roughly 2.5 ps in duration the SH signal had three peaks with the separation in time between each of the peaks being equal to the 3.3 ps delay between the pulses. This known time difference was used to calibrate the autocorrelator. The CRO calibration was usually 1.1 ps/ 10 μs ± 10 % .

7.2.2 Intensity autocorrelators based on Potassium Dihydrogen Phosphate

A KDP crystal was used in intensity autocorrelators to measure pulses at 1054 nm and 527 nm, mainly for the amplified 1054 nm pulse and the SH pulse from the GVMSHG system. It was more desirable to use the LBO crystal for other measurements because it has a higher effective nonlinearity.

The KDP crystal used in the autocorrelators was a 10 mm x 10 mm x 1 mm thick crystal cut at 90^0. Unlike the LBO crystal this crystal can frequency double 527 nm light. However, the non-collinear phase matching angle is close to 90^0. So instead of tuning the crystal angle for a fixed crossing angle, as in the LBO autocorrelators, the crossing angle was chosen for a fixed crystal angle. This did not prove a problem experimentally as the wavelength did not change. Figure 7-4 shows the crossing half-angle for frequency doubling any wavelength between 0.52 μm to 1.1 μm for a 90^0 cut KDP crystal.

Near 1 μm the crossing angle is 20^0 and is insensitive to wavelength. This indicates that the GVM is very low and the spectral acceptance bandwidth is very large. Indeed the GVM between the 527 nm and 1054 nm radiation is very low at -53 fs/cm and the spectral bandwidth is greater than 10 nm-mm. However, the angular acceptance angle is 2.54 mrad-cm [5], which restricted the beam waist to being greater than 13 μm, and the beam walk-off is 23 mrad meaning that the e and o rays separated by 15 μm over the 1 mm crystal thickness.

For frequency doubling 527 nm light the GVM is greater at 335 fs/mm, giving a spectral bandwidth around 2.8 nm-mm. This restricted the use of the KDP crystal to frequency doubling 527 nm pulses with pulse durations longer than 300 to 500 fs due to the larger GVM. The angular acceptance angle is 5 mrad-cm and the walk-off angle is around 16 mrad.

The two autocorrelators used in the experiments with the GVMSHG system are shown in Figure 7-5. In both cases the incoming beam was split into two equal intensity beams by an appropriate 50 % reflectivity mirror. The beam that passed through the beamsplitter was delayed relative to the other beam by an AR coated right-angle prism on a Newport motion controlled translation stage. When 527 nm pulses were measured the beams crossed at an internal angle of 5.2^0, an
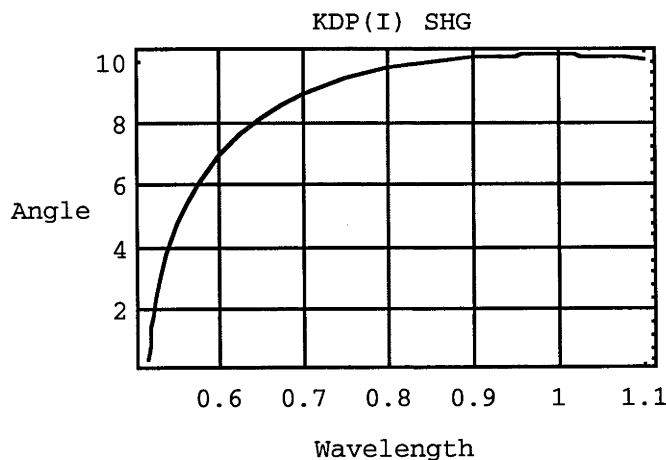

Figure 7-4 : The crossing half-angle in degrees for non-collinear phase matched type I, SHG in a KDP crystal cut at 90^0. The wavelength is in μm.

external crossing angle of 7.7^0. The 1054 nm pulses crossed at 20^0, an external crossing angle of 30^0. So, for the 527 nm beams it was possible to use a lens with focal length of 250 mm and to have the beams separated by ~ 34 mm at the lens but for the 1054 nm beams it was better to use a long focal length lens before the autocorrelator to focus the beams and to tilt the folding mirrors so that the beams crossed at the correct angle within the KDP crystal. The SH autocorrelation signal was detected by a reversed-biased, UV enhanced Si:PIN detector. The signal from the detector was then sent to a CRO and the BoxCar integrator. The CRO was used to adjust the gate on the BoxCar so that it was integrating the signal from the detector. The trigger for the BoxCar was supplied by the Nd:YLF amplifiers. The BoxCar averaged over a number of pulses before sending the signal to a chart recorder. This electronic arrangement was used for both autocorrelators.

Calibration of these autocorrelators was the same as for the slow scan LBO autocorrelator.

To measure the 527 nm pump pulses for the OPO the LBO crystal in the slow scan autocorrelator was replaced with the 1 mm thick KDP crystal. The lens and the separation of the two incoming beams were adjusted to give the correct crossing angle. Also the normal Si:PIN detector was replaced with the UV enhanced detector to detect the 263 nm autocorrelation signal. The rest of the experimental arrangement remained the same.

7.3 SHG interferometric autocorrelation

If an intensity autocorrelation is recorded in conditions where the two beams interfere with each other, for example, when the two beams overlap and are travelling parallel each other, then the SH autocorrelation signal is dependent on the amplitude and phase of the pulse [6]. The normalised envelope of this interferometric signal is given by the following equation.

$$g_2(\tau) = \frac{\int_{-\infty}^{\infty} \left| \left\{ E(t) \pm E(t-\tau) \right\}^2 \right|^2 dt}{2 \int_{-\infty}^{\infty} \left| E^2(t) \right|^2 dt}$$

Where the upper envelope of the rapidly varying interferometric signal is given by the addition sign and the lower envelope is given by the subtraction sign. In Chapter 2 and 3 the transform-limited interferometric autocorrelations were shown with the experimental autocorrelations. The same method as used to fit the transform-limited intensity autocorrelation was used to fit the transform-limited interferometric autocorrelation using g_2 instead of G_2.

As two transform-limited pulses pass through each other the SH signal varies rapidly as the pulses interfere with each other. The peak intensity of the upper envelope is 8 times the intensity of the SH signal when the pulses are well separated in time (the SH intensity due to one pulse). The intensity of the lower envelope drops to zero due to destructive interference. Any phase distortion in the pulse will alter the shape of the envelope yielding specific information about the phase distortion. To completely recover the amplitude and phase of the pulse requires the intensity autocorrelation and the spectrum of the pulse, as well as, the interferometric autocorrelation. [1] contains many references relevant to interferometric autocorrelation, including methods for extracting information about the pulse from an interferometric autocorrelation.
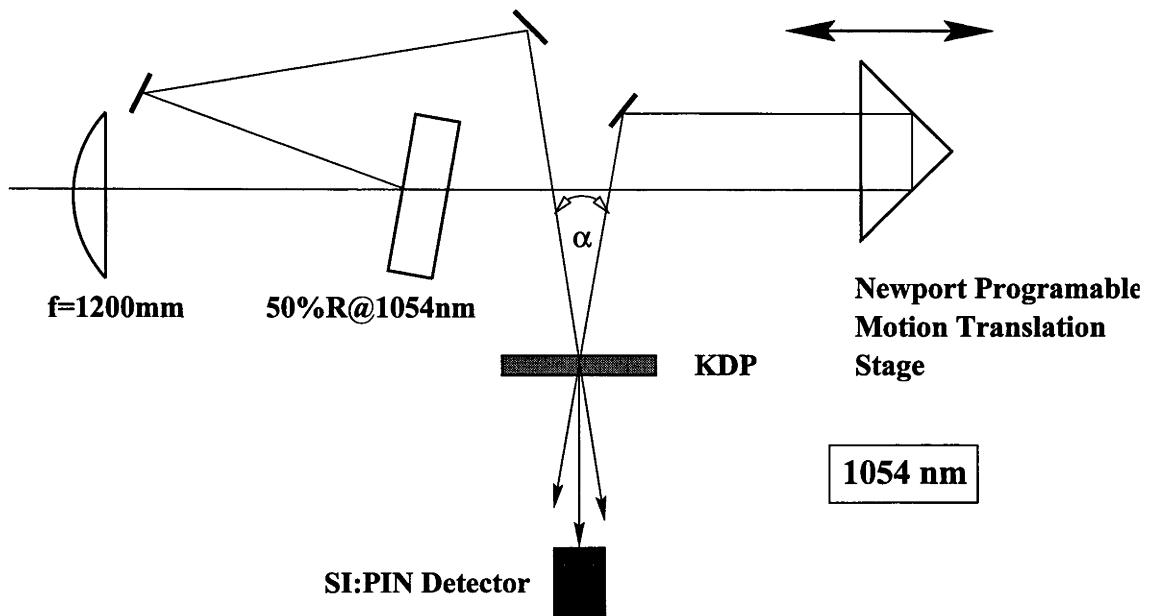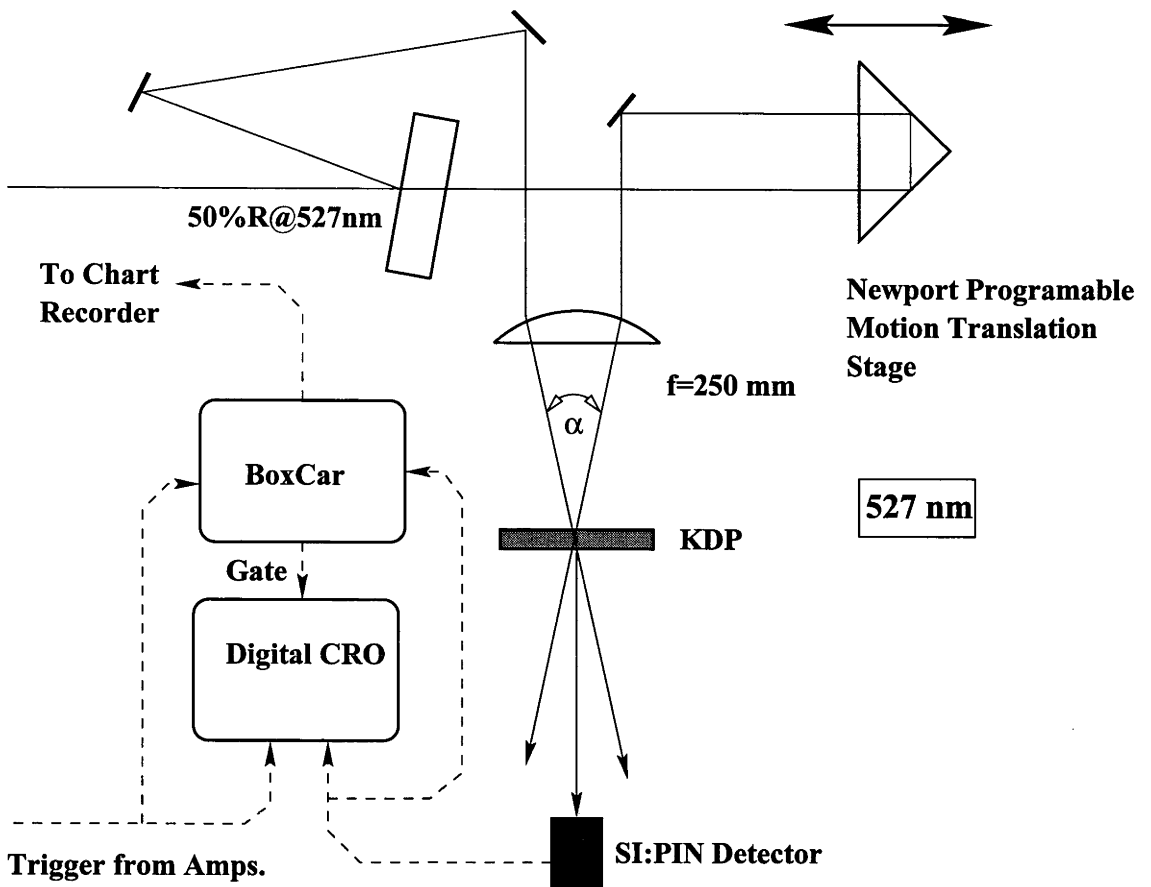
Figure 7-5 : The experimental arrangement of the two SHG intensity autocorrelators used to measure pulses at 527 nm (top) and 1054 nm (bottom) using type I, SHG in a 1 mm thick KDP crystal cut at 90^0. α is the crossing angle of the beams.
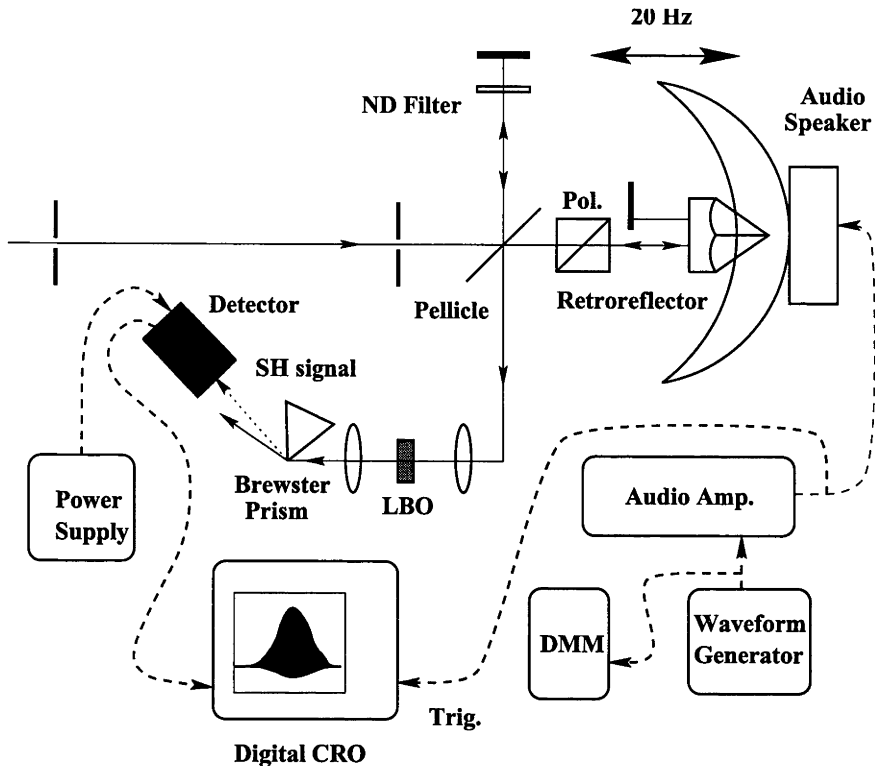
Figure 7-6 : The experimental layout of the LBO SHG interferometric autocorrelator.

The interferometric autocorrelator used a LBO crystal that was identical to the one used in the LBO intensity autocorrelators. The experimental arrangement is shown in Figure 7-6. The beam to be measured was split into two equal intensity beams by a pellicle beamsplitter. One beam was reflected off a protected Aluminium mirror and the other beam passed through a retroreflector and was then reflected by another Al mirror. The retroreflector was mounted in a 7 inch audio speaker which oscillated at 20 Hz. The travel range of the speaker was controlled by the magnitude of a Sine wave signal sent to an audio amplifier, which powered the speaker, from a waveform generator. The retroreflector rotated the polarisation of the beam because of out-of-plane reflections; so a polarising beamsplitter cube was used to control the polarisation state of the reflected beam. It was necessary to place a neutral density filter in the other arm to compensate for the losses due to this polariser to keep both beams of equal intensity. The angle of the two Al mirrors and the Pellicle were adjusted until the two beams were travelling parallel and overlapped each other. The beam was focussed into the LBO crystal and the SH autocorrelation signal was separated from the fundamental beam by a Brewster angle prism. Since the beam to be measured was s-polarised the SH beam was p-polarised and did not suffer any loss due to the prism. The signal was detected by a ThorLabs PDA150 amplified Si detector, or if the interferometric signal power was low, by a Thorn EMI quartz window photomultiplier tube (PMT). The autocorrelator had high losses, mainly due to double passing the Pellicle beamsplitter, so the PMT was used for measurements of the signal pulses from the dual-arm OPO. The interferometric autocorrelations of the compressed 1054 nm pulse from the fibre-diffraction grating were taken with the amplified Si detector. Both detectors had high gain and very fast response times.
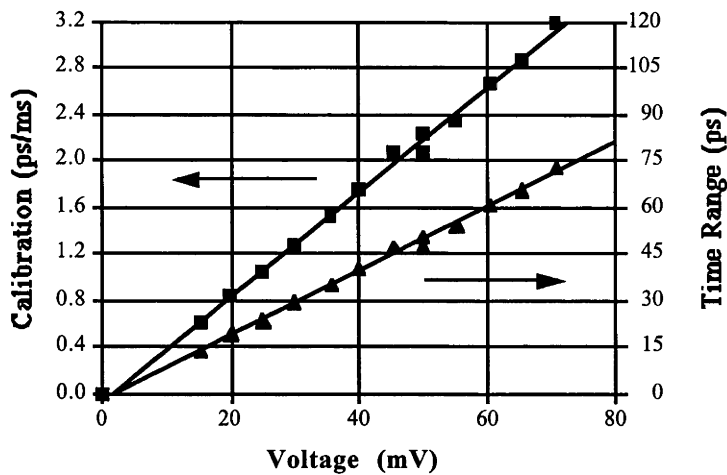
Figure 7-7 : The calibration factor and time range of the LBO SHG interferometric autocorrelator with increasing signal voltage from the waveform generator.

To calibrate this interferometric autocorrelator involved using the same method used to calibrate the slow scan LBO intensity autocorrelator. Since there was an external trigger, provided by the waveform generator, it was possible to measure the shift in time on the digital CRO when a piece of glass was inserted into one of the arms of the interferometer. The compressed 1054 nm pulse was used to align and to calibrate the autocorrelator. The delay between the two arms was adjusted so that the autocorrelation signal was in the center of the travel range of the speaker because the travel was linear at this point. Then a know time delay was inserted into one arm using a piece of glass. The autocorrelation signal shifted in time on the CRO display. Care was taken that the shifted autocorrelation signal still lay away from the edges of the travel range of the speaker. This calibration was done with increasing voltage from the waveform generator. The results are shown in Figure 7-7. For the measurements presented in this thesis the voltage was 41.5 mV giving a calibration factor of 1.8 ps/ms and a time range of 41 ps.

This autocorrelator was easy to use and align and provided good interferometric autocorrelations of various picosecond pulses. The only disadvantages were the high losses associated with double passing the Pellicle beamsplitter and the noise problems with having a low SH signal.

7.4 Self diffraction frequency resolved optical gating

Details relating to this pulse measurement method have already been covered in detail in Chapter 5, Section 5.4.

7.5 Spectrometers

Two types of spectrometers were used in experiments. A high-resolution spectrometer that had a 1024 pixel Reticon array for recording spectra electronically and a small, computer controlled, low-resolution optical multichannel analyser.

The high resolution spectrometer was a GCA/McPherson 2051, 1 m, scanning monochromator. For measurements of spectra with wavelengths less than 1.1 μm a Aluminium coated 1200 lines/mm grating was used while for wavelengths above this a 300 lines/mm grating was used. This spectrometer had a motor which moved the grating so that it could scan across a wavelength range at a prescribed speed in Angstroms/minute. To calibrate this spectrometer two different lasers with known wavelengths were used and the

168

scan meter was set to zero at the beginning of the motor drive's translation range. To find the spectrometer resolution a cw, diode pumped 1064 nm laser (a Coherent DPSS 1064 nm laser) was used. It had a linewidth of 50 MHz, which was much narrower than the spectrometer resolution. Typically, with the entrance slit shut down to ~ 5 μm in width and using the 1200 lines/mm grating the spectrometer resolution was 0.6 to 0.8 Angstroms. For the 300 lines/mm grating the resolution was expected to by ~1.8 times worse [7].

The output from this spectrometer was detected by a Si:PIN detector, for wavelengths less than 1.1 μm, or a Ge detector, for wavelengths greater than 1.1 μm, and the spectra were recorded on a chart recorder by scanning the spectrometer across the peak intensity wavelength. Similar to the LBO intensity autocorrelators, when measuring the spectra of the signal or idler pulse from the OPO the detector signal was sent to a lock-in amplifier, with the reference signal from the chopper, before being sent to the chart recorder. The spectrometer was also fitted with a 1024 pixel Reticon array that could measure the spectra directly. This could only be used for spectra with narrow bandwidths which was why the broad signal and idler spectra were recorded using a chart recorder.

To monitor the spectra of the signal pulses from the OPO a small Alton Instruments Lamda Series LS-2000 spectrometer and PCCD detector were used. This spectrometer used a concave imaging diffraction grating, with a resolution of ~ 1 nm from 800 to 900 nm, and a computer controlled 2048 channel linear CCD array. The software application that ran the spectrometer controlled the gain and exposure time of the CCD detector, as well as, whether single or multiple exposures were taken. To calibrate this spectrometer two lasers of know wavelengths, that lay within the spectral range of the CCD array (normally around 250 nm), were used. It was normally used to monitor the spectral behaviour of the signal pulses in the OPO. Since the signal pulse could oscillate on widely spaced, multiple wavelengths it was used to ensure that the signal did not change its spectral behaviour when measurements were being taken.

It was also used in the SD FROG measurements of the amplified 1054 nm pulse from the Nd:YLF amplifier chain. In that measurement the Reticon array on the McPherson was exchanged with the Lamda PCCD detector. In this way multiple exposures could be taken, allowing a FROG trace to be taken.

7.6 References

[1]   J.-C. Diels and W. Rudolph, *Ultrashort laser pulse phenomena*: Academic Press, Inc., 1996.

[2]   K. L. Sala, G. A. Kenney-Wallace, and G. E. Hall, "CW autocorrelation measurements of picosecond laser pulses," *IEEE J. Quant. Electrons.*, vol. QE-16, p. 990, 1980.

[3]   S. Lin, J. Y. Huang, J. Ling, C. Chen, and Y. R. Shen, "Optical parametric amplification in a lithium triborate tunable from 0.65 μm to 2.5 μm," *Appl. Phys. Lett.*, vol. 59, p. 2805, 1991.

[4]   S. Lin, B. Wu, F. Xie, and C. Chen, "Phase matching retracing behaviour for second harmonic generation in LBO crystal," *J. Appl. Phys.*, vol. 73, p. 1029, 1993.

[5]   D. Eimerl, "Electro-optic, linear, and nonlinear optical properties of KDP and its isomorphs," *Ferroelectrics*, vol. 72, p. 95, 1987.

[6]   J.-C. M. Diels, J. J. Fontaine, I. C. McMicheal, and F. Simoni, "Control and measurement of ultrashort pulse shapes (in amplitude and phase) with femtosecond accuracy," *Applied Optics*, vol. 24, p. 1270, 1985.

[7]   S. P. Davis, *Diffraction grating spectrographs*. New York: Holt, Reinhart and Winston, 1970.

8. Summary and Conclusions

The aim of this thesis was to develop an optical parametric amplification system based on Nd:YLF lasers and amplifiers to produce ~ GW level, sub-500 fs pulses that were easily wavelength tunable from 1.3 μm to 1.6 μm (see Figure 8-1). These pulses were to be produced from two OPA crystals that were pumped by high power, ultrashort, compressed 527 nm pulses from a novel GVMSHG system and seeded by ps signal pulses from a synchronously pumped OPO based on LBO. The pump pulses for the OPO were provided by frequency doubling the pulses from a fibre-diffraction grating pulse compressor that compressed the 1054 nm pulses from a cw, mode-locked Nd:YLF "Antares" laser, which acted as the master oscillator. The high power, ps fundamental pulses for the GVMSHG system were provided by two Nd:YLF amplifiers that amplified and compressed the pulses from the same Antares laser.

It is desirable for the pump pulses for the OPO to be as short as possible, making the production of sub-500 fs pulses from the OPAs easier to achieve, to be as close to transform-limited as possible and to have enough peak power to drive the OPO many times above threshold, where stable operation can be achieved. Since the pulses from the Antares laser were 60 ps in duration, with a maximum peak power of 4.5 kW, it was decided to employ a standard optical fibre - diffraction grating pulse compressor to compress the 1054 nm pulses in time to the more useful value of ~ 2.5 ps in duration while enhancing the peak power of the compressed pulses to 16 kW. The fibre-diffraction grating pulse compressor performed well and to theoretical expectations. While this method did not produce transform-limited pulses, by frequency doubling the compressed pulses in a 15 mm long LBO, type I SHG crystal the 527 nm pulses were much closer to being transform limited. They were, at worst, 1.5 times the transform limit for a Sech^2 pulse, and the more likely, within 20 % of being transform-limited Gaussian pulses. They were 2.3 ps in duration and had peak powers of 6.5 kW. This was more than enough to drive the OPO well above threshold. Without the pulse compressor, ~ 45 ps, ~ 900 W pump pulses were produced through direct SHG of the Antares laser.
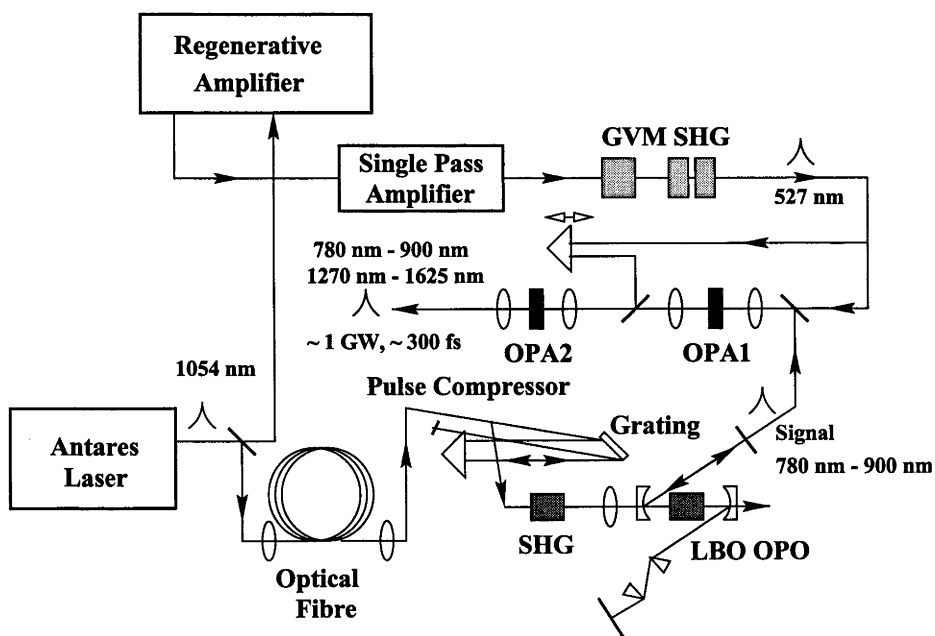

Figure 8-1 : A detailed experimental layout of the optical parametric amplification system.

The OPO was based on a 10 mm long LBO crystal that used temperature-tuned, type I, non-critically phase matching to typically produce wavelength tunable ~ 2 ps pulses from 780 nm to 900 nm for the signal pulse and from 1270 nm to 1625 nm for the idler pulse. LBO employing this phase matching arrangement was chosen because it had distinct advantages over other possible nonlinear crystals such as KTP and BBO. While a singly resonant oscillator (SRO) has a much higher threshold than a doubly resonant oscillator (DRO), the SRO provides much more stable operation than the DRO. The 6.5 kW pump pulses from the fibre-diffraction pulse compressor could drive the LBO OPO more than 6 times above threshold, when there were minimal cavity losses, higher than previous ps, synchronously pumped LBO OPOs have achieved. The threshold for the OPO with minimal losses was found to be near 1 kW, indicating that threshold could not have been achieved without the frequency doubled compressed pump pulses.

With the OPO operating without any intracavity elements except the LBO crystal and minimal cavity losses internal conversion efficiencies of ~ 70 % (the theoretical maximum) were achieved at greater than 4 times above threshold. Typically, Gaussian-like ~ 2 ps, ~ 1 kW signal and idler, non-transform-limited pulses were produced at more than ~ 3 times above threshold, and, as expected by theory, the signal and idler pulses were ~ 1.2 ps in duration (~ 0.5 Δt_{pump}) and closer to transform-limited near threshold. It was noticed at this stage that the resonated signal would sometimes oscillate on more than one wavelength simultaneously and that while the signal beam profile remained close to a TEM_{00} mode the idler beam profile could change from a Gaussian-like beam profile into a ring shaped beam profile when the cavity length was shortened. This made the idler pulses unsuitable for use as seed pulses for the OPAs, as originally planned. Effort was henceforth put into making the signal pulses single frequency and close to transform-limited making the suitable as the seed pulses for the OPAs.

To do so meant changing the OPO from a one-arm cavity to a dual-arm cavity so that a dispersion compensating prism pair could be inserted into one of the arms and an output coupler into the other, where the circulating beam was not spectrally dispersed. At the same time the pump beam was made fully cw. Previously the beam from the Antares laser had been chopped to reduce the average power to protect the optical fibre from damage. The fibre mount was successfully redesigned so that the full cw power of the Antares laser could be used without damaging the fibre. This allowed SHG interferometric autocorrelations to be performed on the signal pulses from the dual-arm OPO to determine the level of and source of the phase modulation occurring in the cavity.

For the dual-arm OPO operating without the prism pair the OPO could be driven up to 3.5 times above threshold where the internal conversion efficiency was 50 %. The interferometric autocorrelations showed that the signal pulses suffered from frequency chirping due to the combined effects of GVD, SPM and XPM occurring in the cavity. With a specifically designed SF10 prism pair inserted into one of the arms of the OPO the frequency chirping evident in the "free running" OPO signal pulses was effectively compensated. The interferometric autocorrelations showed no evidence of frequency chirping and agreed with the pulse durations measured from the intensity autocorrelations to within experimental error. The signal pulses from this "stabilised" OPO had peak powers from 130 W to 200 W and had pulse durations near 1.5 ps. The stabilised OPO could be driven up to 2.25 times above threshold where the internal conversion efficiency was ~ 40 %. At a prism insertion depth of 1 mm the OPO performed very well, operating stably and reliably and producing near transform-limited, wavelength tunable signal pulses from 780 nm to 900 nm.

It was found that the ring shaped idler beams from the LBO OPO were caused by non-collinear phase matching. One property of synchronously pumped OPOs is that cavity length detuning will cause the oscillating pulse's wavelength to shift. This is because the oscillating pulse experiences a higher gain if it shifts its wavelength to one with an

appropriate group velocity that compensates for the induced timing error between the pump pulse and the resonated pulse. The wavelength causes a phase mismatch into the parametric process which limits the extent the resonated pulse can shift its wavelength. In the LBO OPO as the cavity length was shortened the phase mismatch could be compensated by phase matching a few milliradians off the x-axis of the LBO crystal, ie. by non-collinear phase matching. This would cause the ring shaped idler beam profiles. The signal beam profiles always remained Gaussian because the beam was constrained by the optical cavity.

The widely spaced, multiple wavelength oscillation was not necessarily associated with the appearance of the ring shaped idler beam profiles. In some cases the idler beam profiles remained Gaussian-like over the entire cavity length detuning range while the signal would oscillate on multiple wavelengths. The ring shaped idler beam profiles were sometimes observed when there was only one signal wavelength. The multiple wavelength oscillation was attributed to a complex interaction between phase modulation and parametric gain in the OPO. The multiple wavelength oscillation only occurred when the free running OPO was operating more than ~ 3 times above threshold where there was considerable phase modulation. The OPO appears to preferentially amplify the peaks of SPM/XPM signal spectra, usually resulting in two separate wavelengths oscillating simultaneously in the cavity. The temporal pulse profile of the signal and idler pulses is expected to be a strongly amplitude and phase modulated Gaussian-like pulse with the modulation period equal to 1/beat frequency of the two separate wavelengths.

The pump pulses for the OPAs were provided by group velocity mismatched (GVM) SHG in two 1.75 cm KDP crystals cut for type II frequency doubling of 1054 nm. The fundamental pulse passed through a 1 inch long KDP crystal before entering the two SHG crystals to delay the e-ray with respect to the o-ray fundamentals by 3.3 ps. The 1054 nm fundamental pulse was provided by two Nd:YLF amplifiers. A ring regenerative Nd:YLF amplifier amplified a chirped pulse from the Antares laser, increasing the energy from ~ 13 nJ to up to 1.5 mJ while simultaneously reducing the pulse duration from 60 ps to 6 ps. A single pulse Nd:YLF amplifier then amplified the pulse to up to ~ 18 mJ. Initial measurements of this fundamental pulse found that it was close to being transform-limited, within experimental errors. However, the GVMSHG performed poorly. The energy conversion from fundamental into SH was in significant disagreement with numerical simulations performed to model the GVMSHGsystem. It was expected from the numerical simulations that the SH pulse would be compressed to a central peak ~ 200 fs in duration with low sidelobes at a total fundamental intensity of 4.5 GW/cm^2, and that the Gaussian beam averaged energy conversion would be between 35 % to 45 % at this intensity. Further investigation found that the fundamental beam was excessively divergent in one plane and this was attributed to thermal loading in the Nd:YLF laser rod of the single pass amplifier. The problem was alleviated by reducing the firing rate of the amplifiers from 20 Hz to below 10 Hz and by adjusting the orientation of the KDP crystals so that the o-ray axis was aligned with the more divergent plane of the fundamental beam. However, when using this corrected beam the SH pulse showed only small amounts of pulse compression to ~ 2 ps in the central portion of the beam at much higher intensities than theoretically expected. At this stage it was suspected that the fundamental beam may suffer from phase modulation. Self diffraction frequency resolved optical gating (SD FROG) measurements of the fundamental pulse revealed that the pulse was indeed phase modulated, with the phase modulation consisting primarily of a linear frequency chirp. It was argued that since the effective phase mismatch due to the phase modulation in the pulse was at least as great as the effective phase mismatch due to the SHG gain and much greater than the effect of GVM that it would significantly affect the SH pulse compression. A diffraction grating pulse compressor, constructed by Prof. Luther-Davies at the time of writing of this thesis, compressed the fundamental pulse from 6 ps to 4 - 4.5 ps in duration. It is expected that since the frequency chirping has now been compensated that the GVMSHGwill perform to theoretical expectations when experiments are conducted in the near future.

172

Numerical simulations were conducted of a two crystal optical parametric amplification system. The first OPA, OPA1, was chosen to be a 4 mm long LBO crystal using type I critical phase matching. The 527 nm pump Gaussian pulses for OPA1 was taken to be 500 fs to 1 ps in duration with a peak power of 320 MW (a small portion of the SH pulse from the GVMSHGsystem), giving a intensity of 20 GW/cm^2 in OPA1. The seed pulses for OPA1 were taken to be Gaussian pulses 1.5 ps to 2 ps in duration with peak powers from 25 W to 125 W. These are typical of the pulses that were provided by the stabilised LBO OPO. The pulse duration's of the output pulse were found to be independent of the initial seed signal pulse duration and only weakly dependent on the pulse duration of the pump pulse. The gain of OPA1 was ~ 1 x 10^5 providing ~ 300 fs, ~ 1 MW signal pulses from 800 nm to 900 nm when the Gaussian beam profile of the pump beam was taken into account. The peak power of the output pulses varied linearly with variation in wavelength and seed signal peak power. As expected it was very sensitive to variations in pump power due to the high gain involved.

The second OPA, OPA2, was modelled on a 12 mm KD*P, type I OPA; a 3 mm LBO, type I OPA; a 2 mm BBO, type I OPA; and a 2.5 mm BBO, type II OPA. Taking the 300 to 500 fs, ~ 1 MW signal pulse from OPA1 as the seed pulses for amplification and 527 nm, 500 fs to 1 ps, 2.5 GW Gaussian pulses as the pump pulses, giving a maximum pump intensity was 40 GW/cm^2, each OPA2 was modelled. It was found small amounts of predelay can marginally improve the energy conversion. The energy conversion was insensitive to variation in the seed signal peak power and variation in wavelength. The peak power and energy conversion was improved by using pump and seed signal pulses that were as short as possible and of the same value. The pulse duration's of the output pulses were not greatly influenced by changing the peak power, wavelength or the initial pulse duration's of the pump and seed signal pulses. When the Gaussian beam profile of the pump beam was taken into account it is expected that ~ 300 fs, ~ 600 MW signal pulses and ~ 300 fs, ~ 300 MW idler pulses will be produced from OPA2. The overall stability of the OPAs would be dependent on the temporal stability of the compressed SH pulse from the GVMSHGsystem. However, the peak power and energy conversion of the output pulses were not very sensitive to variations in pump or seed signal power.

The best OPA2 would probably be the 2 mm BBO I OPA or a 2.5 mm to 3 mm long LBO I OPA. The KD*P I OPA has insufficient nonlinearity and the BBO II OPA has a restrictive spectral acceptance bandwidth. Though this restrictive bandwidth may be useful in constraining any excessive bandwidth of the output pulses.

The lack of a suitable SH pulse from the GVMSHG system at this time prevented experiments with the OPAs.

The last Chapter reported the diagnostic tools mainly used to measure the temporal characteristics of the various pulses throughout this thesis. To measure the wavelength variable signal and idler pulses from the OPO LBO based intensity and interferometric autocorrelators were used. The intensity autocorrelator measured the temporal intensity of the pulses using slow scanning (~ 1 min) or fast scanning (~ 200 Hz). The interferometric autocorrelator revealed information about the phase structure of the pulses. The high power 1054 nm and 527 nm pulses from the GVMSHGsystem were recorded using a KDP SHG intensity autocorrelator. The phase modulation in the high power 1054 nm pulses was measured using a SD FROG apparatus. All the diagnostic tools performed well and reliably, providing important information about pulses and the devices used to produce them.

8.1 Future work

The work in this thesis can be extended in a number of ways. The most important, of course, is to use the reduced chirped, ~ 4.5 ps, 1054 nm pulses from the Nd:YLF amplifiers to generate a compressed SH pulse from the GVMSHG system so that the OPAs can be constructed and tested. This can happen at anytime in the near future.

Other work that could be perform includes modelling the free running LBO OPO to quantitatively find the mechanisms behind the widely spaced, multiple wavelength oscillation and improving the fibre-diffraction grating pulse compressor so that it performs more efficiently with the full cw beam.